Kinetic discriminations for selective analysis in complex mixtures : applications in imaging

Jérôme Querard

To cite this version:

Jérôme Querard. Kinetic discriminations for selective analysis in complex mixtures : applications in imaging. Analytical chemistry. Université Pierre et Marie Curie - Paris VI, 2015. English. NNT : 2015PA066169 . tel-01213050

HAL Id: tel-01213050
https://theses.hal.science/tel-01213050
Submitted on 7 Oct 2015

UNIVERSITÉ PIERRE ET MARIE CURIE

École doctorale 388 :
Chimie Physique et Chimie Analytique de Paris Centre

Laboratoire PASTEUR - UMR 8640
Pôle de Chimie Bio-Physique

Kinetic discriminations for selective analysis in complex mixtures - Applications in imaging

Présentée par

Jérôme QUÉRARD

Thèse de doctorat de Chimie-Physique

Dirigée par

Ludovic JULLIEN et Thomas LE SAUX

Présentée et soutenue publiquement le vendredi 12 juin 2015

Devant le jury composé de :

M. Dr.	Emmanuel	BEAUREPAIRE	Rapporteur
M. Dr.	Dominique	BOURGEOIS	Examinateur
M. Prof.	Dieter	BRAUN	Examinateur
M. Dr.	Arnaud	GAUTIER	Invité
M. Prof.	Ludovic	JULLIEN	Directeur de thèse
M. Dr.	Andrey	KLYMCHENKO	Rapporteur
M. Dr.	Thomas	LE SAUX	Co-encadrant
M. Prof.	Emmanuel	MAISONHAUTE	Examinateur

List of abbreviations

DFHBI :	3,5-difluoro-4-hydroxybenzylidene imidazolidinone
DNA :	Deoxyribonucleic acid
FACS :	Fluorescence-activated cell sorting
FCS :	Fluorescence correlation spectroscopy
FLIM :	Fluorescence lifetime imaging microscopy
FP :	Fluorescent protein
FRET :	Förster resonance energy transfer
GFP :	Green fluorescent protein
HBI :	Hydroxybenzylidene imidazolidinone
IC :	Internal conversion
ISC :	Inter system crossing
LED :	Light-emitting diode
ND :	Not determined
OLID :	Optical lock-in detection
OPIOM :	Out-of-phase imaging after optical modulation
OPTIMAL :	Out-of-phase titration after modulation of activating light
PAFP :	Photoactivatable fluorescent protein
PDMS :	Polydimethylsiloxane
PCR :	Polymerase chain reaction
PSFP :	Photoshiftable fluorescent protein
QD :	Quantum dot
RNA :	Ribonucleic acid
RSFP :	Reversibly (photo)-switchable fluorescent protein
SAFIRe :	Synchronously amplified fluorescence imaging recovery
SELEX :	Systematic evolution of ligands by exponential enrichment
SPIM :	Single-plane illumination microscopy
UV :	Ultra violet

Contents

1 General Introduction 13

- 1.1 A singular chemical mixture : the living cell . . . 14
- 1.2 Imaging cellular components . . . 14
  - 1.2.1 General principles in analysis . . . 14
  - 1.2.2 Probes . . . 15
    - 1.2.2.1 Constraints . . . 15
    - 1.2.2.2 Opportunities . . . 15
  - 1.2.3 Observables . . . 16
    - 1.2.3.1 Absorbance . . . 16
    - 1.2.3.2 Raman scattering . . . 17
    - 1.2.3.3 Fluorescence . . . 17
    - 1.2.3.4 Lifetime . . . 19
    - 1.2.3.5 Conclusion . . . 20
  - 1.2.4 Actions . . . 20
    - 1.2.4.1 The action parameters . . . 20
    - 1.2.4.2 The perturbation strategy . . . 22
    - 1.2.4.3 The retrieval of the kinetic information . . . 23
  - 1.2.5 Conclusion . . . 23
- 1.3 Fluorescent probes . . . 24
  - 1.3.1 Small organic fluorescent dyes . . . 24
  - 1.3.2 Fluorescent nanoparticles . . . 24
  - 1.3.3 Fluorescent proteins . . . 25
  - 1.3.4 Turn on fluorescent probes . . . 26
  - 1.3.5 Conclusion . . . 26
- 1.4 State-of-the-art : Optical imaging techniques exploiting the kinetic information of a photo-active targeted probe . . . 27
  - 1.4.1 Fluorescence lifetime imaging microscopy (FLIM) . . . 27
    - 1.4.1.1 Principle . . . 27
    - 1.4.1.2 Implementation . . . 29

1.4.2 Optical lock-in detection (OLID) 29
1.4.2.1 Principle 29
1.4.2.2 Experimental validation 30
1.4.3 Synchronously Amplified Fluorescence Image Recovery (SAFIRe) 32
1.4.3.1 Principle 32
1.4.3.2 Experimental validation 33
1.5 Conclusion 37

2 A first realization : one color OLID 39
2.1 Introduction 39
2.1.1 Context 39
2.1.2 Presentation of Spinach 40
2.1.2.1 Identification of fluorescent RNA-fluorogen complexes 40
2.1.2.2 Recent developments of the Spinach system 42
2.1.3 Presentation of the article 43
2.2 Article 1 : Photochemical properties of Spinach and its use in selective imaging 45
2.2.1 Introduction 46
2.2.2 Results 47
2.2.3 Discussion 49
2.2.4 Conclusion 51
2.2.5 Material and Methods 51
2.2.6 Acknowledgments 53
2.2.7 Notes and references 53
2.3 Supporting Information 55
2.3.1 Theoretical model for the *cis*-DFHBI-Spinach RNA association experiments 57
2.3.2 Theoretical analyses 58
2.3.2.1 The generic dynamic model 58
2.3.2.2 Analysis of the reduced two state model 60
2.3.2.3 Analysis of the reduced three state model 67
2.3.3 Theoretical computations 69
2.3.4 Supplementary Figures 71
2.3.5 References 72

3 The theoretical framework : Out-of-phase titration after modulation of activating light (OPTIMAL) for selective and quantitative detection 73
3.1 Introduction 73
3.1.1 Context 73
3.1.1.1 Temperature modulation and quadrature detection 73

3.1.1.2 Another control parameter for a probing reaction 77
3.1.2 Presentation of the article 78
3.2 Article 2 : Expanding discriminative dimensions for analysis and imaging . . . 79
3.2.1 Introduction 80
3.2.2 Optimizing the response of a photoswitchable probe to periodic illumination 81
3.2.2.1 The model 81
3.2.2.2 Concentration response to constant illumination 82
3.2.2.3 Concentration response to sinusoidal modulation of small amplitude 82
3.2.2.4 Concentration response to square wave modulation of small amplitude 83
3.2.2.5 Concentration response to periodic modulations of large amplitude 83
3.2.3 Application to selective and quantitative detection of a photoswitchable probe 84
3.2.3.1 Out-of-phase response of the overall observable 85
3.2.3.2 Out-of-phase response of the fluorescence intensity 85
3.2.4 Discussion 85
3.2.4.1 A separation-free selective and quantitative analytical protocol 85
3.2.4.2 Experimental implementation 87
3.2.4.3 Fields of application 88
3.2.4.4 New challenges for probe development 88
3.2.5 Conclusion 88
3.2.6 References 88
3.3 Supporting Information 91
3.3.1 Reduction of photo(physical)chemical mechanisms to a two-state exchange 93
3.3.1.1 A photoswitchable probe 93
3.3.1.2 A three-state electronic model 94
3.3.1.3 A four-state model associated to titration of an analyte A 96
3.3.2 Kinetic analysis of the two-state model 99
3.3.2.1 The model 99
3.3.2.2 Light-jump experiments 99
3.3.2.3 Light modulation experiments 101
3.3.3 Retrieval of concentrations from the observables 117
3.3.3.1 Extraction of $\mathfrak{S}^0$, $\mathfrak{S}^{\mathrm{n,in}}$ and $\mathfrak{S}^{\mathrm{n,out}}$ from the overall signal $S(t)$ . . 117
3.3.3.2 Quantifying a targeted component 117

3.3.4 Improvement of the spatial resolution 121
3.3.4.1 Fluorescence imaging at zeroth order 121
3.3.4.2 Out-of-Phase Fluorescence imaging at first order 122
3.3.4.3 Comparison of the spatial resolutions from the fluorescence imaging protocols at zeroth- and first-order 122
3.3.5 References 123

4 Out-of-phase imaging after optical modulation (OPIOM) 125
4.1 Introduction 125
4.1.1 Context 125
4.1.2 Presentation of Reversibly Photoswitchable Fluorescent Proteins 130
4.1.2.1 Dronpa and its variants 130
4.1.2.2 Mechanism of photoswitching in the Dronpa family 133
4.1.2.3 Other RSFPs 134
4.1.2.4 Using reversibly photoswitchable fluorescent proteins 136
4.1.3 Investigated systems for experimental validation 137
4.1.4 Presentation of the article 137
4.2 Article 3 : Photoswitching kinetics and phase sensitive detection add discriminative dimensions for selective fluorescence imaging 140
4.3 Supporting Information 146
4.3.1 Legends of Figures 2 and 3 148
4.3.2 Materials and methods 149
4.3.2.1 Cloning 149
4.3.2.2 Protein production and purification 150
4.3.2.3 Mammalian cell culture and transfection 150
4.3.2.4 Zebrafish experiments 151
4.3.2.5 Spectroscopic instruments 151
4.3.2.6 Microfluidic device 152
4.3.2.7 Microscopy epifluorescence setup 152
4.3.2.8 Single plane illumination (SPIM) setup 153
4.3.2.9 Softwares 154
4.3.3 Supplementary text 1: Photoswitchable fluorophore responses to light modulations 155
4.3.3.1 The model 155
4.3.3.2 Response to light jumps 155
4.3.3.3 Response to sinusoidal light modulation of small amplitude . . 156
4.3.3.4 Optimal out-of-phase response 157
4.3.3.5 Response to periodic light modulation of large amplitude 159

4.3.3.6 Retrieval of concentrations from the fluorescence intensity . . . 160
4.3.3.7 Selective and quantitative detection 162
4.3.4 Supplementary Text 2: Reduction of photo(physical)chemical mechanisms to a two-state exchange 164
4.3.4.1 A photoswitchable probe 164
4.3.4.2 A three-state electronic model 165
4.3.5 Supplementary text 3: Significance of irreversible bleaching for OPIOM application 168
4.3.6 Supplementary text 4: Determination of the kinetic parameters through light jump experiments 170
4.3.7 Supplementary text 5: Determination of the kinetic parameters through light modulation experiments 172
4.3.8 Supplementary text 6: Imaging protocols 174
4.3.8.1 Video acquisition 174
4.3.8.2 Microdevice imaging 175
4.3.8.3 Cell imaging and zebrafish embryo imaging with epifluorescence microscopy 175
4.3.8.4 Embryo imaging with Single Plane Illumination Microscopy . . 176
4.3.8.5 Image filtering 176
4.3.8.6 Evaluation of contrast enhancement associated to OPIOM image processing 176
4.3.9 Supplementary Figures 177
4.3.10 Matlab code for OPIOM imaging 185
4.3.11 References 187

5 Out-of-phase imaging after optical modulation with two colors 189
5.1 Introduction 189
5.2 Two-color OPIOM 190
5.2.1 Principle 190
5.2.2 Determination of the photochemical parameters 191
5.2.3 Application in imaging 192
5.2.3.1 Selective and quantitative imaging 192
5.2.3.2 Selective imaging in cells 195
5.2.3.3 Selective imaging in multicellular organisms 197
5.2.4 Conclusion 198
5.3 Supporting information 199
5.3.1 Supplementary text 1: Photoswitchable fluorophore responses to illuminations 199

5.3.1.1 The model 199
5.3.1.2 Response to light jumps 199
5.3.1.3 Response to sinusoidal light modulation of small amplitude . . 200
5.3.1.4 Optimal out-of-phase response 202
5.3.1.5 Response to periodic light modulation of large amplitude 203
5.3.1.6 Retrieval of concentrations from the fluorescence intensity . . . 206
5.3.1.7 Selective and quantitative detection 207
5.3.2 Supplementary text 2: Imaging protocols 210
5.3.3 Materials and methods 213

6 Discussion **215**
6.1 Comparison of FLIM, OLID, SAFIRe and OPIOM 215
6.1.1 Contrast enhancement 215
6.1.2 Choice of the illumination conditions 216
6.1.3 The retrieval of the kinetic information 216
6.1.4 Selectivity 217
6.1.5 Quantitative character 219
6.1.6 Acquisition time and temporal resolution 220
6.1.7 Experimental setup, wide-field imaging and 3D-resolved imaging 221
6.2 Development of photoswitchable probes for OPTIMAL and OPIOM 221
6.2.1 RSFPs for one-color OPIOM 222
6.2.2 RSFPs for two-color OPIOM 222
6.2.3 RSFPs for multiplexed observations 222
6.2.4 Turn on fluorescent probes 223
6.A OPIOM and Spinach (Theoretical analyses) 224
6.A.1 The generic dynamic model 224
6.A.2 The reduced dynamic model 225
6.A.3 Kinetic analysis 226
6.A.3.1 Assumptions 226
6.A.3.2 Sinusoidal modulation of small amplitude 228

7 General conclusion and perspectives **233**
7.1 Photochromism and light modulation 233
7.2 Perspectives 234
7.2.1 FRET and OPIOM 234
7.2.2 Brainbow and OPIOM 235
7.2.3 Remote sensing in plants 236

8 Experimental Part **239**
8.1 Probes production 239
8.2 Spectroscopic Instruments 239
8.3 Determination of the kinetic parameters of the RSFPs 239
8.4 Systems 240
8.5 Microscopy setups 240
8.6 Imaging protocols 240

Bibliography **243**

Chapter 1

General Introduction

Analytical chemistry aims at identifying and quantifying one or several species of interest in a mixture. This task may seem obvious if we refer to the solutions that are analyzed during practical chemistry courses. Nevertheless, 'real' mixtures to analyze are much more complex. For instance, a synthesis usually leads to a mixture containing the product of interest with additional side-products whose nature and properties are unknown. Biological media are chemical mixtures of exceptional interest and significance. Their investigation and detailed analysis require developing analytical tools fulfilling the demanding constraints resulting from their singular features. Indeed, biological samples such as a living cell are highly complex. In particular, multiplexed observation of myriads of mixture components with the highest possible spatiotemporal resolution appears highly desirable. As we shall see later, one attractive road to address this challenge relies on exploiting the rich kinetic signature of probes engaged in a reactive network. The selectivity for targeting a given mixture component then results from the capability to address a network of reactions characterized by its topology as well as by its rate constants. This general introduction is organized as follows. After emphasizing on the singularity of living cells contents as chemical mixtures, we examine the three key actors - probes, observables, and action - intervening for cell imaging. We eventually review the state of the art of cell imaging exploiting kinetic information of targeted photo-active probes. We end up with the definition of the goals and the presentation of the manuscript of this PhD work.

1.1 A singular chemical mixture : the living cell

With respect to classical mixtures addressed in Analytical Chemistry, a living cell displays several features making it highly singular.

- A cell contains an extremely large number of mixture components (10^4 - 10^6) rather similar (e.g. proteins, RNAs).
- The concentrations of the mixture components cover more than a ten orders of magnitude range.[1–3]
- A cell exhibits a spatial heterogeneity as evidenced from the presence of numerous interacting compartments present in a cell and from the 2D-heterogeous organization of the cell membrane. Within the cells, cytoskeleton maintains the intracellular arrangement of the organelles such as the nucleus, mitochondria... whereas the cytoplasm contains macromolecules (e.g. proteins, RNAs...), small molecules and ions.
- At steady-state, different processes take place at various timescales (protein production, phosphorylation, translocation...).
- A cell is an out-of-equilibrium alive state that exchanges energy and matter with the external medium.

Novel dedicated analytical tools (in particular non-invasive) have to be developed to face such features.

1.2 Imaging cellular components

1.2.1 General principles in analysis

An analytical method must be selective to accurately quantify the species of interest in the investigated mixture. Indeed, analyzing consists in differentiating the target from the other mixture components. Thus, the first question to address is : what are the differences between the components of a mixture ? Detecting a targeted species within a complex mixture requires a probe. As a consequence, the second question is : which probe should be chosen to target a given component ? Other considerations are here expected to intervene for choosing the probe. Thus, the associated observable should be carefully analyzed in terms of selectivity, sensitivity, biocompatibility... Moreover, one should also consider the actions that can be applied on the system to read-out the signal of the probe (see below).

1.2.2 Probes

This subsection addresses the constraints and the opportunities provided by endogenous and exogenous probes for imaging cellular components.

1.2.2.1 Constraints

Addressing a given component in a mixture without any separation requires a probe, which can be either endogenous or exogenous. Ideally, to be able to target any component in the mixture requires establishing commensurability between the discriminative efficiency and the number of mixture components.

1.2.2.2 Opportunities

The first category of probes is composed of structural probes. They integrate either specific atoms or functional groups, which are generally read-out by a spectroscopy. In the biological context, endogenous probes are not enough numerous to permit discrimination of the myriads of similar cellular components. Indeed, only 92 atoms are stable which is not commensurable with the number of mixture components. The succession of atoms in a molecule leads to the formation of organic functional groups. Again, biomolecules (e.g. proteins, nucleic acids) contains essentially the same functions that does not allow to distinguish them. To circumvent these limitations, exogenous probes have been used to specifically label a desired mixture component. If this exogenous probe exhibits unnatural chemical functions or singular spectroscopic properties, it can be employed to give a unique signature.

The second category of probes is composed of probing reactions. The targeted mixture component is not anymore directly read-out. In contrast, it is engaged in one (or more) chemical reaction(s) and it is now the signal from a reporting exogenous reagent, which is used to retrieve information on the targeted component. The prototype of this approach is the titration, which relies on a titrating reagent added to the medium to be analyzed that probes specifically the analyte of interest thanks to a chemical reaction. With respect to structural probes, securing selectivity for addressing a given mixture component does not anymore originate from the labeling step, but from the specificity of the reaction of the reporting reagent with the targeted component. In a first approach, the selectivity may result from a difference between the equilibrium constants associated to each mixture component regarding the chemical reaction. Nevertheless, in a mixture containing similar components, a probe may exhibit close affinities for several targets. To overcome this issue, selectivity needs to be improved. Relying on kinetics instead of thermodynamics permits to increase the number of discriminative parameters. Indeed, in the most simple case (two-state exchange), two independent rate constants instead of one single thermodynamic constant are associated to the titration reaction for each component of the mixture. Thus, titration under kinetic control gives access to a space of discriminative parameters of larger dimension.

1.2.3 Observables

The observable used for reading-out the signature from the label(s) involved in the probe (an intensity, a lifetime...) contributes to determine the selectivity (via the ratio of its bandwidth over its dynamic range) and the sensitivity (via the minimal detectable probe concentration, which determines the fraction of mixture components to be explored) of the probe analysis. It also governs the spatiotemporal resolution, which can be obtained for cell imaging. This subsection lists the most important observables, which have been currently used to image living cells.

1.2.3.1 Absorbance

The ability of a solution containing a probe to absorb light is quantified by its absorbance[a] A. The Beer-Lambert law expresses the absorbance of the probe as a function of its concentration c when excited at the wavelength λ_E :

$$A = \varepsilon(\lambda_E) l c \tag{1.2}$$

where $\varepsilon(\lambda_E)$ denotes the molar absorption coefficient of the probe at wavelength λ_E and l the optical path of the sample. As a result, measuring the absorbance enables to determine the concentration of the probe either with the value of the molar absorption coefficient or with a calibration curve.

The absorbance governs the contrast observed in bright-field microscopy. In this case, the sample is illuminated with white light from the bottom. The transmitted light is detected through the ocular. Thus, in a typical image from bright-field microscopy, the sample appears dark with a bright background due to the absorption of light by the dense areas of the sample. The contrast is generally poor. In addition, due to the heterogeneity of the biological medium, light scattering can interfere with the absorption phenomenon.

Sensitivity The detection limit in absorption spectroscopy is around 1 μM.[4] In the case of low absorbance measurements, two large signals slightly different are compared.[5] This results in a relatively low sensitivity of a microscopy based on absorbance.

---

[a] The absorbance A of a solution can be expressed as function of the incident I^0 and transmitted I_T light intensities :

$$A = \log\left(\frac{I^0}{I_T}\right) \tag{1.1}$$

1.2.3.2 Raman scattering

Molar absorption coefficients for transitions between vibrational levels are smaller than the ones associated to transitions between electronic states, which restricts their use to image the most abundant components of cells. In addition, the water signals can strongly interfere with infra-red light absorption. However, Raman scattering can be used to reveal vibrational levels of a molecule. Raman effect is an inelastic process : the scattered photons have either a lower (Stokes) or a larger (anti-Stokes) energy compared to the one of the incident photons.[6] The energy difference between the incident and scattered photons corresponds to the energy difference between two vibrational states. Raman microspectroscopy is a label-free technique for cell imaging but with limited speed and sensitivity.[7] Advanced Raman techniques such as Coherent anti-Stokes Raman scattering (CARS)[8,9] and Stimulated Raman Scattering (SRS)[10,11] have recently emerged with a significant improvement of the sensitivity.

1.2.3.3 Fluorescence

Upon absorption of a photon of appropriate wavelength, a fluorophore is promoted to its first excited singlet electronic state S_1. The excited molecule returns to its fundamental electronic state (S_0) in different manners (see Figure 1.1).

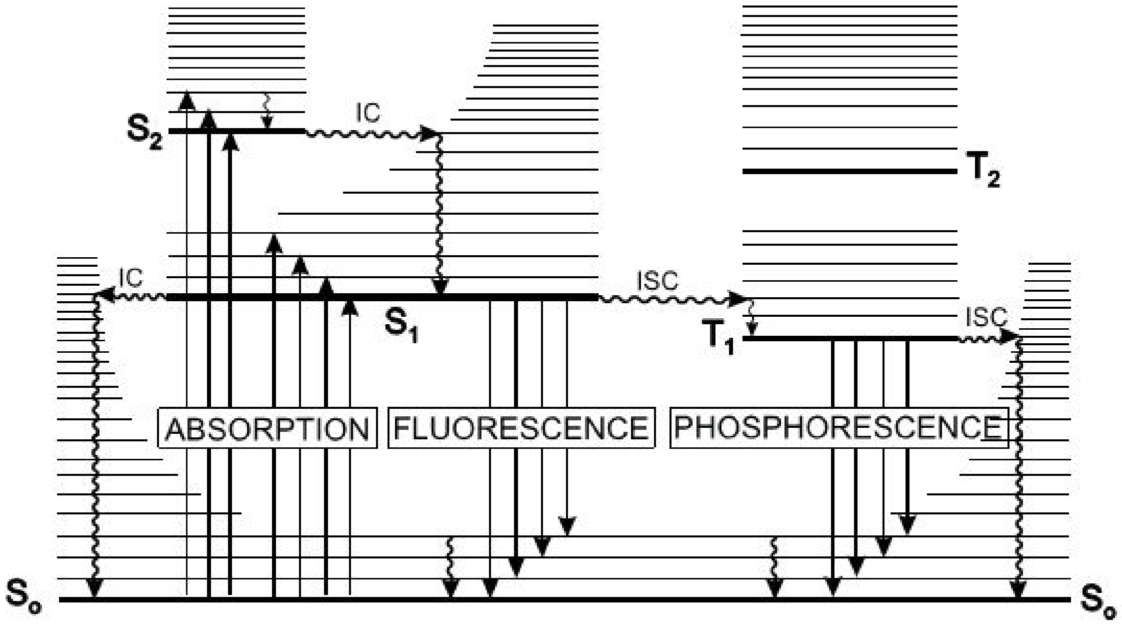

Figure 1.1: Perrin-Jablonski diagram. The singlet electronic states are denoted S_0, S_1, S_2... and the triplet electronic states T_1, T_2... The vibrational levels associated to each electronic state are also indicated. IC : Internal conversion, ISC : Inter system crossing (see text). Adapted from Valeur.[5]

The relaxation $S_1 \rightarrow S_0$ accompagnied by the emission of photons is called fluorescence.

The general expression of the fluorescence emission detected at λ_F of a fluorescent probe at concentration c excited at λ_E is[5] :

$$I_F(\lambda_E, \lambda_F) = kF_\lambda(\lambda_F) I^0(\lambda_E) \left\{1 - \exp\left[2.3\varepsilon(\lambda_E) lc\right]\right\} \tag{1.3}$$

where

- the proportionality factor k depends on several parameters such as the solid angle through which the instrument collects fluorescence, the bandwidth of the monochromators and the sensitivity of the apparatus
- $F_\lambda(\lambda_F)$ represents the emission spectrum of the fluorescent probe (it is the intensity of fluorescence per absorbed photon as a function of the wavelength of the emitted photons)
- $I^0(\lambda_E)$ is the intensity of the incident light at λ_E

In diluted solutions, a first-order expansion of Eq. 1.3 leads to :

$$I_F(\lambda_E, \lambda_F) = 2.3kF_\lambda(\lambda_F) I^0(\lambda_E)\varepsilon(\lambda_E) lc \tag{1.4}$$

This relation shows that the fluorescence emission is proportional to the concentration of the probe only at low absorbances. If the wavelengths of excitation and detection do not vary, the emission fluorescence can be simply written :

$$I_F = Q \times I^0 \times c \tag{1.5}$$

where Q is generally called brightness of the probe.

Since few molecules exhibit fluorescence, microscopies based on this observable are usually highly selective.

Sensitivity Compared to spectrophotometry, fluorometry is up to 1000 times more sensitive.[5] This results from the fact that fluorescence intensity is measured above a low background level. This singular property has led to the engineering of a large collection of fluorescent probes and the development of many microscopies based on fluorescence for investigating biological samples.

Resolution The spatial resolution when fluorescence is employed as observable is limited by the diffraction limit at the considered wavelength which is $\sim \lambda/2$. Hence, in fluorescence microscopy, the spatial resolution is around 250-300 nm. Several super-resolution techniques have been developed to break this diffraction limit (see the introduction of chapter 4) enabling to reach a spatial resolution of a few tens of nanometers.

Limitations Even though the most widely employed techniques for bio-imaging are based on fluorescence spectroscopy, several limitations especially in terms of selectivity are encountered in biological media.

Intrinsic to biological media As already mentioned, the biological samples are generally heterogeneous so as to generate light scattering that can interfere with the signal of interest. In addition, cells and multicellular organisms contain endogenous fluorophores such as tryptophan emitting in ultraviolet range and flavins or riboflavins emitting in the visible spectrum. This phenomenon called autofluorescence results in a high background in fluorescence microscopy. Using bright fluorescent probes often enables to overcome this issue. Nevertheless, the tissue in organisms remains highly autofluorescent.

Intrinsic to fluorescent probes Multiplexed imaging consists in visualizing simultaneously several biomolecules of interest. For this purpose, they are labeled with fluorescent probes having different emission wavelengths to be able to distinguish them. The different probes can be imaged alternatively using appropriate emission filters combined with excitation sources. However, the emission bands of most fluorophores are relatively broad. As a consequence, only a few biomolecules can be simultaneously imaged in fluorescence microscopy. Beyond three or four, the emission spectra of the probes tend to overlap and it is not anymore possible to discriminate the differently labeled biomolecules using emission wavelength. This phenomenon is called spectral crowding.

1.2.3.4 Lifetime

In addition to fluorescence, there are other de-excitation pathways of the first singlet state S_1 (see Figure 1.1) :

- Internal conversion : non-radiative transition between two electronic states with the same spin multiplicity followed by a vibrational relaxation to the fundamental vibrational level of the final electronic state;

- Intersystem crossing and subsequent processes : non-radiative transition between two isoenergetic vibrational levels belonging to two electronic states of different multiplicities ($S_1 \rightarrow T_1$). The de-excitation of the triplet state T_1 toward the fundamental singlet state S_0 occurs either with emission of a photon (phosphorescence) or non-radiatively.

The excited-state lifetime measures the average duration that the molecule remains in its excited state.[5] For a first excited singlet state S_1 that deexcites by fluorescence, the typical value is around a few nanoseconds. In the case of the first triplet state T_1, the lifetime varies between 1 μs to 1s.[5] Thus, two emitters in the same wavelength range could be discriminated if they exhibit distinct excited-state lifetimes.

1.2.3.5 Conclusion

Among the different observables we reviewed in this subsection, fluorescence seems to be the most attractive due to its high selectivity and sensitivity resulting in numerous applications for cell imaging.

1.2.4 Actions

In most cases, one acquires a single observable associated to the exogenous label borne either by the targeted component (for structural probes) or by its reporting reagent (for probing reactions). However, a single observable may provide too limited opportunities for multiplexed observation (e.g. spectral crowding). Furthermore, as we have seen in subsection 1.2.3, interferences (e.g. autofluorescence, light scattering...) often intervene in complex biological media so as to necessitate more sophisticated approaches to efficiently discriminate the desired signal against the interfering background.

Relying on kinetic discrimination of reactive schemes in which exogenous probes are engaged is particularly fruitful. Indeed, provided they can be appropriately revealed, topology as well as rate constants governing these reactive schemes yield as many discriminating parameters to specifically target a given reactive probe. To reveal the chemical dynamics of the reaction(s) in which the exogenous probe is involved, we follow a strategy, which has been often used to investigate physical, chemical and also biological systems. It consists in the sequence :

1. perturbation of the system
2. response of the system to the perturbation
3. study of the response of the system by the operator

1.2.4.1 The action parameters

Revealing the chemical dynamics of the reaction(s) in which the exogenous probe is engaged requires to perturb one (or several) rates of these reactions. Therefore, the general theoretical frame is the one of relaxation methods.[12] First, rates can be modified by changing concentrations. Second, rates can be changed by altering the values of the rate constants upon perturbing physical parameters such as temperature or pressure. This subsection will introduce the different possibilities with their pros and cons.

Concentration In chemistry and biology, the delivery of known amounts of chemicals is of major importance. The usual way is to introduce the active species mechanically in the system. Pipettes and syringes of different formats permit to achieve this goal. However, they are invasive, which may be detrimental to fragile samples, such as a targeted cell in a living organism. An attractive alternative is to activate the release of the active species from an inactive precursor by using a non-invasive trigger (e.g. light). Nevertheless, the quantification of the delivered amount remains a significant issue.[13] First, calibration of the triggering beam can be rendered difficult due to the heterogenous nature of complex systems such as a living organism. Second, the local concentration of the inactive precursor is not necessary known, the delivery of a specific concentration of the active species is thus difficult. To tackle this quantification issue, one possible way is to simultaneously release a reporter in addition to the desired substrate. Quantitative analysis then can be done simply from analyzing the increase in the reporter signal.[13] This approach corresponds to the caged compounds that release a fluorescent reporter in addition to the active species. Combined with light, these caged compounds have enabled to greatly improve the temporal and spatial resolution for concentration jumps of active species. This kind of chemical has been the subject of many investigations in the group.[13–17]

Temperature Most chemical reactions including biological processes exhibit a significant activation enthalpy, meaning that the rate of the reaction can be controlled by temperature. This parameter has been widely used to investigate mechanisms and determine rate constants.[12] Its modulation can be implemented in many ways by relying on microdevice,[18–20] infrared laser[21–23] or nanoparticle[24–26] as modulated heating sources. Furthermore, temperature modulation of small amplitude is non-invasive and compatible with *in vivo* imaging.[22]

Pressure Pressure can also make vary the rate constant of a reaction if its activation volume $\Delta_r V^{\neq}$ is sufficiently large. This parameter has been employed particularly to investigate acid-base reactions especially ionization of neutral acids.[12] However, large jumps of pressure are needed to observe significant change in rate constants.[12] They are accompanied simultaneously by a variation of temperature.[12] In addition to pressure jumps methods, ultrasonic techniques have been widely used for analyzing chemical relaxation.[27] The propagation of sound waves through a medium is accompanied by small periodic pressure, temperature and density fluctuations.[12,27] Thus, it can be used to introduce changes of the rate constant of a reaction due to pressure and/or temperature variations. In addition, ultrasonic waves are compatible with living organisms since they are employed for instance in ultrasonography .

Light In the particular case of a photo-chemical reaction, light is the trigger of choice to modify the value of the rate constants simply by changing the intensity of the excitation light. This parameter exhibits numerous advantages :

- it is non-invasive;

- it is compatible with *in vivo* imaging as showed by the numerous microscopes developed for imaging of living cells or organisms;
- it is easily modulatable : for instance, the intensity of the light emitted by a LED can be modified simply by modulating the driving current in the circuit;
- temporal resolution : optical methods exhibit the best temporal resolution accessible in chemistry. It can reach microsecond[28] and even the femtosecond range when using a pulsed laser;[29]
- the spatial resolution of the optical methods is also very good : a light beam can be focalized up to the diffraction limit at the considered wavelength. In addition, the biphoton excitation reaches an even better resolution since only the volume corresponding to the focal point of the lens yields to photoactivation. This volume is of the order of one femtoliter and so three orders of magnitude smaller than a cell.[30]

1.2.4.2 The perturbation strategy

As we explained before, relying on kinetics instead of thermodynamics increases the number of discriminative parameters. Revealing the chemical dynamics of the reaction is achieved by applying a perturbation that forces the system out-of-equilibrium. Two kinds of perturbation can been used: (i) jumps of parameter values; (ii) periodic modulation of the parameter values.

Jump of parameter values Let us consider a chemical system at equilibrium. A perturbation is brought to the system by a sudden change of an external parameter such as temperature, pressure or concentration. The chemical dynamics is observed by monitoring the temporal evolution of the concentration of one or several species immediately following the perturbation. In fact, we investigate the relaxation of the system toward its new equilibrium state. Such methods are called jump or transient methods.[12,27] When the amplitude of the perturbation is small enough and in the simplest case (exchange between two states), the time-dependence of the monitored concentration decays mono-exponentially permitting to extract the relaxation time associated to the chemical reaction.

Periodic modulation of parameter values In this case, an oscillating perturbation is applied that periodically forces the chemical system out-of-equilibrium. Beyond the relaxation time associated to the reaction, the system enters a forced and permanent regime. This second class of relaxation methods is known as stationary methods.[12,27] This leads to an oscillation of the concentrations of the species involved in the reaction with an amplitude and a phase lag compared to the periodic excitation that depend on the value of the product of the relaxation time by the angular frequency of the excitation.[12,27] The analysis of the dependence of the response of the system on the excitation angular frequency provides information about the dynamics of the system and in particular the relaxation time associated to the reaction. This strategy has been employed to determine rate constants and chemical mechanisms[12,31] and to separate overlapping bands in infrared spectroscopy.[32,33]

Pros and cons The jump methods seems easier to implement than periodic methods. Keeping constant the action parameter value appears more simple than making it oscillate with a specific forced function. Nevertheless, employing a periodic perturbation enables to accumulate the signal over several periods. This feature permits to average the noise and thereby results in an improved signal-to-noise ratio. In addition, a lock-in detection scheme can be employed for the demodulation of the periodic signal (see below).

1.2.4.3 The retrieval of the kinetic information

Various approaches have been explored to exploit kinetic information to selectively target the response from a given reactive exogenous probe. The simplest way is to correlate the overall response of the imaged medium to kinetic perturbation with the response of the pure reactive exogenous probe to be imaged.[34] Nevertheless, it is necessary to employ a reference that undergoes the same perturbation as the whole sample. OLID, which will be introduced later in the introduction adopts this approach. The second strategy is to rely on a kinetic model of the targeted reactive exogenous probe to specifically retrieve its contribution from the overall response of the medium. In this case, no reference is needed but the kinetic model has to be validated and to be not so much affected by the environment. As we shall see later, SAFIRe and OPIOM adopted this principle.

At that point, it is worth to note that the strategies developed for signal processing in electronics or in radio transmission could be very useful toward imaging.[34] Periodic signals can be easily demodulated thanks to Fourier transform. In addition, the lock-in[35] or synchronous detection is employed to extract signals that are up to hundreds or thousands times smaller than the noise level. This technique consists in extracting the modulated amplitude and phase of a signal of interest at a specific frequency (frequency-locked). The noise is strongly reduced since the contributions at all frequencies apart the targeted one are eliminated. Related approaches have been already implemented in optical imaging.[20–22]

1.2.5 Conclusion

Based on the singular features of the biological medium and on the previous considerations, an attractive microscopy to image living cells should fulfill several constraints. First, it should be non-invasive. Second, it should exploit the chemical dynamics of a reaction in which the exogenous probe is involved to give access to a space of discriminative parameters of large dimension. Third, fluorescence should be retained as the observable due to its favorable sensitivity. Fourth, employing a periodic light excitation to reveal the kinetics of the probe seems attractive.

In the following sections, we briefly introduce the fluorescent probes that are currently employed for imaging biological samples. We then review the different imaging techniques relying on the kinetic information of the targeted photo-active probe reported in the literature.

1.3 Fluorescent probes

Several classes of fluorescent probes have been developped for imaging in cell biology and in particular for studying the behavior of proteins.[36] In the following, we focus on small organic fluorescent dyes, fluorescent nanoparticles (quantum dots), fluorescent proteins (FPs) and small genetic encoded tags that can bind organic dyes. The aim is not to be exhaustive but to compare their main features.

1.3.1 Small organic fluorescent dyes

Numerous small organic fluorophores have been designed for chemical labeling of biological molecules. They have been optimized in terms of wavelength range, brightness and photostability. Many of them such as FITC®, Alexa®, Texas Red® are commercially available. The main advantage of these probes is their small size avoiding the disturbance of the natural function of the labeled biomolecule.[37,38] Since these fluorophores do not exhibit specificity for any particular protein, several methods have been developed to target these small molecules to the protein of interest.[37–39] The simplest approach is to conjugate the organic fluorophore to an antibody to enable protein detection (immunolabeling).[36] The protein of interest can be fused with an additional small polypeptide tag that binds specifically to a fluorophore (tetracysteine tag and biarsenical compound).[37,39] Another approach is based on a protein tag (SNAP-tag) that can be fused to any protein of interest and further specifically and covalently tagged with a fluorescent dye.[40]

1.3.2 Fluorescent nanoparticles

Quantum dots (QDs) are fluorescent semiconductor nanocrystals whose size is generally comprised between 1 and 10 nm. They possess unique optical properties due to the quantum confinement effect[41,42] and offer several advantages, such as size- and composition-tunable emission from visible to infrared wavelengths, large absorption coefficients across a wide spectral range, and very high levels of brightness[43] and photostability.[44,45] They are generally composed of atoms belonging to groups II and VI elements (e.g. CdSe and CdTe).[46]

The development of coatings rendering QDs water soluble and allowing conjugation to protein-targeting molecules such as antibodies or streptavidin is crucial for biological applications.[46–52] QDs were employed for real-time visualization of single-molecule motion in single living cells[53,54] and tracking of intracellular processes over long periods of time (minutes to hours) due to their high photostability.[55] QDs enabled also targeting and imaging of tumors in live animals.[56]

The potential cytotoxicity of QDs is an important issue. Derfus *et al* showed that CdSe QDs are highly toxic to cultured cells under UV illumination for long periods of time, due to the release of toxic cadmium ions into the culture medium.[57] However, QDs with a stable polymer coating have been found to be essentially nontoxic to cells and animals.[58] The study of the cellular toxicity and *in vivo* degradation mechanisms of QD probes are still important topics.[51] The large size of QDs when functionalized with biomolecules (~ 10 to 30 nm) prevents effective cell penetration.[36,51] QDs exhibit also non-specificity issues since they are not genetically encoded.

1.3.3 Fluorescent proteins

The most famous fluorescent protein (FP) is probably the green fluorescent protein (GFP) discovered in the jellyfish *Aequorea victoria* five decades ago.[59,60] Gene cloning[61] of GFP and its heterologous expression[62] in prokaryotic and eukaryotic cells have revolutionised cell biological imaging.[63–65] Many FPs have been developed to cover the whole visible spectrum[36,65–67] : BFP (blue), CFP (cyan), YFP (yellow), 'mFruits' series (mOrange,[68] mCherry,[68] mStrawberry). Far-red emitting FPs are also highly demanded since tissue light-penetration is increased at higher wavelength (~650 - 1100 nm).[66] A far-red FP named mPlum emitting at 649 nm was designed.[69] Great efforts have been made to create GFP variants with better folding,[70] improved brightness (enhanced GFP,[71,72] enhanced YFP), faster maturation (turboGFP), better photostability.[73]

The main application of FPs is protein labeling by cloning a fusion protein composed of the FP and the targeted protein (with a perfect specificity of the labeling due to the genetic encoding). Its localization or movements can be then detected by the fluorescence of the FP. However, it is necessary to check that the protein is functional and its properties remain natural. Generally, using tetrameric FPs to tag the protein of interest gives rise to aggregation of the fusion protein and disturbance of its function and localization due to the large size of the label.[66] Thus, many variants have been designed to reduce the oligomerization tendency of their parent proteins and create monomeric FPs.[68,74]

In adddition to the usual FPs, some of them such as photoactivatable fluorescent proteins (PA-FPs) exhibit particular photophysical/photochemical behaviors. Indeed, their fluorescence emission can be shifted or turned on or turned off (reversibly or irreversibly) with light of appropriate wavelenth.[75–77] We will introduce more specifically the reversible photoswitchable fluorescent proteins later in the manuscript.

1.3.4 Turn on fluorescent probes

Aptamers are short sequences of nucleic acids that bind specifically with a high affinity to a target. The high affinity and specificity of aptamers for their target can be illustrated by the following example. An RNA molecule that binds to theophyllin (see Figure 1.2) with a dissociation constant K_d equal to 0.3 μM was identified.[78] The binding affinity of the same RNA molecule to caffein is 10000-fold lower (K_d = 3 mM)[78] even if theophyllin and caffein only differ by one methyl group.

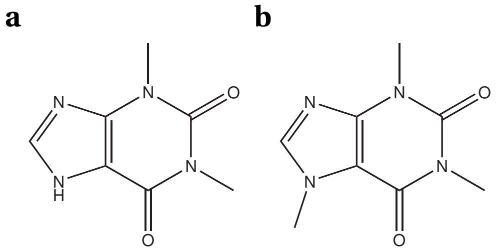

Figure 1.2: Structure of (**a**) theophyllin and (**b**) caffein.

Some aptamers have been reported to activate fluorescence of small organic dyes.[79,80] This phenomenom is called fluorogenicity. The RNA sequence forms specific contacts with the dye (also called fluorogen) preventing intramolecular motions. Thus, fluorescence becomes the major de-excitation pathway of the excited fluorogen. An interesting system is Spinach in which the fluorescence of a GFP-like chromophore (not fluorescent in solution) is elicited when it binds to the RNA sequence.[81,82] This system will be introduced in details in the introduction of chapter 2.

These turn on fluorescent probes display several advantages. They are genetically encoded probes like FPs. They should exhibit in addition a better resistance to photobleaching since the fluorogen should be refreshed in the cavity of the aptamer after photobleaching. Eventually, the fluorescence can be activated and deactivated at will by addition or withdrawal of the fluorogen.

1.3.5 Conclusion

As fluorescent exogenous probe, we chose in this work the ones that are genetically encoded due to the perfect specificity of the labeling step. Moreover, the cell penetration issues are avoided with this approach. Eventually, this kind of probes allows us to investigate multicellular organisms at the different stages of their development using for instance stable lines (e.g. transgenic zebrafishes or mices).

1.4 State-of-the-art : Optical imaging techniques exploiting the kinetic information of a photo-active targeted probe

This section will more specifically review the few imaging techniques relying on kinetic information of targeted probes using light as action parameter, which have been presently reported in the literature.

1.4.1 Fluorescence lifetime imaging microscopy (FLIM)

1.4.1.1 Principle

Fluorescence Lifetime Imaging Microscopy (FLIM) is based on the difference of the excited-state lifetimes of fluorophores.[83] Early applications consisted in recording fluorescence after a certain time-delay instead of the prompt fluorescence to improve contrast (see Figure 1.3). One of the first example of time-resolved imaging microscopy was proposed by Jovin *et al.*[83] A fluorescent dye called acridine orange (AO) exhibiting a triplet state was employed. The luminescence lifetime of this fluorophore is much more longer when it is intercalated within DNA than when it is aggregated in the tissue of a cell.

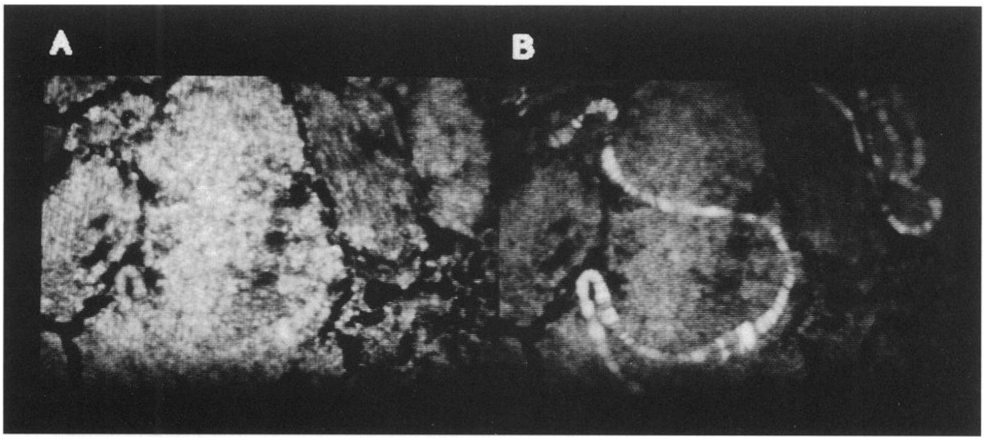

Figure 1.3: Time-resolved imaging microscopy of an acridine orange stained polytene chromosome that is covered with tissue. (A) Prompt fluorescence image. (B) Phosphorescence image, recorded after a time delay. Adapted from Jovin *et al.*[83]

In the prompt fluorescence image (Figure 1.3A), the chromosome is obscured by fluorescence emitted from dye bound to the overlying tissue. On the contrary, the chromosome is clearly visible in the phosphorescence image (Figure 1.3B), which is seen only after a time delay, because the dye bound to the tissue emits less delayed luminescence.

The current FLIM imaging methods relies on the same principle. Assume that a cell has two regions labeled with two probes exhibiting different lifetimes but with the same steady-state fluorescence emission. We can suppose otherwise as in the example displayed in Figure 1.3 that the cell contains a probe whose lifetime depends on the environment. The intensity image does not allow to distinguish the two areas of the cell. On the contrary, if the lifetimes of the two probes can be measured, the two regions (or environments) can be discriminated. The resulting FLIM or lifetime image is the map of the fluorescence lifetimes associated to the fluorescence decay detected at each pixel (see Figure 1.4).

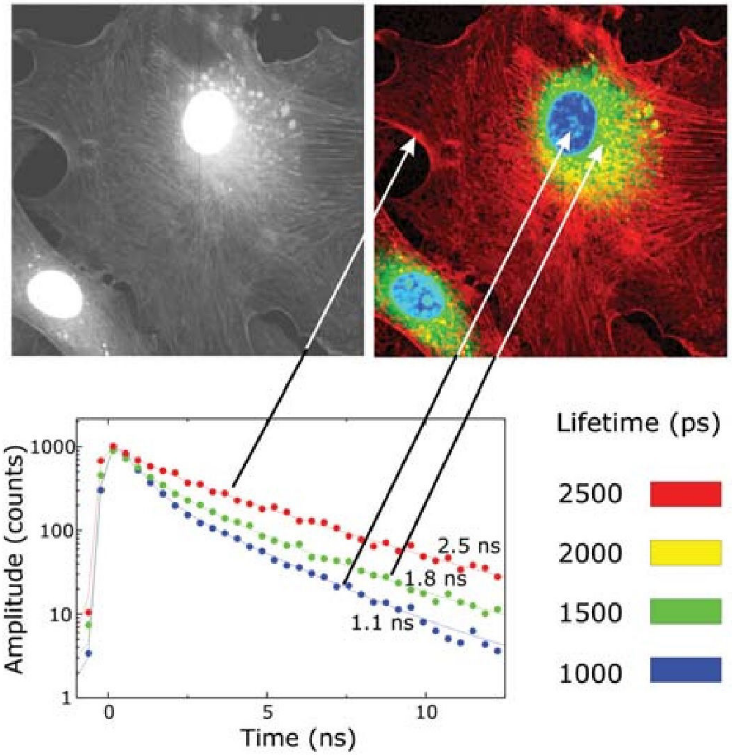

Figure 1.4: Intensity (left) and lifetime image (right) of bovine artery endothelial cells. The nuclei were stained with DAPI for DNA (blue), F-actin was stained with Bodipy FL-phallacidin (red) and the mitochondria were stained with MitoTracker Red CMX Ros (green). Adapted from Lakowicz.[84]

FLIM allows to discriminate two emitters based on a difference of their lifetimes but does not permit to quantify them since the lifetime does not depend on the probe concentration.[5,84] Nevertheless, the excited-state lifetime of a fluorophore is sensitive to its local environment. Thus, imaging lifetime provides information on local physical parameters (e.g. microviscosity) and on the molecular effects of ions, pH, biomolecules... in biological samples.[5,84,85] In particular, exploiting the fluorescence lifetime allows to study these phenomena independently of variations of the fluorophore concentration.[85]

1.4.1.2 Implementation

FLIM can be implemented in three different ways[84,85] to determine the excited-state lifetime of a fluorophore.

Time-domain FLIM A pulsed laser excites the fluorophores. The fluorescence intensity is measured after various time delays following the excitation pulse of the laser using a gated detection allowing to reconstruct the time-resolved fluorescence decay. Fitting the temporal evolution of the fluorescence decay with usually a single mono-exponential gives access to the fluorescence lifetime of the fluorophore.

Frequency-domain FLIM This approach utilizes sinusoidally modulated light excitation produced with a continuous laser and an acousto-optical modulator. This results in a fluorescence signal that is also sinusoidally modulated but with a different modulation depth and with a phase delay relative to the excitation signal. The fluorescence lifetime can be determined from measurements of the relative modulation and the phase delay. These experimental parameters can be conveniently measured using a lock-in detection scheme.

Time-correlated single-photon counting (TCSPC) This FLIM implementation relies on detecting individual photons at low fluorescence fluxes. A histogram is then built up by plotting the number of individual detected photons as a function of their arrival time on the detector. The lifetime is then extracted from the histogram.

1.4.2 Optical lock-in detection (OLID)

1.4.2.1 Principle

Optical lock-in detection[86,87] (OLID) measures the amplitude of the cross-correlation observed between a fluorescence signal detected at an imaged pixel and a reference one. It exploits the reversible light-driven switching of a photoswitchable fluorescent probe between two states of different brightnesses. The photoswitchable probe undergoes several cycles of optical switching by alternating illumination with light of appropriate wavelengths. The resulting modulated fluorescence signal of the photoswitchable target is then isolated from the non-modulated background by cross-correlating the temporal dependence of the fluorescence intensity of each pixel with a reference waveform at zero lag time. Therefore, the measurement evaluates the degree of similarity between the two trajectories. In a cellular imaging context, this reference can be located either outside the cell (micron-sized beads coated with the optical switch are added to the sample) or inside a cell (e.g. a region in the field of view exhibiting the highest depth of modulation is identified and chosen as reference).[86] The cross-correlation coefficient for each pixel $\rho(x, y)$ is computed using Eq 1.6 :

$$\rho(x,y) = \frac{1}{N}\sum_{i=1}^{N}\frac{\left[I_F(x,y,i)-\mu_I(x,y)\right]\left[R(i)-\mu_R\right]}{\sigma_I(x,y)\sigma_R} \tag{1.6}$$

where $I_F(x,y,i)$ is the detected fluorescence emission at pixel (x,y) at the i-th frame during the switching cycle, $R(i)$ is the fluorescence emission of the reference at the i-th frame (N is the total number of frames), $\mu_I(x,y)$ and μ_R are the mean values, and $\sigma_I(x,y)$ and σ_R are the standard deviation values of the fluorescence intensity of pixel (x,y) and the reference waveform respectively.[b]

The correlation image (CI) which is the map of the cross-correlation coefficient values is finally obtained. Since conventional fluorophores (like GFP) or autofluorescent background are not expected to exhibit optical switching, their fluorescence emission will not be correlated with the reference waveform. Thus, a region dominated by non-modulated background fluorescence will exhibit a low or zero value of the correlation coefficient. On the contrary, the cross-correlation coefficient in an area containing optical switches will be close to one.

1.4.2.2 Experimental validation

OLID has been validated using both small organic molecules generally derived from the spiropyran/merocyanin system (BIPS, see Figure 1.5**a** and **b**) or genetically encoded optical switches (from the Dronpa family, which will be introduced in details in the introduction of chapter 4) for imaging in living cells and tissue.[86]

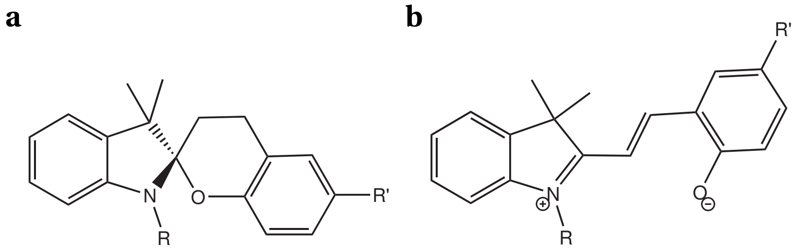

Figure 1.5: Structure of BIPS in the non-fluorescent SP (**a**) and the fluorescent MC (**b**) states. (Nitro-BIPS : R = $-(CH_2)_{10}CH_3$ and R'= NO_2).

---

[b] The mean and the standard deviation values of the fluorescence intensity at pixel (x,y) are calculated thanks to Eqs. 1.7 and 1.8

$$\mu_I(x,y) = \frac{1}{N}\sum_{i=1}^{N} I_F(x,y,i) \tag{1.7}$$

$$\sigma_I(x,y) = \sqrt{\frac{1}{N}\sum_{i=1}^{N}\left(I_F(x,y,i)-\mu_I(x,y)\right)^2} \tag{1.8}$$

A NitroBIPS acting as a membrane targeting probe was imaged within a living *Xenopus* spinal cord. In addition, using a Dronpa-actin fused protein, neurons (see Figure 1.6) and muscles were successfully imaged in living zebrafish embryos.[86] In particular, the improvement in contrast in the correlation image enabled to distinguish fine structures which emitted only a weak fluorescence signal in comparison to the background level (see Figures 1.6A and B).

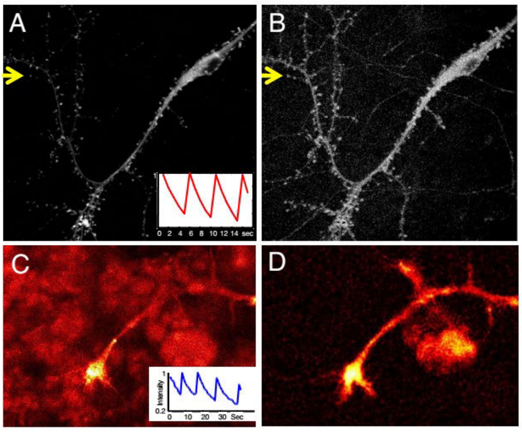

Figure 1.6: OLID-imaging of Dronpa in cultured mammalian neurons (**A**,**B**) and *Xenopus* spinal cord explant (**C**,**D**). (**A**) Fluorescence-intensity image of Dronpa-actin transiently expressed in rat P1 hippocampal neurons. (**B**) Correlation image of Dronpa-actin of same field as in **A** improves contrast and reveals finer processes and dendritic spines. (**C**) Image of the fluorescence intensity of Dronpa-actin within the growth cone of a motor neuron in a live, deskinned *Xenopus* embryo. (**D**) Correlation image of Dronpa-actin for image field shown in **C**. The Insets show normalized fluorescence intensity of the internal reference over a few cycles of optical switching. Adapted from Marriott *et al.*[86]

Further refinements of the technique with FRET pairs composed of a fluorescent donor and an optical switch acceptor were implemented allowing an optical lock-in detection of FRET efficiency.[88] Recently, this combined OLID-FRET approach was employed to improve contrast in immunofluorescence imaging microscopy.[89] An anti-actin antibody co-labelled with a fluorescent Cy3 donor (see Figure 1.7) and a photochromic acceptor NISO (a derivative of BIPS) was designed. Using light of appropriate wavelengths, the acceptor is reversibly switched between an absorbing (MC) state and a non-absorbing (SP) state resulting in a modulation of cyanine fluorescence emission, due to Förster resonance energy transfer. The OLID analysis is performed as described before and enables to visualize sharper and better-defined actin filaments in cells.[89] Several synthetic probes useful for the OLID-FRET protocol were designed and characterized.[90]

Recently, Marriott *et al* proposed a modified version of OLID by changing the algorithm for the image processing.[91] Up to now, the internal reference was determined manually by the user who chose the pixel whose fluorescence intensity exhibited the largest modulation

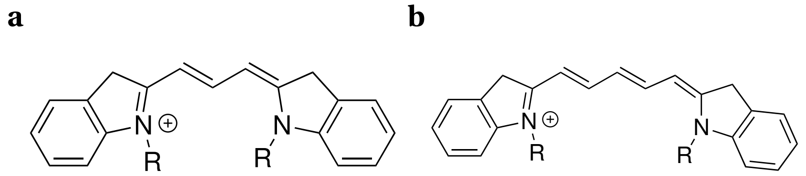

Figure 1.7: Structure of the Cy3 (**a**) and Cy5 (**b**) fluorophores.

over the switching cycles. A method was proposed to detect automatically the reference pixel using the function $S(x,y)$ denoted 'scope' by Marriott *et al*[91] :

$$S(x,y) = \frac{1}{N}\sum_{i=1}^{N}\left(L_{max}(x,y,i) - L_{min}(x,y,i)\right) \tag{1.9}$$

where $L_{max}(x,y,i)$ (respectively $L_{min}(x,y,i)$) is the local maximum (respectively minimum) fluorescence intensity at pixel (x,y) of the i-th switching cycle and N is the number of cycles used to calculate the scope value. The pixel exhibiting the largest scope value is chosen as the reference point. The cross-correlation analysis is then performed as described before using the temporal dependence of the fluorescence detected at the reference point as waveform reference. In order to better reject the noise and the background, a modified correlation image (MCI) was constructed by computing a scope-weighted correlation value[91] :

$$w\rho(x,y) = S(x,y)\cdot\rho(x,y) \tag{1.10}$$

where $\rho(x,y)$ is the cross-correlation coefficient evaluated with Eq. 1.6.

In some cases, a significant contrast enhancement can be obtained simply by computing a scope-weighted fluorescence intensity without calculating the cross-correlation coefficient.[92]

1.4.3 Synchronously Amplified Fluorescence Image Recovery (SAFIRe)

1.4.3.1 Principle

Dickson *et al* proposed to modulate only the fluorescence signal of fluorophores of interest without modulating the background to avoid the need of a reference waveform. His approach is coined Synchronously Amplified Fluorescence Image Recovery (SAFIRe) and has been generally validated with fluorescent probes possessing long-lived dark state(s).[93] A primary light source promotes the probe from its ground-state S_0 to its excited-states : S_1 and T_1 (see Figure 1.1). A secondary light source is used to depopulate the transient long-lived dark states of the fluorescent probe faster than they normally decay. Modulating the intensity of the secondary light source allows to dynamically alter the fluorophore excited-state populations. The SAFIRe image corresponds to the map of the amplitude of the fluorescence modulation obtained after Fourier transformation of the temporal dependence of the fluorescence signal of each pixel. The choice of the wavelength of the secondary excitation is crucial. Since endogenous fluorophores in biological media absorb mostly in the blue-green wavelength range, the modulation of the background is limited by exciting with long wavelengths (red). Furthermore, to avoid any additional fluorescence signal due to direct excitation with the secondary light source, its wavelength is chosen to be longer than the one of the collected fluorescence. As a consequence, SAFIRe implementation requires specific fluorophores with dark states whose maximum absorption is red-shifted compared to the fluorescence emission. A fluorescent probe with no dark state or with a dark state absorbing at wavelengths shorter than the fluorescence emission maximum is not suited to this implementation scheme and is called non-modulatable.

1.4.3.2 Experimental validation

SAFIRe has been first demonstrated with silver nanodots[94] and organic fluorophores (xanthene[93] and Cy5[95]). Since SAFIRe requires fluorescent systems whose dark states absorb at longer wavelengths than those of fluorescence emission, it greatly limits the pool of usable fluorophores.[96] To overcome this issue, an approach combining SAFIRe and FRET was proposed.[96] The donor of the FRET pair is excited with the primary light source whose energy is transfered to the acceptor. This provides the possibility to excite simultaneously the acceptor with light of longer wavelength than the donor fluorescence emission maximum. Thus, the direct excitation of the acceptor inhibits the FRET transfer and results in an increase in the fluorescence emission of the donor. This concept was experimentally evidenced using DNA hairpin whose ends are composed of a FRET pair (see Figure 1.8).[96] To apply the SAFIRe

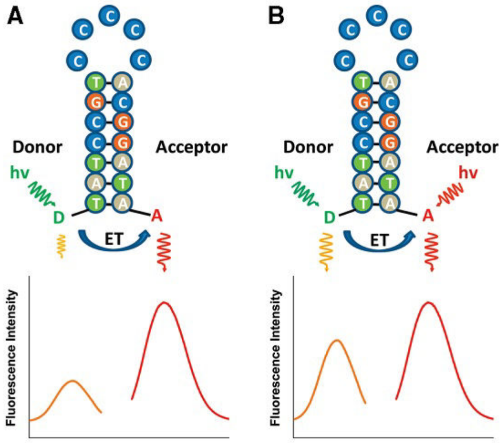

Figure 1.8: Scheme of a hairpin exhibiting FRET with donor and acceptor fluorophores. (A) Typical FRET process when only the donor is excited, leading to highly quenched donor fluorescence. (B) Simultaneous acceptor direct excitation inhibits FRET, thereby increasing and enabling modulation of donor fluorescence. Adapted from Richards *et al.*[96]

scheme to fluorophores without any dark-states, an approach based on stimulated emission was proposed.[97] A second laser beam overlapping the first one decreases the fluorescence due to stimulated emission. Turning on and off the second laser modulates the population of the emissive state and so the fluorescence signal. The wavelength of the secondary laser was chosen to be longer than the fluorescence emission. Thus, the emissive state plays the role of the dark state in the regular SAFIRe protocol.[97]

Application in imaging The SAFIRe scheme was applied in bioimaging using two modulatable fluorescent proteins (AcGFP[98] and modBFP-H148K[99]). AcGFP was employed to selectively image mitochondria-targeted AcGFP against EGFP background fluorescence or nuclear EGFP in cells since EGFP is not modulatable.[98]

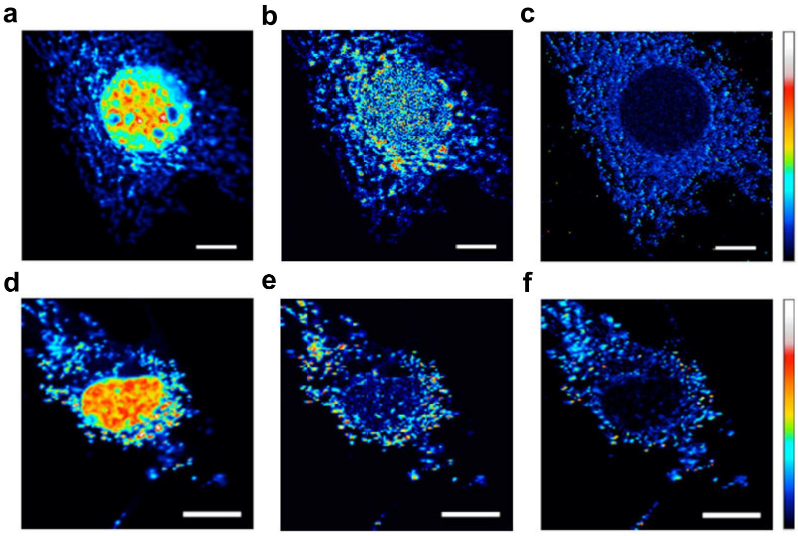

Figure 1.9: Selective fluorescence recovery of mitochondria-targeted AcGFP from nuclear targeted EGFP fluorescence in fixed (**a-c**) and living (**d-f**) NIH 3T3 mouse fibroblasts in a confocal arrangement. The primary laser intensity was held at 5.9 kW·cm^2 and the secondary intensity (64 kW·cm^2) was modulated at 300 Hz. (**a,d**) Raw fluorescence image of AcGFP-labeled mitochondria and EGFP. (**b,e**) Demodulated image of the same field of view as in **a** and in **d**. (**c,f**) Ratio image of demodulated signal to raw fluorescence. Scale bar: 10 μm. Adapted from Jablonski *et al.*[98]

To avoid the confocal arrangement leading to long acquisition time, Dickson *et al* performed epifluorescence wide-field imaging with SAFIRe but only with a reduced field of view.[99] This was achieved by overlapping of a defocused primary laser and a smaller secondary laser (disk of ~10 μm in diameter). Applying the SAFIRe protocol with mitochondria-labeled modBFP-H148K enabled to reduce the autofluorescent background in living cells.[99] Comparing the two disks (before and after demodulation) shows a relative reduction of the autofluorescent background (see Figure 1.10).

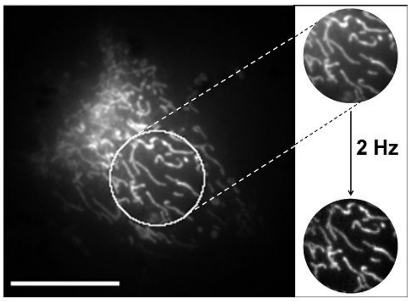

Figure 1.10: Live cell demodulation of mitochondria-targeted modBFP-H148K. Raw fluorescence image upon 405 nm illumination, autofluorescent background and blue modBFP-H148K-mitochondria emission are collected. Coillumination at 514.5 nm, modulated at 2 Hz is applied only within the white circle. (upper disk) Raw fluorescence image upon coillumination. (lower circle) Demodulated image. Scale bar is 20 μm. Adapted from Jablonski *et al.*[99]

SAFIRe was also employed to image fluorophores up to 6 mm deep within a medium mimicking skin tissue, composed of a highly scattering and fluorescent background.[100]

Frequency dependence A modulatable fluorophore is characterized by the lifetime τ_c of its dark-state. Thus, the modulation depth of the signal of a modulatable fluorophore submitted to modulated excitation depends on the excitation frequency f. Indeed, if $f \ll \frac{1}{\tau_c}$, the populations of the ground- and the dark-state follow the variations of the excitation, the modulation depth is maximal. On the contrary, if $f \gg \frac{1}{\tau_c}$, the two populations have not enough time to respond to the perturbation and the modulation depth goes to zero. The frequency-dependence of the modulation depth of the protein AcGFP is displayed in Figure 1.11.

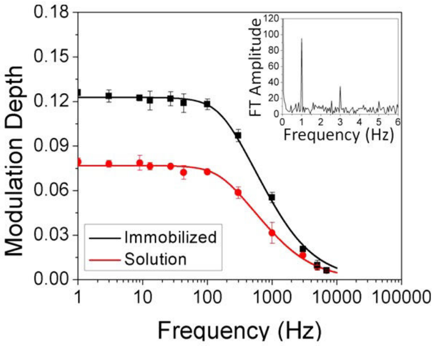

Figure 1.11: Modulation frequency dependence of AcGFP enhancement at 561 nm for immobilized (red) and diffusing (black) molecules. The modulation depth at each frequency was computed by normalizing the doubled Fourier transform of each time trace by the number of data points and by its DC component. The inset shows the Fourier transform of the square-wave-modulated fluorescence of AcGFP at 1 Hz. Adapted from Jablonski *et al.*[98]

The Eq 1.11 has been proposed to account for the dependence of the modulation depth m of a modulatable fluorophore with a characteristic time τ_c on frequency f

$$m(f) = \frac{A}{\sqrt{\left(2\pi f \tau_c\right)^2 + 1}} \tag{1.11}$$

where A is a constant.[101] Fitting the frequency-response of a modulatable probe with Eq 1.11 allows to extract the associated lifetime τ_c.

Quantitative detection SAFIRe allows to quantify fluorophore concentrations in high background solutions.[102] Diluted solutions of Cy5 (see Figure 1.7) with identical concentrations were prepared either with the non-modulatable Texas Red fluorophore (constant concentration) or without (control solutions). The concentrations were determined both with FCS (Fluorescence Correlation Spectroscopy) and SAFIRe. Figure 1.12A displays the results obtained by FCS. The number of Cy5 molecules in the presence of Texas Red is plotted as a function of the number of molecules of Cy5 determined with the control solutions. The titration curve is not linear due to the contribution of Texas Red to fluorescence. As showed by figure 1.12B, plotting the modulated signal amplitude of samples with or without Texas Red as a function of the number of Cy5 molecules (determined by FCS from the control solutions) gives nearly identical linear dependence since the contribution of the non-modulatable Texas Red is extinguished. Thus, SAFIRe enables to accurately estimate the concentration of Cy5 even in the presence of a high background.[102]Recently, several cyanine derivatives were synthesized and characterized to identify the ones exhibiting the highest modulation depth.[101]

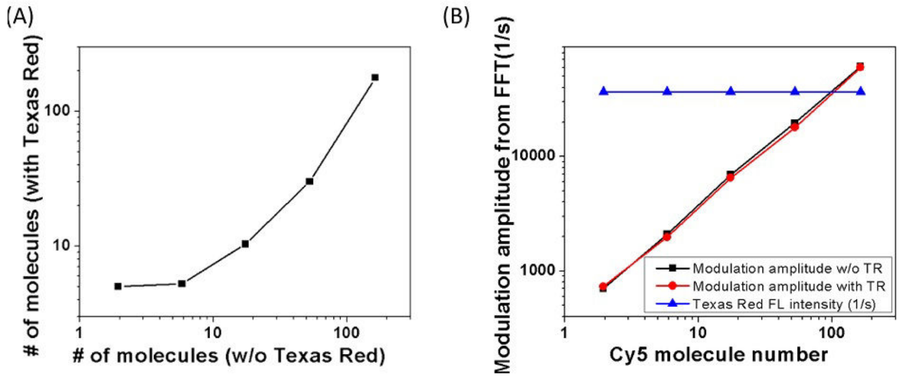

Figure 1.12: (A) Highly non linear titration of the numbers of Cy5 molecules with and without constant Texas Red background when FCS was used to determine the numbers of fluorophores. (B) Plots of the FFT amplitude vs the number of Cy5 molecules, showing that the modulation amplitude is independent of the presence of non-modulatable Texas Red background. Adapted from Hsiang *et al.*[102]

1.5 Conclusion

The goal of my PhD was to develop a cheap and simple imaging protocol allowing to selectively detect and quantify a targeted species in a complex mixture such as a living cell.

For the record, an attractive imaging method for imaging cellular components should exhibit the following features :

- being non-invasive
- using fluorescence as the observable
- relying on the chemical dynamics of a probing reaction in which the exogenous probe is engaged
- using a genetically encoded exogenous probe

In the previous section, we showed in addition that light could be a powerful tool to bring a significant gain in selectivity to fluorescence imaging techniques by exploiting the kinetic signature of photo-active probes. As a result, we tried during this PhD to implement and conceive selective imaging methods based on this principle. In particular, we chose photochromism as the probing reaction and light as the action parameter.

Among the techniques described in the literature, OLID is a very simple protocol but it uses two light sources to drive the dynamics of the photoswitching in its original implementation. Therefore, we wondered whether this method could be implemented using a single light source to activate and readout the photochromic behavior of the targeted chromophore. To evaluate this one color implementation, we identified in the literature a fluorescent probe that could potentially be photochromic given the structure of its chromophore.

From another point of view, our group had already developed an approach enabling to perform a titration under kinetic control using temperature modulation (it will be introduced in details in the introduction of chapter 3). We wanted to adapt this strategy to design our own selective imaging technique relying on photochromism and light modulation.

This manuscript is divided in six chapters. The first one deals with establishing a dynamic model accounting for the photochromic behavior of a fluorogenic system which we identified in the literature. We consequently imaged this system by the OLID scheme for its selective imaging. The second chapter describes the extensive theoretical framework we built to design our selective analytical protocol based on light modulation and photochromism.

The third chapter is about the experimental validation of our approach in the context of fluorescence imaging. The fourth chapter introduces the improvement in terms of temporal resolution that we brought to our original protocol using two light sources. The fifth chapter discusses and compares our own strategy with the selective optical imaging techniques reported in the literature and evoked in the introduction. The last chapter concludes this PhD work and proposes a few perspectives.

Chapter 2

A first realization : one color OLID

2.1 Introduction

2.1.1 Context

With the original OLID protocol, Marriott *et al* used two light sources to drive the photoswitching.[86] OLID application with a single color requires a reversible optical switch whose state generated upon illumination relaxes back thermally with a reasonable relaxation time for imaging purpose. Based on the requirements evoked in the General introduction, we identified in the literature a good candidate. It consists in the association between a genetically encoded RNA aptamer and a fluorogen yielding a fluorescent complex[81] whereas the free fluorogen is not. This system called Spinach has been employed as a fluorescent tag for imaging RNA.[81] The fluorogen is a dye that resembles the chromophore in GFP. This species is known to be photochromic.[103,104] Thus, we assumed that the Spinach system could potentially exhibit a photochemical behavior.

The development of a one-color OLID protocol based on this system required first to evidence the photochromic behavior of Spinach. In addition, an extensive characterization of (i) the kinetic (association rate constant k_{on} and dissociation rate constant k_{off}) and thermodynamic (dissociation constant K_d) properties of the complexation reaction and (ii) the photochromic behavior of Spinach was needed to permit an application in a wide range of experimental conditions.

In the following, we present in details the Spinach system and its recent developments. We then introduce my first article reporting the photochemical behavior of the Spinach system and the implementation of the one-color OLID protocol.

2.1.2 Presentation of Spinach

Green fluorescent protein (GFP) and its derivatives used as fluorescent tags revolutionized the study of proteins in living systems.[36,105,106] They have inspired Jaffrey to recently propose a similar approach for RNA tagging with fluorescent labels.[81] The fluorescent tag is composed of an RNA aptamer that binds a fluorogen resembling the chromophore in GFP (4-hydroxybenzylidene imidazolinone (HBI)) and activates its fluorescence.

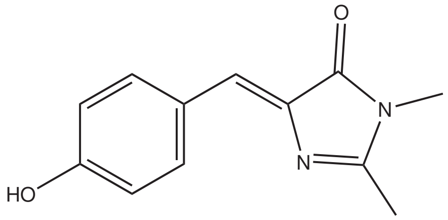

Figure 2.1: Structure of the chromophore of GFP (HBI).

2.1.2.1 Identification of fluorescent RNA-fluorogen complexes

Several GFP-like fluorogens were synthesized by derivatization of HBI.[81] A general procedure called systematic evolution of ligands by exponential enrichment (SELEX)[107,108] was followed to select the RNA sequences able to bind the targeted fluorogen.

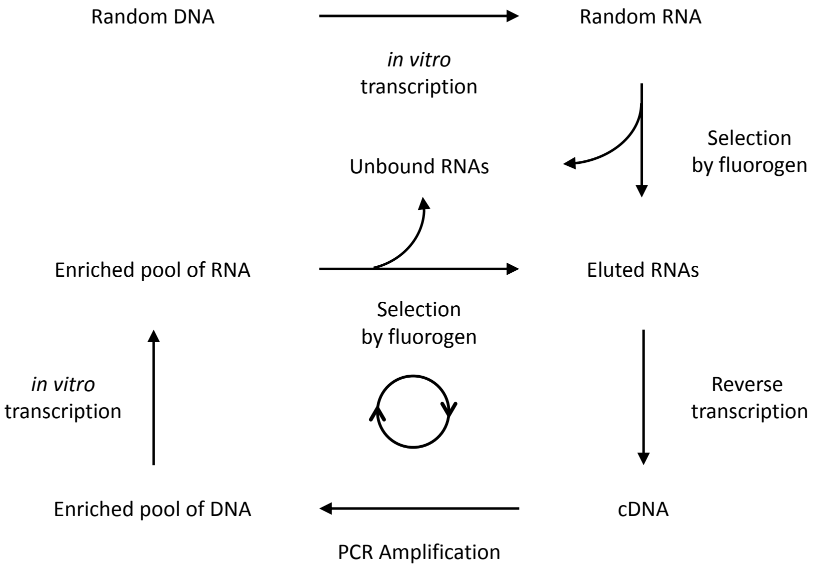

Figure 2.2: SELEX procedure to select RNA sequences binding a fluorogen.

A DNA template is constructed with randomized sequences at specific positions. After *in vitro* transcription, a library containing typically ~ 10^{13} / 10^{14} RNA molecules is obtained.[81] The RNAs are then mixed with the fluorogen which is immobilized on an agarose matrix by a linker. The RNAs with low affinities for the targeted fluorogen are discarded whereas the bound RNA sequences are eluted. A reverse transcription is performed on the eluted RNAs to synthesize the complementary DNA copies, which are amplified using a PCR. A new pool of RNA sequences is obtained after *in vitro* transcription of the amplified DNA copies which can be used to start the next round of SELEX. The procedure is repeated several times up to get the best binding ligands. The fluorescence of the RNA pool in the presence of the fluorogen is checked after each round. Among the selected RNAs, the one that induces the highest fluorescence increase upon binding the fluorogen was identified and sequenced. An *in vitro* characterization was then performed to determine the photophysical properties of the fluorescent RNA-fluorogen complex and its dissociation constant K_d.

The brighest RNA aptamer-fluorogen complex was called Spinach-DFHBI. By introducing two fluorine atoms in the aromatic ring of HBI, the DFHBI fluorogen (3,5-difluoro-4-hydroxybenzylidene imidazolidinone) was obtained (see Figure 2.3).

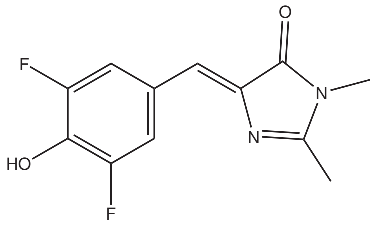

Figure 2.3: Structure of DFHBI.

An RNA aptamer (Spinach) was selected at neutral pH against the basic state of DFHBI due to its low pK_a (5.5).[81] The Spinach-DFHBI complex (K_d = 537 nM)[81] exhibits an excitation maximum at 469 nm and an emission maximum at 501 nm (see Figure 2.4). The quantum yield of fluorescence of the resulting complex is 0.72 (20% higher than EGFP) and its molar brightness is 53% of EGFP.[81] The spectral properties of the complexes can be tuned either by using further SELEX screens or changing the fluorogen. Thus a family of fluorescent tags emitting in the different regions of visible spectrum has been developped.[81]

The Spinach probe has been used to tag ribosomal 5S RNAs in living mammalian cells enabling to observe localization changes under stress conditions.[81] Spinach-based sensors have been subsequently designed to report for metabolites or proteins in living cells.[82,109–111] Moreover Spinach has been further employed to characterize and monitor in real time mRNA synthesis *in vitro*[112] and *in vivo.*[113]

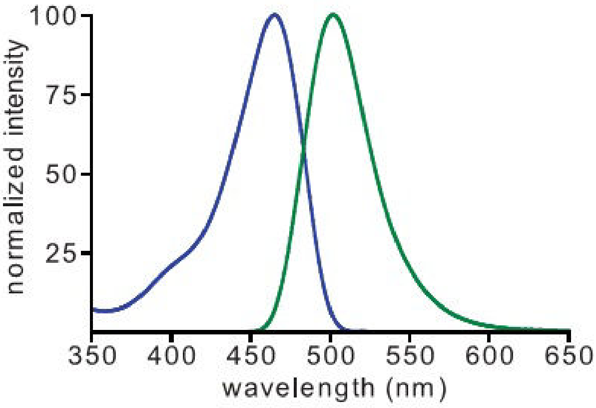

Figure 2.4: Normalized excitation (blue) and emission (green) spectra of Spinach-DFHBI complex. Adapted from Paige et al.[81]

2.1.2.2 Recent developments of the Spinach system

Improving the properties of fluorescent RNA-fluorogen complexes Further characterizations showed a thermal instability and a poor folding of Spinach.[114] Moreover, when Spinach is fused to RNAs, its fluorescence is reduced compared to the one measured *in vitro.* A variant of Spinach called Spinach2 was selected based on the improvement of thermal stability, better folding and brightness with photophysical properties similar to Spinach.[114]

Spinach2 bound to DFHBI has fluorescence excitation maximum of 447 nm and fluorescence emission of 501 nm.[114] These wavelengths are not optimal for filter cubes usually employed for imaging green fluorescence on microscopes.[115] Instead of changing the aptamer sequence which had been optimized for sensing metabolites, two fluorogens (DFHBI-1T and DFHBI-2T, see Figure 2.5) derived from DFHBI were synthesized by substituting the imidazole ring with an electron-withdrawing group. The resulting Spinach2-DFHBI-1T (DFHBI-2T respectively) complex exhibits red-shifted absorption and emission maxima which are more compatible with standard GFP (respectively YFP) filter cubes.[115]

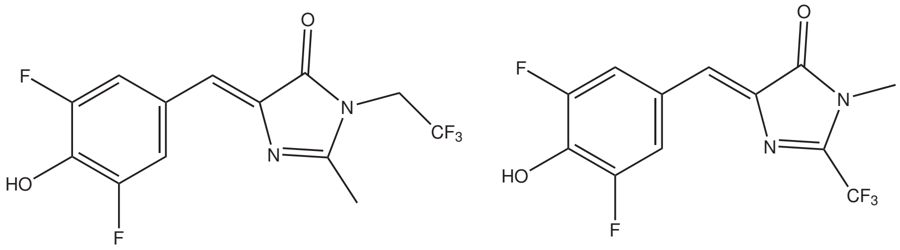

DFHBI-1T

DFHBI-2T

Figure 2.5: Structure of DFHBI-1T and DFHBI-2T.

A new protocol for rapid identification of RNA-fluorogen complexes highly compatible with cellular expression With usual SELEX procedure, the RNA aptamers are selected only on their ability to bind fluorogens, which is not sufficient to switch on the fluorescence of fluorogens.[116] In addition, the selected RNAs are not necessarily optimized to function in cells.[114,116] A novel selection procedure has been proposed based on the binding of RNA aptamers to fluorogens and fluorescence-activated cell sorting (FACS) of aptamers expressed in *Escherichia coli* (*E. coli*).[116] In this protocol, six rounds of SELEX were performed on a library containing ~ 10^{14} RNAs to select the best binding aptamers. The RNA pool was then reverse transcribed and cloned into bacterial expression plasmids. The library was transformed into *E. coli* and transcription was induced. Bacteria were incubated with the fluorogen and sorted with FACS to isolate the aptamers exhibiting the highest fluorescence. FACS sorting was performed at 37°C to select the thermostable aptamers at this temperature. Based on a directed evolution approach and using again the combined SELEX-FACS selection procedure, an RNA sequence (shorter than Spinach2, thus minimizing perturbations in the labeled RNA) optimized for performance in cellullar environment was identified. When bound to DFHBI-1T, this aptamer called Broccoli displays photophysical properties and a brightness close to the ones of Spinach2.[116]

Structural basis of Spinach fluorescence The crystal structures of Spinach with and without bound fluorogen have been recently solved, which provides some insights for designing new fluorogen-binding RNA aptamers.[117,118]

2.1.3 Presentation of the article

We first attempted to reproduce the results reported in the original paper by starting with the photophysical properties of the Spinach-DFHBI system. Preliminary experiments revealed a reversible photochemical behavior in the Spinach system, which was not described before. Indeed, under continuous illumination with blue light, we observed a fluorescence decay of the Spinach-DFHBI complex over time, which completely recovered after standing in the dark.

My first article precisely deals with establishing the dynamic model accounting for this unexpected photochemical behavior and its application in the context of selective imaging. Using ^{1}H-NMR spectrometry and light-jump experiments, we first demonstrated that *cis*-DFHBI alone undergoes reversible *cis*-*trans* photoisomerization, whose kinetics has been thoroughly characterized. We then investigated the photochemical behavior of the Spinach system. We discuss in the article the different models we proposed to account for the fluorescence decay of the Spinach probe upon illumination. We eventually converged toward a four-state mechanism accounting for our observations. It consists in (i) a non-covalent binding of Spinach with both *cis*-DFHBI and *trans*-DFHBI giving rise to Spinach-*cis*-DFHBI and Spinach-*trans*-DFHBI complexes and (ii) an interconversion by photoisomerization between the two DFHBI stereoisomers in both bound and free states. Thus, light can be used to control the exchange dynamics between these four states of different brightnesses. As an outcome, we implemented a selective fluorescence imaging protocol (one color OLID) based on the photochemical properties of Spinach.

2.2 Article 1 : Photochemical properties of Spinach and its use in selective imaging

Chemical Science

RSC Publishing

EDGE ARTICLE

Photochemical properties of Spinach and its use in selective imaging†

Cite this: *Chem. Sci.*, 2013, **4**, 2865

Pengcheng Wang,‡[ab] Jérôme Querard,‡[a] Sylvie Maurin,[a] Sarang S. Nath,[a] Thomas Le Saux,*[ac] Arnaud Gautier*[a] and Ludovic Jullien*[ac]

Received 17th March 2013
Accepted 24th April 2013

DOI: 10.1039/c3sc50729g

www.rsc.org/chemicalscience

The progress in imaging instrumentation and probes has revolutionized the way biologists look at living systems. Current tools enable both observation and quantification of biomolecules, allowing the measurement of their complex spatial organization and the dynamic processes in which they are involved. Here, we report reversible photoconversion in the Spinach system, a recently described fluorescent probe for RNA imaging. Upon irradiation with blue light, the Spinach system undergoes photoconversion to a less fluorescent state and fully recovers its signal in the dark. Through thermodynamic titration, stopped-flow, and light-jump experiments, we propose a dynamic model that accounts for the photochemical behavior of the Spinach system. We exploit the dynamic fluorogen exchange and the unprecedented photoconversion properties in a non-covalent fluorescence turn-on system to significantly improve signal-to-background ratio during long-term microscopy imaging.

Introduction

Advances in fluorescence tools have revolutionized the field of molecular and cell biology.[1,2] Highlighted among these techniques are optical probes based on the green fluorescent protein (GFP) and its variants, which have enabled a subcellular understanding of the complex spatial organization and dynamic behaviors of proteins.[2,3] The discovery of reversible photoswitchable fluorescent proteins[4] that interconvert between states of distinct brightnesses has subsequently led to powerful techniques, including time-resolved protein tracking,[5] super-resolution microscopy[6–9] and high contrast imaging.[10] The archetypes of the reversible photoswitchable fluorescent proteins are green fluorescent protein, dronpa[4] and its variants,[11,12] which photoconvert when illuminated with blue light and recover their initial fluorescence by thermal relaxation in the dark or on photoexcitation with UV.

Recently, the Spinach probe has been introduced as an RNA mimic of GFP.[13,14] The Spinach system has been successfully employed as a fluorescent tag for tracking ribosomal 5S RNA in mammalian cells[13] and as a reporter within RNA-based sensors for metabolites in *Escherichia coli*.[14] To induce a high fluorescence signal,[13] the system relies on the non-covalent binding between an RNA aptamer (Spinach) and the phenolate form of an acidic ($\mathrm{p}K_\mathrm{a} = 5.5$)[13] fluorogen termed *cis*-3,5-difluoro-4-hydroxybenzylidene imidazolinone (*cis*-DFHBI) (Scheme 1).

The DFHBI fluorogen is structurally similar to the 4-hydroxybenzylidene imidazolinone chromophore, which is responsible for photoinduced *cis–trans* isomerization during optical switching in dronpa.[15] We have thus been interested in examining whether the Spinach system would exhibit an analogous behavior. Light jump experiments were first used to show that Spinach was indeed photochemically active. We then performed complementary thermokinetic experiments in order to derive a consistent dynamic model that accounted for the photochemical behavior of Spinach. After analyzing our experimental data with various models, we concluded that our observations were compatible with reversible transitions among four distinct states, two of which involve the well-known *cis–trans* photoisomerization of GFP-like chromophores.[16,17] We exploited the reversible light-driven drop of Spinach brightness to selectively

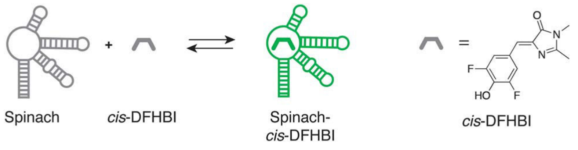

Scheme 1 Spinach system. The non-covalent binding interaction between the non-fluorescent ionized *cis*-DFHBI fluorogen and the Spinach RNA aptamer yields a fluorescent adduct.

---

[a] *École Normale Supérieure, Département de Chimie, UMR CNRS-ENS-UPMC 8640, 24 rue Lhomond, 75231 Paris Cedex 05, France. E-mail: thomas.lesaux@ens.fr; arnaud.gautier@ens.fr; ludovic.jullien@ens.fr*

[b] *Institut Curie, Centre de Recherche, CNRS, UMR 176, 26 rue d'Ulm, Paris F-75248, France*

[c] *UPMC Univ Paris 06, 4 Place Jussieu, 75232 Paris Cedex 05, France*

† Electronic supplementary information (ESI) available: Theoretical framework for the various dynamic models evaluated to explain the Spinach photoconversion (including Fig. S1 and S2), complementary computations and data (including Fig. S3–S7). See DOI: 10.1039/c3sc50729g

‡ These authors contributed equally.

image Spinach in the presence of interfering fluorophores using the optical lock-in detection (OLID) protocol, which has been recently introduced for enhanced-contrast imaging.[10]

Results

cis-DFHBI was reported to give a stable (dissociation constant $K_{d,1} = 0.5$ μM) and bright (quantum yield of fluorescence: 0.72) complex with Spinach with maxima of excitation and emission at 469 and 501 nm respectively.[13] The Spinach system is typically used by adding an excess of the DFHBI fluorogen to the medium containing target RNA molecules to be labeled. Thus, we examined the behavior of a solution containing 0.1 μM of Spinach and 1 μM of DFHBI. When we monitored its fluorescence emission upon illuminating continuously at 464 nm, a corresponding loss of fluorescence was observed at 498 nm. The fluorescence decay fitted a mono-exponential curve with a half-life of 1 min at a light intensity of 9×10^{-9} Ein s^{-1} (Fig. 1a). After turning off the light source, the fluorescence of the solution returned to its initial value with a half-time of 4.6 min. From this experiment, we concluded that light absorption by the Spinach system caused a thermally reversible photochemical conversion.

To interpret this photochemical behavior, we first investigated if the unbound DFHBI fluorogen was displaying photochromic behavior. In response to illumination at the maximum absorption wavelength (405 nm[13]), the fluorescence emission at 498 nm of a solution containing only DFHBI (20 μM) was strongly attenuated. Continuous illumination quickly led to a photostationary state (half-time of 8 s at a light intensity of 2×10^{-8} Ein s^{-1}) (Fig. 1b). When illumination was subsequently stopped, the DFHBI solution recovered its initial fluorescence (half-time of 4.6 min) (Fig. 1b). Relying on the photochemical behavior of *cis*-DFHBI analogues,[16–18] we hypothesized that the thermally reversible *cis*-DFHBI photoconversion could be a *cis–trans* photoisomerization. The photoisomerized 4-hydroxybenzylidene imidazolinone chromophore of GFP has been reported to exhibit a slow thermal relaxation in deuterated DMSO, thus rendering it accessible to NMR spectroscopy.[18] The ^{1}H-NMR spectra of *cis*-DFHBI solutions in deuterated DMSO were recorded before and after illumination at 405 nm (Fig. 2). In addition to the original peaks associated with *cis*-DFHBI (Fig. 2a), new signals assigned to the aromatic and ethylenic protons of the *trans*-DFHBI stereoisomer appeared after illumination (Fig. 2b). These peaks disappeared when the solution was subsequently left in the dark (Fig. 2c). These results were strongly indicative that the thermally reversible *cis*-DFHBI photochemical behavior was indeed a *cis–trans* photoisomerization.

The previous results suggested that the Spinach photochemical behavior could be explained by considering two types of exchange processes: (i) non-covalent binding between DFHBI and Spinach RNA and (ii) *cis–trans* DFHBI photoisomerization. To evaluate the relevance of this assumption, we performed a series of experiments aimed at independently analyzing (i) the

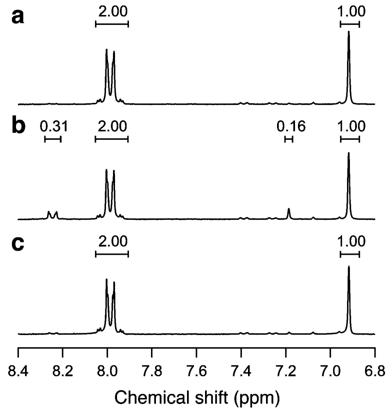

Fig. 2 ^{1}H-NMR study of *cis*-DFHBI photoisomerization. ^{1}H-NMR spectra of a solution containing *cis*-DFHBI in deuterated DMSO (a) before illumination at 405 nm; (b) 4 min after turning off the 405 nm illumination. The new signals associated with *trans*-DFHBI are integrated using the *cis*-DFHBI signals as references; (c) after maintaining the illuminated solution for 48 h in the dark. Zoom in of the aromatic/ethylenic area; $T = 293$ K.

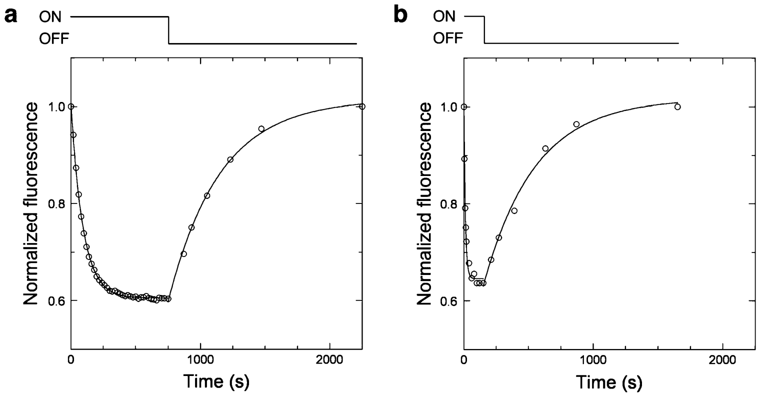

Fig. 1 Evidence for photochemical activity of the Spinach system and *cis*-DFHBI. Temporal evolution of the fluorescence emission at 498 nm upon illuminating (ON) solutions containing either (a) Spinach (0.1 μM) and DFHBI (1 μM) with illumination at 464 nm (9×10^{-9} Ein s^{-1}) or (b) DFHBI (20 μM) with illumination at 405 nm (2×10^{-8} Ein s^{-1}) and during dark-state recovery (OFF). Circles: experimental points; solid lines: exponential fits. Solvent: pH 7.4 HEPES buffer. $T = 293$ K.

thermokinetic features associated with the non-covalent interaction between *cis*-DFHBI and Spinach RNA and (ii) the photochemical properties of the DFHBI fluorogen.

First, we determined the dissociation constant $K_{d,1}$ of the Spinach–*cis*-DFHBI complex (denoted **1B** in Scheme 2) by analyzing the fluorescence emission of solutions containing DFHBI (100 nM) and Spinach RNA at various concentrations (Fig. 3a). To eliminate any possible contribution originating from the photogeneration of *trans*-DFHBI, samples were kept in the dark for 30 min immediately prior to measurement. The data could be reasonably well-analyzed upon assuming a 1 : 1 stoichiometry of the complex. From fitting the experimental data with eqn (1) (Fig. 3a), we extracted the dissociation constant, $K_{d,1} = 1.3 \pm 0.2$ μM, and the relative brightness (involving the molar absorption coefficients and the quantum yields of fluorescence emission) of the bound and unbound states of *cis*-DFHBI (resp. **1B** and **1F**), $q_1 = \varepsilon_{1B}\phi_{1B}/\varepsilon_{1F}\phi_{1F} = 500 \pm 100$ (see also Table 1). This was in good agreement with previously reported values ($K_{d,1} = 0.5$ μM and $q_1 = 2000$ in ref. 13).

Next, we used stopped-flow experiments to determine the rate constants $k_{+,1}$ and $k_{-,1}$ associated with the formation and the dissociation of the Spinach–*cis*-DFHBI complex. Fig. 3b displays the temporal evolution of the fluorescence emission measured at 498 nm after excitation at 464 nm at various *cis*-DFHBI concentrations. As expected (see ESI†), we observed an exponential increase of the fluorescence upon fast mixing of *cis*-DFHBI and Spinach RNA. The steady-state was reached with a relaxation time $\tau_{1,\pm}$ given in eqn (2). The extracted values of $1/\tau_{1,\pm} = k_{+,1}1F_{tot} + k_{-,1}$ were subsequently plotted as a function of the total *cis*-DFHBI concentration. After a linear fit, we extracted the association rate constant $k_{+,1} = 8.1 \times 10^4$ M^{-1} s^{-1} from the slope (Fig. 3c). Concordant with our previous assumption, this value is in the range expected for the association rate constant between an RNA aptamer and a small molecule.[19–21] The dissociation rate constant derived from the *y*-intercept showed significant measurement error, so we estimated $k_{-,1}$ by the relationship $k_{-,1} = K_{d,1}k_{+,1}$, which yielded a value of 1.4×10^{-1} s^{-1} (Table 1). Quantitative results are summarized in Table 1.

Finally, we investigated the kinetics of *cis*-DFHBI photoisomerization. We recorded the temporal evolutions of the fluorescence emission at 510 nm of a 100 μM DFHBI solution continuously illuminated at 470 nm at various light intensities (Fig. S6a†). Individual traces obeyed the exponential temporal evolution predicted by eqn (3). Linearly plotting the rate constant of the fluorescence decay as a function of light intensity subsequently yielded the sum of the *cis*-to-*trans* and *trans*-to-*cis* photoisomerization action quantum yields, $\varepsilon_{1F}\phi_{12,F} + \varepsilon_{2F}\phi_{21,F} = 15.6$ m^2 mol^{-1}, and the rate constant of the thermally driven *trans*–*cis*-DFHBI isomerization, $k^{\Delta}_{21,F} = 3.2 \times 10^{-3}$ s^{-1} (Fig. S6b†).

Based on these results, we attempted to interpret the photochemical behavior of the Spinach system. Although the first set of experiments were performed with the fluorogen in excess (Fig. 1a), theoretical analysis showed that experimental conditions in which Spinach RNA was in excess would greatly facilitate a comprehensive interpretation of the results (see ESI†). We thus repeated the photoconversion experiment under conditions where Spinach RNA was in excess to DFHBI. To further control the dynamic parameters, we adopted a low enough light intensity such that the photochemical reactions could be safely assumed to be rate limiting with respect to the binding reactions (see ESI†). When we monitored the temporal evolution of the fluorescence emission of solutions containing 0.1 μM *cis*-DFHBI and increasing concentrations of Spinach RNA, we observed, as previously, a mono-exponential decay under all conditions of Spinach RNA concentration (Fig. S7†). The evolution of fluorescence amplitude and the rate constant of fluorescence decay were monitored at varying concentrations of Spinach RNA (Fig. 4a and b). Increasing the concentration of Spinach RNA from 1.8 to 20 μM results in a 2-fold decrease in loss of fluorescence amplitude and a 4-fold increase of the rate constant.

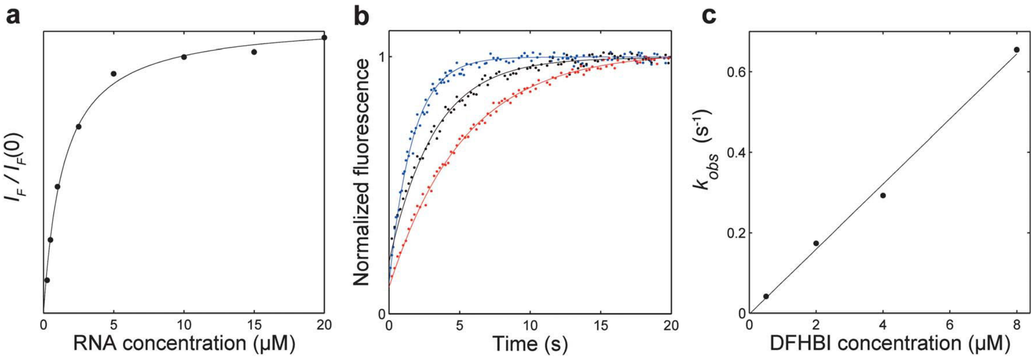

Fig. 3 Analysis of the thermokinetic properties associated with the non-covalent interaction between *cis*-DFHBI and the Spinach RNA aptamer. (a) Measurement of the dissociation constant. Fluorescence intensity was recorded as a function of Spinach concentration in a solution containing a constant concentration of DFHBI (100 nM) at chemical equilibrium. Markers: experimental points; solid line: fit with eqn (1). (b) Temporal evolution of fluorescence intensity upon mixing solutions of 0.2 μM Spinach RNA and *cis*-DFHBI (at varying concentrations; red, black, blue: 2, 4, 8 μM) using stopped-flow. Markers: experimental points; solid line: fit with eqn (2). (c) Dependence of the observed association rate constants ($k_{obs} = k_{+,1}1F_{tot} + k_{-,1}$) on total *cis*-DFHBI (**1F**) concentration. Markers: experimental points; solid line: linear fit yielding the value of $k_{+,1}$ from the slope. $\lambda_{exc} = 464$ nm; $\lambda_{em} = 498$ nm; solvent: pH 7.4 HEPES buffer; $T = 293$ K.

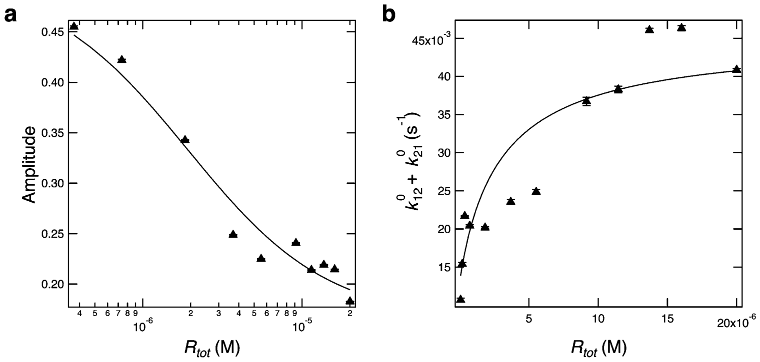

Fig. 4 Normalized loss of fluorescence amplitude (a) and rate constant (b) associated with fluorescence decay due to photoconversion of the Spinach system (0.1 µM *cis*-DFHBI + 1.8–20 µM Spinach RNA) when varying the total concentration R_{tot} in Spinach RNA. Markers: experimental points; solid line: global fit with eqn (4) and eqn (5) and (6). Solvent: pH 7.4 HEPES buffer; $T = 293$ K.

Along with the previous experiments, thermally driven reverse isomerization was monitored by taking fluorescence measurements at discrete time-points after turning off the light source. Solutions at photosteady state were maintained in the dark, and their fluorescence emissions were measured after various times of recovery. The increase in fluorescence emission was then plotted as a function of time to extract the rate constant k_{21}^{Δ} of the thermal return reaction for each RNA concentration. Subsequent analysis showed that the RNA concentration had almost no influence on the magnitude of the rate constant of the thermal return in the range of study (Fig. 5).

Discussion

To account for the fluorescence decay of Spinach upon illumination, we evaluated the relevance of several dynamic models. We began with the simplest kinetic model and progressed towards those of increasing complexity in accordance with experimental observations. The theory for each investigated model is reported in the ESI.† Simple analytical expressions could be derived since the relaxation times associated with Spinach–DFHBI binding and the photochemical processes were not time-correlated. Based on our experimental results (see the relaxation times in Fig. 3b and S7†), we could simplify the dynamic models by assuming the binding steps to be fast on the time scale of the photochemically driven evolution (see ESI†).

As the timescales of thermal return were similar (4.6 min) for the *trans*-DFHBI and the Spinach system, we first tested if a model involving only two exchange processes—(i) non-covalent binding between *cis*-DFHBI and Spinach RNA and (ii) *cis*–*trans* DFHBI photoisomerization (Scheme 2a)—could explain the Spinach photochemical behavior. In this case, illumination would promote *cis*–*trans* DFHBI isomerization, leading to a decrease of the concentration of the *cis*-DFHBI–Spinach complex and a lowered fluorescence emission. To evaluate this preliminary model, we derived theoretical expressions that described the temporal evolution of fluorescence intensity upon applying a light jump (see eqn (82) in the ESI†) to a solution containing *cis*-DFHBI and excess Spinach RNA. Indeed, the mono-exponential decays observed in Fig. S7†

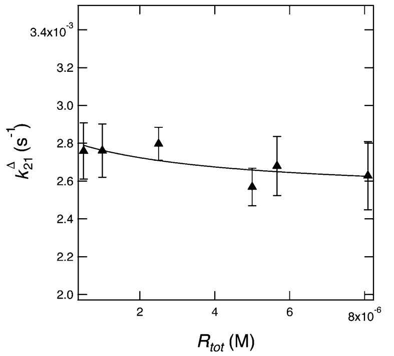

Fig. 5 Dependence of the rate constant k_{21}^{Δ} associated with thermal return of the Spinach system (0.1 µM *cis*-DFHBI and 1.8–20 µM Spinach RNA) on the total concentration R_{tot} in Spinach RNA. Markers: experimental points; solid line: fit with eqn (6) with $I^0 = 0$. Solvent: pH 7.4 HEPES buffer; $T = 293$ K.

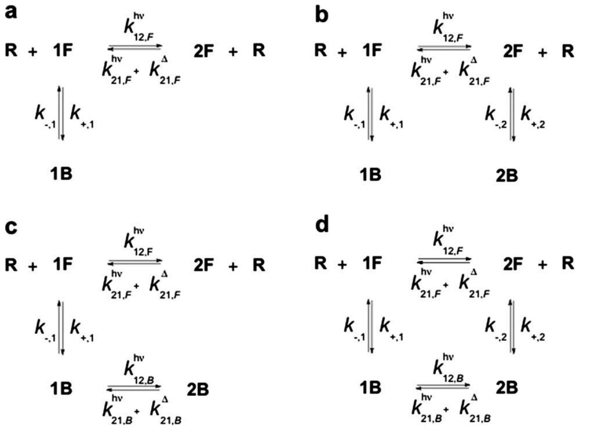

Scheme 2 Dynamic models (a–d) were evaluated to explain the photochemical behavior of the Spinach system. For simplicity, we introduced the symbols **1F**, **2F**, **1B**, and **2B** to represent *cis*-DFHBI, *trans*-DFHBI, Spinach–*cis*-DFHBI, and Spinach–*trans*-DFHBI respectively. $k_{i,j}$ denote rate constants and the superscripts $h\nu$ and Δ respectively denote photochemical and thermal contributions.

matched the behavior predicted by the theory. However, the observed evolution of fluorescence amplitude and the rate constant of fluorescence decay (Fig. 4) were not adequately supported by this model, which predicted (i) a zero loss of fluorescence amplitude at large total concentrations of Spinach RNA and (ii) a decreasing rate constant with increasing total concentration of Spinach RNA (see ESI†). This discrepancy was sufficient to exclude the preliminary model.

Since the loss of fluorescence amplitude was not zero at large Spinach RNA concentrations, we evaluated a second dynamic model in which non-covalent binding between the *trans*-DFHBI stereoisomer and Spinach RNA can also occur (Scheme 2b). Indeed, RNA aptamers capable of this type of discrimination between two stereoisomers of a photochromic molecule have been reported, but generation of effective variants remains difficult, with at best, a ten- to fifty-fold difference in affinity.[22–24] Once again, the mono-exponential temporal evolution of fluorescence intensity was in agreement with theoretical predictions (see eqn (77), (78), (85) and (86) in the ESI†). Moreover, by fixing the parameters $K_{d,1}$, $\varepsilon_{1F}\phi_{12,F} + \varepsilon_{2F}\phi_{21,F}$, and $k^{\Delta}_{21,F}$ to values that were identified through independent experiments (Table 1), we could account for the amplitude of fluorescence decay at varying Spinach RNA concentrations using this model. As with the previous model however, this second model predicted a decrease in the rate constant of the fluorescence decay in response to increasing total concentrations of Spinach RNA (see ESI†). Again, this trend disagreed with the experimental results (Fig. 4b) and allowed us to discard the second model.

Next, we examined the three-exchange processes mechanism shown in Scheme 2c. In addition to *cis–trans* DFHBI photoisomerization and non-covalent binding between *cis*-DFHBI and the Spinach RNA aptamer, this third model took into account the reversible photoconversion of the *cis*-DFHBI bound state to a fourth state. However, since the non-covalent binding steps are much faster than the photoconversion steps (*vide supra*), the theory predicted a biexponential temporal evolution of the fluorescence intensity (see eqn (101)–(104) in the ESI†), which was not supported by our experimental results and disqualified this third dynamic model.

Table 1 Values for the kinetic, thermodynamic, and brightness constants associated with the four state model. ε_i and ϕ_i refer to the molar absorption coefficient and the quantum yield of fluorescence of the species *i*. $\phi_{lm,i}$ represents the quantum yield of photoconversion from state *li* to state *mi*. Solvent: pH 7.4 HEPES buffer; $T = 293$ K

Parameters	Value[a]
$K_{d,1}$	1.3×10^{-6} M
$k_{+,1}$	8.1×10^{4} M^{-1} s^{-1}
$k_{-,1}$	1.4×10^{-1} s^{-1}
$\varepsilon_{1F}\phi_{12,F} + \varepsilon_{2F}\phi_{21,F}$	15.6 m^2 mol^{-1}
$k^{\Delta}_{21,F}$	3.2×10^{-3} s^{-1}
$\varepsilon_{1F}\phi_{12,F}$	10.9 m^2 mol^{-1}
$\varepsilon_{2F}\phi_{21,F}$	4.7 m^2 mol^{-1}
$\varepsilon_{1B}\phi_{12,B}$	16.3 m^2 mol^{-1}
$\varepsilon_{2B}\phi_{21,B}$	29.7 m^2 mol^{-1}
$K_{d,2}$	4.0×10^{-6} M
$\varepsilon_{2B}\phi_{2B}/\varepsilon_{1B}\phi_{1B}$	0.3 ± 0.2
$k^{\Delta}_{21,B}$	2.5×10^{-3} s^{-1}

[a] At $\lambda = 470$ nm; except for $Q_{2B}/Q_{1B} = \varepsilon_{2B}\phi_{2B}/\varepsilon_{1B}\phi_{1B}$, errors on extracted values are 20%.

We finally evaluated a fourth model consisting of a four-state mechanism (Scheme 2d) to explain the observed temporal evolution of fluorescence intensity. This model considered interactions between Spinach and both *cis*- and *trans*-DFHBI, thus yielding the corresponding fluorescent bound states, Spinach–*cis*-DFHBI and Spinach–*trans*-DFHBI. The two isomers also interconvert by photoisomerization in both the bound and unbound states, while thermally driven exchange only contributes to *trans–cis* isomerization. The theory for this fourth model was able to account for the temporal evolution of fluorescence decay, as well as the loss of fluorescence amplitude and the rate constant as a function of Spinach RNA concentration (see eqn (4)–(6)). By fixing the parameters $K_{d,1}$, $\varepsilon_{1F}\phi_{12,F} + \varepsilon_{2F}\phi_{21,F}$, and $k^{\Delta}_{21,F}$ to values found in Table 1, a global fit (Fig. 4) enabled complete extraction of the remaining thermokinetic and photochemical parameters of the system (Table 1).

The robustness of the global fit was evaluated to yield a confidence interval for the dissociation constant of the Spinach–*trans*-DFHBI complex, $K_{d,2}$ or the ratio of the brightness of the *trans*-DFHBI and *cis*-DFHBI bound states Q_{2B}/Q_{1B}. Specifically, we systematically fitted the experimental data shown in Fig. 4 upon forcing the value of either $K_{d,2}$ (with Q_{2B}/Q_{1B} as a floating parameter) or Q_{2B}/Q_{1B} (with $K_{d,2}$ as a floating parameter). Adopting a threshold for the upper value of the χ-square test, we eventually derived $K_{d,2} = 4 \pm 1$ μM and $Q_{2B}/Q_{1B} = 0.3 \pm 0.2$ (see Table 1).

Our analysis confirmed that *cis*-DFHBI gives a stable ($K_{d,1} = 1.3$ μM) complex with Spinach. It further showed that *cis*-DFHBI photoconverts into *trans*-DFHBI with 2.5% photoisomerization quantum yield, and that *trans*-DFHBI also interacts with Spinach to yield a fluorescent complex that is three-fold less stable and one third dimmer. The rather similar affinity of Spinach for the *cis* and *trans* stereoisomers is rather unsurprising. Reported RNA aptamers of photochromic molecules exhibit a modest selectivity in discriminating photochemically exchanging states. Moreover, Spinach has been evolved by systematic evolution of ligands by exponential enrichment (SELEX) without any strategy for discriminating the two stereoisomers.

With the set of parameters given in Table 1, our kinetic analysis further showed that we could reproduce both the amplitude (0.40) and the relaxation time (87 s) of the fluorescence loss observed in Fig. 1a by illuminating a solution of 0.1 μM Spinach and 1 μM DFHBI with 9×10^{-9} Ein s^{-1} light intensity at 464 nm; theoretical analysis (see ESI†) yielded values of amplitude loss and relaxation time of 0.38 and 94 s respectively (see Fig. S3a and b†). For these experimental conditions, our four-state dynamic model predicted that a solution of 0.1 μM Spinach and 1 μM DFHBI would contain free Spinach, Spinach–*cis*-DFHBI, and Spinach–*trans*-DFHBI in a ratio of 8.5 : 3 : 1 respectively (see Fig. S3c and d†). Additionally, our model suggested that the amplitude and the rate of photoswitching could be tuned by varying the light intensity (Fig. S3a and b†). Interestingly, the analysis also indicated that one could tailor the amplitude and the relaxation time of photoswitching by precisely controlling the relative concentrations of DFHBI and Spinach (Fig. S4 and S5†).

Our study suggested that the thermally reversible photoconversion of the Spinach probe could introduce new opportunities for imaging. In particular, we thought that Spinach could display excellent potential for enhanced-contrast imaging of RNA molecules using OLID, an imaging technique that allows the specific isolation of a photo-induced fluorescence signature produced by a photochemically active fluorescent probe in a background of light-insensitive signals.[10] We demonstrated the effectiveness of the Spinach probe for OLID by imaging a mixture of 1 μm beads coupled with either Spinach or fluorescein in the presence of DFHBI (5 μM). Photoconversion was induced by 2.5 s of illumination at 470 nm followed by 5 min of darkness over 5 cycles (Fig. 6a–c). Fluorescence micrographs were recorded at 525 nm (at 4 images s^{-1}) during illumination at 470 nm. The transition between the two states was repeated over 5 cycles with no loss of fluorescence of the Spinach-coupled beads, as predicted from the permanent renewing of fresh DFHBI molecules within the aptamer. While the fluorescence intensity of Spinach-coupled beads was strongly altered by the applied optical perturbation, the fluorescence intensity of fluorescein-coupled beads remained steady over repeated illumination cycles (Fig. 6d). To selectively amplify the signal from the Spinach–DFHBI complex on the recorded micrographs, we evaluated the time-dependent intensity profiles of each pixel against that of a reference pixel, which exhibited photoconversion behavior, using a previously reported cross-correlation function.[10] By emphasizing the unique optical signature of the Spinach probe against unmodulated signals, we were able to eliminate contributions from fluorescein and background (Fig. 6e and f). This experiment showed the effectiveness of OLID in selectively enhancing detection of Spinach-modified species in a background of unrelated fluorescent species.

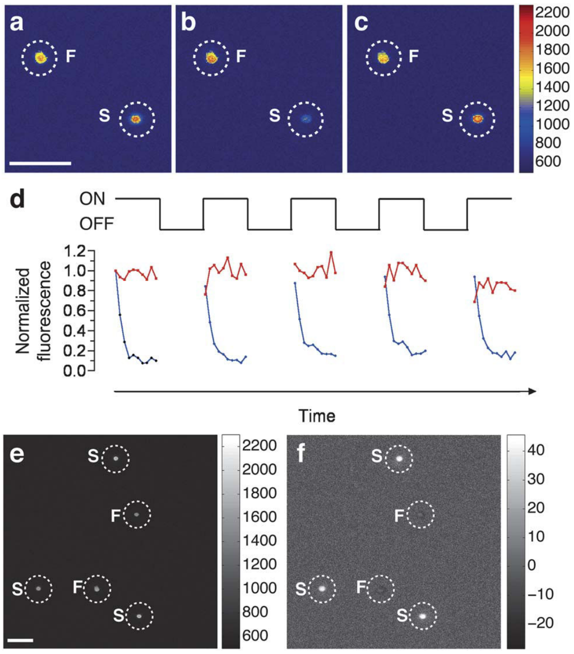

Fig. 6 Enhanced-contrast imaging of Spinach complex through OLID. 1 μm beads coupled with either Spinach (S) or fluorescein (F) in the presence of 5 μM DFHBI in pH 7.4 HEPES buffer were subjected to optical cycling (ON: 2.5 s, OFF: 5 min). Fluorescence images were recorded at (a) 0 s and (b) 2.5 s after illumination and (c) 5 min after dark-state recovery. (d) Intensity profiles of one pixel from a Spinach-covered bead (blue trace) and fluorescein-covered bead (red trace) over 5 ON/OFF cycles. (e) Fluorescence image before OLID treatment. (f) The time dependent behavior of each pixel was cross-correlated with a reference pixel exhibiting photoconversion behavior. The processed image effectively extinguished unmodulated fluorescence arising from fluorescein-beads. Scale bar, 10 μm.

Conclusion

The Spinach RNA probe exhibits a previously unreported photochemical behavior that can be reasonably well-explained with a dynamic model incorporating the (i) non-covalent binding between DFHBI stereoisomers and Spinach RNA to yield two fluorescent bound states, Spinach–*cis*-DFHBI and Spinach–*trans*-DFHBI, and the (ii) photochemical interconversion between two stereoisomers, *cis*-DFHBI and *trans*-DFHBI, as well as between the two complexes, Spinach–*cis*-DFHBI and Spinach–*trans*-DFHBI, by photoisomerization. Compared to other fluorescence turn-on probes,[25] the Spinach system consists of a particular optical signature that combines both photochromism and fluorogenicity due to permanent renewing of the chromophore. These properties in turn provide attractive features such as tunability of the amplitude and the rate constant associated with photoconversion. Such versatility could be adapted into imaging methods, such as OLID, that exploit dynamic exchanges between states of different brightness.

Materials and methods

DFHBI synthesis

DFHBI was synthesized according to the previously reported procedure.[13] The protocols were slightly modified to maximize the purity and yield of the final product.

Synthesis of (*Z*)-2,6-difluoro-4-((2-methyl-5-oxooxazol-4(5*H*)-ylidene)methyl)phenyl acetate (I). A solution of *N*-acetylglycine (296 mg, 2.54 mmol), sodium acetate (208 mg, 2.54 mmol), and 4-hydroxy-3,5-difluorobenzaldehyde (400 mg, 2.54 mmol), in acetic anhydride (1 mL) was purged with argon, and stirred at 110 °C for 2 h. After allowing the solution to cool to room temperature, iced ethanol (10 mL) was added and the resulting mixture was stirred overnight at 4 °C. The precipitate was filtered and thoroughly washed with cold ethanol. After drying, the intermediate **I** was obtained as a pale yellow powder (470 mg, 81%): ^{1}H-NMR (300 MHz, $CDCl_3$) δ 7.80 (d, $J = 8.5$ Hz, 2H), 7.00 (s, 1H), 2.46 (s, 3H), 2.43 (s, 3H).

Synthesis of (*Z*)-4-(3,5-difluoro-4-hydroxybenzylidene)-1,2-dimethyl-1*H*-imidazol-5(4*H*)-one (*cis*-DFHBI). A solution containing **I** (200 mg, 0.71 mmol), dry potassium carbonate (148 mg, 1.1 mmol), and 40% aqueous methylamine (0.3 mL) was refluxed in dioxane (4 mL) for 3 h. After cooling and neutralization with acetic acid (6 mL), ethyl acetate was added and the organic phase was extensively washed with concentrated NaCl solution. The organic layer was dried with anhydrous sodium sulfate and the solvent was evaporated. The resulting crude solid was triturated several times with chloroform to eliminate soluble impurities and to provide *cis*-DFHBI as a dark yellow powder (77 mg, 43%): ^{1}H-NMR (300 MHz, DMSO-d$_6$) δ 7.99 (d, $J = 9.9$ Hz, 2H), 6.92 (s, 1H), 3.10 (s, 3H), 2.38 (s, 3H).

In vitro Spinach transcription

In vitro transcription of Spinach was carried out according to reported procedures.[13] DNA template oligomers corresponding to the Spinach sequence were ordered from Sigma-Aldrich. Appropriate primers were used to amplify the template and append a T7 promoter sequence. PCR products were then transcribed in 20 μL reactions containing a final DNA concentration of 200 nM using the MEGAshortscript T7-kit (Invitrogen). The resulting RNA was treated with DNase and purified with the MEGAclear kit (Invitrogen). Five transcription reactions were typically pooled together during the purification step to obtain a higher concentration of RNA.

Buffer and solutions

All experiments were performed in HEPES buffer (pH 7.4, 40 mM HEPES, 125 mM KCl, 5 mM MgCl$_2$, 1× salmon sperm DNA). DFHBI solutions were diluted from a 20 mM stock in DMSO. All final samples used for spectroscopic measurements contained less than 0.1% DMSO (v/v).

Functionalization of beads

Biotinylated RNA was attached to 1 μm streptavidin coated beads (Dynabeads MyOne Streptavidin C1, Invitrogen). To functionalize the RNA with biotin, a well-structured 35 nt handle sequence was introduced at the 3′ end of Spinach: 5′-GCUCUAGGCCGCGAUUAAAUUCCAACAUGGAUGCU-3′. The resulting Spinach mutant was hybridized with a biotinylated DNA sequence complementary to the appended handle such that the biotin emerged from the 3′ end of the modified Spinach sequence. Functionalization of RNA–biotin was verified by fluorescence correlation spectroscopy, which revealed a 1.7 fold increase in the diffusion coefficient of the Spinach–DFHBI complex upon binding streptavidin in solution.

NMR experiments

DFHBI reversible photoisomerization was directly evidenced by ^{1}H-NMR spectrometry recorded on a Bruker AM 300 spectrometer. *cis*-DFHBI (2 mg) was dissolved in deuterated DMSO (0.5 mL) and the resulting solution was transferred to a 5 mm NMR glass tube. Illumination of the NMR tube content was performed at 405 ± 15 nm up to the steady-state (light flux $I^0(405) = 1.35 \times 10^{-4}$ Ein s^{-1} m^{-2} for 15 min).

Spectroscopic instruments

Fluorescence measurements used for thermodynamic and photochemical calculations were acquired on an LPS 220 spectrofluorometer (PTI, Monmouth Junction, NJ), equipped with a thermoregulated holder held at 20 °C by circulating baths. The 500 μL samples were placed in 1 cm (path length of the incident light) × 0.2 cm quartz cuvettes (Hellma). Light intensity was controlled by varying the current on a LED light supply and precise photon flux densities were measured with a Nova II powermeter (Laser Measurement Instruments).

Thermokinetic analysis

The dissociation constant $K_{\text{d},1}$ of the Spinach–*cis*-DFHBI complex **1B** was determined by following fluorescence emission ($\lambda_{\text{exc}} = 464$ nm and $\lambda_{\text{em}} = 498$ nm) as a function of RNA concentration in a fixed 100 nM solution of DFHBI. RNA concentration was varied by sequentially adding aliquots of a RNA/DFHBI mixture at a constant concentration of DFHBI. To eliminate any putative contribution originating from the photogeneration of *trans*-DFHBI, samples were kept in the dark for 30 min immediately prior to measurement. The data were analyzed assuming a 1 : 1 stoichiometry of the complex, for which the following formula can be derived:

$$\frac{I_{\text{F}}(R_{\text{tot}})}{I_{\text{F}}(0)} = q_1 + \frac{1-q_1}{2}\left[\sqrt{\left(\frac{R_{\text{tot}}}{F_{\text{tot}}} - 1 + \frac{K_{\text{d},1}}{F_{\text{tot}}}\right)^2 + \frac{4\,K_{\text{d},1}}{F_{\text{tot}}}} - \left(\frac{R_{\text{tot}}}{F_{\text{tot}}} - 1 + \frac{K_{\text{d},1}}{F_{\text{tot}}}\right)\right] \quad (1)$$

where $I_{\text{F}}(0)$ is the fluorescence intensity of the fluorophore in the absence of RNA, $I_{\text{F}}(R_{\text{tot}})$ is the fluorescence intensity at chemical equilibrium after addition of RNA at total concentration R_{tot}, q_1 is the ratio $\varepsilon_{1\text{B}}\phi_{1\text{B}}/\varepsilon_{1\text{F}}\phi_{1\text{F}}$ (*i.e.* the relative brightness of the bound and unbound states of DFHBI), and F_{tot} is the total concentration of DFHBI.

The rate constants corresponding to the dissociation and association of the Spinach–*cis*-DFHBI complex **1B** ($k_{-,1}$ and $k_{+,1}$) were determined by stopped-flow experiments. Using a RX2000 rapid kinetic stopped flow accessory (Applied Photophysics, Leatherhead, UK), two 500 μL solutions, A and B, were mixed with typical dead times of 100 ms and the fluorescence intensity was recorded over time at 10 Hz. Solution A contained Spinach RNA (**R**) and solution B contained *cis*-DFHBI (final concentrations 0.2 μM and 2–8 μM, respectively). Samples were excited at 464 nm and fluorescence emission was monitored at 498 nm. To minimize any contribution from the *trans*-DFHBI stereoisomer, samples were kept in the dark for 30 min immediately prior to injection, and the intensity of light was maintained at a level where no photoisomerization was observed on the timescale of the experiments. The temporal evolution of the normalized fluorescence intensity $I_{\text{F}}(t)/I_{\text{F}}(0)$ was analyzed with the following formula:

$$\frac{I_{\text{F}}(t)}{I_{\text{F}}(0)} = 1 + q_1 k_{+,1} R_{\text{tot}}\,\tau_{1,\pm}\left(1 - \text{e}^{-t/\tau_{1,\pm}}\right) \quad (2)$$

where $\tau_{1,\pm} = 1/(k_{+,1}1F_{\text{tot}} + k_{-,1})$ is the relaxation time associated with the complex formation (see ESI† for the derivation).

Photoconversion experiments

The temporal evolution of the normalized fluorescence intensity $I_{\text{F}}(t)/I_{\text{F}}(0)$ from the illuminated *cis*-DFHBI solution was analyzed with the following formula (see eqn (79)–(81) in the ESI†):

$$\frac{I_F(t)}{I_F(0)} = 1 + \left(\frac{Q_{2F}}{Q_{1F}} - 1\right) \frac{k^0_{12,F}}{k^0_{12,F} + k^0_{21,F}} \left[1 - e^{-\left(k^0_{12,F}+k^0_{21,F}\right)t}\right] \quad (3)$$

where Q_{2F}/Q_{1F}, $k^0_{12,F}$, and $k^0_{21,F}$ designate the relative brightness of *trans*-DFHBI with respect to *cis*-DFHBI, and the rate constants associated with the conversions from the *cis*-to-*trans* and from the *trans*-to-*cis* DFHBI states respectively. In the considered experimental geometry,[26] one has additionally $k^0_{12,F} = 2.3\varepsilon_{1F}\phi_{12,F}I^0$ and $k^0_{21,F} = 2.3\varepsilon_{2F}\phi_{21,F}I^0 + k^{\Delta}_{21,F}$, where I^0 is the light intensity.

The temporal evolution of the normalized fluorescence intensity $I_F(t)/I_F(0)$ from the illuminated solution of the Spinach system shown in Fig. 5 was analyzed with the following formula (see eqn (77), (78), (87) and (88) in the ESI†):

$$\frac{I_F(t)}{I_F(0)} = 1 + (Q_r - 1)\frac{k^0_{12}}{k^0_{12} + k^0_{21}} \left[1 - e^{-\left(k^0_{12}+k^0_{21}\right)t}\right] \quad (4)$$

where $Q_r = (Q_{2B}/Q_{1B})(K_{d,1} + R_{tot}/K_{d,2} + R_{tot})$, in which Q_{1B} and Q_{2B} denote the molecular brightness of **1B** and **2B** respectively. k^0_{12}, and k^0_{21} designate the apparent rate constants associated with the conversions from the *cis*-to-*trans* and from the *trans*-to-*cis* DFHBI states respectively. In the considered experimental geometry, one has additionally:

$$k^0_{12} = 2.3\frac{\varepsilon_{1F}\phi_{12,F}K_{d,1} + \varepsilon_{1B}\phi_{12,B}R_{tot}}{K_{d,1} + R_{tot}}I^0 \quad (5)$$

$$k^0_{21} = 2.3\frac{\varepsilon_{2F}\phi_{21,F}K_{d,2} + \varepsilon_{2B}\phi_{21,B}R_{tot}}{K_{d,2} + R_{tot}}I^0 + \frac{k^{\Delta}_{21,F}K_{d,2} + k^{\Delta}_{21,B}R_{tot}}{K_{d,2} + R_{tot}} \quad (6)$$

Optical lock-in detection (OLID)

Fluorescence images were acquired at 525 ± 15 nm (F525-30; Semrock; Rodchester, NY) on a home-built microscope equipped with a dichroic mirror (F524-628; Semrock) mounted with a Luca-R CCD camera (Andor Technology, Belfast, UK), an LED light source (LXML-PB01 from Philips Lumileds, San Jose, CA) filtered at 480 ± 20 nm (HQ 480-40 from Chroma Technology Corp, Rockingham, VT), and collimated with a 50 mm lens (AC254-50-A1,Thorlabs, Newton, NJ) through a 60× objective (UplanApo, NA 1.20 W; Olympus, Hamburg, Germany). Recorded micrographs were appended sequentially by excluding the dark state recovery during periods of no illumination.

The time-dependent intensity profiles of each pixel were evaluated against a reference pixel located within a photochromic fluorescent bead, using a previously reported cross-correlation function:[10]

$$\mathrm{Corr}(x,y) = \sum_t \frac{\left(I(x,y,t) - \langle I(x,y,t)\rangle\right)\left(I_{ref}\left(x_{ref},y_{ref},t\right) - \left\langle I_{ref}\left(x_{ref},y_{ref},t\right)\right\rangle\right)}{\sigma_I\sigma_{ref}} \quad (7)$$

where $I(x,y,t)$ (resp. $I_{ref}(x_{ref},y_{ref},t)$) is the fluorescence intensity at pixel (x,y) (resp. (x_{ref},y_{ref}), *e.g.* within the reference) at a time t during the photoconversion cycle. $\langle I(x,y,t)\rangle$ and $\langle I_{ref}(x_{ref},y_{ref},t)\rangle$, and σ_I and σ_{ref} respectively designate the mean values and the standard deviation (std) values of the fluorescence intensity at the considered pixels. The correlation values generated an intensity-independent image that favored pixels with a time-varying fluorescence signature similar to that of the reference.

Acknowledgements

We thank David Bensimon, Shimon Weiss, and Vincent Croquette for fruitful discussions. This work has been supported by a FEBS Distinguished Young Investigator Award and a FEBS Follow-up Research Fund awarded to A. Gautier, a Charpak Scholarship awarded to S. Nath by the French Embassy in New Delhi (India), and the ANR (PCV 2008, Proteophane; Blanc 2010, T-KiNet). This work has also been supported by the Region Ile-de-France in the framework of C'Nano IdF. C'Nano IdF is the nanoscience competence of Paris Region, supported by CNRS, CEA, MESR and Region Ile-de-France.

Notes and references

1 B. Giepmans, S. Adams, M. Ellisman and R. Tsien, *Science*, 2006, **312**, 217–224.

2 B. Wu, K. D. Piatkevich, T. Lionnet, R. H. Singer and V. V. Verkhusha, *Curr. Opin. Cell Biol.*, 2011, **23**, 310–317.

3 N. Shaner, P. Steinbach and R. Tsien, *Nat. Methods*, 2005, **2**, 905–909.

4 R. Ando, H. Mizuno and A. Miyawaki, *Science*, 2004, **306**, 1370–1373.

5 D. M. Chudakov, T. V. Chepurnykh, V. V. Belousov, S. Lukyanov and K. A. Lukyanov, *Traffic*, 2006, **7**, 1304–1310.

6 M. Fernández-Suárez and A. Y. Ting, *Nat. Rev. Mol. Cell Biol.*, 2008, **9**, 929–943.

7 M. Hofmann, C. Eggeling, S. Jakobs and S. W. Hell, *Proc. Natl. Acad. Sci. U. S. A.*, 2005, **102**, 17565–17569.

8 E. Betzig, G. H. Patterson, R. Sougrat, O. W. Lindwasser, S. Olenych, J. S. Bonifacino, M. W. Davidson, J. Lippincott-Schwartz and H. F. Hess, *Science*, 2006, **313**, 1642–1645.

9 J. Lippincott-Schwartz and G. H. Patterson, *Trends Cell Biol.*, 2009, **19**, 555–565.

10 G. Marriott, S. Mao, T. Sakata, J. Ran, D. K. Jackson, C. Petchprayoon, T. J. Gomez, E. Warp, O. Tulyathan, H. L. Aaron, E. Y. Isacoff and Y. Yan, *Proc. Natl. Acad. Sci. U. S. A.*, 2008, **105**, 17789–17794.

11 A. C. Stiel, S. Trowitzsch, G. Weber, M. Andresen, C. Eggeling, S. W. Hell, S. Jakobs and M. C. Wahl, *Biochem. J.*, 2007, **402**, 35.

12 R. Ando, C. Flors, H. Mizuno, J. Hofkens and A. Miyawaki, *Biophys. J.*, 2007, **92**, L97–L99.

13 J. S. Paige, K. Y. Wu and S. R. Jaffrey, *Science*, 2011, **333**, 642–646.

14 J. S. Paige, T. Nguyen-Duc, W. Song and S. R. Jaffrey, *Science*, 2012, **335**, 1194.

15 M. Andresen, A. C. Stiel, S. Trowitzsch, G. Weber, C. Eggeling, M. C. Wahl, S. W. Hell and S. Jakobs, *Proc. Natl. Acad. Sci. U. S. A.*, 2007, **104**, 13005–13009.

16 G. Abbandonato, G. Signore, R. Nifosì, V. Voliani, R. Bizzarri and F. Beltram, *Eur. Biophys. J.*, 2011, **40**, 1205–1214.

17 J. Dong, F. Abulwerdi, A. Baldridge, J. Kowalik, K. M. Solntsev and L. M. Tolbert, *J. Am. Chem. Soc.*, 2008, **130**, 14096–14098.

18 J. Dong, K. M. Solntsev, O. Poizat and L. M. Tolbert, *J. Am. Chem. Soc.*, 2007, **129**, 10084–10085.

19 M. P. Elenko, J. W. Szostak and A. M. van Oijen, *J. Am. Chem. Soc.*, 2009, **131**, 9866–9867.

20 J. K. Wickiser, M. T. Cheah, R. R. Breaker and D. M. Crothers, *Biochemistry*, 2005, **44**, 13404–13414.

21 J. K. Wickiser, W. C. Winkler, R. R. Breaker and D. M. Crothers, *Mol. Cell*, 2005, **18**, 49–60.

22 H.-W. Lee, S. G. Robinson, S. Bandyopadhyay, R. H. Mitchell and D. Sen, *J. Mol. Biol.*, 2007, **371**, 1163–1173.

23 D. D. Young and A. Deiters, *ChemBioChem*, 2008, **9**, 1225–1228.

24 G. Hayashi, M. Hagihara and K. Nakatani, *Chem.–Eur. J.*, 2009, **15**, 424–432.

25 C. Szent-Gyorgyi, B. A. Schmidt, Y. Creeger, G. W. Fisher, K. L. Zakel, S. Adler, J. A. J. Fitzpatrick, C. A. Woolford, Q. Yan, K. V. Vasilev, P. B. Berget, M. P. Bruchez, J. W. Jarvik and A. Waggoner, *Nat. Biotechnol.*, 2008, **26**, 235–240.

26 M. Emond, T. Le Saux, S. Maurin, J.-B. Baudin, R. Plasson and L. Jullien, *Chem.–Eur. J.*, 2010, **16**, 8822–8831.

2.3 Supporting Information

Photochemical properties of Spinach and its use in selective imaging (Supporting information)

Pengcheng Wang,[a,b] Jérôme Querard,[a] Sylvie Maurin,[a] Sarang S. Nath,[a]
Thomas Le Saux,[a,c],* Arnaud Gautier,[a],* Ludovic Jullien[a,c],*

[a]*Ecole Normale Supérieure, Département de Chimie,*
UMR CNRS-ENS-UPMC Paris 06 8640 Pasteur,
24, rue Lhomond, 75231 Paris Cedex 05, France.
E-mail: Thomas.Lesaux@ens.fr, Arnaud.Gautier@ens.fr, Ludovic.Jullien@ens.fr

[b]*Institut Curie, Centre de Recherche, UMR 176 CNRS-Institut Curie,*
26 rue d'Ulm, 75248 Paris, France.

[c]*UPMC Univ Paris 06,*
4 Place Jussieu, 75232 Paris Cedex 05, France.

1 Theoretical model for the *cis*-DFHBI-Spinach RNA association experiments

In the absence of any photoisomerization, the temporal evolution of the solution composition resulting from mixing solutions of *cis*-DFHBI and Spinach RNA is governed by Eq.(1):

$$\mathbf{R} + \mathbf{1F} \quad \underset{k_{-,1}}{\overset{k_{+,1}}{\rightleftharpoons}} \quad \mathbf{1B} \tag{1}$$

The kinetic law associated with reaction (1) in a homogeneous solution follows:

$$\frac{d1B(t)}{dt} = k_{+,1}\,1F(t)R(t) - k_{-,1}\,1B(t). \tag{2}$$

Being in excess with respect to R in the series of stopped-flow experiments, the concentration of fluorophore **1F** was assumed constant in both mixed solutions such that $1F(t) = 1F_{tot}$. Upon considering the total concentration in **R**, $R_{tot} = R(t) + 1B(t)$, Eq. (2) yields:

$$1B(t) = \frac{k_{+,1}1F_{tot}}{k_{+,1}1F_{tot} + k_{-,1}}\left(1 - e^{-t/\tau_{1,\pm}}\right) R_{tot}, \tag{3}$$

with

$$\tau_{1,\pm} = (k_{+,1}1F_{tot} + k_{-,1})^{-1}. \tag{4}$$

Eq.(3) can be used to derive the temporal dependence of the normalized fluorescence intensity $I_F(t)/I_F(0)$:

$$\frac{I_F(t)}{I_F(0)} = 1 + q_1 k_{+,1} R_{tot} \tau_{1,\pm}\left(1 - e^{-t/\tau_{1,\pm}}\right), \tag{5}$$

where $q_1 = \frac{Q_{1B}}{Q_{1F}}$ designates the relative brightness between **1B** and **1F**.

2 Theoretical analyses

In this section, we theoretically analyze the dynamic behavior of the models displayed in Scheme 2 of the Main Text. Sharing in common nodes and exchanging processes, those dynamic models only differ by the number of considered nodes and exchanging processes. Instead of exploring stepwise those models, we first consider the most complete model (shown in Scheme 2d), from which we derive the behavior of the simpler models.

2.1 The generic dynamic model

The generic dynamic model is a four-state mechanism consisting of two *trans*-DFHBI states (bound and unbound) in addition to the previously reported *cis* states of DFHBI. Both *cis*- and *trans*-DFHBI interact with Spinach RNA to yield the corresponding fluorescent bound states, Spinach-*cis*-DFHBI and Spinach-*trans*-DFHBI. The two isomers interconvert by photoisomerization in both the bound and unbound states while only *trans*-*cis* isomerization may occur by thermally-driven exchange. For simplicity, this section uses the symbols **1F**, **2F**, **1B**, and **2B** to represent *cis*-DFHBI, *trans*-DFHBI, Spinach-*cis*-DFHBI, and Spinach-*trans*-DFHBI respectively. The associated rate constants are presented in Figure S1, where the superscripts hv and Δ respectively denote photochemical and thermal contributions.[a]

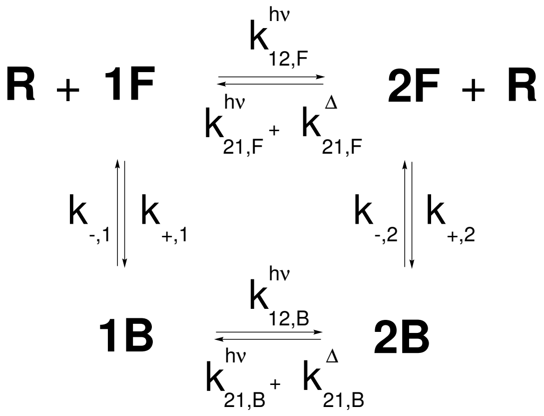

Figure S1: Four-state mechanism accounting for the photochemical and complexation behavior of a photochromic fluorogen in the presence of a receptor.

The theoretical framework closely mirrors that described in a previous work by Emond et al.[1] The concentration profiles within the four state model are governed by the equations:

---

[a] ^{1}H-NMR evidence suggests a high purity of the **1F** state prior to illumination, i.e. $k^{\Delta}_{12,F} \ll k^{\Delta}_{21,F}$. Thermal contributions were thus neglected for the forward exchange from **1F** and **2F** to **1B** and **2B** respectively.

$$\frac{d1B}{dt} = -\left(k_{\mathbf{1B\to 1F}} + k_{\mathbf{1B\to 2B}}\right) 1B + k_{\mathbf{2B\to 1B}}\, 2B + k_{\mathbf{1F\to 1B}}\, R\, 1F \tag{6}$$

$$\frac{d2B}{dt} = k_{\mathbf{1B\to 2B}}\, 1B - \left(k_{\mathbf{2B\to 2F}} + k_{\mathbf{2B\to 1B}}\right) 2B + k_{\mathbf{2F\to 2B}}\, R\, 2F \tag{7}$$

$$\frac{d1F}{dt} = k_{\mathbf{1B\to 1F}} 1B - \left(k_{\mathbf{1F\to 1B}}\, R + k_{\mathbf{1F\to 2F}}\right) 1F + k_{\mathbf{2F\to 1F}}\, 2F \tag{8}$$

$$\frac{d2F}{dt} = k_{\mathbf{2B\to 2F}} 2B + k_{\mathbf{1F\to 2F}}\, 1F - \left(k_{\mathbf{2F\to 2B}}\, R + k_{\mathbf{2F\to 1F}}\right) 2F \tag{9}$$

The temporal dependence of concentrations cannot be obtained in the most general case. However, it can be analyzed in asymptotic situations according to the nature of the rate-limiting steps, which are associated to either the photochemical reactions or the complexation reactions. Crossing between both kinetic regimes typically occurs when the relaxation times associated to the photoisomerization and the complexation reactions are equal. Relying on the values subsequently extracted for the Spinach system at the micromolar concentrations used in the present study (*vide infra*), we predicted that photoisomerization would remain rate-limiting up to 2.25×10^{-2} ein.s^{-1}.m^{-2},[b] a value lying much above our typical light flux. Thus we reduced further theoretical analysis in the following to the regimes where photoisomerization is rate-limiting.

The different dynamic models shown in Scheme 2 correspond to particular values of the rate constants involved in Figure S1. The most general situation corresponding to non-zero values is shown in Scheme 2d. Schemes 2b and 2c are respectively associated to zero values for $k_{12,B}^{h\nu,0}$ and $k_{21,B}^{h\nu,0} + k_{21,B}^{\Delta}$, and for $k_{+,2}$ and $k_{-,2}$, whereas Scheme 2a is associated to zero values for $k_{12,B}^{h\nu,0}$, $k_{21,B}^{h\nu,0} + k_{21,B}^{\Delta}$, $k_{+,2}$, and $k_{-,2}$.

Depending on the values of the rate constants $k_{+,2}$ and $k_{-,2}$, two different reduced schemes result from the reduction of the mechanism displayed in Figure S1 upon considering that photoisomerization is rate-limiting. In the most general situation, $k_{+,2}$ and $k_{-,2}$ adopt non-zero values; then the reduced mechanism involves the exchange between two reduced species (Figure S2a : Two state model). In contrast, when both $k_{+,2}$ and $k_{-,2}$

---

[b] On the one hand, the relaxation time in a regime where photochemistry is rate-limiting was calculated for increasing light intensities using Eq.(54) and the parameters displayed in Table 1 of the Main Text. On the other hand, the relaxation time in a regime where complexation is rate-limiting was similarly calculated using Eq.(10) which originates from reducing to the corresponding two state model in the case $R_{tot} \ll F_{tot}$:

$$\tau_{\pm}^{F,0} = \frac{1}{k_{+}^{0} F_{tot} + k_{-}^{0}} \tag{10}$$

with

$$k_{+}^{0} = \frac{k_{+,1}^{\Delta} + k_{+,2}^{\Delta}\, K_{F}^{h\nu,\Delta,0}}{1 + K_{F}^{h\nu,\Delta,0}} \tag{11}$$

$$k_{-}^{0} = \frac{k_{-,1}^{\Delta} + k_{-,2}^{\Delta}\, K_{B}^{h\nu,\Delta,0}}{1 + K_{B}^{h\nu,\Delta,0}} \tag{12}$$

and

$$K_{F}^{h\nu,\Delta,0} = \frac{k_{12,F}^{h\nu,0}}{k_{21,F}^{h\nu,0} + k_{21,F}^{\Delta}} \tag{13}$$

$$K_{B}^{h\nu,\Delta,0} = \frac{k_{12,B}^{h\nu,0}}{k_{21,B}^{h\nu,0} + k_{21,B}^{\Delta}}. \tag{14}$$

Then we derived the light intensity for which the two relaxation times were equal.

are equal to zero, the reduced mechanism involves three species and two exchanges (Figure S2b : Three state model).

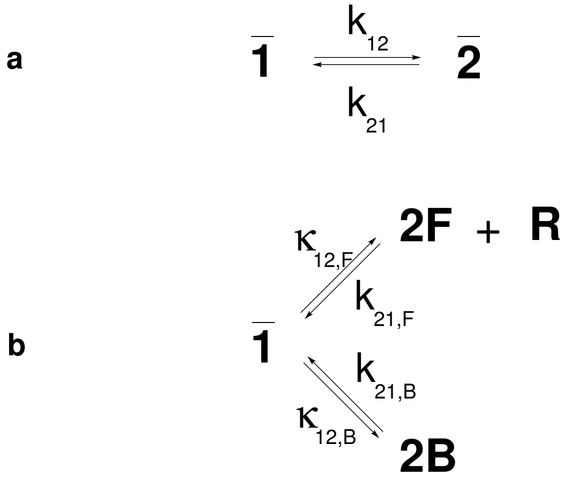

Figure S2: : Models resulting from reduction of the mechanism shown in Figure S1 upon considering that photoisomerization is rate-limiting. **a**: Two state model where $k_{+,2}$ and $k_{-,2}$ adopt non-zero values; **b**: Three state model with $k_{+,2}$ and $k_{-,2}$ equal to zero.

2.2 Analysis of the reduced two state model

In the "low"-illumination regime with non-zero values for $k_{+,2}$ and $k_{-,2}$ (Figure S2a), it is meaningful to introduce the average species $\overline{\mathbf{1}}$ and $\overline{\mathbf{2}}$ (concentrations $\overline{1} = 1F + 1B$ and $\overline{2} = 2F + 2B$). The "instantaneous" concentrations in **1F**, **1B**, **2F** and **2B** then follow[c],

$$1F = \frac{1}{1 + K_1^{\Delta} R}\overline{1} \tag{15}$$

$$1B = \frac{K_1^{\Delta} R}{1 + K_1^{\Delta} R}\overline{1} \tag{16}$$

$$2F = \frac{1}{1 + K_2^{\Delta} R}\overline{2} \tag{17}$$

$$2B = \frac{K_2^{\Delta} R}{1 + K_2^{\Delta} R}\overline{2} \tag{18}$$

where

$$K_1^{\Delta} = \frac{k_{+,1}^{\Delta}}{k_{-,1}^{\Delta}} \tag{19}$$

$$K_2^{\Delta} = \frac{k_{+,2}^{\Delta}}{k_{-,2}^{\Delta}}. \tag{20}$$

Thus Eqs.(6–9) transform into Eq.(21):

$$\frac{d\overline{1}}{dt} = -\frac{d\overline{2}}{dt} = -k_{12}\,\overline{1} + k_{21}\,\overline{2} \tag{21}$$

---

[c] The association constants, K_1^{Δ} and K_2^{Δ} are the inverse of the dissociation constants $K_{d,1}$ and $K_{d,2}$. Furthermore, $k_{+,1}$ and $k_{-,1}$ have been replaced with $k_{+,1}^{\Delta}$ and $k_{-,1}^{\Delta}$ to articulate that these rate constants are only affected by temperature rather than light.

with

$$k_{12} = \frac{k_{12,F}^{h\nu} + k_{12,B}^{h\nu}\, K_1^{\Delta} R}{1 + K_1^{\Delta} R} \tag{22}$$

$$k_{21} = \frac{\left(k_{21,F}^{h\nu} + k_{21,F}^{\Delta}\right) + \left(k_{21,B}^{h\nu} + k_{21,B}^{\Delta}\right)\, K_2^{\Delta} R}{1 + K_2^{\Delta} R}. \tag{23}$$

In the most general case, Eq.(21) has no analytical solution, because k_{12} and k_{21} are time-dependent as a result of the $R(t)$ term. However, a tractable temporal dependence of the concentrations after a light jump from 0 to I^0 can be obtained in two regimes:

- The total concentration of the receptor (R_{tot}) is much larger than that of the fluorogen (F_{tot}): $R_{tot} \gg F_{tot}$. Then

$$k_{12} = \frac{k_{12,F}^{h\nu} + k_{12,B}^{h\nu}\, K_1^{\Delta} R_{tot}}{1 + K_1^{\Delta} R_{tot}} \tag{24}$$

$$k_{21} = \frac{\left(k_{21,F}^{h\nu} + k_{21,F}^{\Delta}\right) + \left(k_{21,B}^{h\nu} + k_{21,B}^{\Delta}\right)\, K_2^{\Delta} R_{tot}}{1 + K_2^{\Delta} R_{tot}}. \tag{25}$$

  This case is relevant to analyze the experiments reported in the Main Text when $R_{tot} \gg F_{tot}$.

- The change of light intensity generates a perturbation of the solution composition of small amplitude. As a consequence, Eq.(21) can be solved at first order of light perturbation. This case is relevant to analyze the experiments reported in the Main Text when $F_{tot} \gg R_{tot}$.

2.2.1 Case $R_{tot} \gg F_{tot}$

In such a regime, the apparent rate constant k_{12} and k_{21} can be considered constant and equal to k_{12}^0 and k_{21}^0 given by

$$k_{12}^0 = \frac{k_{12,F}^{h\nu,0} + k_{12,B}^{h\nu,0}\, K_1^{\Delta} R_{tot}}{1 + K_1^{\Delta} R_{tot}} \tag{26}$$

$$k_{21}^0 = \frac{\left(k_{21,F}^{h\nu,0} + k_{21,F}^{\Delta}\right) + \left(k_{21,B}^{h\nu,0} + k_{21,B}^{\Delta}\right)\, K_2^{\Delta} R_{tot}}{1 + K_2^{\Delta} R_{tot}}. \tag{27}$$

Since $F_{tot} = \overline{1} + \overline{2}$, Eq.(21) becomes:

$$-\frac{d\left(\overline{2} - \overline{2}^0\right)}{dt} = \left(k_{12}^0 + k_{21}^0\right)\left(\overline{2} - \overline{2}^0\right) \tag{28}$$

without any restriction on the amplitude of light jump. Then Eq.(28) leads to

$$\overline{2} - \overline{2}^0 = \overline{1}^0 - \overline{1} = -\overline{2}^0 \exp\left(-\frac{t}{\tau_{12}^0}\right) \tag{29}$$

where

$$\begin{aligned}
\overline{2}^0 &= \frac{K_{12}^0}{1+K_{12}^0}F_{tot} && (30)\\
\overline{1}^0 &= \frac{1}{1+K_{12}^0}F_{tot} && (31)\\
1F^0 &= \frac{1}{1+K_1^\Delta R_{tot}}\overline{1}^0 && (32)\\
2F^0 &= \frac{1}{1+K_2^\Delta R_{tot}}\overline{2}^0 && (33)\\
1B^0 &= \frac{K_1^\Delta R_{tot}}{1+K_1^\Delta R_{tot}}\overline{1}^0 && (34)\\
2B^0 &= \frac{K_2^\Delta R_{tot}}{1+K_2^\Delta R_{tot}}\overline{2}^0 && (35)\\
R^0 &= R_{tot} - \left(\frac{K_1^\Delta R_{tot}}{1+K_1^\Delta R_{tot}} + \frac{K_2^\Delta R_{tot}}{1+K_2^\Delta R_{tot}}K_{12}^0\right)\frac{1}{1+K_{12}^0}F_{tot} \sim R_{tot} && (36)\\
\tau_{12}^0 &= \frac{1}{k_{12}^0+k_{21}^0} && (37)\\
K_{12}^0 &= \frac{k_{12}^0}{k_{21}^0} && (38)
\end{aligned}$$

In Eqs.(30–38), $\overline{2}^0$, $\overline{1}^0$, $1F^0$, $1B^0$, $2F^0$, $2B^0$, R^0, τ_{12}^0, and K_{12}^0 respectively denote the steady-state values of $\overline{2}$, $\overline{1}$, $1F$, $1B$, $2F$, $2B$, and R, the apparent relaxation time associated to the photochemical reactions, and the apparent photoisomerization constant of the fluorogen **F**, in the presence of light at constant intensity I^0.

2.2.2 Case of a perturbation of small amplitude

In this regime, there is no restriction on the relative concentrations of **R** and **F**. Thus the apparent rate constant k_{12} and k_{21} cannot be anymore considered constant at the investigated time scale. To be able to perform analytical calculations, we consider that the light jump generates a perturbation of small amplitude. Then we solve Eq.(21) at first order of the light perturbation upon writing:

$$\begin{aligned}
\overline{2} &= \overline{2}^0 + \varepsilon\overline{2}^1(t) && (39)\\
\overline{1} &= \overline{1}^0 - \varepsilon\overline{2}^1(t) && (40)\\
R &= R^0 + \varepsilon R^1(t) && (41)
\end{aligned}$$

where $\overline{1}^0$, $\overline{2}^0$, and R^0 denote the steady-state value of the concentrations when light of intensity I^0 is applied on the system.[d] Note that it is the same first order term which intervenes in Eqs. (39) and (40) since $\overline{1}+\overline{2} = \overline{1}^0+\overline{2}^0 = F_{tot}$.

In a first step, the relation existing between $\overline{2}^1(t)$ and $\varepsilon R^1(t)$ is extracted. In relation to Eqs.(15–18), we

---

[d] The analytical expressions of these concentrations cannot be obtained. Indeed the steady-state concentration R^0 is governed by a polynomial equation, which has no analytical solution. In contrast, those values can be derived numerically.

first derive:

$$\begin{aligned} \frac{1}{1+K_i^\Delta R} &= \frac{1}{1+K_i^\Delta R^0}\left(1-\frac{K_i^\Delta R^1}{1+K_i^\Delta R^0}\varepsilon\right) && (42)\\ \frac{K_i^\Delta R}{1+K_i^\Delta R} &= \frac{K_i^\Delta R^0}{1+K_i^\Delta R^0}\left(1+\frac{R^1}{R^0\left(1+K_i^\Delta R^0\right)}\varepsilon\right) && (43) \end{aligned}$$

with $i = 1$ or 2. Derivation of Eqs.(42,43) only requires that $K_i^\Delta \varepsilon R^1 \ll 1 + K_i^\Delta R^0$. This condition is fulfilled in the most general case as soon as $\varepsilon R^1 \ll R^0$ where the light jump causes a small change of the concentration in **R**. However, it is also interestingly fulfilled without any restriction on the relative values of R^0 and εR^1 when the **R** concentration is low enough so as to have $K_i^\Delta R_{tot} \ll 1$. Then one has both $K_i^\Delta R^0 \ll 1$ and $K_i^\Delta \varepsilon R^1 \ll 1$. This case is relevant to analyze the experiments described in the Main Text.

Then we use Eqs.(16,18) and the conservation law

$$R_{tot} = R + 1B + 2B \qquad (44)$$

to yield

$$R^1 = \gamma \overline{2}^1 \qquad (45)$$

with

$$\gamma = \frac{\frac{K_1^\Delta R^0}{1+K_1^\Delta R^0} - \frac{K_2^\Delta R^0}{1+K_2^\Delta R^0}}{1 + \frac{K_1^\Delta \overline{1}^0}{\left(1+K_1^\Delta R^0\right)^2} + \frac{K_2^\Delta \overline{2}^0}{\left(1+K_2^\Delta R^0\right)^2}} \qquad (46)$$

The temporal dependence of k_{12} and k_{21}

$$\begin{aligned} k_{12}(t) &= \frac{k_{12,F}^{h\nu,0} + k_{12,B}^{h\nu,0}\, K_1^\Delta R(t)}{1+K_1^\Delta R(t)} && (47)\\ k_{21}(t) &= \frac{\left(k_{21,F}^{h\nu,0} + k_{21,F}^\Delta\right) + \left(k_{21,B}^{h\nu,0} + k_{21,B}^\Delta\right)\, K_2^\Delta R(t)}{1+K_2^\Delta R(t)} && (48) \end{aligned}$$

is then extracted at first order using Eqs.(41,45). We derived

$$\begin{aligned} k_{12}(t) &= k_{12}^0 + \left(k_{12,B}^{h\nu,0} - k_{12,F}^{h\nu,0}\right)\frac{K_1^\Delta \varepsilon\gamma}{\left(1+K_1^\Delta R^0\right)^2}\overline{2}^1(t) && (49)\\ k_{21}(t) &= k_{21}^0 + \left(k_{21,B}^{h\nu,0} - k_{21,F}^{h\nu,0}\right)\frac{K_2^\Delta \varepsilon\gamma}{\left(1+K_2^\Delta R^0\right)^2}\overline{2}^1(t) && (50) \end{aligned}$$

with

$$\begin{aligned} k_{12}^0 &= \frac{k_{12,F}^{h\nu,0} + k_{12,B}^{h\nu,0}\, K_1^\Delta R^0}{1+K_1^\Delta R^0} && (51)\\ k_{21}^0 &= \frac{\left(k_{21,F}^{h\nu,0} + k_{21,F}^\Delta\right) + \left(k_{21,B}^{h\nu,0} + k_{21,B}^\Delta\right)\, K_2^\Delta R^0}{1+K_2^\Delta R^0}. && (52) \end{aligned}$$

Eq.(21) is then solved upon using the expressions (39,40,49,50). We derived

$$\frac{d\overline{2}^1}{dt} + \frac{1}{\tau_{12}^0}\overline{2}^1 = 0 \tag{53}$$

with

$$\tau_{12}^0 = \frac{1}{k_{12}^0 + k_{21}^0 + \left(\gamma_{21}^0\overline{2}^0 - \gamma_{12}^0\overline{1}^0\right)} \tag{54}$$

where

$$\gamma_{12}^0 = \left(k_{12,B}^{h\nu,0} - k_{12,F}^{h\nu,0}\right)\frac{K_1^\Delta\gamma}{\left(1+K_1^\Delta R^0\right)^2} \tag{55}$$

$$\gamma_{21}^0 = \left(k_{21,B}^{h\nu,0} - k_{21,F}^{h\nu,0}\right)\frac{K_2^\Delta\gamma}{\left(1+K_2^\Delta R^0\right)^2} \tag{56}$$

Considering that the **2** states are not present at initial time, we then obtain:

$$\varepsilon\overline{2}^1(t) = \overline{2} - \overline{2}^0 = \overline{1}^0 - \overline{1} = -\overline{2}^0\exp\left(-\frac{t}{\tau_{12}^0}\right) \tag{57}$$

where

$$\overline{2}^0 = \frac{K_{12}^0}{1+K_{12}^0}F_{tot} \tag{58}$$

$$\overline{1}^0 = \frac{1}{1+K_{12}^0}F_{tot} \tag{59}$$

$$R^0 = R_{tot} - \left(\frac{K_1^\Delta R^0}{1+K_1^\Delta R^0}\overline{1}^0 + \frac{K_2^\Delta R^0}{1+K_2^\Delta R^0}\overline{2}^0\right) \tag{60}$$

$$K_{12}^0 = \frac{k_{12}^0}{k_{21}^0} \tag{61}$$

Equipped with Eqs.(15–18,39,40,42,43) one has also at first order

$$1F(t) = 1F^0 - \frac{1+K_1^\Delta R^0 + K_1^\Delta\gamma\overline{1}^0}{\left(1+K_1^\Delta R^0\right)^2}\varepsilon\overline{2}^1(t) \tag{62}$$

$$1B(t) = 1B^0 + \frac{K_1^\Delta\gamma\overline{1}^0 - K_1^\Delta R^0\left(1+K_1^\Delta R^0\right)}{\left(1+K_1^\Delta R^0\right)^2}\varepsilon\overline{2}^1(t) \tag{63}$$

$$2F(t) = 2F^0 + \frac{1+K_2^\Delta R^0 - K_2^\Delta\gamma\overline{2}^0}{\left(1+K_2^\Delta R^0\right)^2}\varepsilon\overline{2}^1(t) \tag{64}$$

$$2B(t) = 2B^0 + \frac{K_2^\Delta\gamma\overline{2}^0 + K_2^\Delta R^0\left(1+K_2^\Delta R^0\right)}{\left(1+K_2^\Delta R^0\right)^2}\varepsilon\overline{2}^1(t) \tag{65}$$

with

$$1F^0 = \frac{1}{1+K_1^\Delta R^0}\overline{1}^0 \tag{66}$$

$$1B^0 = \frac{K_1^\Delta R^0}{1+K_1^\Delta R^0}\overline{1}^0 \tag{67}$$

$$2F^0 = \frac{1}{1+K_2^\Delta R^0}\overline{2}^0 \tag{68}$$

$$2B^0 = \frac{K_2^\Delta R^0}{1+K_2^\Delta R^0}\overline{2}^0 \tag{69}$$

In Eqs.(58–65), $\overline{2}^0$, $\overline{1}^0$, R^0, $1F^0$, $1B^0$, $2F^0$, $2B^0$, τ_{12}^0, K_{12}^0 respectively denote the steady-state value of $\overline{2}$, $\overline{1}$, R, $1F$, $1B$, $2F$, $2B$, the apparent relaxation time associated to the photochemical reactions, and the apparent photoisomerization constant of the fluorogen **F**, in the presence of light at constant intensity I^0.

2.2.3 Analysis of the fluorescence emission

Fluorescence emission $I_F(t)$ originates from summing the individual contributions of the fluorogen-derived species **1F**, **2F**, **1B**, and **2B**. Denoting Q_i for the molecular brightness, one has

$$I_F(t) = (Q_{1F}1F + Q_{2F}2F + Q_{1B}1B + Q_{2B}2B)\, I^0 \tag{70}$$

where the expressions of $1F$, $2F$, $1B$, and $2B$ depend on the experimental regimes.

The expressions of $1F$, $2F$, $1B$, and $2B$ can be retrieved from Eqs.(15–18) and (29–38) or (57–69). Then one has:

$$I_F = \left[A^0 + (Q_1 - Q_2)\,\overline{2}^0 \exp\left(-\frac{t}{\tau_{12}^0}\right)\right] I^0 \tag{71}$$

with

$$A^0 = Q_{1F}1F^0 + Q_{2F}2F^0 + Q_{1B}1B^0 + Q_{2B}2B^0 \tag{72}$$

and

- Case $R_{tot} \gg F_{tot}$:

$$Q_2 = \frac{Q_{2F} + Q_{2B}K_2^{\Delta}R_{tot}}{1 + K_2^{\Delta}R_{tot}} \tag{73}$$

$$Q_1 = \frac{Q_{1F} + Q_{1B}K_1^{\Delta}R_{tot}}{1 + K_1^{\Delta}R_{tot}} \tag{74}$$

- Case of a perturbation of small amplitude:

$$Q_2 = \frac{1 + K_2^{\Delta}R^0 - K_2^{\Delta}\gamma\overline{2}^0}{\left(1 + K_2^{\Delta}R^0\right)^2}Q_{2F} + \frac{K_2^{\Delta}\gamma\overline{2}^0 + K_2^{\Delta}R^0\left(1 + K_2^{\Delta}R^0\right)}{\left(1 + K_2^{\Delta}R^0\right)^2}Q_{2B} \tag{75}$$

$$Q_1 = \frac{1 + K_1^{\Delta}R^0 + K_1^{\Delta}\gamma\overline{1}^0}{\left(1 + K_1^{\Delta}R^0\right)^2}Q_{1F} + \frac{K_1^{\Delta}R^0\left(1 + K_1^{\Delta}R^0\right) - K_1^{\Delta}\gamma\overline{1}^0}{\left(1 + K_1^{\Delta}R^0\right)^2}Q_{1B} \tag{76}$$

Moreover assuming that the system contains only $\overline{\mathbf{1}}$ before illumination and that the brightnesses of both free states can be neglected in the presence of their corresponding bound states (which is the case in the explored regime of Spinach RNA concentration), the temporal evolution of photoinduced fluorescence-loss given in Eq.(71) yields:

$$I_F(t) = I_F(0)\left[1 + (Q_r - 1)\frac{k_{12}^0}{k_{12}^0 + k_{21}^0}\left(1 - e^{-(k_{12}^0 + k_{21}^0)t}\right)\right] \tag{77}$$

with

$$Q_r = \frac{Q_{2B}}{Q_{1B}} \times \frac{K_{d,1} + R_{tot}}{K_{d,2} + R_{tot}} \tag{78}$$

where $I_F(0)$ is the initial fluorescence intensity at $t = 0$, $I_F(t)$ is the fluorescence intensity at time t, and Q_{2B} and Q_{1B} denote the molecular brightnesses of **2B** and **1B** respectively.

2.2.4 Application to various dynamic models

Photoisomerization of the *cis*-DFHBI fluorogen In relation to the photoisomerization of the *cis*-DFHBI fluorogen in the absence of Spinach RNA which was investigated in an independent experiment, we first derive the temporal dependence of the normalized fluorescence intensity upon applying a light jump from 0 to I^0. Hence we adapted Eq.(71) to derive

$$I_F(t) \;=\; I_F(0)\left[1+\left(\frac{Q_{2F}}{Q_{1F}}-1\right)\frac{k_{12}^0}{k_{12}^0+k_{21}^0}\left(1-e^{-(k_{12}^0+k_{21}^0)t}\right)\right] \tag{79}$$

with

$$k_{12}^0 \;=\; k_{12,F}^{h\nu,0} \tag{80}$$

$$k_{21}^0 \;=\; k_{21,F}^{h\nu,0}+k_{21,F}^{\Delta}. \tag{81}$$

Photoisomerization and complexation of the *cis*-DFHBI fluorogen (Scheme 2a) In the regime considered in the Main Text ($R_{tot} \gg F_{tot}$), Eq.(77,78) adopt different expressions upon assuming that the system contains only $\overline{\mathbf{1}}$ before illumination and that the brightnesses of both free states can be neglected in the presence of the bound state(s) (which is the case in the explored regime of Spinach RNA concentration). In the case of the dynamic model displayed in Scheme 2a, one has

$$I_F(t) \;=\; I_F(0)\left[1-\frac{k_{12}^0}{k_{12}^0+k_{21}^0}\left(1-e^{-(k_{12}^0+k_{21}^0)t}\right)\right] \tag{82}$$

with

$$k_{12}^0 \;=\; \frac{K_{d,1}}{K_{d,1}+R_{tot}}k_{12,F}^{h\nu,0} \tag{83}$$

$$k_{21}^0 \;=\; k_{21,F}^{h\nu,0}+k_{21,F}^{\Delta} \tag{84}$$

When R_{tot} is much larger than $K_{d,1}$, k_{12}^0 becomes notably vanishing. As a consequence, one expects the loss of fluorescence amplitude to vanish and the rate of fluorescence decay ($k_{12}^0+k_{21}^0$) to decrease, when the total concentration of **R** is increased.

Photoisomerization of *cis*-DFHBI and complexation of both *cis*- and *trans*-DFHBI stereoisomers (Scheme 2b) In the case of the dynamic model displayed in Scheme 2b, Eqs.(77,78) are valid with

$$k_{12}^0 \;=\; \frac{K_{d,1}}{K_{d,1}+R_{tot}}k_{12,F}^0 \tag{85}$$

$$k_{21}^0 \;=\; \frac{K_{d,2}}{K_{d,2}+R_{tot}}k_{21,F}^0. \tag{86}$$

When R_{tot} is much larger than $K_{d,1}$ and $K_{d,2}$, both k_{12}^0 and k_{21}^0 become notably vanishing. As a consequence, one expects the rate of fluorescence decay ($k_{12}^0+k_{21}^0$) to vanish when the total concentration of **R** is increased.

Photoisomerization of and complexation of both *cis*- and *trans*-DFHBI stereoisomers (Scheme 2d) In the case of the dynamic model displayed in Scheme 2d, Eqs.(77,78) are valid with

$$k^0_{12} = \frac{k^0_{12,F}\, K_{d,1} + k^0_{12,B}\, R_{tot}}{K_{d,1} + R_{tot}} \tag{87}$$

$$k^0_{21} = \frac{k^0_{21,F}\, K_{d,2} + k^0_{21,B}\, R_{tot}}{K_{d,2} + R_{tot}}. \tag{88}$$

2.3 Analysis of the reduced three state model

In the "low"-illumination regime with zero values for $k_{+,2}$ and $k_{-,2}$ (Figure S2b), one can now introduce only one average species $\bar{\mathbf{1}}$ with concentration $\bar{1} = 1F + 1B$. The "instantaneous" concentrations in **1F** and **1B** again follow,

$$1F = \frac{1}{1+K^{\Delta}_1 R}\bar{1} \tag{89}$$

$$1B = \frac{K^{\Delta}_1 R}{1+K^{\Delta}_1 R}\bar{1} \tag{90}$$

where

$$K^{\Delta}_1 = \frac{k^{\Delta}_{+,1}}{k^{\Delta}_{-,1}}. \tag{91}$$

Thus Eqs.(6–9) transform into Eqs.(92–94):

$$\frac{d\bar{1}}{dt} = -\left(\kappa_{12,F} + \kappa_{12,B}\right)\,\bar{1} + k_{21,F}\,2F + k_{21,B}\,2B \tag{92}$$

$$\frac{d2F}{dt} = \kappa_{12,F}\,\bar{1} - k_{21,F}\,2F \tag{93}$$

$$\frac{d2B}{dt} = \kappa_{12,B}\,\bar{1} - k_{21,B}\,2B \tag{94}$$

with

$$\kappa_{12,F} = \frac{1}{1+K^{\Delta}_1 R}k^{h\nu}_{12,F} \tag{95}$$

$$k_{21,F} = k^{h\nu}_{21,F} \tag{96}$$

$$\kappa_{12,B} = \frac{K^{\Delta}_1 R}{1+K^{\Delta}_1 R}k^{h\nu}_{12,B} \tag{97}$$

$$k_{21,B} = k^{h\nu}_{21,B} + k^{\Delta}_{21,B}. \tag{98}$$

When $R_{tot} \gg F_{tot}$, the system of linear differential equations (92–94) possesses two non trivial negative eigenvalues λ_+ and λ_- associated to two relaxation times τ_+ and τ_- given in the expression (99)

$$\lambda_{\pm} = -\frac{1}{\tau_{\pm}} = -\frac{1}{2}S \pm \frac{1}{2}\sqrt{S^2 - 4\left(\kappa_{12,F}k_{21,B} + k_{21,F}k_{21,B} + k_{21,F}\kappa_{12,B}\right)} \tag{99}$$

with

$$S = \kappa_{12,F} + k_{21,F} + \kappa_{12,B} + k_{21,B}. \tag{100}$$

Upon assuming that the contribution of the free states **1F** and **2F** to the overall fluorescence emission can be neglected, the temporal evolution of the fluorescence emission occurring after a jump of light intensity from 0 to I^0 is

$$I_F(t) \quad = \quad \overline{1}^0 \left(a_0 + a_+ e^{\lambda_+ t} + a_- e^{\lambda_- t} \right) I^0 \tag{101}$$

with

$$a_0 \quad = \quad \frac{1}{\lambda_+ \lambda_-} \frac{K_1^{\Delta} R_{tot}}{1 + K_1^{\Delta} R_{tot}} k_{21,F} \left[Q_{1B} k_{21,B} + Q_{2B} k_{12,B}^{h\nu} \right] \tag{102}$$

$$a_+ \quad = \quad \frac{1}{\lambda_+ \left(\lambda_+ - \lambda_-\right)} \frac{K_1^{\Delta} R_{tot}}{1 + K_1^{\Delta} R_{tot}} \left(k_{21,F} + \lambda_+\right) \left[Q_{1B} \left(k_{21,B} + \lambda_+\right) + Q_{2B} k_{12,B}^{h\nu} \right] \tag{103}$$

$$a_- \quad = \quad \frac{1}{\lambda_- \left(\lambda_- - \lambda_+\right)} \frac{K_1^{\Delta} R_{tot}}{1 + K_1^{\Delta} R_{tot}} \left(k_{21,F} + \lambda_-\right) \left[Q_{1B} \left(k_{21,B} + \lambda_-\right) + Q_{2B} k_{12,B}^{h\nu} \right] \tag{104}$$

where $\overline{1}^0 = 1F^0 + 1B^0$ designate the steady-state value of the concentration in *cis*-species.

With this model, one correspondingly expects a bi-exponential decay of the temporal evolution of the fluorescence emission.

3 Theoretical computations

The equations (54), (71), (66), (67), (68) and (69) have been first used to compute the relaxation time τ_{12}^0 and the normalized fluorescence loss $\frac{(Q_1-Q_2)\overline{2}^0}{A^0+(Q_1-Q_2)\overline{2}^0}$ as well as the steady-state concentrations $1F^0$, $1B^0$, $2F^0$, and $2B^0$ at R_{tot} = 0.1 μM and F_{tot} = 1 μM for various values of the light intensity I^0 upon using the Spinach-DFHBI features displayed in Table 1 of the Main Text. The results are displayed in Figure S3.

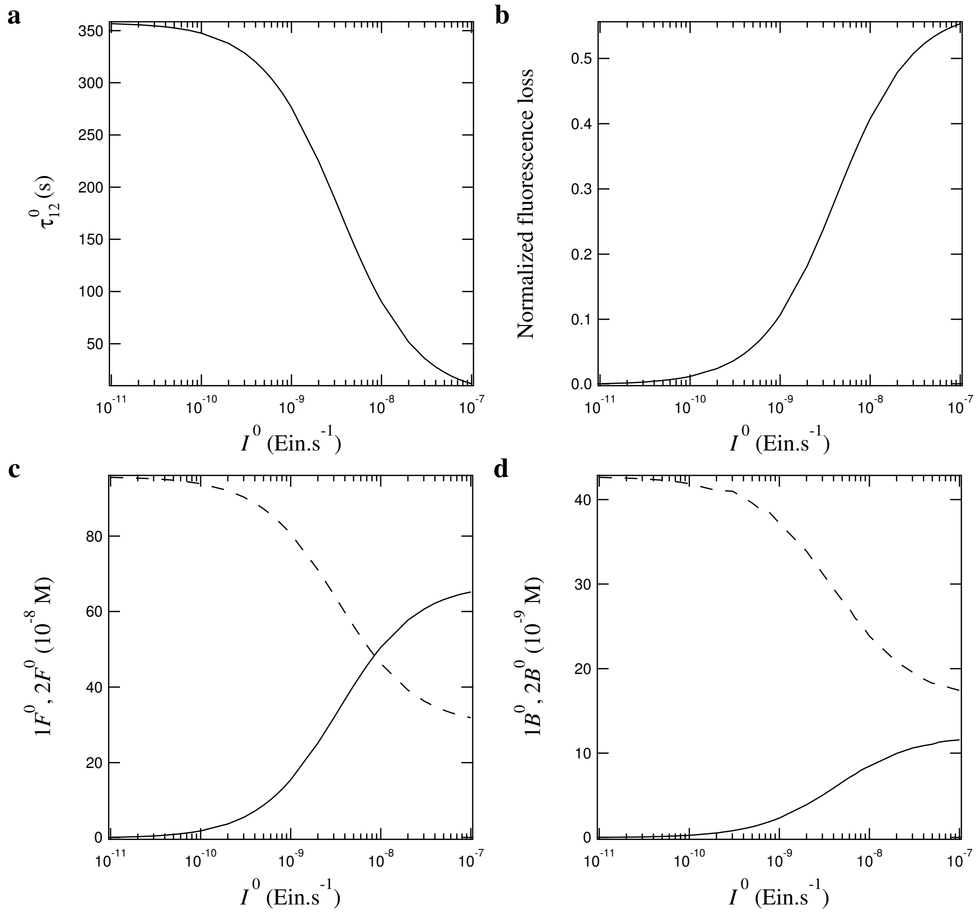

Figure S3: Theoretical computation of the dependence of the relaxation time τ_{12}^0 (**a**), the normalized fluorescence loss $\frac{(Q_1-Q_2)\overline{2}^0}{A^0+(Q_1-Q_2)\overline{2}^0}$ (**b**), the free (**c**; $1F^0$: dotted line; $2F^0$: solid line) and bound (**d**; $1B^0$: dotted line ; $2B^0$: solid line) state concentrations on the light intensity I^0 using Eqs. (54), (71), (66), (67), (68) and (69) respectively. R_{tot} = 0.1 μM; F_{tot} = 1 μM.

The same set of equations have been also used to compute the dependence of the relaxation time τ_{12}^0, the normalized fluorescence loss $\frac{(Q_1-Q_2)\overline{2}^0}{A^0+(Q_1-Q_2)\overline{2}^0}$, and the steady-state concentrations $1F^0$, $1B^0$, $2F^0$, and $2B^0$ at light intensity I^0= 9.0 $\times 10^{-9}$ ein·s^{-1} for various values of the total concentrations R_{tot} and F_{tot} upon using the Spinach-DFHBI features displayed in Table 1. The results are displayed in Figures S4a,b and S5a,b.

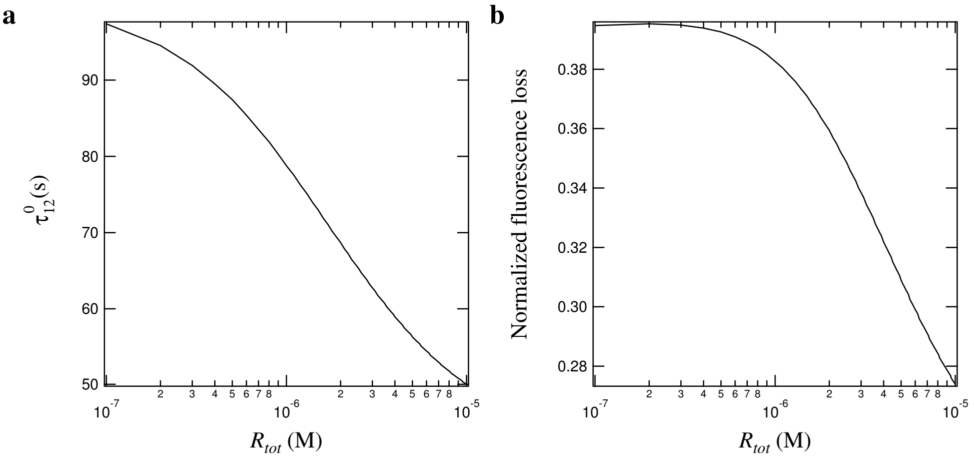

Figure S4: Theoretical computation of the dependence of the relaxation time τ_{12}^0 (**a**) and the normalized fluorescence loss $\frac{(Q_1-Q_2)\overline{2}^0}{A^0+(Q_1-Q_2)\overline{2}^0}$ (**b**) on the total RNA concentration at F$_{tot}$ = 1 μM and I^0= 9.0 $\times 10^{-9}$ ein·s^{-1} using Eqs. (54) and (71) respectively.

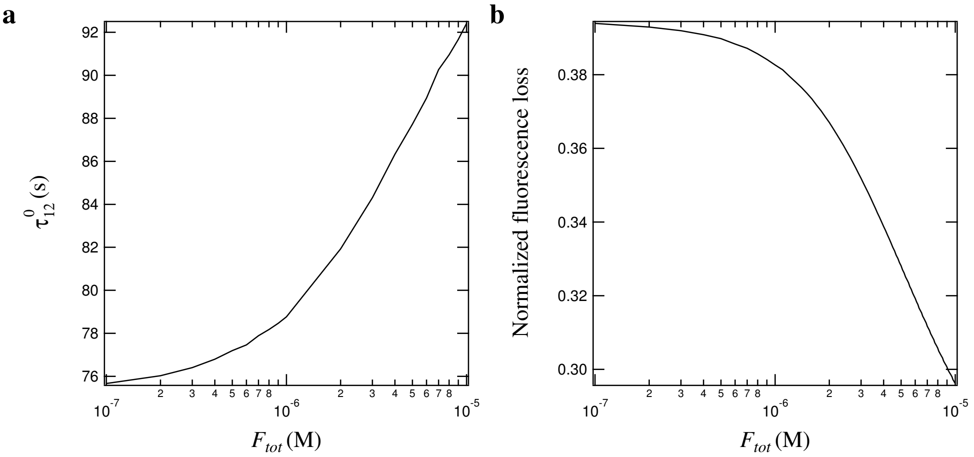

Figure S5: Theoretical computation of the dependence of the relaxation time τ_{12}^0 (**a**) and the normalized fluorescence loss $\frac{(Q_1-Q_2)\overline{2}^0}{A^0+(Q_1-Q_2)\overline{2}^0}$ (**b**) on the total DFHBI concentration at R$_{tot}$ = 1 μM and I^0= 9.0 $\times 10^{-9}$ ein·s^{-1} using Eqs. (54) and (71) respectively.

The significance of the relative total concentrations R_{tot} and F_{tot} on the relaxation time and on the normalized fluorescence loss is weaker than the one of the light intensity I^0. In fact, it essentially reflects the difference of the photochemical properties between the free and bound DFHBI states (see Table 1).

4 Supplementary Figures

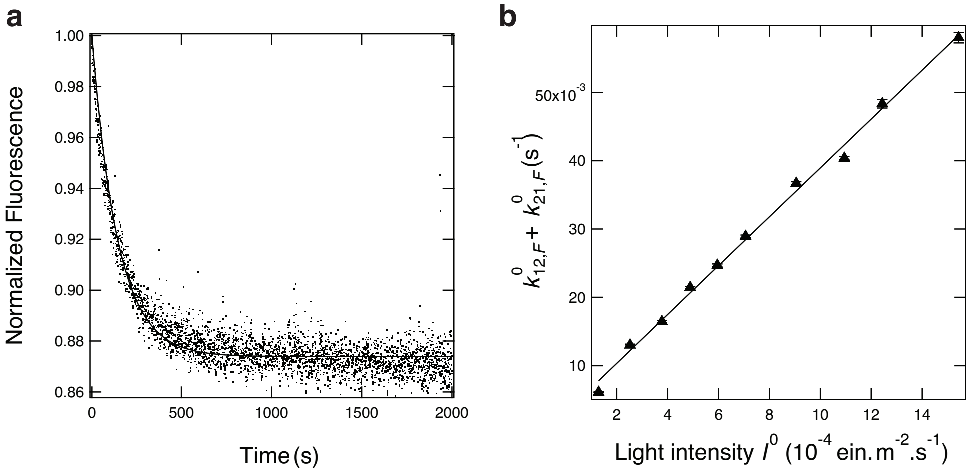

Figure S6: Kinetics of *cis*-DFHBI photoisomerization. **a**: Temporal evolution of the normalized fluorescence emission at 510 nm upon illuminating a 100 μM *cis*-DFHBI solution with 470 nm light (5×10^{-9} ein.s^{-1}). Dots: experimental points; solid line: exponential fit with Eq.(3) of the Main Text; **b**: Dependence of the rate constant associated to the fluorescence decay $k^0_{12,F} + k^0_{21,F}$ on light intensity I^0. Markers: experimental points; solid line: linear fit. Solvent: pH 7.4 Hepes buffer; T = 293 K.

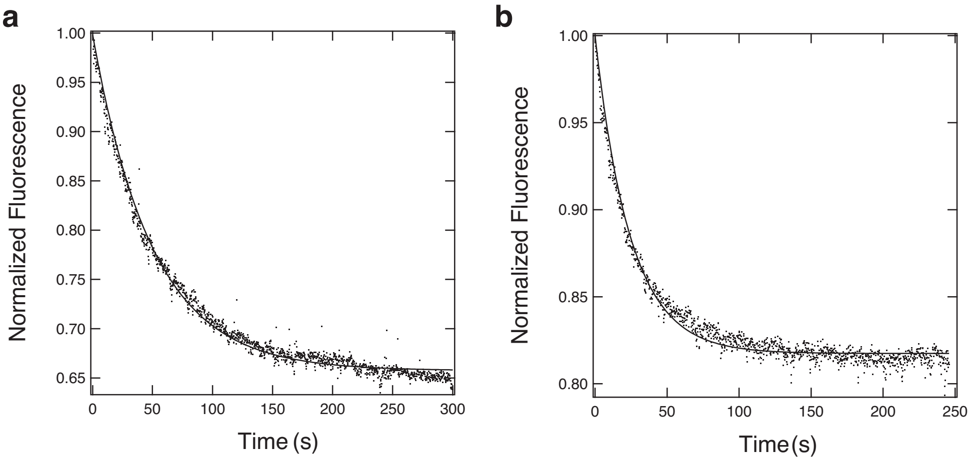

Figure S7: Decay of fluorescence emission at 498 nm of the Spinach system upon illuminating at 470 nm. Temporal evolution of the normalized fluorescence emission at 498 nm upon illuminating a solution containing 0.1 μM cis-DFHBI and 1.8 (**a**) or 20 (**b**) μM Spinach RNA with 470 nm light (1.7×10^{-8} ein.s^{-1}). Dots: experimental points; solid line: exponential fit with Eq.(4) of the Main Text. Solvent: pH 7.4 Hepes buffer; T = 293 K.

References

[1] M. Emond, T. Le Saux, S. Maurin, J.-B. Baudin, R. Plasson, L. Jullien, *Chem. Eur. J.* **16**, 8822-8831 (2010).

[2] J. Dong, F. Abulwerdi, A. Baldridge, J. Kowalik, K. M. Solntsev, L. M. Tolbert, *J. Am. Chem. Soc.*, 130, 14096-14098 (2008).

[3] J. S. Paige, K. Y. Wu, S. R. Jaffrey, *Science* **333**, 642-646 (2011).

Chapter 3

The theoretical framework : Out-of-phase titration after modulation of activating light (OPTIMAL) for selective and quantitative detection

3.1 Introduction

3.1.1 Context

In this subsection, we first present the protocol which was originally introduced in the group to perform a titration (and imaging) under kinetic control.[20,119] We then expose the general features of the new imaging approach that we introduced based on light modulation, photochromism and quadrature detection.

3.1.1.1 Temperature modulation and quadrature detection

Employing a periodic modulation of temperature had been chosen to reveal the dynamics of a titration reaction.

The model We consider the association between an analyte A_1 with a probe P to form a product A_2 as probing reaction

$$A_1 + P \underset{k_-}{\overset{k_+^P}{\rightleftharpoons}} A_2 \tag{3.1}$$

where k_+^P and k_- are respectively the forward and the backward rate constants. In a regime of a large excess of P, the mechanism can be reduced to a simple exchange between A_1 and A_2, with an apparent rate constant $k_+ = k_+^P\,[P]$.

$$A_1 \underset{k_-}{\overset{k_+}{\rightleftharpoons}} A_2 \tag{3.2}$$

A sinusoidal modulation of the temperature T is applied to the system around T_0 with a small amplitude βT_0 ($\beta \ll 1$) at a radial frequency ω

$$T = T_0\left[1 + \beta \sin(\omega t)\right] \tag{3.3}$$

The dependence of the kinetic constants $k_\pm$ on temperature T is given by the Arrhenius' law : $k_\pm = r_\pm \exp(-E_\pm / RT)$ where R is the ideal gas constant, $r_\pm$ the pre-exponential factor and $E_\pm$ the activation energy. Assuming that neither $r_\pm$ nor $E_\pm$ vary in the investigated range of temperature, a first-order expansion in the perturbation shows that modulating the temperature T results in a modulation of the kinetic constants $k_\pm$:

$$k_\pm(t) = k_\pm^0\left[1 + \beta \frac{E_\pm}{RT_0} \sin(\omega t)\right] \tag{3.4}$$

with

$$k_\pm^0 = r_\pm \exp\left(\frac{E_\pm}{RT_0}\right) \tag{3.5}$$

Beyond the relaxation time $\tau^0 = \frac{1}{k_+^0 + k_-^0}$, the system enters into a permanent and forced regime. The concentrations $A_i(t)$ in each species are constituted of three terms : a constant term A_i^0 and two oscillating terms at radial frequency ω in phase and out-of-phase with the temperature whose amplitudes are respectively A_i^{1sin} and A_i^{1cos} :

$$A_i(t) = A_i^0 + \beta\left[A_i^{1sin} \sin(\omega t) + A_i^{1cos} \cos(\omega t)\right] \tag{3.6}$$

A_i^0 is the concentration in A_i at chemical equilibrium at T_0

$$A_1^0 = \frac{1}{1 + K^0} A_{tot} \tag{3.7}$$

$$A_2^0 = \frac{K^0}{1 + K^0} A_{tot} \tag{3.8}$$

where A_{tot} is the total concentration in the { A$_1$, A$_2$ } couple and $K^0 = k_+^0 / k_-^0$ is the apparent equilibrium constant of the reaction 3.2 at T_0. In addition, the amplitudes of the in- and out-of-phase oscillating terms are given by

$$A_1^{1sin} = -A_2^{1sin} = -\frac{\Delta H}{RT_0} \frac{K^0}{(1 + K^0)^2} \frac{1}{1 + (\omega\tau^0)^2} A_{tot} \tag{3.9}$$

$$A_1^{1cos} = -A_2^{1cos} = \frac{\Delta H}{RT_0} \frac{K^0}{(1 + K^0)^2} \frac{\omega\tau^0}{1 + (\omega\tau^0)^2} A_{tot} \tag{3.10}$$

where $\Delta H = E_+ - E_-$ is the standard enthalpy of the exchange reaction 3.2.

Optimal out-of-phase response Studying the dependence of A_1^{1sin} and A_1^{1cos} on K^0 and the adimensionnal relaxation time $\omega\tau^0$ reveals two distinct behaviors. Contrary to A_1^{1sin}, A_1^{1cos} exhibits a peaked response. The coordinates of this extremum are given by the two simple equations (called resonance conditions in the following) :

$$K^0 = 1 \tag{3.11}$$

$$\omega\tau^0 = 1 \tag{3.12}$$

The first resonance condition results from the optimization of the term $\frac{K^0}{(1+K^0)^2}$. It shows that A_1 and A_2 needs to be in equal proportions to maximize the out-of-phase response, so that temperature modulation induces the largest relative variations in their concentrations. Optimizing the term $\frac{\omega\tau^0}{1+(\omega\tau^0)^2}$ requires that the radial frequency of the temperature modulation matches the relaxation time associated to the exchange reaction. In the regime $\omega \ll \frac{1}{\tau^0}$, the system follows the perturbation and the concentrations respond in phase with the thermal excitation : A_1^{1sin} reaches its largest value whereas A_1^{1cos} cancels. If $\omega \gg \frac{1}{\tau^0}$, the exchange is slow compared to the temperature oscillations. The system has not enough time to respond, both A_1^{1sin} and A_1^{1cos} tend to zero. As a consequence, the out-of-phase response is specific of the targeted analyte A_1 since the coordinates of the optimum of A_1^{1cos} depend exclusively on the thermokinetic properties of the reaction in which it is engaged. Extracting the out-of-phase response enables to selectively retrieve from the global signal the contribution of the analyte A_1.

Quadrature detection This approach has been experimentally validated *in vitro* using a hybridization reaction to selectively titrate a green fluorescent oligonucleotide in a mixture containing interfering compounds. Preliminary experiments enabled to identify the resonance conditions involved in the reaction between the fluorescent analyte A_{t1} and the probe P. Several mixtures were injected in a microfluidic chip (see Figure 3.1a). Solutions containing increasing concentrations of the targeted analyte A_{t1} at a constant concentration in the probe P were prepared (channels 1 to 3). Two interfering compounds A_{NR} and A_{MB} were also added to these mixtures. Channel 4 contained only the analyte A_{t1} and the probe P and was used for calibration. Channel 5 was filled with only A_{NR} and A_{MB} to control the selectivity of the protocol. To monitor the amplitude and the phase of the temperature excitation, a molecular thermometer emitting in the red was added to the channel 4.

A thermal forcing around T_0 = 306 K with an amplitude equal to βT_0 = 0.6 K at a radial frequency 23.65 rad·s^{-1} was applied. The fluorescence intensity variations were recorded for 625 periods. Time-averaging of the whole movie yielded the image displayed in Figure 3.1b. It corresponds to the result obtained with a titration performed at constant temperature T_0 (chemical equilibrium at T_0). Using this image to titrate the A_{t1} analyte gives rise to an overestimate of its concentration due to the contribution of the interfering compounds. The out-

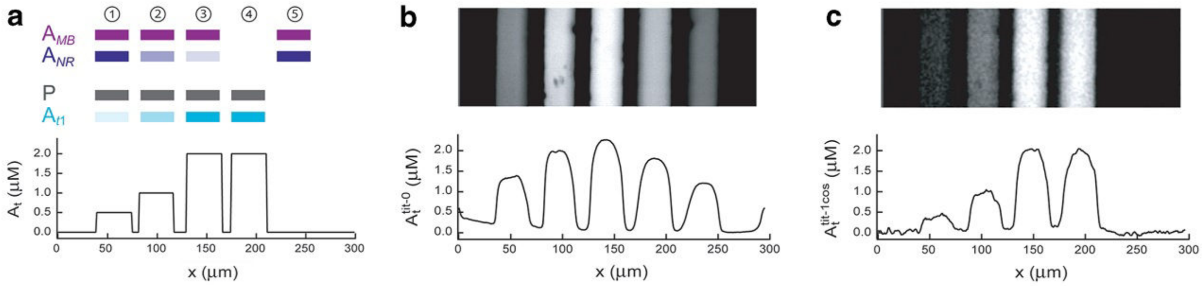

Figure 3.1: Titration of the A_{t1} target by the probe P in a mixture containing two interfering compounds : the non reactive A_{NR} and the fast-exchanging A_{MB}. (**a**) Scheme representing the various samples' initial composition and corresponding A_t profile. (**b**)Fluorescence emission at equilibrium at $T_0 = 306$ K and corresponding A_t^{tit-0} trace. (**c**) Out-of-phase response of the fluorescence emission upon harmonic forcing around T_0 ($\omega = 23.65$ rad·s^{-1}, $\beta = 0.002$) and corresponding $A_t^{tit-1cos}$ trace. Adapted from Zrelli et al.[20]

of-phase response of each pixel was then extracted from the movie using a phase-sensitive detection scheme. The resulting image is displayed Figure 3.1c. In this case, the concentration of the A_{t1} target is accurately estimated since the contribution of the non-resonant species is extinguished.

Limitations linked to theory Analytical expressions of the concentrations and the resonance conditions are only retrieved in the case of a temperature modulation of a small amplitude. As a result, the probe signal varies faintly due to small modulation that renders difficult (and possibly not reliable) the extraction of the out-of-phase response. To overcome this issue, a modulation of large amplitude could be employed but it is not compatible with *in vivo* samples. Indeed a variation of 30 K (which represents 10 % of room temperature) cannot be employed. Moreover, since most of chemical reactions depend on temperature, its modulation can alter the properties of the components of a living cell and perturb not only the targeted reaction but also other biological processes. Thus, it could be difficult to deconvolute the different responses giving rise to a selectivity issue.

Limitations linked to experimental implementation Implementing a temperature modulation remains quite difficult : it indeed requires a dedicated set-up[21–23] or a heating microdevice.[18–20] In particular, temperature excitation needs to be uniform. This is crucial to have the same resonance conditions everywhere in the sample. In addition, a non-uniform temperature profile may induce spatial variations of the refractive index rendering complicated the optical corrections. Since biological samples (e.g. cell) are highly inhomogenous, it is even more difficult to have a uniform temperature excitation within the sample. To tackle this issue, the heating device is generally oversized to avoid any edge effect. Moreover, the amplitude of the temperature modulation (β) diminishes when the frequency of the excitation increases.[119] The typical value of the cutoff frequency f_c (corresponding to the frequency where the amplitude of the temperature modulation drops by 71 % of its largest value) varies from ~ 10 Hz to ~ 1 kHz depending on the heating device and the geometry of the thermal excitation. In addition, temperature modulation can induce dilation and compression of the solvent of the sample (the regular value of a dilation coefficient for a liquid is ~ 10^{-3} K^{-1}) resulting in concentration variations.

Despite these limitations, temperature modulation can be applied with various chemical reactions since there is a coupling with temperature as soon as the reaction enthalpy is different from zero. This control parameter is very interesting for *in vitro* applications but is more complicated to implement for *in vivo* applications.

3.1.1.2 Another control parameter for a probing reaction

Based on the preceding results (using the periodic perturbation of a control parameter to reveal the dynamics of a chemical reaction), we have adopted a similar approach to design a selective and quantitative analytical protocol.

Since we wanted to design a protocol which could be used by many laboratories, we looked for another control parameter. Light satisfies the criteria we developed in the General Introduction. Indeed, it is non-invasive and compatible with *in vivo* imaging. In addition, its modulation is easily feasible even with commercially available microscopes.

The probing reaction that we adopted is the photochemical reaction involved in the reversible photoswitching of photochromic probes. At large enough time scale, the dynamic behavior of these photoswitchable probes upon illumination can be modeled by a light-driven two-state exchange :

$$\mathbf{1} \quad \underset{k_{21}(t)}{\overset{k_{12}(t)}{\rightleftharpoons}} \quad \mathbf{2} \tag{3.13}$$

where $k_{12}(t)$ and $k_{21}(t)$ are respectively the forward and the backward rate constants which depend linearly on the intensity of light $I(t)$:

$$k_{12}(t) = \sigma_{12} I(t) \tag{3.14}$$

$$k_{21}(t) = \sigma_{21} I(t) + k_{21}^{\Delta} \tag{3.15}$$

σ_{12} and σ_{21} are the molecular action cross-sections for photoisomerization whereas k_{21}^{Δ} is the rate constant of the thermally-driven relaxation from the state **2** to the state **1**.

By analogy,[20] a periodic modulation of monochromatic light was chosen to modulate the rate constants $k_{12}(t)$ and $k_{21}(t)$

$$I(t) = I^0 \left[1 + \varepsilon \sin(\omega t)\right] \tag{3.16}$$

where I^0 is the average light intensity, ω the radial frequency of the light modulation with an amplitude εI^0.

Thus, the light-driven two-state exchange 3.13 and the expressions of the rate constants $k_{12}(t)$ and $k_{21}(t)$ closely mirror those written in the subsection 3.1.1.1. As a consequence, a similar behavior (resonance of the out-of-phase first-order response) was expected when a monochromatic light modulation is applied to a photochromic probe.

3.1.2 Presentation of the article

My second article deals with the extensive theoretical framework of the approach 'monochromatic light modulation, photochromism and quadrature detection' which was dubbed OPTIMAL for Out-of-Phase TItration after Modulation of Activating Light.

In the paper, we successively investigate the concentration response of a photoswitchable probe submitted to a sinusoidal or a square wave modulation of small or large amplitude. Similarly to temperature modulation, optimizing the out-of-phase concentration response gives rise to two simple resonance conditions on the average light intensity and the radial frequency of the light modulation in the case of a modulation of small amplitude. In contrast, analytical expressions cannot be derived when a light modulation of large amplitude is applied to the photochromic system. As a result, we evaluated the validity of the two previous resonance conditions in the case of a modulation of large amplitude using numerical calculations. We have concluded that adopting the analytical expressions of the resonance conditions for a large amplitude modulation (sinusoidal as well as square wave) causes an error which has the same order of magnitude as the experimental errors. Then, we studied the retrieval of the out-of-phase concentration response from the overall signal or observable. In particular, we investigated the out-of-phase response of the fluorescence emission in the context of an application compatible with imaging. Finally, we discuss the advantages of this approach compared to classical analysis relying on constant illumination. The potential applications of this separation-free protocol are also highlighted : the selective and quantitative detection of a targeted photoswitchable probe in (i) a mixture containing other probes or interfering compounds or (ii) a phase of interest if an environment-sensitive probe is incorporated into a heterogeneous medium.

3.2 Article 2 : Expanding discriminative dimensions for analysis and imaging

Chemical Science

EDGE ARTICLE

View Article Online
View Journal

Cite this: DOI: 10.1039/c4sc03955f

Received 19th December 2014
Accepted 18th February 2015

DOI: 10.1039/c4sc03955f

www.rsc.org/chemicalscience

Expanding discriminative dimensions for analysis and imaging†‡

Jérôme Querard,[abc] Arnaud Gautier,*[abc] Thomas Le Saux*[abc] and Ludovic Jullien*[abc]

Eliminating the contribution of interfering compounds is a key step in chemical analysis. In complex media, one possible approach is to perform a preliminary separation. However purification is often demanding, long, and costly; it may also considerably alter the properties of interacting components of the mixture (*e.g.* in a living cell). Hence there is a strong interest for developing separation-free non-invasive analytical protocols. Using photoswitchable probes as labelling and titration contrast agents, we demonstrate that the association of a modulated monochromatic light excitation with a kinetic filtering of the overall observable is much more attractive than constant excitation to read-out the contribution from a target probe under adverse conditions. An extensive theoretical framework enabled us to optimize the out-of-phase concentration first-order response of a photoswitchable probe to modulated illumination by appropriately matching the average light intensity and the radial frequency of the light modulation to the probe dynamics. Thus, we can selectively and quantitatively extract from an overall signal the contribution from a target photoswitchable probe within a mixture of species, photoswitchable or not. This simple titration strategy is more specifically developed in the context of fluorescence imaging, which offers promising perspectives.

Introduction

One of the main challenges for chemists remains being able to quantify a specific analyte in highly complex systems such as biological or medical samples.[1–3] A crude sample (*e.g.* cell extract), like those found in diagnostics assays,[4] drug screening,[5,6] or metabolites quantification,[7] may contain up to 10^4 to 10^5 rather similar components at concentrations covering ten orders of magnitude. Analysis requires in general challenging sample conditioning and preliminary purifications. Selective detection is even more challenging when the sample has to remain in its native state (*e.g.* living cells). Non-invasive methods have thus to be adopted. The archetype of such methods is fluorescence microscopy, which has revolutionised the way one observes biological samples.[8,9] However relying on fluorescence as read-out presents several limitations. Hence multiplexed observations of more than a few fluorescent species are difficult because of spectral crowding resulting from the large emission bandwidth of most fluorophores. Moreover biological media often produce high levels of scattering and autofluorescence at optical wavelengths, which interfere with the signals of interest and diminish the contrast. There is therefore a strong need for approaches enabling to circumvent the selectivity issue in the context of both analysis and imaging.

To detect a target in a complex medium, one needs a probe. This probe can be intrinsic, *i.e.* present in the target (atoms or functional groups). However it is often difficult to find an intrinsic probe that is unique for a target. For instance, biomolecules (*e.g.* proteins, nucleic acids) are essentially composed of the same functionalities. Alternatively, exogenous probes with unnatural chemical functions or singular spectroscopic properties can be used to give a unique signature and act as contrast agents. Additional selectivity can be observed if the exogenous probe is engaged in a reactive process. This is typically the strategy of titration experiments, where one observes a reagent specifically probing the analyte of interest thanks to a chemical reaction. Selectivity classically results from the difference between the equilibrium constants associated to the titration reaction. Relying on kinetics[10] opens further dimensions to improve selectivity by increasing the number of discriminating parameters: in the most simple case, *two* independent rate constants instead of only *one* thermodynamic constant are associated to the titration reaction for each system component. In this account, we exploit chemical kinetics to introduce a simple and cheap protocol for selective analysis or

---

[a] *Ecole Normale Supérieure-PSL Research University, Département de Chimie, 24, rue Lhomond, F-75005 Paris, France. E-mail: Arnaud.Gautier@ens.fr; Thomas.Lesaux@ens.fr; Ludovic.Jullien@ens.fr; Tel: +33 4432 3333*

[b] *Sorbonne Universités, UPMC Univ Paris 06, PASTEUR, F-75005, Paris, France*

[c] *CNRS, UMR 8640 PASTEUR, F-75005, Paris, France*

† This article is dedicated to Prof. Manfred Eigen.

‡ Electronic supplementary information (ESI) available: Reduction of photo-(physical)chemical mechanisms to a two-state exchange, kinetic analysis of the two-state model, retrieval of concentrations from the observables, improvement of the spatial resolution. See DOI: 10.1039/c4sc03955f

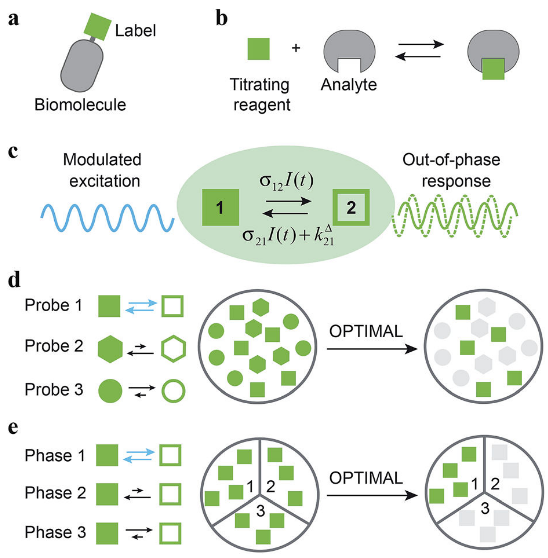

Fig. 1 Out-of-Phase TItration after Modulation of Activating Light (OPTIMAL) for selective detection of a photoswitchable probe. When illuminated, a photoswitchable probe (green square) used either (a) as a label or (b) as a titrating reagent exchanges between two distinguishable states **1** and **2** (c). With a periodic modulated light, its response signal is modulated with a phase shift. The amplitude of the out-of-phase (or quadrature-delayed) first-order component of its response is optimal when the average intensity and the angular frequency of the modulated light match the dynamic parameters of the probe. Accordingly, when the modulated light is tuned to its dynamics, the photoswitchable probe is the only species giving a significant signal in quadrature detection. This enables its selective detection in (d) a mixture of interfering probes or species displaying different dynamics or, if its dynamics is environment-sensitive, in (e) a specific phase of a heterogeneous multiphasic medium.

imaging of a probe used either as a label (Fig. 1a) or as a titrating reagent (Fig. 1b).

Kinetic information can be uncovered by relaxation methods,[11] where an externally driven excitation forces the system out-of-equilibrium.[12–17] Recently, selective imaging protocols relying on kinetic filtering have been implemented upon modulating the probe signal using light[18–31] or temperature[32–34] as external triggers. In this work, we adopted light as a non-invasive and easily modulatable trigger. We additionally chose photo-switchable probes, which interconvert between two states upon light illumination and correspondingly exhibit several discriminating parameters that can be used to optimize an efficient dynamic contrast (Fig. 1c).[35] As we already showed in the context of selective analysis and separation,[32,34,36–38] modulation of a control parameter can reveal intrinsic chemical kinetics upon periodically forcing the system out-of-equilibrium. By analogy, we adopted a periodically oscillating monochromatic light excitation, which modulates the extent of the photochemical reaction, thereby modulating the reporting signal. Beyond favoring discrimination against background noise by means of a lock-in detection[39] such a modulation enables subsequent kinetic filtering. More precisely, we show theoretically how tuning both the average intensity and the frequency of the modulated monochromatic light excitation permits to simply and selectively extract from the overall signal the contribution from a photoswitchable probe of interest within a mixture of species, photoswitchable or not. Hence it will be possible to specifically retrieve the contribution from a targeted probe in a mixture of interfering probes (Fig. 1d), or the contribution originating from a specific compartment when a medium-sensitive probe is incorporated in a heterogeneous multiphasic medium (Fig. 1e). We correspondingly dubbed our approach OPTIMAL for Out-of-Phase TItration after Modulation of Activating Light. In particular, it generalizes the fluorescence imaging approach OPIOM (Out-of-Phase Imaging after Optical Modulation) we recently introduced,[40] which enables selective and quantitative imaging of photoswitchable fluorescent proteins.

Optimizing the response of a photoswitchable probe to periodic illumination

The model

The dynamic behavior of a photoswitchable probe **P** illuminated with a light of intensity $I(t)$ can be described by the two-state exchange (1)

$$\mathbf{1} \underset{k_{21}(t)}{\overset{k_{12}(t)}{\rightleftharpoons}} \mathbf{2} \tag{1}$$

where the thermodynamically more stable state **1** is photochemically converted to the thermodynamically less stable state **2** at rate constant

$$k_{12}(t) = \sigma_{12}I(t), \tag{2}$$

from which it can relax back to the initial state **1** either by a photochemically- or a thermally-driven process at rate constant

$$k_{21}(t) = \sigma_{21}I(t) + k_{21}^{\Delta}, \tag{3}$$

where $\sigma_{21}I(t)$ and k_{21}^{Δ} are respectively the photochemical and the thermal contributions of the rate constant. In that case, the molecular action cross-sections for photoisomerization σ_{12} and σ_{21} and the thermal rate constant k_{21}^{Δ} fully define the behavior of the photoswitchable probe.

It is worth to mention that the following theoretical development involving a truncation of the kinetic equations to various orders of the light intensity could be applied to other mechanisms possibly involving non-linearities. However the scheme (1) provides simple expressions. Furthermore it is already relevant to model several multi-step mechanisms, which can be dynamically reduced to light-driven exchanges between two states.[41–43] Hence, in ESI,† we first demonstrate that this scheme satisfactorily accounts for the behavior of photochromic probes. Then we show that it describes as well the dynamics of (i) a chromophore yielding singlet and triplet states upon illuminating and (ii) a photoswitchable probe sensing an analyte present in excess as long as photochemical steps are rate-limiting.

Concentration response to constant illumination

When the system is submitted to a constant illumination defined by the intensity $I(t) = I^0$, the forward and backward rate constants become

$$k_{12}(t) = k_{12}^0 = \sigma_{12} I^0 \tag{4}$$

$$k_{21}(t) = k_{21}^0 = \sigma_{21} I^0 + k_{21}^{\Delta}. \tag{5}$$

After a transient regime defined by the relaxation time $\tau_{12}^0 = 1/(k_{12}^0 + k_{21}^0)$, the system reaches a photostationary state characterized by the apparent photoisomerization constant $K_{12}^0 = k_{12}^0/k_{21}^0$. The concentrations of **1** and **2**, noted respectively 1^0 and 2^0, are then given by

$$1^0 = P_{\text{tot}} - 2^0 = \frac{1}{1 + K_{12}^0} P_{\text{tot}} \tag{6}$$

where P_{tot} is the total concentration of **P**.

Concentration response to sinusoidal modulation of small amplitude

To evaluate the behavior of such system upon illumination with a periodically modulated light, we first consider a sinusoidally modulated illumination oscillating around the averaged value I^0 at angular frequency ω and with a small amplitude εI^0 ($\varepsilon \ll 1$) such that

$$I(t) = I^0[1 + \varepsilon \sin(\omega t)]. \tag{7}$$

Temporal dependence of the concentrations. After introducing the expression (7) into eqn (2) and (3), the system of differential equations governing the temporal evolution of the concentrations in **1** and **2** is solved at the first-order expansion in the light perturbation (see ESI†). Beyond the relaxation time τ_{12}^0, one enters into the forced and permanent regime where the concentration $i = i^0 + \varepsilon i^1(t)$ in each species **i** (**i** = **1** or **2**) oscillates around a mean value i^0 (corresponding to the concentration of **i** at steady-state associated to the photon flux I^0; see eqn (6)) at the angular frequency ω but with a phase delay of $\phi_{12} = \arctan(\omega\tau_{12}^0)$

$$2^1(t) = -1^1(t) = \frac{\rho_{12}^0 \tau_{12}^0 p_{21}^{\Delta}}{\sqrt{1 + (\omega\tau_{12}^0)^2}} \sin(\omega t - \phi_{12}). \tag{8}$$

In eqn (8), $\rho_{12}^0 = k_{12}^0 1^0 = k_{21}^0 2^0$ and $p_{21}^{\Delta} = k_{21}^{\Delta}/(\sigma_{21} I^0 + k_{21}^{\Delta})$ respectively designate the steady-state rate of reaction (1) and the relative thermal contribution to the relaxation of state **2** upon illuminating at I^0.

The phase-delayed oscillating concentrations i can also be written

$$i(t) = i^0 + \varepsilon[i^{1,\text{in}} \sin(\omega t) + i^{1,\text{out}} \cos(\omega t)] \tag{9}$$

where $\varepsilon i^{1,\text{in}} \sin(\omega t)$ and $\varepsilon i^{1,\text{out}} \cos(\omega t)$ are in-phase and out-of-phase (or quadrature-delayed) oscillating terms at angular frequency ω. The amplitudes $i^{1,\text{in}}$ and $i^{1,\text{out}}$ of the in-phase and out-of-phase oscillating terms are (see ESI†)

$$2^{1,\text{in}} = -1^{1,\text{in}} = \rho_{12}^0 \tau_{12}^0 p_{21}^{\Delta} \frac{1}{1 + (\omega\tau_{12}^0)^2} \tag{10}$$

$$2^{1,\text{out}} = -1^{1,\text{out}} = -\rho_{12}^0 \tau_{12}^0 p_{21}^{\Delta} \frac{\omega\tau_{12}^0}{1 + (\omega\tau_{12}^0)^2} \tag{11}$$

or similarly

$$2^{1,\text{in}} = -1^{1,\text{in}} = p_{21}^{\Delta} \frac{K_{12}^0}{\left(1 + K_{12}^0\right)^2} \frac{1}{1 + (\omega\tau_{12}^0)^2} P_{\text{tot}} \tag{12}$$

$$2^{1,\text{out}} = -1^{1,\text{out}} = -p_{21}^{\Delta} \frac{K_{12}^0}{\left(1 + K_{12}^0\right)^2} \frac{\omega\tau_{12}^0}{1 + (\omega\tau_{12}^0)^2} P_{\text{tot}} \tag{13}$$

to make explicit the proportionality of $2^{1,\text{in}}$ and $2^{1,\text{out}}$ with the total **P** concentration.

Optimal out-of-phase response. Fig. 2a and b displays the dependence of the normalized in-phase $|1_{\text{norm}}^{1,\text{in}}| = |1^{1,\text{in}}/P_{\text{tot}}|$ and out-of-phase $|1_{\text{norm}}^{1,\text{out}}| = |1^{1,\text{out}}/P_{\text{tot}}|$ amplitudes on the control parameters I^0 and ω for a given photoswitchable probe **P** characterized by the triplet of parameters (σ_{12}, σ_{21}, k_{21}^{Δ}). In contrast to the in-phase amplitude, the out-of-phase amplitude exhibits a single optimum when the control parameters (I^0, ω) verify

$$I^0 = \frac{k_{21}^{\Delta}}{\sigma_{12} + \sigma_{21}} \tag{14}$$

$$\omega = 2k_{21}^{\Delta} \tag{15}$$

with full widths at half-maximum $4\sqrt{2}k_{21}^{\Delta}/(\sigma_{12} + \sigma_{21})$ along I^0 and $4\sqrt{3}k_{21}^{\Delta}$ along ω. The normalized out-of phase amplitude $|1_{\text{norm}}^{1,\text{out}}|$ is then equal to $\sigma_{12}/[8(\sigma_{12} + \sigma_{21})]$.

The optimization of $1^{1,\text{out}}$ results from the independent optimisation of the terms $p_{21}^{\Delta} K_{12}^0 P_{\text{tot}}/(1 + K_{12}^0)^2$ and $\omega\tau_{12}^0/[1 + (\omega\tau_{12}^0)^2]$ in eqn (13). From the expression (6) using eqn (4) and (5), one can calculate $d2^0/d \ln I^0$ to show that $\varepsilon p_{21}^{\Delta} K_{12}^0 P_{\text{tot}}/(1 + K_{12}^0)^2$ measures the composition shift $\delta 2^0$ from the steady-state 2^0 after a light intensity jump of amplitude εI^0. It depends on I^0 and is maximized in a regime of intermediate illumination, in which thermally- and photochemically-driven reactions occur at the same rate such that $k_{21}^{\Delta} = (\sigma_{12} + \sigma_{21})I^0$ (see eqn (14)). When the light intensity is too low, the thermal relaxation dominates the photoisomerization and the light intensity jump εI^0 cannot significantly shifts the photoswitchable probe from the state **1**. Conversely, when the light intensity is too large, the thermal relaxation does not contribute anymore to the dynamics of the exchange (1): the relative proportions in states **1** and **2** become independent of the light intensity, so there is no composition shift induced by the light jump. The second optimized term, $\omega\tau_{12}^0/[1 + (\omega\tau_{12}^0)^2]$, is maximized upon matching the radial frequency of the light modulation ω with the exchange relaxation time τ_{12}^0 so that $\omega\tau_{12}^0 = 1$ (see eqn (14) and (15)). When $\omega \gg 1/\tau_{12}^0$, the exchange is slow compared to the light variations and the couple {**1**, **2**} has not enough time to respond: both $i^{1,\text{in}}$ and

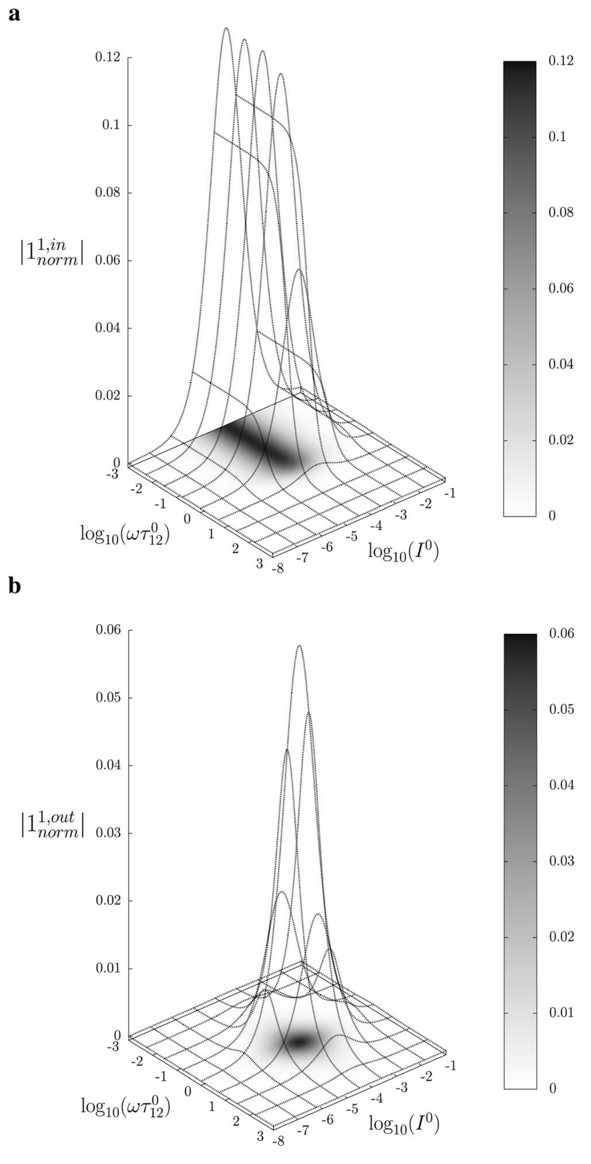

Fig. 2 Theoretical computation of the response of a photoswitchable fluorophore $1 \rightleftharpoons 2$ submitted to light harmonic forcing of small amplitude. The absolute values of the normalized amplitudes of the in-phase and out-of-phase oscillations in 1 concentration, $|1^{1,\text{in}}_{\text{norm}}|$ (a) and $|1^{1,\text{out}}_{\text{norm}}|$ (b) respectively, are plotted *versus* the light flux I^0 (in ein s^{-1} m^{-2}) and the adimensional relaxation time $\omega\tau^0_{12}$. $\sigma_{12} = 73$ m^2 mol^{-1}, $\sigma_{21} = 84$ m^2 mol^{-1}, $k^{\Delta}_{21} = 1.5 \times 10^{-2}$ s^{-1}. See eqn (12) and (13).

$i^{1,\text{out}}$ vanish. Conversely, when $\omega \ll 1/\tau^0_{12}$, $i^{1,\text{out}}$ cancels, so the concentrations of **1** and **2** oscillate in phase with the light modulation.

Concentration response to square wave modulation of small amplitude

As an experimentally relevant extension of the previous case, we analyzed the behavior of the system upon illumination with a square wave light modulation of weak amplitude around the averaged value I^0. We adopted its Fourier series expansion

$$I(t) = I^0\left[1 + \frac{4\varepsilon}{\pi}\sum_{p=0}^{\infty}\frac{1}{2p+1}\sin[(2p+1)\omega t]\right] \qquad (16)$$

with $\varepsilon \ll 1$ upon choosing the starting time ($t = 0$) halfway through the first pulse.

Temporal dependence of the concentrations. The expression (16) was introduced into eqn (2) and (3) and the system of differential equations governing the temporal evolution of the concentrations in **1** and **2** was again solved at the first-order expansion in the light perturbation (see ESI†). In the forced and permanent regime observed beyond the relaxation time τ^0_{12}, the concentration i in each species **i** ($\mathbf{i} = \mathbf{1}$ or **2**) now oscillates around i^0 at multiple angular frequencies $(2p + 1)\omega$

$$i(t) = i^0 + \varepsilon\sum_{p=0}^{\infty}\left[i^{1,\text{in}}_{(2p+1)}\sin[(2p+1)\omega t] + i^{1,\text{out}}_{(2p+1)}\cos[(2p+1)\omega t]\right] \qquad (17)$$

where the amplitudes of the in-phase and out-of-phase oscillating terms at angular frequency $(2p + 1)\omega$ are (see ESI†)

$$2^{1,\text{in}}_{(2p+1)} = -1^{1,\text{in}}_{(2p+1)} = \frac{4}{\pi}\frac{\rho^0_{12}\tau^0_{12}p^{\Delta}_{21}}{2p+1}\frac{1}{1+(2p+1)^2(\omega\tau^0_{12})^2} \qquad (18)$$

$$2^{1,\text{out}}_{(2p+1)} = -1^{1,\text{out}}_{(2p+1)} = -\frac{4}{\pi}\frac{\rho^0_{12}\tau^0_{12}p^{\Delta}_{21}}{2p+1}\frac{(2p+1)\omega\tau^0_{12}}{1+(2p+1)^2(\omega\tau^0_{12})^2}. \qquad (19)$$

Except for the numerical factor $4/\pi$, the expressions (10), (11) and (18), (19) for $p = 0$ are similar. This observation suggests that the resonance conditions (14) and (15) valid for the optimization of $1^{1,\text{out}}$ with the weak sinusoidal light modulation at radial frequency ω are equally relevant to optimize the amplitude $1^{1,\text{out}}_{(1)}$ when the system is submitted to a weak square wave light modulation of fundamental radial frequency ω. In fact, this conclusion would equally apply for any periodic light modulation of small amplitude with fundamental radial frequency ω. Indeed, at first order, the amplitude of the out-of-phase modulation of the concentrations of the species **1** and **2** at radial frequency ω only originates from the sinusoidal modulation at radial frequency ω in the Fourier series associated to the light modulation.

Concentration response to periodic modulations of large amplitude

The use of a modulation of small amplitude is favorable to derive simple analytical expressions. However, it generates only small variations of the probe signal because of the small modulation, which is a drawback to reliably extract the out-of-phase amplitude of the first order response from the experimental signal. To overcome this limitation, we analyzed the response of a photoswitchable probe to the preceding periodic illuminations but with a large modulation amplitude α. Thus we adopted

$$I(t) = I^0[1 + \alpha \sin(\omega t)] \tag{20}$$

and

$$I(t) = I^0\left\{1 + \frac{4\alpha}{\pi}\sum_{p=0}^{\infty}\frac{1}{2p+1}\sin[(2p+1)\omega t]\right\} \tag{21}$$

for the sinusoidal and square wave modulation respectively. In particular, the latter periodic illumination is of simple experimental implementation (on–off illumination switching).

Temporal dependence of the concentrations. The ESI† details the calculations referring to these two modulations of large amplitude. In this paragraph, we only introduce the calculation guideline, which is common to both types of modulations. The light intensity can be written

$$I(t) = I^0[1 + \alpha h(\omega t)] \tag{22}$$

where $h(\omega t)$ designate a periodic function with fundamental radial frequency ω. Eqn (22) was used to express the rate constants with eqn (2) and (3). Then, upon expanding the concentration expressions as

$$2 = 2^0 + \alpha f(\omega t) \tag{23}$$

$$1 = 1^0 - \alpha f(\omega t), \tag{24}$$

the system of differential equations governing the temporal evolution of the concentrations in **1** and **2** becomes

$$\frac{\mathrm{d}f(\theta x)}{\mathrm{d}x} = -f(\theta x) + [a - bf(\theta x)]h(\theta x) \tag{25}$$

where

$$x = \frac{t}{\tau_{12}^0} \tag{26}$$

$$a = \rho_{12}^0 p_{21}^{\Delta} \tau_{12}^0 \tag{27}$$

$$b = \alpha(\sigma_{12} + \sigma_{21})I^0\tau_{12}^0 \tag{28}$$

$$\theta = \omega\tau_{12}^0. \tag{29}$$

Beyond the relaxation time τ_{12}^0, one enters into a permanent regime in which $f(\theta x)$ is a continuous periodic function. In contrast to the situation of light modulation of small amplitude, one cannot anymore restrict the $f(\theta x)$ analysis to the first-order. The $f(\theta x)$ function has to be expressed as a Fourier series

$$f(\theta x) = a_0 + \sum_{n=1}^{+\infty}[a_n \cos(n\theta x) + b_n \sin(n\theta x)] \tag{30}$$

where a_n and b_n designate the amplitudes of the n-th components of the Fourier series. The a_n and b_n terms can be extracted from eqn (25) upon identifying the amplitudes of the components of same order. Then one can obtain the expressions of the concentrations in **1** and **2**:

$$2 = 2^0 + \alpha\left\{a_0 + \sum_{n=1}^{+\infty}[a_n \cos(n\theta x) + b_n \sin(n\theta x)]\right\} \tag{31}$$

$$1 = 1^0 - \alpha\left\{a_0 + \sum_{n=1}^{+\infty}[a_n \cos(n\theta x) + b_n \sin(n\theta x)]\right\}. \tag{32}$$

Consequently, at steady-state, a large periodic modulation of illumination now causes modulation of the concentrations in **1** and **2** at an infinite number of radial frequencies. Eqn (31) and (32) can be transformed to explicit the amplitudes $\mathrm{i}^{\mathrm{n,in}}$ and $\mathrm{i}^{\mathrm{n,out}}$ of the in-phase and out-of phase terms oscillating at the radial frequency $n\omega$. The concentration of **i** can be now written

$$i = \mathrm{i}^{\circ} + \alpha\sum_{n=1}^{+\infty}\left[\mathrm{i}^{\mathrm{n,in}}\sin(n\omega t) + \mathrm{i}^{\mathrm{n,out}}\cos(n\omega t)\right]. \tag{33}$$

Interestingly, i°, $\mathrm{i}^{\mathrm{n,in}}$ and $\mathrm{i}^{\mathrm{n,out}}$ are proportional to P_{tot}. Indeed eqn (25) can be transformed into

$$\frac{\mathrm{d}f(\theta x)}{\mathrm{d}x} + f(\theta x)[1 + bh(\theta x)] = ah(\theta x). \tag{34}$$

Neither b nor $h(\theta x)$ depend on P_{tot} (see eqn (20), (21) and (26–29)). In contrast, a is proportional to P_{tot} (see eqn (6) and (27)). Derivation being a linear operation, eqn (34) then implies that $f(\theta x)$ is proportional to P_{tot}. The system of equations giving access to a_n and b_n being linear (see ESI†), all the a_n and b_n amplitudes are individually proportional to P_{tot}. Finally, we use eqn (31–33) to deduce that i°, $\mathrm{i}^{\mathrm{n,in}}$ and $\mathrm{i}^{\mathrm{n,out}}$ are proportional to P_{tot}.

We showed that, in the case of light modulation of small amplitude, the out-of-phase amplitudes of the concentration modulation at radial frequency ω are optimal when the resonance conditions (14) and (15) are fulfilled. In the absence of analytical expressions for $\mathrm{1}^{\mathrm{1,out}}$ and $\mathrm{2}^{\mathrm{1,out}}$, such conclusions cannot be directly derived in the case of periodic light modulation of large amplitude. We correspondingly evaluated their relevance by means of numerical calculations (see ESI†). For harmonic forcing as well as square wave modulation in a regime of large amplitude modulation, we could show that $|\mathrm{1}_{\mathrm{norm}}^{\mathrm{1,out}}|$ exhibits an optimum in the space (I^0, ω), which position and amplitude are very close to those observed with a sinusoidal modulation of small amplitude. In fact, the error done when taking the analytical expression of the resonance conditions valid only for a modulation of small amplitude is always less than 20%, no matter which amplitude α is used. Such an error would be of the order of magnitude of the experimental errors done when fixing the average light intensity and radial frequency to their values at resonance, $I^{0,R}$ and ω^R.

Application to selective and quantitative detection of a photoswitchable probe

In the preceding section, we demonstrated that, for a photoswitchable probe submitted to a periodic modulated light, the out-of-phase first-order response of the concentration could be maximized by appropriately choosing both the average light intensity and the radial frequency of the light modulation. However, in general, concentrations are retrieved from a signal. In this section, we analyze whether the out-of-phase response of the signal can be used for selective detection of a photoswitchable probe.

Out-of-phase response of the overall observable

The overall observable O (*e.g.* absorbance, electrophoretic mobility, …) from the photoswitchable probe results from the individual contributions of the states **1** and **2**. We assume that this observable varies linearly with the concentrations in **1** and **2**. We note Q_i the response factor of **i** linking signal and concentration (hereafter considered as constant). We can write

$$O(t) = Q_1 1(t) + Q_2 2(t). \tag{35}$$

In the general case of a periodic modulation of large amplitude, using the expressions of $1(t)$ and $2(t)$ given in eqn (33), the expression of the signal $O(t)$ becomes

$$O(t) = \mathfrak{O}^{o} + \sum_{n=1}^{\infty}\left[\mathfrak{O}^{\mathfrak{n,in}} \sin(n\omega t) + \mathfrak{O}^{\mathfrak{n,out}} \cos(n\omega t)\right], \tag{36}$$

where (see ESI†)

$$\mathfrak{O}^{\mathfrak{1,out}} = (Q_2 - Q_1)\alpha \mathfrak{2}^{\mathfrak{1,out}}. \tag{37}$$

As shown in eqn (37), $\mathfrak{O}^{\mathfrak{1,out}}$ is directly proportional to $\mathfrak{2}^{\mathfrak{1,out}}$, which was shown above to be optimal when the resonance conditions (14) and (15) are fulfilled. Hence, the analysis of the out-of-phase first-order response $\mathfrak{O}^{\mathfrak{1,out}}$ of the overall observable $O(t)$ allows for the selective and quantitative detection of a photoswitchable probe. Note that $\mathfrak{O}^{\mathfrak{1,out}}$ can be easily extracted from the overall signal $O(t)$ *via* lock-in amplification, which enables to further improve the signal to noise ratio (see ESI†).

Out-of-phase response of the fluorescence intensity

Fluorescence emission is a particularly relevant observable to apply the present protocol.[44] In small molecules, combining fluorescence emission and photochromism is difficult since both processes are often competitive mechanisms for relaxation of the excited states.[45] In contrast, such a combination is widely found in photochromic fluorescent proteins which have recently led to powerful techniques including time-resolved protein tracking,[46] super-resolution microscopy[47–50] and high contrast imaging.[19,20] Moreover we recently showed that hybrid systems composed of a photoconvertible fluorogen that fluoresces upon binding to an acceptor provide an attractive two-component approach.[51]

Compared to other observables, the fluorescence intensity $I_F(t)$ includes an additional signal convolution since it is not only proportional to concentrations, but also proportional to the light intensity. Thus, considering that both concentrations of the states **1** and **2**, and light intensity are modulated, the fluorescence emission $I_F(t)$ can be written

$$I_F(t) = O(t)I(t) \tag{38}$$

with Q_i being the molecular brightness of **i**. In the general case of a periodic modulation of large amplitude, one obtains

$$I_F(t) = \mathfrak{I}_{\mathfrak{I}}^{o} + \sum_{n=1}^{\infty}\left[\mathfrak{I}_{\mathfrak{I}}^{\mathfrak{n,in}} \sin(n\omega t) + \mathfrak{I}_{\mathfrak{I}}^{\mathfrak{n,out}} \cos(n\omega t)\right]. \tag{39}$$

where (see ESI†)

$$\mathfrak{I}_{\mathfrak{I}}^{\mathfrak{1,out}} = \alpha(Q_2 - Q_1)I^0\left[\mathfrak{2}^{\mathfrak{1,out}} + g\left(\mathfrak{2}^{\mathfrak{n,in}},\ \mathfrak{2}^{\mathfrak{n,out}}\right)\right] \tag{40}$$

with $n \geq 1$. For a sinusoidal or square wave modulation of small amplitude, $g(\mathfrak{2}^{\mathfrak{n,in}}, \mathfrak{2}^{\mathfrak{n,out}}) = 0$ but it is non-vanishing in the case of a periodic modulation of large amplitude.

In a regime of sinusoidal or square wave modulation of small amplitude, the out-of-phase amplitude of the fluorescence emission, $\mathfrak{I}_{\mathfrak{I}}^{\mathfrak{1,out}}$, is proportional to $\mathfrak{2}^{\mathfrak{1,out}}$ and exhibits a resonant behavior. In contrast, such a conclusion cannot be directly drawn in the case of periodic modulation of large amplitude since analytical expressions are cumbersome. We therefore evaluated its relevance by means of numerical calculations using typical values found for photoswitchable fluorescent proteins.[52–56] To evaluate the possible interference originating from the second order term $g(\mathfrak{2}^{\mathfrak{n,in}}, \mathfrak{2}^{\mathfrak{n,out}})$, we used eqn (40) to numerically compute the dependence of $\mathfrak{I}_{\mathfrak{I}}^{\mathfrak{1,out}}$ on ω and I^0 (see ESI†). Hence we showed that the position and the amplitude of its optimum are similar independently on the nature and amplitude of the light modulation.

Therefore, the out-of-phase first-order fluorescence emission enables the selective and quantitative detection of a photoswitchable probe. Easily extracted from the overall signal $I_F(t)$ with the benefit of synchronous detection (see ESI†), it additionally provides an improved spatial resolution compared to usual fluorescence detection (see ESI†), which is an advantage for imaging.

Discussion

Our theoretical framework suggests that the out-of-phase first-order response to a periodically modulated light excitation under resonant conditions is appropriate to isolate the contribution of a photoswitchable probe of interest when the observable linearly depends on concentrations. Compared to a classical analysis that relies on an observation in absence of concentration modulation, this feature provides a simple protocol to perform selective and quantitative analyses in complex media without any preliminary separation.

A separation-free selective and quantitative analytical protocol

Instead of analyzing the behavior of a given photoswitchable probe upon varying the values of the control parameters I^0 and ω, we now examine which photoswitchable probe can be specifically addressed at fixed values of I^0 and ω.

Dynamic contrast. In a mixture of photoswitchable probes, dynamic contrast will originate from differences in the triplet of parameters (σ_{12}, σ_{21}, k_{21}^{Δ}). At fixed values of I^0 and ω, the optimized out-of-phase first-order response to a periodically modulated light excitation originates from matching (i) the rate constants for the thermally- and photochemically-driven reactions (see eqn (14)) and (ii) the exchange relaxation time τ_{12}^0 with the radial frequency of the light modulation ω (see eqn (14) and (15)). We correspondingly use the ($\sigma_{12} + \sigma_{21}$, k_{21}^{Δ}) dynamic set to characterize the dynamic behavior of the photoswitchable probes illuminated at average intensity I^0 and radial frequency ω. Fig. 3a and b displays the dependence of the normalized in-phase $|1_{\text{norm}}^{1,\text{in}}| = |1^{1,\text{in}}/P_{\text{tot}}|$ and out-of-phase $|1_{\text{norm}}^{1,\text{out}}| = |1^{1,\text{out}}/P_{\text{tot}}|$ amplitudes on $(\sigma_{12} + \sigma_{21})I^0/\omega$ and k_{21}^{Δ}/ω for a weak sinusoidal light modulation. In contrast to the in-phase amplitude, the out-of-phase amplitude exhibits a single optimum centered on

$$\sigma_{12} + \sigma_{21} = \frac{\omega}{2I^0} \tag{41}$$

$$k_{21}^{\Delta} = \frac{\omega}{2}. \tag{42}$$

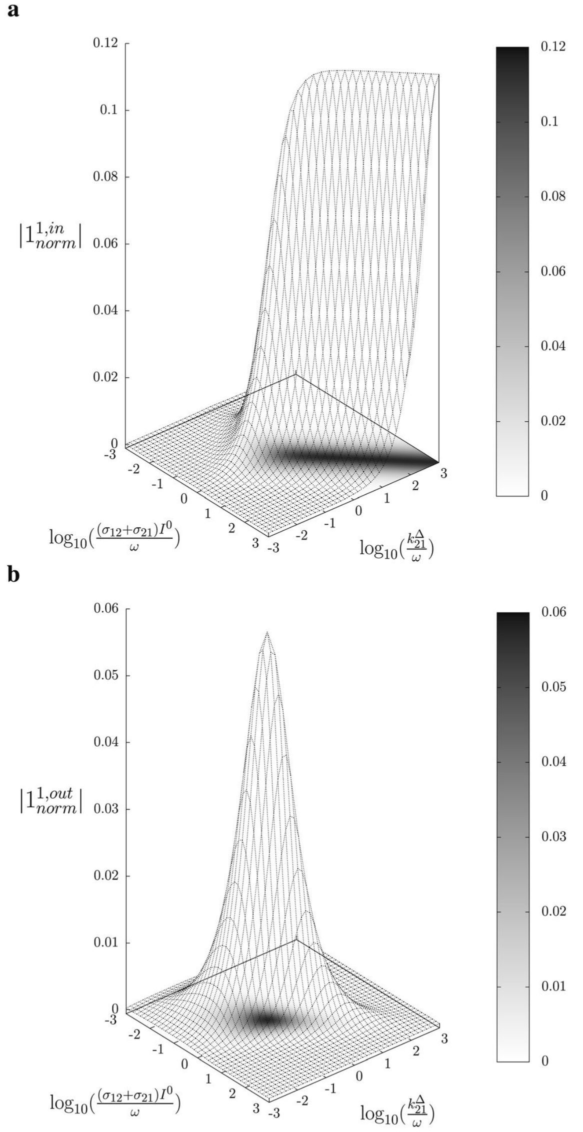

Fig. 3 Theoretical computation of the response of a photoswitchable probe $1 \rightleftharpoons 2$ submitted to light harmonic forcing of small amplitude at fixed values of I^0 and ω. The normalized amplitudes of the in-phase and out-of-phase oscillations in **1** concentration, $|1_{\text{norm}}^{1,\text{in}}|$ (a) and $|1_{\text{norm}}^{1,\text{out}}|$ (b) respectively, are plotted *versus* $(\sigma_{12} + \sigma_{21})I^0/\omega$ and k_{21}^{Δ}/ω for $\sigma_{12}/(\sigma_{12} + \sigma_{21}) = 0.46$. See eqn (12) and (13).

At fixed values of I^0 and ω, eqn (41) and (42) show that one can selectively isolate the contribution from the monodimensional $\left(\sigma_{12}, \frac{\omega}{2I^0} - \sigma_{12}, \frac{\omega}{2}\right)$ manifold in the three-dimensional (σ_{12}, σ_{21}, k_{21}^{Δ}) space of photoswitchable probes. Among the manifold members, the $|1_{\text{norm}}^{1,\text{out}}| = \sigma_{12}/[8(\sigma_{12} + \sigma_{21})]$ amplitude is ruled by the $\sigma_{12}/(\sigma_{12} + \sigma_{21})$ photochemical parameter. $|1_{\text{norm}}^{1,\text{out}}|$ is maximal $\left(\frac{1}{8}\right)$ for the $\left(\frac{\omega}{2I^0}, 0, \frac{\omega}{2}\right)$ photoswitchable probe. However the amplitude of all the manifold members notably remains of the same order of magnitude as long as σ_{12} does not drop much below the σ_{21} range.

Selective and quantitative detection. The above discussion shows that optimizing the out-of-phase response by choosing a couple (I^0, ω) that verifies the resonance conditions (14) and (15) opens an interesting way to selectively image and quantify a photoswitchable probe **P** in the presence of interfering compounds **X** (of total concentrations X_{tot}), each defined by a different set of parameters ($\sigma_{12,X}$, $\sigma_{21,X}$, $k_{21,X}^{\Delta}$). Note that **X** can be non-photoswitchable: in that case $\sigma_{12,X} = \sigma_{21,X} = 0$ and $k_{21,X}^{\Delta} = 0$. To illustrate this, we take a simplified case of a mixture containing photoswitchable probes, whose only the state **1** yields an observable signal, and possessing all the same brightness Q_1. In that case, a protocol relying on illumination at constant light intensity I^0 leads to a signal S^0 which is proportional to the sum of the contributions of the different probes such that:

$$S^0 \propto 1_P^0 + \sum_X 1_X^0 = \left(1_P^0/P_{\text{tot}}\right)P_{\text{titration}}^0 \tag{43}$$

where

$$P_{\text{titration}}^0 = P_{\text{tot}} + \sum_X \frac{\left(1_X^0/X_{\text{tot}}\right)}{\left(1_P^0/P_{\text{tot}}\right)} X_{\text{tot}} > P_{\text{tot}} \tag{44}$$

When the signal S^0 is used to titrate the concentration of **P** upon assuming that only the reactant of interest is present, the titration result $P_{\text{titration}}^0$ always overestimates the total concentration P_{tot} because of the contributions of the interfering compounds (see Fig. 4a).

In contrast, the corresponding out-of-phase first-order response to light modulation $\mathfrak{S}^{1,\text{out}}$

$$\mathfrak{S}^{1,\text{out}} \propto 1_P^{1,\text{out}} + \sum_X 1_X^{1,\text{out}} = \left(1_P^{1,\text{out}}/P_{\text{tot}}\right)P_{\text{titration}}^{1,\text{out}} \tag{45}$$

where

$$P_{\text{titration}}^{1,\text{out}} = P_{\text{tot}} + \sum_X \frac{\left(1_X^{1,\text{out}}/X_{\text{tot}}\right)}{\left(1_P^{1,\text{out}}/P_{\text{tot}}\right)} X_{\text{tot}} \tag{46}$$

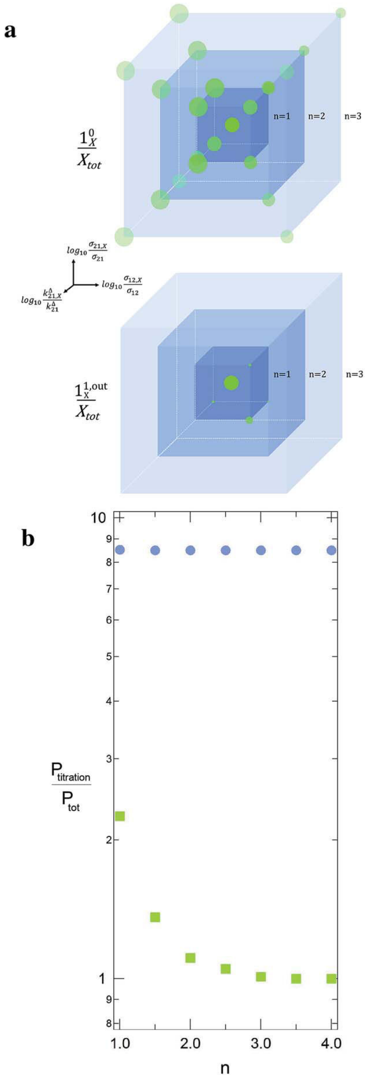

Fig. 4 Theoretical computation of $P_{titration}$ in seven different equimolar mixtures, which include the targeted triplet (σ_{12}, σ_{21}, k^{Δ}_{21}) plus eight other interfering ones. In each sample labelled n, the latter species correspond to the eight ($\sigma_{12,X}$, $\sigma_{21,X}$, $k^{\Delta}_{21,X}$) sets placed on the nodes of a cube centered on (σ_{12}, σ_{21}, k^{Δ}_{21}) and which mesh size is n in decimal logarithmic units (a; the individual responses ($1_X^0/X_{tot}$) and ($1_X^{1,out}/X_{tot}$) have been used to define the sphere radius associated to each ($\sigma_{12,X}$, $\sigma_{21,X}$, $k^{\Delta}_{21,X}$) set in ($1^0/P_{tot}$) and ($1^{1,out}/P_{tot}$) units). The n-dependence of the ratio of $P_{titration}$ to the effective target concentration P_{tot} is displayed in b for both the constant light intensity (disks) and the OPTIMAL (squares) methods. $\sigma_{12} = 73$ m^2 mol^{-1}, $\sigma_{21} = 84$ m^2 mol^{-1}, $k^{\Delta}_{21} = 1.5 \times 10^{-2}$ s^{-1}; $I^0 = k^{\Delta}_{21}/(\sigma_{12} + \sigma_{21}) = 9.6 \times 10^{-5}$ ein s^{-1} m^{-2}, $\omega = 2k^{\Delta}_{21} = 3 \times 10^{-2}$ rad s^{-1}.

enables to determine P_{tot} when the light parameters (I^0, ω) are tuned to the resonance conditions of **P**. Indeed, the term $1_P^{1,out}$ is then maximal while the terms $1_X^{1,out}$ are negligible (Fig. 3b). Thus, the signal from **P** now dominates those of the other probes, and the titration result $P^{1,out}_{titration}$ is approximately equal to P_{tot} (see Fig. 4a). Fig. 4b illustrates for various mixtures the superiority of this second strategy over measurements performed at constant light intensity: whereas all the $P^0_{titration}$ are several times larger than the actual P_{tot} concentration, the discrepancy between $P^{1,out}_{titration}$ and P_{tot} becomes negligible as soon as (σ_{12}, σ_{21}, k^{Δ}_{21}) deviates from ($\sigma_{12,X}$, $\sigma_{21,X}$, $k^{\Delta}_{21,X}$).

Experimental implementation

This theoretical analysis suggests that it is possible to selectively and quantitatively visualize a given photoswitchable probe defined by the triplet of parameters (σ_{12}, σ_{21}, k^{Δ}_{21}) by simply analysing the out-of-phase (or quadrature-delayed) first-order component of the overall signal resulting from an illumination with a light of average intensity I^0 and periodically modulated at fundamental angular frequency ω so as to fulfil the resonance conditions (14) and (15) (Fig. 1).

To selectively address a photoswitchable probe of interest used for analyte labelling necessitates to preliminarily measure the sum of its molecular action cross-sections for photoisomerization $\sigma_{12} + \sigma_{21}$ and its thermal rate constant k^{Δ}_{21}, which can be easily performed, for instance, with a series of simple light jump experiments.[40,51] Once the parameters $\sigma_{12} + \sigma_{21}$ and k^{Δ}_{21} are known, one fixes the parameters I^0 and ω of the modulated illumination so as to fulfil the resonance conditions (14) and (15) of the photoswitchable probe. Then one extracts the out of phase first-order response $\mathfrak{S}^{1,out}$ from the acquired probe signal $S(t)$ (possibly contaminated by the contribution of interfering compound). One subsequently aims at extracting from $\mathfrak{S}^{1,out}$ the total probe concentration $P^{1,out}_{tot}$, which quantifies the labelled analyte. Although theoretical expressions could make possible to directly retrieve the concentrations of the photoswitchable probe from the observed signal, it is probably easier to proceed by calibration upon acquiring the signal from the pure photoswitchable probe at a reference concentration P^{cal}_{tot} under the same illumination conditions (see ESI†). Then

$$P^{1,out}_{tot} = \frac{\mathfrak{S}^{1,out}}{\mathfrak{S}^{1,out,cal}} P^{cal}_{tot}. \qquad (47)$$

When the photoswitchable probe is used as a titrating reagent, to fulfil the resonance conditions for the parameters I^0 and ω first requires an initial guess since the apparent molecular action cross-sections for photoisomerization and thermal rate constant now depend on the concentration of the targeted analyte A_{tot} (see ESI†). In fact, as usually encountered in any titration protocol, one should have an order of magnitude of the latter value before proceeding. Moreover, in contrast to the previous situation, the information sought for is not anymore P_{tot} but A_{tot}, which is contained in the amplitude of the **P** response to the light modulation (see ESI†). However, the latter amplitude is also proportional to P_{tot} and one has first to remove this dependence, for instance by relying on a ratiometric analysis, where one collects the overall signal upon adopting a same illumination but under two conditions of observation (*e.g.* by recording the fluorescence emission at two different wavelengths). Hence, the analyzed observable is now the ratio $\rho^{1,out} = \mathfrak{S}_1^{1,out}/\mathfrak{S}_2^{1,out}$ of the out-of-phase first-order amplitudes of the signal collected under the two observation conditions (see ESI†). Calibration now requires to preliminarily investigate the dependence of $\rho^{1,\text{out}}$ on A_{tot}. Then quantification can be simply achieved by recording the observable from a calibrating solution where the photoswitchable probe is used to sense a known concentration $A_{\text{tot}}^{\text{cal}}$. The concentrations of the analyte, which is retrieved at first-order, is eventually

$$A_{\text{tot}}^{1,\text{out}} = \frac{\rho^{1,\text{out}}}{\rho^{1,\text{out,cal}}} A_{\text{tot}}^{\text{cal}}. \tag{48}$$

Fields of application

The possibility to selectively and quantitatively retrieve the signal from a probe of interest without any separation is especially attractive when dealing with complex unknown systems.

Selective and quantitative detection in a mixture of probes. As a first field of application, one can think of selectively and quantitatively detecting a probe of interest in a system containing multiple probes or interfering compounds. This application could be especially useful in living cells, both to perform multiplexed observations as well as to overcome the contribution of endogenous components (Fig. 1a).

Selective and quantitative detection in a heterogeneous system. Another attractive field of application deals with the analysis or imaging of heterogenous systems. Indeed the brightness as well as the thermokinetic features of a probe often strongly depend on its environment. Thus, in a highly heterogeneous system (*e.g.* a living cell), it may be especially hazardous to retrieve a quantitative information from the probe signal acquired at constant illumination, when one has no information on the probe location. Indeed the collected signal depends on the concentration, the brightness and the thermokinetic features of the probe. In contrast, the out-of-phase first-order probe response strongly depends on the probe thermokinetic properties, which permits to selectively address the probe molecules located in a given phase, in which preliminary experiments for setting resonance conditions and calibration should have been performed. Therefore, the present analytical protocol could be fruitfully used to selectively analyze concentrations in a phase of interest within a multiphasic media (Fig. 1b), without requiring any extensive structural modification of the probe (as it is usually done to drive the probe location) or fluctuation-based protocols[57] to achieve calibration-free concentration measurements.

New challenges for probe development

The relevance and efficiency of the OPTIMAL/OPIOM protocols rely on the availability of appropriate photoswitchable probes. Many photoswitchable organic[58] as well as inorganic[59] platforms are presently available, so as to make promising the development of OPTIMAL labels with different types of observables. Moreover, these platforms have been already extensively implemented in the context of photocontrollable receptors,[60] so as to consider as well their use as OPTIMAL sensors. In the specific OPIOM context, photoswitchable fluorescent proteins are already highly significant probes. However, even in this case developing photoswitchable fluorescent probes fully optimised for OPIOM would enable to increase both the temporal resolution and the signal-to-noise ratio of this new imaging protocol. Indeed, although the above arguments are favorable, the extensive use of the OPTIMAL/OPIOM protocols may be hampered by the lack of a library of suitable engineered photoswitchable probes. This point has already motivated specific developments of photoswitchable fluorescent proteins in the context of SAFIRe.[61] In fact, most available reversibly photoswitchable fluorescent proteins (*e.g.* Dronpa[52]) have been engineered to exhibit extremely slow thermal return after photoconversion. In the context of OPIOM, such a feature is particularly detrimental in terms of fluorescence signal and temporal resolution: at resonance, intensity of light excitation as well as frequency of light modulation are proportional to the rate constant for thermal return (see eqn (14) and (15)). Even upon relying on the fastest Dronpa-3 mutant,[56] we only reached 20 s for the period of light modulation – typically leading to the minute range to record an image.[40] Such conditions are not optimal with respect to dynamic analysis of biological phenomena.[62] A slow thermal return also requires working at low average light intensity, which is not favorable to get a satisfactory signal to noise ratio.[48,63] We currently estimate that temporal resolution in the second range at a satisfactory few tens of W cm^{-2} average light power could be reached with photoswitchable probes exhibiting a relaxation time for thermal return in the 0.1–1 s range. Moreover, in relation to multiplex applications, Fig. 4 shows that it would be relevant to generate libraries of photoswitchable probes with values of their relevant dynamic parameters k_{21}^{Δ} and $\sigma_{12} + \sigma_{21}$ spread over at least two orders of magnitude ranges. Both photoswitchable fluorescent proteins as well as photoswitchable fluorescence turn-on probes are favorable candidates to implement such an engineering.[51,64,65]

Conclusion

By relying on the out-of-phase first-order response to periodic light modulation, OPTIMAL can discriminate – without any separation or washing step – a targeted photoswitchable probe among various interfering compounds, photoswitchable or not. Its experimental implementation is expected to be simple and cheap, just involving one-day preliminary investigations and appropriate tuning of two control parameters, the average intensity and the radial frequency of the modulated illumination, in order to fulfil robust resonance conditions. In particular, the OPTIMAL approach holds promises for selective and quantitative analyses in complex media such as encountered in biology: with optimized photoswitchable probes, the OPTIMAL protocol should make possible to titrate minor or signal-buried components as well as to facilitate multiplexed observations, as we recently demonstrated upon introducing the OPIOM fluorescence imaging approach in integral cells and organisms.[40]

References

1 C. M. Beck II, *Anal. Chem.*, 1994, **66**, 224A–239A.

2 J. A. Pérez-Bustamante, *Fresenius' J. Anal. Chem.*, 1997, **357**, 151–161.

3 D. Harvey, *Modern Analytical Chemistry*, McGraw-Hill, Boston, 2000.

4 T. R. Gingeras, R. Higuchi, L. J. Kricka, Y. M. D. Lo and C. T. Wittwer, *Clin. Chem.*, 2005, **51**, 661–671.

5 R. L. Nicholson, M. Welch, M. Ladlow and D. R. Spring, *ACS Chem. Biol.*, 2007, **2**, 24–30.

6 J. L. Duffner, P. A. Clemons and A. N. Koehler, *Curr. Opin. Chem. Biol.*, 2007, **11**, 74–82.

7 B. D. Bennett, E. H. Kimball, M. Gao, R. Osterhout, S. J. Van Dien and J. D. Rabinowitz, *Nat. Chem. Biol.*, 2009, **5**, 593–599.

8 B. Giepmans, S. Adams, M. Ellisman and R. Tsien, *Science*, 2006, **312**, 217–224.

9 B. Wu, K. D. Piatkevich, T. Lionnet, R. H. Singer and V. V. Verkhusha, *Curr. Opin. Cell Biol.*, 2011, **23**, 310–317.

10 R. Winkler-Oswatitsch and M. Eigen, *Angew. Chem., Int. Ed.*, 1979, **18**, 20–49.

11 M. Eigen and L. de Mayer, *Relaxation Methods in Techniques of Organic Chemistry*, Interscience Publishers, John Wiley and Sons, New York, London, 2nd edn, 1963, vol. VIII, pp. 895–1054.

12 H. Berthoumieux, C. Antoine and A. Lemarchand, *J. Chem. Phys.*, 2009, **131**, 084106.

13 H. Berthoumieux, L. Jullien and A. Lemarchand, *Phys. Rev. E: Stat., Nonlinear, Soft Matter Phys.*, 2007, **76**, 056112.

14 A. Lemarchand, H. Berthoumieux, L. Jullien and C. Gosse, *J. Phys. Chem. A*, 2012, **116**, 8455–8463.

15 F. Closa, C. Gosse, L. Jullien and A. Lemarchand, *J. Chem. Phys.*, 2013, **138**, 244109.

16 D. Baurecht and U. P. Fringeli, *Rev. Mod. Sci. Inst.*, 2001, **72**, 3782–3792.

17 I. Noda and Y. Osaki, *Two-Dimensional Spectroscopy Applications in Vibrational and Optical Spectroscopy*, Wiley, Chichester, 2004.

18 D. Boyer, P. Tamarat, A. Maali, B. Lounis and M. Orrit, *Science*, 2002, **297**, 1160–1163.

19 G. Marriott, S. Mao, T. Sakata, J. Ran, D. K. Jackson, C. Petchprayoon, T. J. Gomez, E. Warp, O. Tulyathan, H. L. Aaron, E. Y. Isacoff and Y. Yan, *Proc. Natl. Acad. Sci. U. S. A.*, 2008, **105**, 17789–17794.

20 Y. Yan, M. E. Marriott, C. Petchprayoon and G. Marriott, *Biochem. J.*, 2011, **433**, 411–422.

21 C. I. Richards, J.-C. Hsiang, D. Senapati, S. Patel, J. Yu, T. Vosch and R. M. Dickson, *J. Am. Chem. Soc.*, 2009, **131**, 4619–4621.

22 C. I. Richards, J.-C. Hsiang and R. M. Dickson, *J. Phys. Chem. B*, 2010, **114**, 660–665.

23 C. I. Richards, J.-C. Hsiang, A. M. Khalil, N. P. Hull and R. M. Dickson, *J. Am. Chem. Soc.*, 2010, **132**, 6318–6323.

24 C. Fan, J.-C. Hsiang, A. E. Jablonski and R. M. Dickson, *Chem. Sci.*, 2011, **2**, 1080–1085.

25 C. Fan, J.-C. Hsiang and R. M. Dickson, *ChemPhysChem*, 2012, **13**, 1023–1029.

26 A. E. Jablonski, J.-C. Hsiang, P. Bagchi, N. Hull, C. I. Richards, C. J. Fahrni and R. M. Dickson, *J. Phys. Chem. Lett.*, 2012, **3**, 3585–3591.

27 S. Sarkar, C. Fan, J.-C. Hsiang and R. M. Dickson, *J. Phys. Chem. A*, 2014, **117**, 9501–9509.

28 J.-C. Hsiang, A. E. Jablonski and R. M. Dickson, *Acc. Chem. Res.*, 2014, **47**, 1545–1554.

29 A. D. Q. Li, C. Zhan, D. Hu, W. Wan and J. Yao, *J. Am. Chem. Soc.*, 2011, **133**, 7628–7631.

30 Z. Tian, W. Wu, W. Wan and A. D. Q. Li, *J. Am. Chem. Soc.*, 2011, **133**, 16092–16100.

31 Z. Tian and A. D. Q. Li, *Acc. Chem. Res.*, 2013, **46**, 269–279.

32 H. Berthoumieux, C. Antoine, L. Jullien and A. Lemarchand, *Phys. Rev. E: Stat., Nonlinear, Soft Matter Phys.*, 2009, **79**, 021906.

33 I. Schoen, H. Krammer and D. Braun, *Proc. Natl. Acad. Sci. U. S. A.*, 2009, **106**, 21649–21654.

34 K. Zrelli, T. Barilero, E. Cavatore, H. Berthoumieux, T. Le Saux, V. Croquette, A. Lemarchand, C. Gosse and L. Jullien, *Anal. Chem.*, 2011, **83**, 2476–2484.

35 Q. Wei and A. Wei, *Chem.–Eur. J.*, 2011, **17**, 1080–1091.

36 L. Jullien, A. Lemarchand and H. Lemarchand, *J. Chem. Phys.*, 2000, **112**, 8293–8301.

37 D. Alcor, V. Croquette, L. Jullien and A. Lemarchand, *Proc. Natl. Acad. Sci. U. S. A.*, 2004, **101**, 8276–8280.

38 D. Alcor, J.-F. Allemand, E. Cogné-Laage, V. Croquette, F. Ferrage, L. Jullien, A. Kononov and A. Lemarchand, *J. Phys. Chem. B*, 2005, **109**, 1318–1328.

39 J. H. Scofield, *Am. J. Phys.*, 1994, **62**, 129–133.

40 J. Querard, T.-Z. Markus, M.-A. Plamont, C. Gauron, P. Wang, A. Espagne, M. Volovitch, S. Vriz, V. Croquette, A. Gautier, T. Le Saux and L. Jullien, *Angew. Chem., Int. Ed.*, 2015, **54**, 2633–2637.

41 G. Marriott, R. M. Clegg, D. J. Arndt-Jovin and T. M. Jovin, *Biophys. J.*, 1991, **60**, 1374–1387.

42 T. Sanden, G. Persson, P. Thyberg, H. Blom and J. Widengren, *Anal. Chem.*, 2007, **79**, 3330–3341.

43 J. Vogelsang, C. Steinhauer, C. Forthmann, I. H. Stein, B. Person-Skegro, T. Cordes and P. Tinnefeld, *ChemPhysChem*, 2010, **11**, 2475–2490.

44 B. Valeur, *Molecular fluorescence: principles and applications*, Wiley-VCH, 2001.

45 T. Fukaminato, *J. Photochem. Photobiol., C*, 2011, **12**, 177–208.

46 D. M. Chudakov, T. V. Chepurnykh, V. V. Belousov, S. Lukyanov and K. A. Lukyanov, *Traffic*, 2006, **7**, 1304–1310.

47 M. Fernandez-Suarez and A. Y. Ting, *Nat. Rev. Mol. Cell Biol.*, 2008, **9**, 929–943.

48 M. Hofmann, C. Eggeling, S. Jakobs and S. W. Hell, *Proc. Natl. Acad. Sci. U. S. A.*, 2005, **102**, 17565–17569.

49 E. Betzig, G. H. Patterson, R. Sougrat, O. W. Lindwasser, S. Olenych, J. S. Bonifacino, M. W. Davidson, J. Lippincott-Schwartz and H. F. Hess, *Science*, 2006, **313**, 1642–1645.

50 J. Lippincott-Schwartz and G. H. Patterson, *Trends Cell Biol.*, 2009, **19**, 555–565.

51 P. Wang, J. Querard, S. Maurin, S. S. Nath, T. Le Saux, A. Gautier and L. Jullien, *Chem. Sci.*, 2013, **4**, 2865–2873.

52 R. Ando, H. Mizuno and A. Miyawaki, *Science*, 2004, **306**, 1370–1373.

53 S. Habuchi, R. Ando, P. Dedecker, W. Verheijen, H. Mizuno, A. Miyawaki and J. Hofkens, *Proc. Natl. Acad. Sci. U. S. A.*, 2005, **102**, 9511–9516.

54 M. Andresen, A. C. Stiel, S. Trowitzsch, G. Weber, C. Eggeling, M. C. Wahl, S. W. Hell and S. Jakobs, *Proc. Natl. Acad. Sci. U. S. A.*, 2007, **104**, 13005–13009.

55 A. C. Stiel, S. Trowitzsch, G. Weber, M. Andresen, C. Eggeling, S. W. Hell, S. Jakobs and M. C. Wahl, *Biochem. J.*, 2007, **402**, 35–42.

56 R. Ando, C. Flors, H. Mizuno, J. Hofkens and A. Miyawaki, *Eur. Biophys. J.*, 2007, L97–L99.

57 S. Charier, A. Meglio, D. Alcor, E. Cogné-Laage, J.-F. Allemand, L. Jullien and A. Lemarchand, *J. Am. Chem. Soc.*, 2005, **127**, 15491–15505.

58 H. Bouas-Laurent and H. Dürr, *Pure Appl. Chem.*, 2001, **73**, 639–665.

59 M.-S. Wang, G. Xu, Z.-J. Zhang and G.-C. Guo, *Chem. Commun.*, 2010, **46**, 361–376.

60 M. Natali and S. Giordani, *Chem. Soc. Rev.*, 2012, **41**, 4010–4029.

61 A. E. Jablonski, R. B. Vegh, J.-C. Hsiang, B. Bommarius, Y.-C. Chen, K. M. Solntsev, A. S. Bommarius, L. M. Tolbert and R. M. Dickson, *J. Am. Chem. Soc.*, 2013, **135**, 16410–16417.

62 R. Milo, P. Jorgensen, U. Moran, G. Weber and G. M. Springer, *Nucleic Acids Res.*, 2010, **38**, D750–D753.

63 R. Y. Tsien, L. Ernst and A. Waggoner, *Fluorophores for Confocal Microscopy: Photophysics and Photochemistry*, Springer Science + Business Media, 3rd edn, 2006.

64 D. Bourgeois and V. Adam, *IUBMB Life*, 2012, **64**, 482–491.

65 X. X. Zhou and M. Z. Lin, *Curr. Opin. Chem. Biol.*, 2013, **17**, 682–690.

3.3 Supporting Information

Expanding discriminative dimensions for analysis and imaging (Supporting information)

J. Querard,[a,b,c] A. Gautier, [a,b,c],*T. Le Saux,[a,b,c],* L. Jullien[a,b,c],*

[a]*Ecole Normale Supérieure-PSL Research University,*
Département de Chimie, 24, rue Lhomond, F-75005 Paris, France.
E-mail: Arnaud.Gautier@ens.fr, Thomas.Lesaux@ens.fr, Ludovic.Jullien@ens.fr

[b]*Sorbonne Universités, UPMC Univ Paris 06,*
PASTEUR, F-75005, Paris, France.

[c] *CNRS, UMR 8640 PASTEUR, F-75005, Paris, France.*

Contents of the Supporting Information

- Reduction of photo-(physical)chemical mechanisms to a two-state exchange;
- Kinetic analysis of the two-state model;
- Retrieval of concentrations from the observables;
- Improvement of the spatial resolution.

1 Reduction of photo(physical)chemical mechanisms to a two-state exchange

In the following subsections, we show that various mechanisms involving light absorption can be reduced to the two-state model (1) at an appropriate time scale.

1.1 A photoswitchable probe

In a first step, we examine the behaviour of a photoswitchable probe. Light absorption is supposed to drive the exchange between two ground singlet states of a probe denoted $\mathbf{S}_{0,i}$ (i=1 or 2). In the considered scheme, the state $\mathbf{S}_{0,1}$ is supposed to be thermodynamically more stable than the state $\mathbf{S}_{0,2}$. Mechanistically, this exchange involves light absorption leading each ground state $\mathbf{S}_{0,i}$ to its corresponding first singlet excited state $\mathbf{S}_{1,i}$. The latter is then assumed to relax either by leading back to the $\mathbf{S}_{0,i}$ state (for instance by emission of a photon when the probe is a photoswitchable fluorophore) or by photoisomerization (yielding the other ground state). The ground state $\mathbf{S}_{0,2}$ can also notably relax thermally toward the more stable $\mathbf{S}_{0,1}$ state. The overall scheme is displayed in Figure S1.

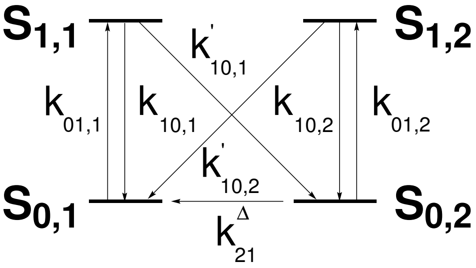

Figure S1: Mechanism accounting for the behaviour of a photoswitchable probe upon illuminating. The arrows and the associated rate constants refer to the exchange processes. See Text.

Relying on the mechanism displayed in Figure S1, we write Eqs.(1–4) to describe the concentration evolutions:

$$\frac{dS_{0,1}}{dt} = -k_{01,1}S_{0,1} + k_{10,1}S_{1,1} + k_{21}^{\Delta}S_{0,2} + k_{10,2}^{'}S_{1,2} \tag{1}$$

$$\frac{dS_{0,2}}{dt} = k_{10,1}^{'}S_{1,1} - \left(k_{01,2} + k_{21}^{\Delta}\right)S_{0,2} + k_{10,2}S_{1,2} \tag{2}$$

$$\frac{dS_{1,1}}{dt} = k_{01,1}S_{0,1} - \left(k_{10,1} + k_{10,1}^{'}\right)S_{1,1} \tag{3}$$

$$\frac{dS_{1,2}}{dt} = k_{01,2}S_{0,2} - \left(k_{10,2} + k_{10,2}^{'}\right)S_{1,2}. \tag{4}$$

In Figure S1, the rate constants $k_{10,i}$ and $k_{10,i}^{'}$ are notably much larger than the rate constants $k_{01,i}$ and k_{21}^{Δ}. $k_{10,i}$ and $k_{10,i}^{'}$ are typically larger than 10^9s^{-1}.[1] In contrast, $k_{01,i}$ is in the 10 s^{-1} range under typical illumination conditions.* Moreover k_{21}^{Δ} is at most in the 10^6 s^{-1} range. Thus it is possible to apply the steady-state approximation to $\mathbf{S}_{1,1}$ and $\mathbf{S}_{1,2}$ beyond the nanosecond time scale. Under such conditions it is meaningful

---

*Using $k_{01,i} = \sigma_{01,i}I^0$ by considering that the typical photon flux at the sample of an illumination setup is $I^0 = 10^{21}$ photons.m^{-2}.s^{-1} and that the molecular cross section for light absorption $\sigma_{01,i} = 2.3\epsilon_i/N_A$ (N_A is the Avogadro number) is in the 10^{-20} m^2/molecule range for the considered probes.

to consider that the states $\mathbf{S}_{0,i}$ and $\mathbf{S}_{1,i}$ are in a fast exchange so as to introduce an average species **i** for which $\mathbf{S}_{0,i}$ and $\mathbf{S}_{1,i}$ contribute in $p_{\mathbf{S}_{0,i}}$ and $p_{\mathbf{S}_{1,i}}$ respective proportions where

$$p_{\mathbf{S}_{0,i}} = \frac{1}{1+K_{01,i}} \tag{5}$$

$$p_{\mathbf{S}_{1,i}} = \frac{K_{01,i}}{1+K_{01,i}} \tag{6}$$

with

$$K_{01,i} = \frac{k_{01,i}}{k_{10,i}+k_{10,i}^{'}}. \tag{7}$$

Under the experimental conditions used in this study, the relative proportions in the excited and ground states are typically $p_{\mathbf{S}_{1,i}} \sim 10^{-8}$ and $p_{\mathbf{S}_{0,i}} \sim 1$.

Considering that the concentration in **i**, i, is equal to $S_{0,i}+S_{1,i}$, Eqs.(1–4) reduce to Eq.(8) beyond the time scale at which the steady-state approximation is valid.

$$\frac{d2}{dt} = -\frac{d1}{dt} = \left(\frac{K_{01,1}}{1+K_{01,1}}k_{10,1}^{'}\right)1 - \left(\frac{K_{01,2}}{1+K_{01,2}}k_{10,2}^{'} + \frac{1}{1+K_{01,2}}k_{21}^{\Delta}\right)2. \tag{8}$$

Considering that, far from saturation, $K_{01,i}$ is proportional to the photon flux I^0 and much lower than 1, one can write:

$$\frac{K_{01,1}}{1+K_{01,1}}k_{10,1}^{'} \simeq K_{01,1}k_{10,1}^{'} = \frac{k_{10,1}^{'}}{k_{10,1}+k_{10,1}^{'}}\sigma_{01,1}I^0 = k_{12}^{h\nu} \tag{9}$$

$$\frac{K_{01,2}}{1+K_{01,2}}k_{10,2}^{'} \simeq K_{01,2}k_{10,2}^{'} = \frac{k_{10,2}^{'}}{k_{10,2}+k_{10,2}^{'}}\sigma_{01,2}I^0 = k_{21}^{h\nu} \tag{10}$$

$$\frac{1}{1+K_{01,2}}k_{21}^{\Delta} \simeq k_{21}^{\Delta}. \tag{11}$$

Hence Eq.(8) can be alternatively written

$$\frac{d2}{dt} = -\frac{d1}{dt} = k_{12}^{h\nu}1 - \left(k_{21}^{h\nu}+k_{21}^{\Delta}\right)2 \tag{12}$$

in which we introduced the notations $k_{12}^{h\nu}$ and $k_{21}^{h\nu}$ to express that the corresponding terms are proportional to the incident photon flux. Eq.(12) is dynamically identical to Eqs.(42–43).

1.2 A three-state electronic model

As a second relevant situation, we analyze the behavior of a chromophore, which light excitation yields its first excited singlet state $\mathbf{S}_1$ from its ground singlet state $\mathbf{S}_0$. $\mathbf{S}_1$ can subsequently relax to the ground state $\mathbf{S}_0$ (for instance by fluorescence emission) or be converted to its first triplet state $\mathbf{T}_1$. $\mathbf{T}_1$ then deexcites to give back the ground state $\mathbf{S}_0$. The overall scheme is displayed in Figure S2.

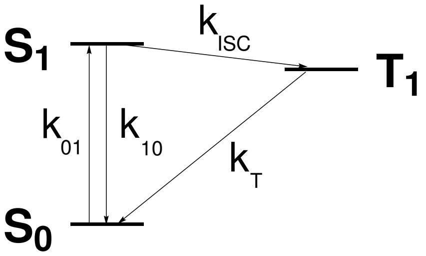

Figure S2: Mechanism accounting for the behaviour of a chromophore yielding its first singlet and triplet excited states upon illuminating. The arrows and the associated rate constants refer to the exchange processes. See Text.

Relying on the mechanism displayed in Figure S2, we write Eqs.(13–15) to describe the concentration evolutions:

$$\frac{dS_0}{dt} = -k_{01}S_0 + k_{10}S_1 + k_T T_1 \tag{13}$$

$$\frac{dS_1}{dt} = k_{01}S_0 - \left(k_{10} + k_{ISC}\right) S_1 \tag{14}$$

$$\frac{dT_1}{dt} = k_{ISC}S_1 - k_T T_1. \tag{15}$$

In Figure S2, the rate constant k_{10} (typically larger than 10^9s^{-1};[1]) is notably much larger than the other rate constants. Again $k_{01,i}$ would be in the 10 s^{-1} under typical illumination conditions. In addition k_{ISC} and k_T are usually in the 10^6 and 10^3–10^6 s^{-1} range.[1] Thus we can apply the steady-state approximation to $\mathbf{S}_1$ beyond the nanosecond time scale. Under such conditions it is meaningful to consider that the states $\mathbf{S}_0$ and $\mathbf{S}_1$ are in a fast exchange so as to introduce an average species **1** for which $\mathbf{S}_0$ and $\mathbf{S}_1$ contribute in $p_{\mathbf{S}_0}$ and $p_{\mathbf{S}_1}$ respective proportions where

$$p_{\mathbf{S}_0} = \frac{1}{1+K_{01}} \tag{16}$$

$$p_{\mathbf{S}_1} = \frac{K_{01}}{1+K_{01}} \tag{17}$$

with

$$K_{01} = \frac{k_{01}}{k_{10}}. \tag{18}$$

Under typical experimental conditions, the relative proportions in the excited and ground states are typically $p_{\mathbf{S}_1} \sim 10^{-8}$ and $p_{\mathbf{S}_0} \sim 1$.

Considering that the concentration in **1**, 1, is equal to $S_0 + S_1$ and denoting $\mathbf{T}_1$ by **2** in the following, Eqs.(13–15) reduce to Eq.(19) beyond the time scale at which the steady-state approximation is valid.

$$\frac{d2}{dt} = -\frac{d1}{dt} = \left(\frac{K_{01}}{1+K_{01}}k_{ISC}\right) 1 - k_T 2. \tag{19}$$

Considering that, far from saturation, K_{01} is proportional to the photon flux I^0 and much lower than 1, one can write:

$$\begin{aligned}\frac{K_{01}}{1+K_{01}}k_{ISC} &\simeq K_{01}k_{ISC}=\frac{1}{k_{10}}\sigma_{01}I^0k_{ISC}=k_{12}^{h\nu} &(20)\\ k_{21}^{\Delta} &= k_T. &(21)\end{aligned}$$

Hence Eq.(19) can be alternatively written

$$\frac{d2}{dt} = -\frac{d1}{dt}=k_{12}^{h\nu}1-k_{21}^{\Delta}2 \qquad (22)$$

in which we introduced the notations $k_{12}^{h\nu}$ to express that the corresponding term is proportional to the incident photon flux. Eq.(22) is dynamically identical to Eqs.(42–43) upon noting that $k_{21}^{h\nu}=0$.

1.3 A four-state model associated to titration of an analyte A

In this last subsection, we reduce the dynamic behavior associated to a photoswitchable sensor. The generic dynamic model is a four-state mechanism consisting of the two exchanging free states of a photoswitchable probe, **1F** and **2F**, which can both bind an analyte **A** to yield the corresponding bound states, **1B** and **2B**. This situation is relevant of a photoswitchable pH-indicator for instance. As in the previous subsections, **1** and **2** states interconvert by photoisomerization in both the bound and free states while only **2** to **1** conversion may occur by thermally-driven exchange. The associated rate constants are presented in Figure S3, where the superscripts hv and Δ respectively denote photochemical and thermal contributions.

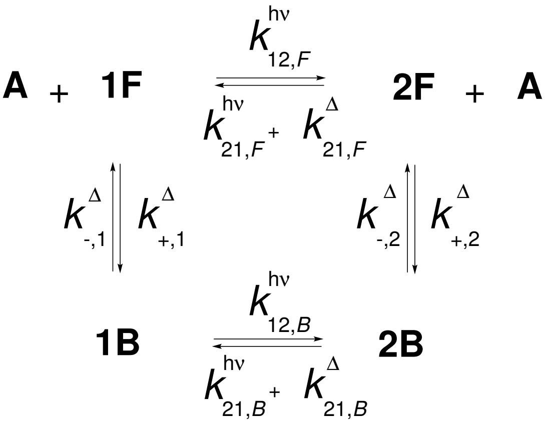

Figure S3: Four-state mechanism accounting for the photochemical and probing behavior of a photoswitchable sensor in the presence of an analyte **A**.

The theoretical framework closely mirrors that described in a previous work by Emond et al.[2] The concentration profiles within the four state model are governed by the equations:

$$\frac{d1B}{dt} = -\left(k_{\mathbf{1B}\rightarrow\mathbf{1F}} + k_{\mathbf{1B}\rightarrow\mathbf{2B}}\right) 1B + k_{\mathbf{2B}\rightarrow\mathbf{1B}}\, 2B + k_{\mathbf{1F}\rightarrow\mathbf{1B}}\, A\, 1F \tag{23}$$

$$\frac{d2B}{dt} = k_{\mathbf{1B}\rightarrow\mathbf{2B}}\, 1B - \left(k_{\mathbf{2B}\rightarrow\mathbf{2F}} + k_{\mathbf{2B}\rightarrow\mathbf{1B}}\right) 2B + k_{\mathbf{2F}\rightarrow\mathbf{2B}}\, A\, 2F \tag{24}$$

$$\frac{d1F}{dt} = k_{\mathbf{1B}\rightarrow\mathbf{1F}} 1B - \left(k_{\mathbf{1F}\rightarrow\mathbf{1B}}\, A + k_{\mathbf{1F}\rightarrow\mathbf{2F}}\right) 1F + k_{\mathbf{2F}\rightarrow\mathbf{1F}}\, 2F \tag{25}$$

$$\frac{d2F}{dt} = k_{\mathbf{2B}\rightarrow\mathbf{2F}} 2B + k_{\mathbf{1F}\rightarrow\mathbf{2F}}\, 1F - \left(k_{\mathbf{2F}\rightarrow\mathbf{2B}}\, A + k_{\mathbf{2F}\rightarrow\mathbf{1F}}\right) 2F \tag{26}$$

The temporal dependence of concentrations cannot be obtained in the most general case. However, it can be analyzed in asymptotic situations according to the nature of the rate-limiting steps, which are associated to either the photochemical reactions or the complexation reactions.† In this account, we are interested to examine the case in which the photochemical steps are rate limiting. Indeed it should be relevant in most sensing situations.‡

In the corresponding "low"-illumination regime, it is meaningful to introduce the average species **1** and **2** (concentrations $1 = 1F + 1B$ and $2 = 2F + 2B$). The "instantaneous" concentrations in **1F**, **1B**, **2F** and **2B** then follow,

$$1F = \frac{1}{1 + K_1^{\Delta} A} 1 \tag{27}$$

$$1B = \frac{K_1^{\Delta} A}{1 + K_1^{\Delta} A} 1 \tag{28}$$

$$2F = \frac{1}{1 + K_2^{\Delta} A} 2 \tag{29}$$

$$2B = \frac{K_2^{\Delta} A}{1 + K_2^{\Delta} A} 2 \tag{30}$$

where

$$K_1^{\Delta} = \frac{k_{+,1}^{\Delta}}{k_{-,1}^{\Delta}} \tag{31}$$

$$K_2^{\Delta} = \frac{k_{+,2}^{\Delta}}{k_{-,2}^{\Delta}}. \tag{32}$$

Thus Eqs.(23–26) transform into Eq.(33):

$$\frac{d1}{dt} = -\frac{d2}{dt} = -k_{12}\, 1 + k_{21}\, 2 \tag{33}$$

---

† Crossing between both kinetic regimes typically occurs when the relaxation times associated to the photoisomerization and the complexation reactions are equal.

‡ The rate constants associated to the photochemical steps adopt the expression $k_{ij,S}^{h\nu} = \sigma_{ij,S}\phi_{ij,S} I^0$ (i and j are equal to 1 or 2 with $i \neq j$, $S = F$ or B). By considering that the typical photon flux at the sample of an illumination setup is $I^0 = 10^{21}$ photons.m^{-2}.s^{-1} and that the molecular cross section for light absorption $\sigma_{01,i} = 2.3\epsilon_i/N_A$ (N_A is the Avogadro number) and the quantum yield $\phi_{ij,S}$ associated to photoisomerization are typically in the 10^{-20} m^2/molecule and 0.1 ranges respectively for the considered probes, we derive $k_{ij,S}^{h\nu} \simeq 1$ s^{-1}. Hence the relaxation times associated to photoisomerizations would be typically in the 1 s range. Such a range is above the order of magnitude of the relaxation times associated to titration reactions. For instance, diffusion-limited reactions (e. g. most proton exchanges[3]) are associated with rate constants in the 10^{10} M^{-1}s^{-1} range. They would give rise to relaxation times below the millisecond for titrating reagents with $10^3 < K_i^{\Delta} < 10^7$ upon assuming K_i^{Δ} (i=1 or 2) to be tailored such that the concentration in analyte **A** is in the range of $1/K_i^{\Delta}$ to get the largest sensitivity.

with

$$k_{12} = \frac{k_{12,F}^{h\nu} + k_{12,B}^{h\nu}\,K_1^{\Delta}A}{1+K_1^{\Delta}A} \tag{34}$$

$$k_{21} = \frac{\left(k_{21,F}^{h\nu} + k_{21,F}^{\Delta}\right) + \left(k_{21,B}^{h\nu} + k_{21,B}^{\Delta}\right)\,K_2^{\Delta}A}{1+K_2^{\Delta}A}. \tag{35}$$

In the most general case, Eq.(33) has no analytical solution, because k_{12} and k_{21} are time-dependent as a result of the $A(t)$ term. However, a tractable temporal dependence of the concentrations upon light excitation can be obtained in the most important sensing situation when the total concentration of the analyte (A_{tot}) is much larger than that of the photoswitchable sensor (P_{tot}): $A_{tot} \gg P_{tot}$.[§] Introducing

$$k_{12} = \frac{k_{12,F}^{h\nu} + k_{12,B}^{h\nu}\,K_1^{\Delta}A_{tot}}{1+K_1^{\Delta}A_{tot}} \tag{36}$$

$$k_{21}^{h\nu} = \frac{k_{21,F}^{h\nu} + k_{21,B}^{h\nu}\,K_2^{\Delta}A_{tot}}{1+K_2^{\Delta}A_{tot}} \tag{37}$$

$$k_{21}^{\Delta} = \frac{k_{21,F}^{\Delta} + k_{21,B}^{\Delta}\,K_2^{\Delta}A_{tot}}{1+K_2^{\Delta}A_{tot}}, \tag{38}$$

Eq.(33) can be alternatively written

$$\frac{d2}{dt} = -\frac{d1}{dt} = k_{12}^{h\nu}1 - \left(k_{21}^{h\nu} + k_{21}^{\Delta}\right)2 \tag{39}$$

in which we introduced the notations $k_{12}^{h\nu}$ and $k_{21}^{h\nu}$ to express that the corresponding terms are proportional to the incident photon flux. Eq.(39) is dynamically identical to Eqs.(42–43).[¶]

[§] The most general case is made complex by the existence of the product of concentrations of the reactants in the dynamic law. In principle, this law could be linearized around chemical equilibrium when light modulation is of small amplitude but it would yield intricate resonance conditions. Moreover, to subsequently implement experimentally these resonance conditions would generally necessitate the knowledge of the overall concentrations of both the probe and the analyte. Whereas to have a guess about the concentration of the analyte is classical in titration protocols (and our final protocol precisely integrates such a guess), we estimated that it would be too demanding prior the titration experiment to have another guess about the concentration of the probe. In particular we had in mind biological applications for which intra-cellular or intra-organism partition of an externally added molecule can be hardly predicted. Therefore we deliberately favored the case where the concentration of the probe is much smaller than the one of the analyte. Classically encountered for titrations, this situation can be easily fulfilled when a sensitive observable such as fluorescence is experimentally implemented.

[¶] In the corresponding regime, one can also derive the average brightnesses of the average states **1** and **2**. Denoting Q_i for the individual brightness of the species **1F**, **2F**, **1B**, and **2B**, one has

$$Q_2 = \frac{Q_{2F} + Q_{2B}K_2^{\Delta}A_{tot}}{1+K_2^{\Delta}A_{tot}} \tag{40}$$

$$Q_1 = \frac{Q_{1F} + Q_{1B}K_1^{\Delta}A_{tot}}{1+K_1^{\Delta}A_{tot}}. \tag{41}$$

2 Kinetic analysis of the two-state model

2.1 The model

We consider relaxation mechanisms which can be reduced to the two-state exchange displayed in Figure S4.

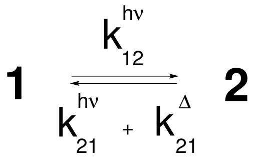

Figure S4: Reduced mechanism accounting for the photochemical behavior of a photoswitchable probe. The most stable state of the probe is here assumed to be **1**, which can switch to the less stable state **2** by photoisomerization. Back reaction from **2** to **1** can occur either by photoisomerization or thermally-driven exchange.

We assume that the system is either homogeneously illuminated or that it can be considered homogeneous at any time of its evolution. Then we rely on the mechanism displayed in Figure S4 to write Eqs.(42–43) describing the concentration evolutions:

$$\frac{d1}{dt} = -\left(k_{\mathbf{1}\rightarrow\mathbf{2}}\right)\, 1 + k_{\mathbf{2}\rightarrow\mathbf{1}}\, 2 \qquad (42)$$

$$\frac{d2}{dt} = k_{\mathbf{1}\rightarrow\mathbf{2}}\, 1 - \left(k_{\mathbf{2}\rightarrow\mathbf{1}}\right)\, 2 \qquad (43)$$

where we make explicit the photochemical and thermal contributions to the rate constants by writing

$$k_{\mathbf{1}\rightarrow\mathbf{2}} = k_{12}^{h\nu} \qquad (44)$$

$$k_{\mathbf{2}\rightarrow\mathbf{1}} = k_{21}^{h\nu} + k_{21}^{\Delta} \qquad (45)$$

where the exponent indicates the nature of the contribution.

In the following, we are interested to derive the theoretical expressions of (i) the concentrations in **1** and **2** (1 and 2 respectively), (ii) the overall observable originating from the photoswitchable probe, and (iii) the convolution of the preceding overall observable with the light excitation (we chose fluorescence emission as a representative example), upon applying either a jump or a periodic modulation of the illumination.

2.2 Light-jump experiments

We here consider that the system is "suddenly"[‖] illuminated, so that the incident surfacic photon flux varies from 0 to I^0:

$$I(t) = I^0 \qquad (46)$$

for $t \geq 0$.

[‖] Note that "suddenly" here refers to a time interval such that Eqs.(42,43) can be considered valid.

2.2.1 Expression of the concentrations

Denoting σ_{12} and σ_{21} the excitation cross sections associated to the transitions from the state **1** to the state **2**, and from the state **2** to the state **1** respectively, the apparent rate constants $k_{12} = k_{12}^{h\nu} = \sigma_{12} I^0$ and $k_{21} = k_{21}^{h\nu} + k_{21}^{\Delta} = \sigma_{21} I^0 + k_{21}^{\Delta}$ can be considered constant and equal to k_{12}^0 and k_{21}^0. Upon introducing the total concentration in photoswitchable probe **P**, $P_{tot} = 1 + 2$, Eqs.(42,43) yield:

$$-\frac{d\left(2 - 2^0\right)}{dt} = \left(k_{12}^0 + k_{21}^0\right)\left(2 - 2^0\right) \tag{47}$$

from which we derive

$$2 - 2^0 = 1^0 - 1 = -2^0 \exp\left(-\frac{t}{\tau_{12}^0}\right) \tag{48}$$

where

$$2^0 = \frac{K_{12}^0}{1 + K_{12}^0} P_{tot} \tag{49}$$

$$1^0 = \frac{1}{1 + K_{12}^0} P_{tot} \tag{50}$$

$$\tau_{12}^0 = \frac{1}{k_{12}^0 + k_{21}^0} \tag{51}$$

$$K_{12}^0 = \frac{k_{12}^0}{k_{21}^0} \tag{52}$$

In Eqs.(48–52), 2^0, 1^0, τ_{12}^0, and K_{12}^0 respectively denote the steady-state value of the concentrations in **2** and **1**, the relaxation time associated to the exchange between the states **1** and **2**, and the apparent photoisomerization constant of the photoswitchable fluorophore **P**, in the presence of light at constant light flux I^0.

2.2.2 Expression of the overall observable from the photoswitchable probe

The overall observable O from the photoswitchable probe results from the individual contributions of the states **1** and **2**. Denoting Q_i for the molecular brightness, one has

$$O(t) = Q_1 1(t) + Q_2 2(t). \tag{53}$$

Upon applying a light jump from 0 to I^0, the overall observable evolves as

$$O(t) = O^0 + \left(Q_1 - Q_2\right) 2^0 \exp\left(-\frac{t}{\tau_{12}^0}\right) \tag{54}$$

where

$$O^0 = Q_1 1^0 + Q_2 2^0. \tag{55}$$

2.2.3 Expression of the fluorescence intensity

We now consider the probe to be fluorescent. Fluorescence intensity $I_F(t)$ can be written

$$I_F(t) \quad = \quad O(t)I(t) = [Q_1 1(t) + Q_2 2(t)]\, I(t) \tag{56}$$

where the expressions of $I(t)$, 1 and 2 can be retrieved from Eqs.(46,48). Then one has:

$$I_F \quad = \quad \left[O^0 + (Q_1 - Q_2)\, 2^0 \exp\left(-\frac{t}{\tau_{12}^0}\right)\right] I^0. \tag{57}$$

2.3 Light modulation experiments

In the following, we successively consider two different types of periodically modulated illumination: (i) a sinusoidal modulation (Figure S5a); (ii) a square wave modulation modelled by its expansion as a Fourier series (Figure S5b; *vide infra*). For each type of modulation, the corresponding cases of small and large modulation are successively considered.

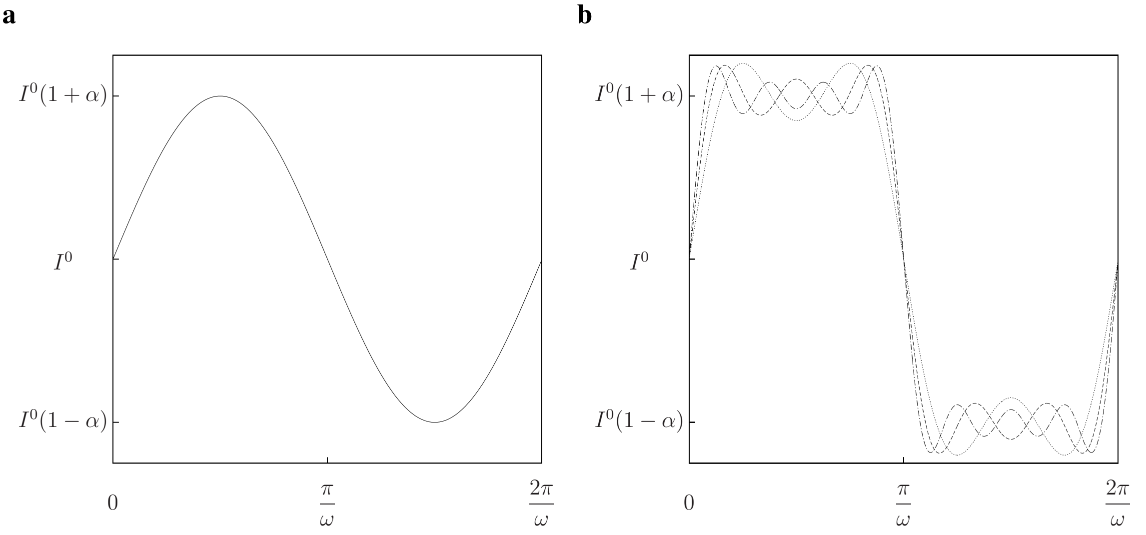

Figure S5: Periodically modulated illuminations, which have been considered in the present study. **a**: Sinusoidal modulation of amplitude α around the average value I^0: $I(t) = I^0 [1 + \alpha \sin(\omega t)]$; **b**: Square wave modulation of amplitude α: $I(t) = I^0 \left\{1 + \frac{4\alpha}{\pi} \sum_{p=0}^{\infty} \frac{1}{2p+1} \sin[(2p+1)\,\omega t]\right\}$ at first- (p=1, dotted line), second- ($p = 2$, dashed line) and third- ($p = 3$, dashed-dotted line) orders of the Fourier series expansion.

2.3.1 Sinusoidal modulation of small amplitude

Expression of the concentrations We first consider that the system is submitted to a weak sinusoidal modulation of illumination around the averaged value I^0. We correspondingly adopt

$$I(t) \quad = \quad I^0 [1 + \varepsilon \sin(\omega t)] \tag{58}$$

with $\varepsilon \ll 1$. One has

$$k_{12}^{h\nu}(t) = k_{12}^{h\nu,0}\left[1+\varepsilon\sin(\omega t)\right] \quad (59)$$

$$k_{21}^{h\nu}(t) = k_{21}^{h\nu,0}\left[1+\varepsilon\sin(\omega t)\right]. \quad (60)$$

The equations (42,43) are solved at first order of the light perturbation upon writing:

$$2 = 2^0+\varepsilon 2^1(t) = 2^0-\varepsilon 1^1(t) \quad (61)$$

$$1 = 1^0-\varepsilon 2^1(t) = 1^0+\varepsilon 1^1(t) \quad (62)$$

$$k_{12}(t) = k_{12}^{h\nu,0}\left[1+\varepsilon\sin(\omega t)\right] \quad (63)$$

$$k_{21}(t) = k_{21}^{h\nu,0}\left[1+\varepsilon\sin(\omega t)\right]+k_{21}^{\Delta} \quad (64)$$

to yield

$$\frac{d2^1}{dt}+\frac{1}{\tau_{12}^0}2^1 = \rho_{12}^0 p_{21}^{\Delta}\sin(\omega t) \quad (65)$$

where

$$\rho_{12}^0 = k_{12}^0 1^0 = k_{21}^0 2^0 \quad (66)$$

$$p_{21}^{\Delta} = \frac{k_{21}^{\Delta}}{k_{21}^{h\nu,0}+k_{21}^{\Delta}}. \quad (67)$$

ρ_{12}^0 and p_{21}^{Δ} designate the steady-state rate of reaction (1) and the relative thermal contribution to **2** relaxation upon illuminating at I^0.

Beyond the relaxation time τ_{12}^0, one enters into a permanent regime in which the respective contributions of the in- and out-phase terms $2^{1,in}$ and $2^{1,out}$ such that $2^1(t) = 2^{1,in}\sin(\omega t)+2^{1,out}\cos(\omega t)$ respectively obey**

$$2^{1,in} = -1^{1,in} = \rho_{12}^0\tau_{12}^0 p_{21}^{\Delta}\frac{1}{1+\left(\omega\tau_{12}^0\right)^2} \quad (71)$$

$$2^{1,out} = -1^{1,out} = -\rho_{12}^0\tau_{12}^0 p_{21}^{\Delta}\frac{\omega\tau_{12}^0}{1+\left(\omega\tau_{12}^0\right)^2}. \quad (72)$$

Upon noting that

$$\rho_{12}^0\tau_{12}^0 = \frac{K_{12}^0}{\left(1+K_{12}^0\right)^2}P_{tot}, \quad (73)$$

** Alternatively, one has

$$2^1(t) = \frac{\rho_{12}^0\tau_{12}^0 p_{21}^{\Delta}}{\sqrt{1+\left(\omega\tau_{12}^0\right)^2}}\sin(\omega t-\phi_{12}) \quad (68)$$

with

$$\cos\phi_{12} = \frac{1}{\sqrt{1+\left(\omega\tau_{12}^0\right)^2}} \quad (69)$$

$$\sin\phi_{12} = \frac{\omega\tau_{12}^0}{\sqrt{1+\left(\omega\tau_{12}^0\right)^2}}. \quad (70)$$

Eqs.(71,72) become

$$2^{1,in} = -1^{1,in} = p_{21}^{\Delta}\frac{K_{12}^{0}}{\left(1+K_{12}^{0}\right)^{2}}\frac{1}{1+\left(\omega\tau_{12}^{0}\right)^{2}}P_{tot} \tag{74}$$

$$2^{1,out} = -1^{1,out} = -p_{21}^{\Delta}\frac{K_{12}^{0}}{\left(1+K_{12}^{0}\right)^{2}}\frac{\omega\tau_{12}^{0}}{1+\left(\omega\tau_{12}^{0}\right)^{2}}P_{tot} \tag{75}$$

Expression of the overall observable from the photoswitchable probe In the case of a sinusoidal modulation of light intensity obeying Eq.(58), the temporal dependence of the overall observable $O(t)$ originates from the temporal dependence of $1^1(t)$ and $2^1(t)$ (given in Eqs.(74,75))

$$O(t) = Q_1 1 + Q_2 2 = O^0 + O^{1,in}\sin(\omega t) + O^{1,out}\cos(\omega t) \tag{76}$$

with

$$O^{1,in} = (Q_2 - Q_1)\, 2^{1,in}\varepsilon \tag{77}$$

$$O^{1,out} = (Q_2 - Q_1)\, 2^{1,out}\varepsilon. \tag{78}$$

Expression of the fluorescence intensity Fluorescence emission $I_F(t)$ is extracted from Eq.(56) by using the temporal dependence (58) of the exciting light source and the expressions of 1 and 2 from Eqs.(49,50) and (61,62). Retaining only the terms up to the first order in the perturbation in the expression

$$I_F(t) = \left[O^0 + O^{1,in}\sin(\omega t) + O^{1,out}\cos(\omega t)\right] I^0 \left[1 + \varepsilon\sin(\omega t)\right] \tag{79}$$

yields[††]

$$I_F(t) = I_F^0 + I_F^{1,in}\sin(\omega t) + I_F^{1,out}\cos(\omega t) \tag{83}$$

with

$$I_F^0 = \left(Q_1 1^0 + Q_2 2^0\right) I^0 \tag{84}$$

$$I_F^{1,in} = \varepsilon\left[\left(Q_1 1^0 + Q_2 2^0\right) + (Q_2 - Q_1)\, 2^{1,in}\right] I^0 = \varepsilon\left[I_F^0 + (Q_2 - Q_1)\, 2^{1,in} I^0\right] \tag{85}$$

$$I_F^{1,out} = \varepsilon\,(Q_2 - Q_1)\, 2^{1,out} I^0. \tag{86}$$

[††] Similarly, using Eq.(68), Eq.(76) can be rewritten to explicit the phase delay between the fluorescence emission and the exciting light :

$$Q_1 1 + Q_2 2 = O^0 + \varepsilon\,(Q_2 - Q_1)\frac{\rho_{12}^0\tau_{12}^0 p_{21}^{\Delta}}{\sqrt{1+\left(\omega\tau_{12}^0\right)^2}}\sin(\omega t - \phi_{12}) \tag{80}$$

Therefore, the temporal dependence of the fluorescence emission given in Eq.(83) becomes :

$$I_F(t) = I_F^0\left[1 + \varepsilon\sin(\omega t) + \varepsilon R_{12}^0\sin(\omega t - \phi_{12})\right] \tag{81}$$

with

$$R_{12}^0 = \frac{Q_2 - Q_1}{Q_1 1^0 + Q_2 2^0}\frac{\rho_{12}^0\tau_{12}^0 p_{21}^{\Delta}}{\sqrt{1+\left(\omega\tau_{12}^0\right)^2}} \tag{82}$$

2.3.2 Square wave modulation of small amplitude

Expression of the concentrations We now consider that the system is submitted to a weak square wave modulation of illumination around the averaged value I^0. We correspondingly adopt

$$I(t) = I^0\left\{1+\frac{4\varepsilon}{\pi}\sum_{p=0}^{\infty}\frac{1}{2p+1}\sin\left[(2p+1)\,\omega t\right]\right\} \tag{87}$$

by choosing the starting time ($t = 0$) in this expansion halfway through the first pulse with $\varepsilon \ll 1$. The equations (42,43) are then solved at first order of the light perturbation upon introducing

$$k_{12}(t) = k_{12}^{h\nu,0}\left\{1+\frac{4\varepsilon}{\pi}\sum_{p=0}^{\infty}\frac{1}{2p+1}\sin\left[(2p+1)\,\omega t\right]\right\} \tag{88}$$

$$k_{21}(t) = k_{21}^{h\nu,0}\left\{1+\frac{4\varepsilon}{\pi}\sum_{p=0}^{\infty}\frac{1}{2p+1}\sin\left[(2p+1)\,\omega t\right]\right\}+k_{21}^{\Delta} \tag{89}$$

$$2 = 2^0+\varepsilon\sum_{p=0}^{\infty}2^1_{(2p+1)} \tag{90}$$

$$1 = 1^0-\varepsilon\sum_{p=0}^{\infty}2^1_{(2p+1)} \tag{91}$$

to yield

$$\sum_{p=0}^{\infty}\frac{d2^1_{(2p+1)}}{dt}+\frac{1}{\tau_{12}^0}\sum_{p=0}^{\infty}2^1_{(2p+1)} = \rho_{12}^0 p_{21}^{\Delta}\frac{4}{\pi}\sum_{p=0}^{\infty}\frac{1}{2p+1}\sin\left[(2p+1)\,\omega t\right]. \tag{92}$$

Beyond the relaxation time τ_{12}^0, one enters into a permanent regime in which the respective contributions of the in- and out-phase terms $2^{1,in}_{(2p+1)}$ and $2^{1,out}_{(2p+1)}$ such that $2^1_{(2p+1)}(t) = 2^{1,in}_{(2p+1)}\sin\left[(2p+1)\,\omega t\right] + 2^{1,out}_{(2p+1)}\cos\left[(2p+1)\,\omega t\right]$ respectively obey

$$2^{1,in}_{(2p+1)} = -1^{1,in}_{(2p+1)} = \rho_{12}^0\tau_{12}^0 p_{21}^{\Delta}\frac{4}{\pi}\frac{1}{2p+1}\frac{1}{1+(2p+1)^2\left(\omega\tau_{12}^0\right)^2} \tag{93}$$

$$2^{1,out}_{(2p+1)} = -1^{1,out}_{(2p+1)} = -\rho_{12}^0\tau_{12}^0 p_{21}^{\Delta}\frac{4}{\pi}\frac{1}{2p+1}\frac{(2p+1)\,\omega\tau_{12}^0}{1+(2p+1)^2\left(\omega\tau_{12}^0\right)^2}. \tag{94}$$

Expression of the overall observable from the photoswitchable probe In the case of a square wave modulation of light intensity obeying Eq.(87), the temporal dependence of the overall observable $O(t)$ originates from the temporal dependence of $1^1_{(2p+1)}(t)$ and $2^1_{(2p+1)}(t)$ (given in Eqs.(93,94))

$$O(t) = Q_1 1+Q_2 2 = O^0+\sum_{p=0}^{\infty}\left\{O^{1,in}_{(2p+1)}\sin\left[(2p+1)\,\omega t\right]+O^{1,out}_{(2p+1)}\cos\left[(2p+1)\,\omega t\right]\right\} \tag{95}$$

with

$$O^{1,in}_{(2p+1)} = \left(Q_2-Q_1\right)2^{1,in}_{(2p+1)}\varepsilon \tag{96}$$

$$O^{1,out}_{(2p+1)} = \left(Q_2-Q_1\right)2^{1,out}_{(2p+1)}\varepsilon. \tag{97}$$

Expression of the fluorescence intensity Fluorescence emission $I_F(t)$ is extracted from Eq.(56) by using the temporal dependence (87) of the exciting light source and the expressions of 1 and 2 from Eqs.(49,50) and (90,91). Retaining only the terms up to the first order in the perturbation in the expression

$$\begin{aligned} I_F(t) = I^0 & \left[O^0 + \sum_{p=0}^{\infty} \left[O^{1,in}_{(2p+1)} \sin\left[(2p+1)\,\omega t\right] + O^{1,out}_{(2p+1)} \cos\left[(2p+1)\,\omega t\right] \right] \right] \times \\ & \left[1 + \frac{4\varepsilon}{\pi} \sum_{p=0}^{\infty} \frac{1}{2p+1} \sin\left[(2p+1)\,\omega t\right] \right] \end{aligned} \quad (98)$$

yields

$$I_F(t) = I_F^0 + \sum_{p=0}^{\infty} \left[I^{1,in}_{F,(2p+1)} \sin\left[(2p+1)\,\omega t\right] + I^{1,out}_{F,(2p+1)} \cos\left[(2p+1)\,\omega t\right] \right] \quad (99)$$

with

$$I^{1,in}_{F,(2p+1)} = \varepsilon \left[\frac{4}{\pi} \frac{1}{2p+1} I_F^0 + (Q_2 - Q_1)\, 2^{1,in}_{(2p+1)} I^0 \right] \quad (100)$$

$$I^{1,out}_{F,(2p+1)} = \varepsilon\,(Q_2 - Q_1)\, 2^{1,out}_{(2p+1)} I^0. \quad (101)$$

2.3.3 Sinusoidal modulation of large amplitude

Expression of the concentrations We now consider that the system is submitted to a large sinusoidal modulation of illumination around the averaged value I^0. We adopt

$$I(t) = I^0 \left[1 + \alpha \sin(\omega t)\right]. \quad (102)$$

Then one has

$$k_{12}^{h\nu}(t) = k_{12}^{h\nu,0} \left[1 + \alpha \sin(\omega t)\right] \quad (103)$$

$$k_{21}^{h\nu}(t) = k_{21}^{h\nu,0} \left[1 + \alpha \sin(\omega t)\right]. \quad (104)$$

The equations (42,43) are solved upon introducing:

$$2 = 2^0 + \alpha f(t) \quad (105)$$

$$1 = 1^0 - \alpha f(t) \quad (106)$$

$$k_{12}(t) = k_{12}^{h\nu,0} \left[1 + \alpha \sin(\omega t)\right] \quad (107)$$

$$k_{21}(t) = k_{21}^{h\nu,0} \left[1 + \alpha \sin(\omega t)\right] + k_{21}^{\Delta} \quad (108)$$

to yield

$$\frac{df(t)}{dt} = -\frac{1}{\tau_{12}^0} f(t) + \rho_{12}^0 p_{21}^{\Delta} \sin(\omega t) - \alpha \left(k_{12}^{h\nu,0} + k_{21}^{h\nu,0}\right) f(t) \sin(\omega t). \quad (109)$$

Upon introducing

$$
\begin{aligned}
x &= \frac{t}{\tau_{12}^{0}} && (110)\\
a &= \rho_{12}^{0} p_{21}^{\Delta} \tau_{12}^{0} && (111)\\
b &= \alpha \left(k_{12}^{h\nu,0} + k_{21}^{h\nu,0} \right) \tau_{12}^{0} && (112)\\
\theta &= \omega \tau_{12}^{0} && (113)
\end{aligned}
$$

Eq.(109) becomes

$$
\frac{df(\theta x)}{dx} = -f(\theta x) + \left[a - bf(\theta x) \right] \sin(\theta x) . \qquad (114)
$$

Beyond the relaxation time τ_{12}^{0}, one enters into a permanent regime in which $f(\theta x)$ is a continuous periodic function. Then $f(\theta x)$ can be expressed as a Fourier series

$$
f(\theta x) = a_0 + \sum_{n=1}^{+\infty} \left[a_n \cos(n\theta x) + b_n \sin(n\theta x) \right] \qquad (115)
$$

where a_n and b_n designate the amplitudes of the n-th components of the Fourier series. The a_n and b_n terms can be extracted from Eq.(114) upon identifying the amplitudes of the components of the same order. We derived

- Zeroth order:

$$
a_0 = -b\frac{b_1}{2} \qquad (116)
$$

- First order:

$$
\begin{aligned}
-a_1\theta &= -b_1 + a - a_0 b + b\frac{a_2}{2} && (117)\\
b_1\theta &= -a_1 - b\frac{b_2}{2} && (118)
\end{aligned}
$$

- Order $n > 1$:

$$
\begin{aligned}
a_n n\theta &= b_n - \frac{b}{2}\left(a_{n+1} - a_{n-1}\right) && (119)\\
b_n n\theta &= -a_n - \frac{b}{2}\left(b_{n+1} - b_{n-1}\right) && (120)
\end{aligned}
$$

from which we obtained the following expressions of the concentrations in **1** and **2**:

$$
\begin{aligned}
2 &= 2^0 + \alpha \left\{ a_0 + \sum_{n=1}^{+\infty} \left[a_n \cos(n\theta x) + b_n \sin(n\theta x) \right] \right\} && (121)\\
1 &= 1^0 - \alpha \left\{ a_0 + \sum_{n=1}^{+\infty} \left[a_n \cos(n\theta x) + b_n \sin(n\theta x) \right] \right\} . && (122)
\end{aligned}
$$

Hence, at steady-state, a large sinusoidal modulation of illumination causes modulation of the concentrations in **1** and **2** at an infinite number of radial frequencies.

Eqs.(121,122) can be transformed to explicit the amplitudes of the concentration modulations at all radial frequencies. Thus we write

$$\begin{aligned} 2 &= \mathfrak{2}^{\mathfrak{o}} + \alpha \sum_{n=1}^{+\infty} \left[\mathfrak{2}^{\mathfrak{n,in}} \sin(n\omega t) + \mathfrak{2}^{\mathfrak{n,out}} \cos(n\omega t) \right] && (123) \\ 1 &= \mathfrak{1}^{\mathfrak{o}} - \alpha \sum_{n=1}^{+\infty} \left[\mathfrak{2}^{\mathfrak{n,in}} \sin(n\omega t) + \mathfrak{2}^{\mathfrak{n,out}} \cos(n\omega t) \right] && (124) \end{aligned}$$

and conversely

$$\begin{aligned} 2 &= \mathfrak{2}^{\mathfrak{o}} - \alpha \sum_{n=1}^{+\infty} \left[\mathfrak{1}^{\mathfrak{n,in}} \sin(n\omega t) + \mathfrak{1}^{\mathfrak{n,out}} \cos(n\omega t) \right] && (125) \\ 1 &= \mathfrak{1}^{\mathfrak{o}} + \alpha \sum_{n=1}^{+\infty} \left[\mathfrak{1}^{\mathfrak{n,in}} \sin(n\omega t) + \mathfrak{1}^{\mathfrak{n,out}} \cos(n\omega t) \right] && (126) \end{aligned}$$

where

$$\begin{aligned} \mathfrak{2}^{\mathfrak{o}} &= 2^0 + \alpha a_0 && (127) \\ \mathfrak{1}^{\mathfrak{o}} &= 1^0 - \alpha a_0 && (128) \\ \mathfrak{2}^{\mathfrak{n,in}} &= -\mathfrak{1}^{\mathfrak{n,in}} = b_n && (129) \\ \mathfrak{2}^{\mathfrak{n,out}} &= -\mathfrak{1}^{\mathfrak{n,out}} = a_n. && (130) \end{aligned}$$

In the case of sinusoidal light modulation of small amplitude, $2^{1,out}$ is optimal when the resonance conditions (14,15) are fulfilled. In the absence of analytical expressions for $\mathfrak{2}^{\mathfrak{1,out}}$, such conclusions cannot be directly derived in the case of a sinusoidal modulation of large amplitude, so we evaluated their relevance by means of numerical calculations.

We first analyzed the dependence of $\mathfrak{1}^{\mathfrak{1,out}} = -\mathfrak{2}^{\mathfrak{1,out}} = -a_1$ on the control parameters ω and I^0. To do so, we analytically retrieved the $2n+1$ unknown parameters (a_0,...,a_n,b_n) upon truncating the Fourier expansion (30) at increasing orders n. Figure S6 displays representative results, which have been obtained with $n = 5$.

Figure S7 displays the dependence of the normalized amplitude, $\mid \mathfrak{1}_{\mathfrak{norm}}^{\mathfrak{1,out}} \mid = \mid \mathfrak{1}^{\mathfrak{1,out}}/P_{tot} \mid$, on the light flux I^0 and the adimensional radial frequency $\omega\tau_{12}^0$ when $\alpha = 1$. Truncation of the Fourier expansion of the $f(\theta x)$ function at the fifth order ($n = 5$) is definitively sufficient to observe convergence: the dependence of $\mid \mathfrak{1}_{\mathfrak{norm}}^{\mathfrak{1,out}} \mid$ on I^0 and ω does not significantly evolve beyond $n = 3$. $\mid \mathfrak{1}_{\mathfrak{norm}}^{\mathfrak{1,out}} \mid$ exhibits an optimum in the space (I^0,ω), which position and amplitude are very close to those observed with a sinusoidal modulation of small amplitude (Table 1).

Note that the error done when taking the analytical expression of the resonance conditions, valid only for a modulation of small amplitude, is always less than 20 %, no matter which amplitude α is used. Such an error would be of the order of magnitude of the experimental errors done when fixing the average light intensity and radial frequency to their values at resonance, $I^{0,R}$ and ω^R.

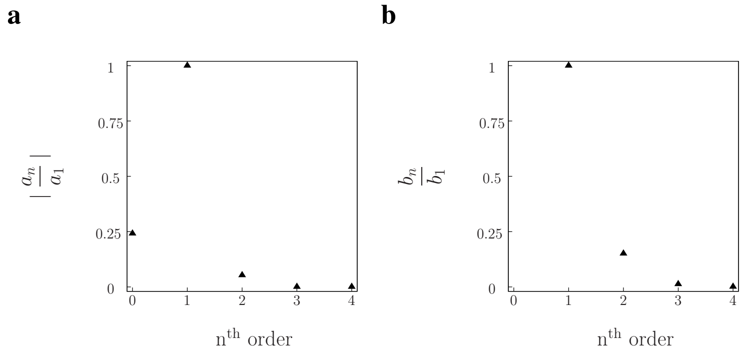

Figure S6: Computation of the amplitudes of the Fourier terms, $\mid a_n \mid$ (**a**) and b_n (**b**), from a solution of a photoswitchable fluorophore **1** $\rightleftharpoons$ **2** submitted to light harmonic forcing in the regime of large (α = 1) amplitude modulation. The numerical computation has been performed upon truncating the Fourier f expansion at the fifth order ($n = 5$). σ_{12} = 73 m^2.mol^{-1}, σ_{21} = 84 m^2.mol^{-1}, $k_{21}^{\Delta} = 1.5 \times 10^{-2}$ s^{-1}, $I^0 = 9.6 \times 10^{-5}$ ein·s^{-1}·m^{-2} and $\omega\tau_{12}^0$ = 1.

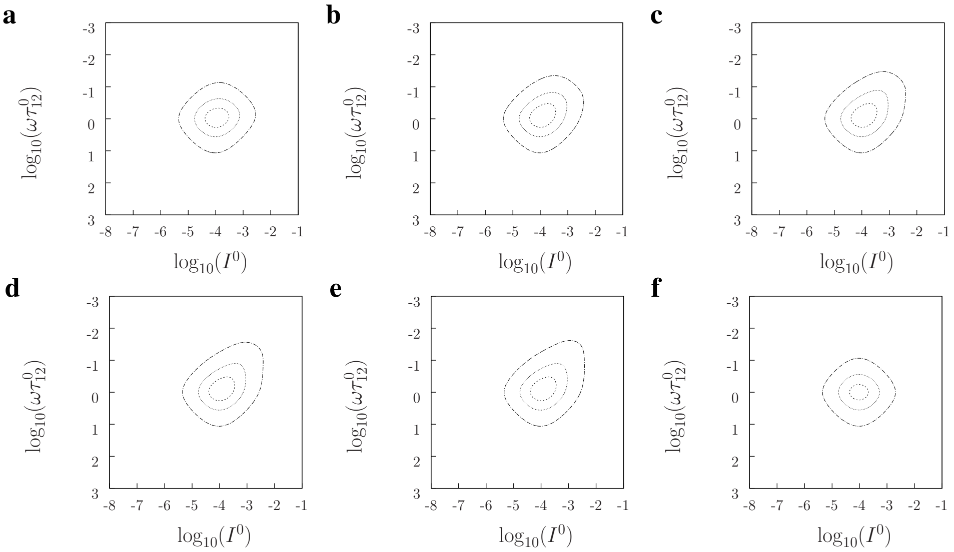

Figure S7: Theoretical dependence of the normalized amplitude of the out-of-phase oscillations in **1** concentration, $\mid \mathfrak{1}_{\mathfrak{norm}}^{\mathfrak{1,out}} \mid = \mid \mathfrak{1}^{\mathfrak{1,out}}/P_{tot} \mid$, of a photoswitchable fluorophore **1** $\rightleftharpoons$ **2** submitted to light harmonic forcing in the regime of large amplitude modulation (α = 1) on the light flux I^0 (in ein·s^{-1}·m^{-2}) and the adimensional radial frequency $\omega\tau_{12}^0$. The numerical computation has been performed upon truncating the Fourier $f(\theta x)$ expansion at various orders n (**a**: 1, **b**: 2, **c**: 3, **d**: 4, **e**: 5). The dependence observed in a regime of small amplitude modulation, $\mid 1_{norm}^{1,out} \mid$, is shown in **f**. σ_{12} = 73 m^2.mol^{-1}, σ_{21} = 84 m^2.mol^{-1}, $k_{21}^{\Delta} = 1.5 \times 10^{-2}$ s^{-1}. The markers correspond to isodensity curves : 0.01 (dot dashed), 0.03 (dot) and 0.05 (dashed).

Expression of the overall observable from the photoswitchable probe In the case of a sinusoidal modulation of large amplitude obeying Eq.(102), the temporal dependence of the overall observable $O(t)$ originates from the temporal dependence of $1^1(t)$ and $2^1(t)$ (given in Eqs.(123,124))

$$O(t) \quad = \quad Q_1 1 + Q_2 2 = \mathfrak{O}^{\mathfrak{o}} + \sum_{n=1}^{\infty} \left[\mathfrak{O}^{\mathfrak{n,in}} \sin(n\omega t) + \mathfrak{O}^{\mathfrak{n,out}} \cos(n\omega t) \right], \tag{131}$$

Amplitude	n	$10^4 \times I^{0,R}$ (ein·s^{-1}·m^{-2})	$10^2 \times \omega^R$ (rad·s^{-1})	$10^2\times \mid \mathfrak{1}^{\mathfrak{1,out}}_{\mathfrak{norm}} \mid$
Small	–	0.96	3.02	5.81
Large	1	1.12	3.02	6.25
Large	2	1.19	2.82	6.38
Large	3	1.19	2.82	6.38
Large	4	1.19	2.82	6.38
Large	5	1.19	2.82	6.38

Table 1: Coordinates and amplitude of the $\mid \mathfrak{1}^{\mathfrak{1,out}}_{\mathfrak{norm}} \mid$ extremum from a photoswitchable fluorophore **1** $\rightleftharpoons$ **2** submitted to light harmonic forcing in the regime of large amplitude modulation (α = 1) as a function of the truncation order n of the Fourier expansion of the $f(\theta x)$ function. The Table also provides the coordinates and the amplitude of $\mid 1^{1,out}_{norm} \mid$ extremum observed in a regime of small amplitude modulation.

with

$$\mathfrak{O}^{\mathfrak{o}} = Q_1\mathfrak{1}^{\mathfrak{o}} + Q_2\mathfrak{2}^{\mathfrak{o}} = Q_1 1^0 + Q_2 2^0 + (Q_2 - Q_1)\,\alpha a_0 \tag{132}$$

$$\mathfrak{O}^{\mathfrak{n,in}} = (Q_2 - Q_1)\,\alpha b_n \tag{133}$$

$$\mathfrak{O}^{\mathfrak{n,out}} = (Q_2 - Q_1)\,\alpha a_n \tag{134}$$

for $n > 0$.

Expression of the fluorescence intensity Fluorescence emission $I_F(t)$ is extracted from Eq.(56) by using the temporal dependence (102) of the exciting light source and the expression of $O(t)$ given in Eq.(131). Then writing

$$I_F(t) = \mathfrak{I}^{\mathfrak{o}}_{\mathfrak{F}} + \sum_{n=1}^{\infty}\left[\mathfrak{I}^{\mathfrak{n,in}}_{\mathfrak{F}} \sin(n\omega t) + \mathfrak{I}^{\mathfrak{n,out}}_{\mathfrak{F}} \cos(n\omega t)\right] \tag{135}$$

we derive

$$\mathfrak{I}^{\mathfrak{o}}_{\mathfrak{F}} = \left(\mathfrak{O}^{\mathfrak{o}} + \frac{1}{2}\alpha\mathfrak{O}^{\mathfrak{1,in}}\right) I^0 \tag{136}$$

$$\mathfrak{I}^{\mathfrak{1,in}}_{\mathfrak{F}} = \left(\alpha\mathfrak{O}^{\mathfrak{o}} + \mathfrak{O}^{\mathfrak{1,in}} - \frac{1}{2}\alpha\mathfrak{O}^{\mathfrak{2,out}}\right) I^0 \tag{137}$$

$$\mathfrak{I}^{\mathfrak{1,out}}_{\mathfrak{F}} = \left(\mathfrak{O}^{\mathfrak{1,out}} + \frac{1}{2}\alpha\mathfrak{O}^{\mathfrak{2,in}}\right) I^0 \tag{138}$$

$$\mathfrak{I}^{\mathfrak{n,in}}_{\mathfrak{F}} = \left[\mathfrak{O}^{\mathfrak{n,in}} + \frac{1}{2}\alpha\left(\mathfrak{O}^{\mathfrak{n-1,out}} - \mathfrak{O}^{\mathfrak{n+1,out}}\right)\right] I^0 \tag{139}$$

$$\mathfrak{I}^{\mathfrak{n,out}}_{\mathfrak{F}} = \left[\mathfrak{O}^{\mathfrak{n,out}} + \frac{1}{2}\alpha\left(\mathfrak{O}^{\mathfrak{n+1,in}} - \mathfrak{O}^{\mathfrak{n-1,in}}\right)\right] I^0 \tag{140}$$

for $n > 1$. As shown in Eqs.(136–140), a large sinusoidal modulation of illumination is expected to cause modulation of the fluorescence intensity at an infinite number of radial frequencies, which are integer multiples of ω.

The zeroth order term $\mathfrak{I}^{\mathfrak{o}}_{\mathfrak{F}}$ can be expressed using Eqs.(84,112,116,129,133,136). We obtained

$$\mathfrak{I}^{\mathfrak{o}}_{\mathfrak{F}} = I_F^0 + \frac{1}{2}\alpha^2 (Q_2 - Q_1)\left[1 - \left(k_{12}^{h\nu,0} + k_{21}^{h\nu,0}\right)\tau_{12}^0\right] \mathfrak{2}^{\mathfrak{1,in}} I^0. \tag{141}$$

In contrast to the out-of-phase first-order response, Eq.(141) shows that the zeroth order response of the fluorescence emission upon sinusoidal light modulation of large amplitude significantly departs from I_F^0, which is observed in the case of a same type of modulation but in a regime of small amplitude.

The first order terms can be expressed using Eqs.(84, 129, 130, 133, 134, 137) and (129, 130, 133, 134, 138) to write

$$\mathfrak{I}_{\mathfrak{F}}^{\mathfrak{1,in}} = \alpha I_F^0 + \alpha \left(Q_2 - Q_1\right) \mathfrak{z}^{\mathfrak{1,in}} I^0 \left[1 - \frac{1}{2}\alpha^2 \left(k_{12}^{h\nu,0} + k_{21}^{h\nu,0}\right) \tau_{12}^0\right] - \frac{1}{2}\alpha^2 \left(Q_2 - Q_1\right) \mathfrak{z}^{\mathfrak{2,out}} I^0 \quad (142)$$

$$\mathfrak{I}_{\mathfrak{F}}^{\mathfrak{1,out}} = \alpha \left(Q_2 - Q_1\right) \mathfrak{z}^{\mathfrak{1,out}} I^0 + \frac{1}{2}\alpha^2 \left(Q_2 - Q_1\right) \mathfrak{z}^{\mathfrak{2,in}} I^0. \quad (143)$$

In reference to the $g\left(\mathfrak{z}^{\mathfrak{n,in}}, \mathfrak{z}^{\mathfrak{n,out}}\right)$ function introduced in the Main Text, one has thus

$$g\left(\mathfrak{z}^{\mathfrak{n,in}}, \mathfrak{z}^{\mathfrak{n,out}}\right) = \frac{1}{2}\alpha \mathfrak{z}^{\mathfrak{2,in}}. \quad (144)$$

To evaluate the possible interference originating from the second order term $g\left(\mathfrak{z}^{\mathfrak{n,in}}, \mathfrak{z}^{\mathfrak{n,out}}\right)$, we used Eq.(40) to numerically compute the dependence of $\mathfrak{I}_{\mathfrak{F}}^{\mathfrak{1,out}}$ on ω and I^0. Figure S8 compares the absolute value of the normalized out-of-phase first-order amplitude $\mid \mathfrak{I}_{\mathfrak{F},\mathfrak{norm}}^{\mathfrak{1,out}} \mid = \mid \mathfrak{I}_{\mathfrak{F}}^{\mathfrak{1,out}}/(Q_2 - Q_1) I^0 \alpha P_{tot} \mid$ obtained in the case of the largest amplitude modulation ($\alpha = 1$) with that obtained for a modulation of small amplitude. The position and the amplitude of the optimum are similar in both cases: we found $I^{0,R} = 1.03 \times 10^{-4}$ ein·s^{-1}·m^{-2}, $\omega^R = 3.09 \times 10^{-2}$rad·s^{-1}, and $\mid \mathfrak{I}_{\mathfrak{F},\mathfrak{norm}}^{\mathfrak{1,out}} \mid = 5.82 \times 10^{-2}$ in the case of a sinusoidal modulation of large amplitude, and $I^{0,R} = 0.96 \times 10^{-4}$ ein·s^{-1}·m^{-2}, $\omega^R = 3.02 \times 10^{-2}$rad·s^{-1}, and $\mid I_{F,norm}^{1,out} \mid = 5.81 \times 10^{-2}$ in the case of a sinusoidal modulation of small amplitude.

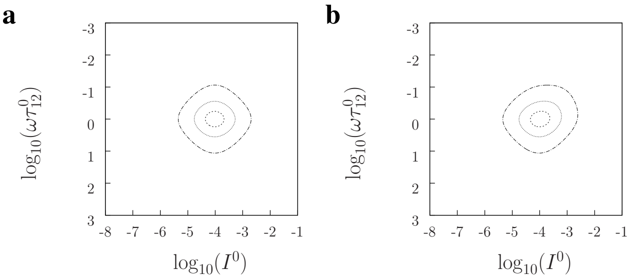

Figure S8: Theoretical dependence of the absolute value of the normalized amplitude of the out-of-phase oscillations of fluorescence intensity, $\mid \mathfrak{I}_{\mathfrak{F},\mathfrak{norm}}^{\mathfrak{1,out}} \mid = \mid \mathfrak{I}_{\mathfrak{F}}^{\mathfrak{1,out}}/(Q_2 - Q_1) I^0 \alpha P_{tot} \mid$, from a solution of a photoswitchable fluorophore **1** $\rightleftharpoons$ **2** submitted to light harmonic forcing in the regime of small (**a**) or large (**b**; α = 1) amplitude modulation on the light flux I^0 (in ein·s^{-1}·m^{-2}) and the adimensional radial frequency $\omega\tau_{12}^0$. The numerical computation has been performed upon truncating the Fourier f expansion at the fifth order ($n = 5$). σ_{12} = 73 m^2.mol^{-1}, σ_{21} = 84 m^2.mol^{-1}, $k_{21}^{\Delta} = 1.5 \times 10^{-2}$ s^{-1}. The markers correspond to isodensity curves : 0.01 (dot dashed), 0.03 (dot) and 0.05 (dashed).

2.3.4 Square wave modulation of large amplitude

Expression of the concentrations We eventually consider that the system is submitted to a square wave modulation of illumination of large amplitude. We correspondingly adopt

$$I(t) = I^0 \left\{ 1 + \frac{4\alpha}{\pi} \sum_{p=0}^{\infty} \frac{1}{2p+1} \sin\left[(2p+1)\,\omega t\right] \right\} \tag{145}$$

by choosing the starting time ($t = 0$) in this expansion halfway through the first pulse.

The equations (42,43) are then solved upon introducing

$$2 = 2^0 + \alpha f(t) \tag{146}$$

$$1 = 1^0 - \alpha f(t) \tag{147}$$

$$k_{12}(t) = k_{12}^{h\nu,0} \left\{ 1 + \frac{4\alpha}{\pi} \sum_{p=0}^{\infty} \frac{1}{2p+1} \sin\left[(2p+1)\,\omega t\right] \right\} \tag{148}$$

$$k_{21}(t) = k_{21}^{h\nu,0} \left\{ 1 + \frac{4\alpha}{\pi} \sum_{p=0}^{\infty} \frac{1}{2p+1} \sin\left[(2p+1)\,\omega t\right] \right\} + k_{21}^{\Delta} \tag{149}$$

to yield

$$\frac{df(t)}{dt} = -\frac{f(t)}{\tau_{12}^0} + \left[\rho_{12}^0 p_{21}^{\Delta} - \alpha \left(k_{12}^{h\nu,0} + k_{21}^{h\nu,0}\right) f(t)\right] \frac{4}{\pi} \sum_{p=0}^{\infty} \frac{1}{2p+1} \sin\left[(2p+1)\,\omega t\right]. \tag{150}$$

Upon introducing x, a, b, and θ given in Eqs.(110–113), Eq.(150) becomes

$$\frac{df(\theta x)}{dx} = -f(\theta x) + \left[a - bf(\theta x)\right] \frac{4}{\pi} \sum_{p=0}^{\infty} \frac{1}{2p+1} \sin\left[(2p+1)\,\theta x\right] \tag{151}$$

Beyond the relaxation time τ_{12}^0, one enters into a permanent regime in which $f(\theta x)$ is a continuous periodic function. Adopting again Eq.(115) for its Fourier series, the a_n and b_n terms can be extracted from Eq.(151) upon identifying the amplitudes of the components of the same order. We derived

- Zeroth order:

$$a_0 = -b\frac{2}{\pi}b_1 \tag{152}$$

- First order:

$$-a_1\theta = -b_1 + \frac{4}{\pi}\left(a - a_0 b\right) + b\frac{2}{\pi} \sum_{p=1}^{\infty} \frac{a_{2p}}{2p-1} \tag{153}$$

$$b_1\theta = -a_1 - b\frac{2}{\pi} \sum_{p=1}^{\infty} \frac{b_{2p}}{2p-1} \tag{154}$$

- Even order $n = 2k$ with $k \in \mathbb{N}^{\star}$:

$$a_{2k} 2k\theta = b_{2k} + b\frac{2}{\pi}\left[\sum_{p=0}^{k-1}\frac{a_{2k-(2p+1)}}{2p+1} - \sum_{p=0}^{\infty}\frac{a_{2k+2p+1}}{2p+1}\right] \quad (155)$$

$$b_{2k} 2k\theta = -a_{2k} - b\frac{2}{\pi}\left[\sum_{p=0}^{\infty}\frac{b_{2k+2p+1}}{2p+1} - \sum_{p=0}^{k-1}\frac{b_{2k-(2p+1)}}{2p+1}\right] \quad (156)$$

- Odd order $n = 2k+1$ with $k \in \mathbb{N}^{\star}$:

$$a_{2k+1}\left(2k+1\right)\theta = b_{2k+1} + \frac{4}{\pi\left(2k+1\right)}\left(a_0 b - a\right) + b\frac{2}{\pi}\left[\sum_{p=0}^{k-1}\frac{a_{2(k-p)}}{2p+1} - \sum_{p=0}^{\infty}\frac{a_{2(k+p+1)}}{2p+1}\right] \quad (157)$$

$$b_{2k+1}\left(2k+1\right)\theta = -a_{2k+1} - b\frac{2}{\pi}\left[\sum_{p=0}^{\infty}\frac{b_{2(k+p+1)}}{2p+1} - \sum_{p=0}^{k-1}\frac{b_{2(k-p)}}{2p+1}\right] \quad (158)$$

from which we can retrieve the expressions of the concentrations in **1** and **2** using Eqs.(121,122). At steady-state, as for the sinusoidal modulation of large amplitude, square wave modulation causes modulation of the concentrations in **1** and **2** at an infinite number of radial frequencies. Eqs.(121,122) can be subsequently transformed to explicit the amplitudes of the concentration modulations at all radial frequencies using Eqs.(123–130).

We showed that, in the case of sinusoidal light modulation of small amplitude, $2^{1,out}$ is optimal when the resonance conditions (14,15) are fulfilled. In the absence of analytical expressions for $\mathtt{2}^{\mathtt{1,out}}$, such conclusions cannot be directly derived in the case of a square wave modulation of large amplitude, so we evaluated their relevance by means of numerical calculations. Compared to the sinusoidal modulation, square wave modulation introduces harmonics at higher frequencies, which could interfere with resonance of the radial frequency. We therefore analyzed the dependence of $\mathtt{1}^{\mathtt{1,out}} = -\mathtt{2}^{\mathtt{1,out}} = -a_1$ on the control parameters, ω and I^0 by analytically retrieving the $2n+1$ unknown parameters (a_0,…,a_n,b_n) upon truncating at the orders p and n in the expansions of the light excitation in Eq.(21) and the $f(\theta x)$ function in Eq.(30). Figure S9 displays representative results, which have been obtained upon truncating at the 3rd and 4th orders the expansions of the light excitation and the $f(\theta x)$ function.

Figure S10 displays the dependence of the normalized amplitude, $\mid \mathtt{1}^{\mathtt{1,out}}_{\mathtt{norm}} \mid = \mid \mathtt{1}^{\mathtt{1,out}}/P_{tot} \mid$, on the light flux I^0 and the adimensional radial frequency $\omega\tau_{12}^0$ when $\alpha = 0.8$ (see also Figure S11 showing that $\mid \mathtt{1}^{\mathtt{1,out}}_{\mathtt{norm}} \mid$ is essentially independent on α).

Truncation in the expansions of the light excitation in Eq.(21) and the $f(\theta x)$ function in Eq.(30) at the 3rd and 4th orders respectively is sufficient to observe convergence: the dependence of $\mid \mathtt{1}^{\mathtt{1,out}}_{\mathtt{norm}} \mid$ on I^0 and ω does not significantly evolve beyond $p = 1$ and $n = 4$. As in the case of sinusoidal modulation of large amplitude, $\mid \mathtt{1}^{\mathtt{1,out}}_{\mathtt{norm}} \mid$ exhibits an optimum in the space (I^0,ω), which position and amplitude are very close to those observed with a sinusoidal modulation of small amplitude (Table 2). Note that the amplitudes are respectively $\mid \mathtt{1}^{\mathtt{1,out}}_{\mathtt{norm}} \mid = 8.16 \times 10^{-2}$ for the square wave modulation of large amplitude and $\frac{4}{\pi} \mid 1^{1,out}_{norm} \mid = 7.40 \times 10^{-2}$ for the modulation of small amplitude ($\frac{4}{\pi}$ is a correcting term resulting from Eq.(21)) (Table 2).

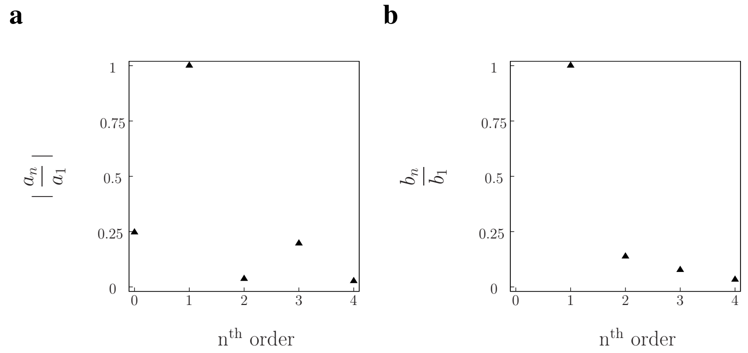

Figure S9: Computation of the normalized amplitude $\mid a_n \mid$ (**a**) and b_n (**b**) from a solution of a photoswitchable fluorophore **1** $\rightleftharpoons$ **2** submitted to square wave forcing (α = 0.8). The numerical computation has been performed upon truncating at the 3rd and 4th truncation orders the expansions of the light excitation and the $f(x)$ function. σ_{12} = 73 m^2.mol^{-1}, σ_{21} = 84 m^2.mol^{-1}, $k_{21}^{\Delta} = 1.5 \times 10^{-2}$ s^{-1}, $I^0 = 9.6 \times 10^{-5}$ ein·s^{-1}·m^{-2} and $\omega\tau_{12}^0$ = 1.

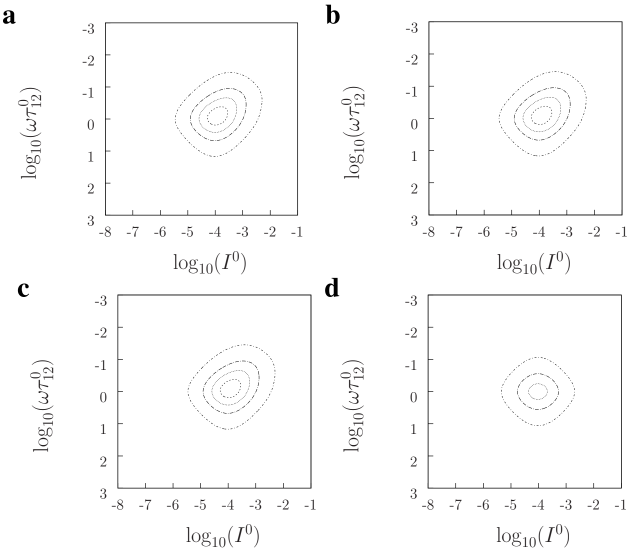

Figure S10: Theoretical dependence of the normalized amplitude of the out-of-phase oscillations in **1** concentration, $\mid \mathtt{1}_{\mathtt{norm}}^{\mathtt{1,out}} \mid = \mid \mathtt{1}^{\mathtt{1,out}}/P_{tot} \mid$, of a photoswitchable fluorophore **1** $\rightleftharpoons$ **2** submitted to light square wave forcing ($\alpha = 0.8$) on the light flux I^0 (in ein·s^{-1}·m^{-2}) and the adimensional radial frequency $\omega\tau_{12}^0$. The numerical computation has been performed upon adopting various values of p and n for the truncation of the orders in the expansions of the light excitation in Eq.(21) and the $f(\theta x)$ function in Eq.(30). $p = 1$ and $n = 4$ (**a**); $p = 2$ and $n = 6$ (**b**); $p = 3$ and $n = 8$ (**c**). The corresponding theoretical dependence of the normalized amplitude of the out-of-phase oscillations of in **1** concentration from a solution of a photoswitchable fluorophore **1** $\rightleftharpoons$ **2** submitted to light harmonic forcing in the regime of small amplitude modulation is displayed in **d** as a reference. σ_{12} = 73 m^2.mol^{-1}, σ_{21} = 84 m^2.mol^{-1}, $k_{21}^{\Delta} = 1.5 \times 10^{-2}$ s^{-1}. The markers correspond to isodensity curves : 0.01 (dot small dashed), 0.03 (dot large dashed), 0.05 (dot) and 0.07 (dashed).

Expression of the overall observable from the photoswitchable probe The expression of the overall observable in the case of a square wave modulation obeying Eq.(145) is identical to the one derived for a sinusoidal modulation. Then Eqs.(131,132,133,134) are here also valid.

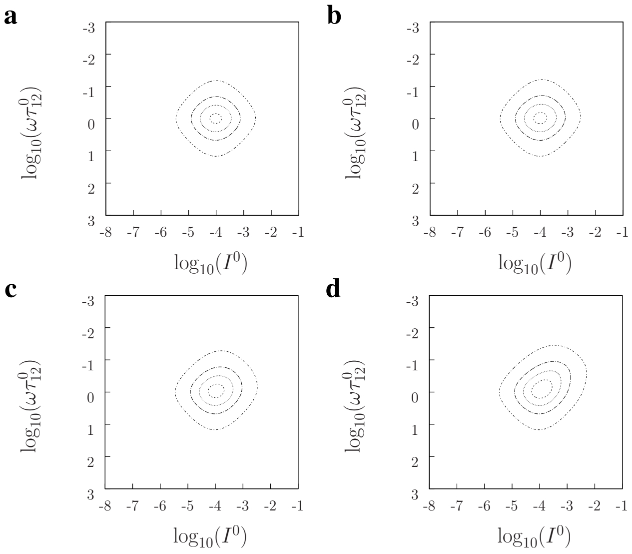

Figure S11: Theoretical dependence of the normalized amplitude of the out-of-phase oscillations in **1** concentration, $\mid \mathfrak{1}^{\mathfrak{1},\mathfrak{out}}_{\mathfrak{norm}} =\mid \mathfrak{1}^{\mathfrak{1},\mathfrak{out}}/P_{tot} \mid$, of a photoswitchable fluorophore $\mathbf{1} \rightleftharpoons \mathbf{2}$ submitted to light square wave forcing on the light flux I^0 (in ein·s^{-1}·m^{-2}) and the adimensional radial frequency $\omega\tau^0_{12}$ for various values of the amplitude modulation α. The numerical computation has been performed upon adopting $p = 1$ and $n = 4$ for the truncation of the orders in the expansions of the light excitation in Eq.(145) and the $f(x)$ function in Eq.(115). $\alpha = 0.2$ (**a**); $\alpha = 0.4$ (**b**); $\alpha = 0.6$ (**c**); $\alpha = 0.8$ (**d**). σ_{12} = 73 m^2.mol^{-1}, σ_{21} = 84 m^2.mol^{-1}, $k^{\Delta}_{21} = 1.5 \times 10^{-2}$ s^{-1}. The markers correspond to isodensity curves : 0.01 (dot small dashed), 0.03 (dot large dashed), 0.05 (dot) and 0.07 (dashed). In contrast to the sinusoidal modulation of large amplitude, we could not numerically compute the behavior at the largest modulation amplitude $\alpha = 1$. This behavior probably originates from the truncation of the expansion of light excitation in Eq.(21). As shown in Figure S5, one observes significant oscillations close to the discontinuity of the square wave function. They most probably generate singularities (e.g. negative values of the concentrations) at too large α values. This explains why we checked that the behavior of the $\mid \mathfrak{1}^{\mathfrak{1},\mathfrak{out}}_{\mathfrak{norm}} \mid$ did not significantly depend on the α value. We correspondingly adopted $\alpha = 0.8$ above.

Expression of the fluorescence intensity Fluorescence emission $I_F(t)$ is extracted from Eq.(56) by using the temporal dependence (145) of the exciting light source and the expression of $O(t)$ given in Eq.(131). Adopting again the expression (135), we derive

- Zeroth order:

$$\mathfrak{I}^{\mathfrak{o}}_{\mathfrak{F}} = \left(\mathfrak{O}^{\mathfrak{o}} + \frac{2\alpha}{\pi}\sum_{p=0}^{\infty}\frac{\mathfrak{O}^{\mathfrak{2p+1},\mathfrak{in}}}{2p+1}\right) I^0 \tag{159}$$

- First order:

$$\mathfrak{I}^{\mathfrak{1},\mathfrak{in}}_{\mathfrak{F}} = \left[\mathfrak{O}^{\mathfrak{1},\mathfrak{in}} + \frac{4\alpha}{\pi}\mathfrak{O}^{\mathfrak{o}} - \frac{2\alpha}{\pi}\left(\sum_{p=0}^{\infty}\frac{\mathfrak{O}^{\mathfrak{2(p+1)},\mathfrak{out}}}{2p+1}\right)\right] I^0 \tag{160}$$

$$\mathfrak{I}^{\mathfrak{1},\mathfrak{out}}_{\mathfrak{F}} = \left[\mathfrak{O}^{\mathfrak{1},\mathfrak{out}} + \frac{2\alpha}{\pi}\left(\sum_{p=0}^{\infty}\frac{\mathfrak{O}^{\mathfrak{2(p+1)},\mathfrak{in}}}{2p+1}\right)\right] I^0 \tag{161}$$

Modulation	p	n	$10^4 \times I^{0,R}$ (ein·s^{-1}·m^{-2})	$10^2 \times \omega^R$ (rad·s^{-1})	$10^2\times \mid \mathfrak{1}^{\mathfrak{1,out}}_{\mathfrak{norm}} \mid$
Sinusoidal	–	–	0.96	3.02	5.81
Square wave	1	4	1.20	2.82	8.16
Square wave	2	6	1.20	2.82	8.16
Square wave	3	8	1.20	2.82	8.16

Table 2: Coordinates and amplitude of the $\mid \mathfrak{1}^{\mathfrak{1,out}}_{\mathfrak{norm}} \mid$ extremum from a photoswitchable fluorophore **1** $\rightleftharpoons$ **2** submitted to light square wave forcing ($\alpha = 0.8$) as a function of the truncation orders p and n in the expansions of the light excitation in Eq.(21) and the $f(\theta x)$ function in Eq.(30). The Table also provides the coordinates and amplitude of $\mid 1^{1,out}_{norm} \mid$ extremum observed in a regime of sinusoidal modulation of small amplitude.

- Even order $n = 2k$ with $k \in \mathbb{N}^\star$:

$$\mathfrak{I}_{\mathfrak{F}}^{\mathfrak{2k,in}} = \left[\mathfrak{O}^{\mathfrak{2k,in}} + \frac{2\alpha}{\pi}\left(\sum_{p=0}^{k-1} \frac{\mathfrak{O}^{\mathfrak{2k-(2p+1),out}}}{2p+1} - \sum_{p=0}^{\infty} \frac{\mathfrak{O}^{\mathfrak{2k+2p+1,out}}}{2p+1}\right)\right] I^0 \tag{162}$$

$$\mathfrak{I}_{\mathfrak{F}}^{\mathfrak{2k,out}} = \left[\mathfrak{O}^{\mathfrak{2k,out}} + \frac{2\alpha}{\pi}\left(\sum_{p=0}^{\infty} \frac{\mathfrak{O}^{\mathfrak{2k+2p+1,in}}}{2p+1} - \sum_{p=0}^{k-1} \frac{\mathfrak{O}^{\mathfrak{2k-(2p+1),in}}}{2p+1}\right)\right] I^0 \tag{163}$$

- Odd order $n = 2k + 1$ with $k \in \mathbb{N}^\star$:

$$\mathfrak{I}_{\mathfrak{F}}^{\mathfrak{2k+1,in}} = \left[\mathfrak{O}^{\mathfrak{2k+1,in}} + \frac{4\alpha}{(2k+1)\,\pi}\mathfrak{O}^{\mathfrak{o}} + \frac{2\alpha}{\pi}\left(\sum_{p=0}^{k-1} \frac{\mathfrak{O}^{\mathfrak{2(k-p),out}}}{2p+1} - \sum_{p=0}^{\infty} \frac{\mathfrak{O}^{\mathfrak{2(k+p+1),out}}}{2p+1}\right)\right] I^0 \tag{164}$$

$$\mathfrak{I}_{\mathfrak{F}}^{\mathfrak{2k+1,out}} = \left[\mathfrak{O}^{\mathfrak{2k+1,out}} + \frac{2\alpha}{\pi}\left(\sum_{p=0}^{\infty} \frac{\mathfrak{O}^{\mathfrak{2(k+p+1),in}}}{2p+1} - \sum_{p=0}^{k-1} \frac{\mathfrak{O}^{\mathfrak{2(k-p),in}}}{2p+1}\right)\right] I^0 \tag{165}$$

As for the sinusoidal modulation of large amplitude, a square wave modulation of illumination is expected to cause modulation of the fluorescence intensity at an infinite number of radial frequencies, which are integer multiples of ω.

The zeroth order term $\mathfrak{I}_{\mathfrak{F}}^{\mathfrak{o}}$ can be expressed using Eqs.(84,112,116,129,133,136). We obtained

$$\frac{\mathfrak{I}_{\mathfrak{F}}^{\mathfrak{o}} - I_F^0}{(Q_2 - Q_1)\,\alpha^2 I^0} = \frac{2}{\pi}\left[1 - \left(k_{12}^{h\nu,0} + k_{21}^{h\nu,0}\right)\tau_{12}^0\right]\mathfrak{2}^{\mathfrak{1,in}} + \frac{2}{\pi}\sum_{p=1}^{\infty}\frac{\mathfrak{2}^{\mathfrak{2p+1,in}}}{2p+1}. \tag{166}$$

In contrast to the out-of-phase first-order response, Eq.(166) shows that the zeroth order response of the fluorescence emission upon square wave light modulation of large amplitude significantly departs from I_F^0, which is observed for a sinusoidal light modulation of small amplitude.

The first order terms can be expressed using Eqs.(129, 130, 133, 134, 137) and (129, 130, 133, 134, 138) to write

$$\frac{\mathfrak{I}_{\mathfrak{F}}^{\mathfrak{1,in}} - \frac{4}{\pi}\alpha I_F^0}{\alpha\,(Q_2 - Q_1)\,I^0} = \mathfrak{2}^{\mathfrak{1,in}}\left[1 - \frac{8}{\pi^2}\alpha^2\left(k_{12}^{h\nu,0} + k_{21}^{h\nu,0}\right)\tau_{12}^0\right] - \frac{2}{\pi}\alpha\sum_{p=0}^{\infty}\frac{\mathfrak{2}^{\mathfrak{2(p+1),out}}}{2p+1} \tag{167}$$

$$\mathfrak{I}_{\mathfrak{F}}^{\mathfrak{1,out}} = \alpha\,(Q_2 - Q_1)\,I^0\left[\mathfrak{2}^{\mathfrak{1,out}} + \frac{2}{\pi}\alpha\sum_{p=0}^{\infty}\frac{\mathfrak{2}^{\mathfrak{2(p+1),in}}}{2p+1}\right]. \tag{168}$$

In reference to the $g\left(\mathfrak{z}^{\mathfrak{n},\mathfrak{in}}, \mathfrak{z}^{\mathfrak{n},\mathfrak{out}}\right)$ function introduced in the Main Text, one has thus

$$g\left(\mathfrak{z}^{\mathfrak{n},\mathfrak{in}}, \mathfrak{z}^{\mathfrak{n},\mathfrak{out}}\right) = \frac{2}{\pi}\alpha\sum_{p=0}^{\infty}\frac{\mathfrak{z}^{\mathfrak{2(p+1)},\mathfrak{in}}}{2p+1}. \tag{169}$$

To evaluate the possible interference originating from this second order term $g\left(\mathfrak{z}^{\mathfrak{n},\mathfrak{in}}, \mathfrak{z}^{\mathfrak{n},\mathfrak{out}}\right)$, we used Eq.(40) to numerically compute the dependence of $\mathfrak{I}_{\mathfrak{F}}^{\mathfrak{1},\mathfrak{out}}$ on ω and I^0. Figure S12 compares the absolute value of the normalized out-of-phase first order amplitude $\mid \mathfrak{I}_{\mathfrak{F},\mathfrak{norm}}^{\mathfrak{1},\mathfrak{out}} \mid = \mid \mathfrak{I}_{\mathfrak{F}}^{\mathfrak{1},\mathfrak{out}}/(Q_2 - Q_1)I^0\alpha P_{tot} \mid$ obtained in the case of the square wave light modulation ($\alpha = 0.8$) with that obtained for a modulation of small amplitude. The position of the optimum is similar in both cases: we found $I^{0,R} = 1.04 \times 10^{-4}$ ein·s^{-1}·m^{-2} and $\omega^R = 3.09 \times 10^{-2}$rad·s^{-1} in the case of a square wave modulation, and $I^{0,R} = 0.96 \times 10^{-4}$ ein·s^{-1}·m^{-2} and $\omega^R = 3.02 \times 10^{-2}$rad·s^{-1} in the case of a modulation of small amplitude. The amplitudes of the optimum fairly compare as well: we computed $\mid \mathfrak{I}_{\mathfrak{F},\mathfrak{norm}}^{\mathfrak{1},\mathfrak{out}} \mid = 7.43 \times 10^{-2}$ in the case of square wave modulation, and $\frac{4}{\pi} \mid \mathfrak{I}_{\mathfrak{F},\mathfrak{norm}}^{\mathfrak{1},\mathfrak{out}} \mid = 7.40 \times 10^{-2}$ in the case of a sinusoidal modulation of small amplitude.

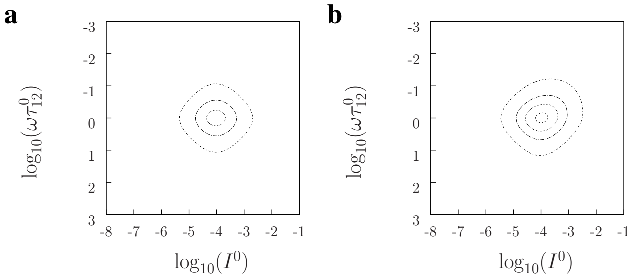

Figure S12: Theoretical dependence of the absolute value of the normalized amplitude of the out-of-phase oscillations of fluorescence intensity, $\mid \mathfrak{I}_{\mathfrak{F},\mathfrak{norm}}^{\mathfrak{1},\mathfrak{out}} \mid$, from a solution of a photoswitchable fluorophore **1** $\rightleftharpoons$ **2** submitted to square wave forcing (**b**; α = 0.8) on the light flux I^0 (in ein·s^{-1}·m^{-2}) and the adimensional radial frequency $\omega\tau_{12}^0$. The numerical computation has been performed upon truncating at the 3rd and 4th truncation orders the expansions of the light excitation and the $f(x)$ function. The corresponding dependence in the regime of small amplitude sinusoidal modulation is displayed in **a**. σ_{12} = 73 m^2.mol^{-1}, σ_{21} = 84 m^2.mol^{-1}, $k_{21}^{\Delta} = 1.5 \times 10^{-2}$ s^{-1}. The markers correspond to isodensity curves : 0.01 (dot small dashed), 0.03 (dot large dashed), 0.05 (dot) and 0.07 (dashed).

3 Retrieval of concentrations from the observables

In the following section, we assume that, upon modulating light, the observable associated to the photoswitchable probe adopts the expression

$$S(t) \quad = \quad \mathfrak{S}^{\mathfrak{o}} + \sum_{n=1}^{\infty} \left[\mathfrak{S}^{\mathfrak{n,in}} \sin\left(n\omega t\right) + \mathfrak{S}^{\mathfrak{n,out}} \cos\left(n\omega t\right) \right], \tag{170}$$

which includes both contributions originating from the exchanging states **1** and **2**. In the absence of convolution with the exciting light intensity, the $\{\mathfrak{S}^{\mathfrak{o}}, \mathfrak{S}^{\mathfrak{n,in}}, \mathfrak{S}^{\mathfrak{n,out}}\}$ set identifies to the $\{\mathfrak{O}^{\mathfrak{o}}, \mathfrak{O}^{\mathfrak{n,in}}, \mathfrak{O}^{\mathfrak{n,out}}\}$ one in reference to Eq.(131). In contrast, when one observes convolution of the concentrations with light intensity like for fluorescence emission, the $\{\mathfrak{S}^{\mathfrak{o}}, \mathfrak{S}^{\mathfrak{n,in}}, \mathfrak{S}^{\mathfrak{n,out}}\}$ terms correspond to the $\{\mathfrak{I}_{\mathfrak{F}}^{\mathfrak{o}}, \mathfrak{I}_{\mathfrak{F}}^{\mathfrak{n,in}}, \mathfrak{I}_{\mathfrak{F}}^{\mathfrak{n,out}}\}$ ones in Eq.(135).

3.1 Extraction of $\mathfrak{S}^{\mathfrak{o}}$, $\mathfrak{S}^{\mathfrak{n,in}}$, and $\mathfrak{S}^{\mathfrak{n,out}}$ from the overall signal $S(t)$

$\mathfrak{S}^{\mathfrak{o}}$, $\mathfrak{S}^{\mathfrak{1,in}}$, and $\mathfrak{S}^{\mathfrak{1,out}}$ can be easily retrieved from the experimental trace of the observed signal $S(t)$ (either global or from each analyzed pixel).

As shown in Eq.(170), $\mathfrak{S}^{\mathfrak{o}}$ can be obtained upon averaging $S(t)$ over an integer number m of periods of the modulated illumination

$$Int^{0} \quad = \quad \frac{1}{mT} \int_{0}^{mT} S(t) dt = \mathfrak{S}^{\mathfrak{o}}. \tag{171}$$

In particular, upon observing fluorescence emission in a regime of sinusoidal light modulation of small amplitude, one has $Int^0 = I_F^0$.

The n-th order amplitudes $\mathfrak{S}^{\mathfrak{n,in}}$ and $\mathfrak{S}^{\mathfrak{n,out}}$ can be extracted from the fluorescence signal upon computing the integrals $Int^{n,in}$ and $Int^{n,out}$

$$Int^{n,in} \quad = \quad \frac{2}{mT} \int_{0}^{mT} S(t) \sin\left(n\omega t\right) dt = \mathfrak{S}^{\mathfrak{n,in}} \tag{172}$$

$$Int^{n,out} \quad = \quad \frac{2}{mT} \int_{0}^{mT} S(t) \cos\left(n\omega t\right) dt = \mathfrak{S}^{\mathfrak{n,out}}. \tag{173}$$

In particular

$$Int^{1,in} \quad = \quad \frac{2}{mT} \int_{0}^{mT} S(t) \sin\left(\omega t\right) dt = \mathfrak{S}^{\mathfrak{1,in}} \tag{174}$$

$$Int^{1,out} \quad = \quad \frac{2}{mT} \int_{0}^{mT} S(t) \cos\left(\omega t\right) dt = \mathfrak{S}^{\mathfrak{1,out}}. \tag{175}$$

Upon observing fluorescence emission in a regime of sinusoidal light modulation of small amplitude, one has $Int^{1,in} = I_F^{1,in}$ and $Int^{1,out} = I_F^{1,out}$, and $Int^{n,in} = I_F^{n,in} = 0$ and $Int^{n,out} = I_F^{n,out} = 0$ for $n > 1$.

3.2 Quantifying a targeted component

In this subsection, we show how the observables $\mathfrak{S}^{\mathfrak{o}}$ and $\mathfrak{S}^{\mathfrak{1,out}}$ can be used to retrieve the concentration of a targeted component in two cases. In the first case, we consider that the photoswitchable probe is used for analyte labelling and that one aims at measuring P_{tot}, which quantifies the labelled analyte. This situation typically refers to the dynamic schemes, which have been introduced in the subsections 1.1 (the label is a photoswitchable fluorophore) and 1.2 (the label is a fluorophore engaged in relaxation from both singlet and triplet excited states). In a second case, we consider that the photoswitchable probe is used for titrating an analyte **A** and that one aims at measuring the concentration of the titrated analyte A_{tot}. This situation has been addressed with the dynamic scheme introduced in subsection 1.3. As in subsection 1.3, we restrict our analysis to the specific case of (i) an analyte in excess ($A_{tot} \gg P_{tot}$) in a kinetic regime where (ii) photochemical reactions are rate-limiting with respect to reactions involving the analyte.

3.2.1 Measuring the total concentration of the photoswitchable probe

The expressions of $\mathfrak{S}^{\mathfrak{o}}$ and $\mathfrak{S}^{1,\mathfrak{out}}$ identify to the ones of $\mathfrak{O}^{\mathfrak{o}}$ and $\mathfrak{O}^{\mathfrak{n},\mathfrak{out}}$ or to $\mathfrak{I}_{\mathfrak{F}}^{\mathfrak{o}}$ and $\mathfrak{I}_{\mathfrak{F}}^{\mathfrak{n},\mathfrak{out}}$ (when one observes convolution of the concentrations with light intensity like for fluorescence emission).

In the absence of light modulation or in a regime of sinusoidal light modulation of small amplitude, the expression of $\mathfrak{S}^{\mathfrak{o}}$ can be deduced from Eqs.(49,50,55,84)

$$\mathfrak{O}^{\mathfrak{o}} = \frac{\mathfrak{I}_{\mathfrak{F}}^{\mathfrak{o}}}{I^0} = Q_1 \frac{1}{1+K_{12}^0} P_{tot} + Q_2 \frac{K_{12}^0}{1+K_{12}^0} P_{tot} \tag{176}$$

where

$$K_{12}^0 = \frac{\sigma_{12} I^0}{\sigma_{21} I^0 + k_{21}^{\Delta}}. \tag{177}$$

In the presence of light modulation, we showed in the Main Text that $\mathfrak{S}^{1,\mathfrak{out}}$ can be reliably evaluated from its expression in the case of a sinusoidal light modulation of small amplitude. We correspondingly used Eqs.(75,78,86) to yield

$$\mathfrak{O}^{1,\mathfrak{out}} = \frac{\mathfrak{I}_{\mathfrak{F}}^{1,\mathfrak{out}}}{I^0} = \varepsilon \left(Q_1 - Q_2\right) p_{21}^{\Delta} \frac{K_{12}^0}{\left(1+K_{12}^0\right)^2} \frac{\omega \tau_{12}^0}{1+\left(\omega \tau_{12}^0\right)^2} P_{tot} \tag{178}$$

where K_{12}^0 is given in Eq.(177) and where

$$p_{21}^{\Delta} = \frac{k_{21}^{\Delta}}{\sigma_{21} I^0 + k_{21}^{\Delta}} \tag{179}$$

$$\tau_{12}^0 = \frac{1}{\left(\sigma_{12}+\sigma_{21}\right) I^0 + k_{21}^{\Delta}} \tag{180}$$

from Eqs.(51,67).

The theoretical expressions (176,178) make possible to directly retrieve the concentrations of the photoswitchable probe from the observed signal. However this approach requires the effort to acquire the values of all parameters involved in these expressions. Alternatively, quantification can proceed by calibration with the pure photoswitchable probe at a reference concentration. Eqs.(176,178) show that $\mathfrak{S}^{\mathfrak{o}}$ and $\mathfrak{S}^{1,\mathfrak{out}}$ are proportional to the overall concentration in photoswitchable probe. Thus quantification can be simply achieved by recording the observable from a calibrating solution of the photoswitchable probe at a known concentration P_{tot}^{cal}. The concentrations of the photoswitchable probe, which are retrieved at zeroth- and first-order, are respectively

$$\begin{aligned} P_{tot}^{0} &= \frac{\mathfrak{S}^{\mathfrak{o}}}{\mathfrak{S}^{\mathfrak{o,cal}}} P_{tot}^{cal} && (181) \\ P_{tot}^{1,out} &= \frac{\mathfrak{S}^{\mathfrak{1,out}}}{\mathfrak{S}^{\mathfrak{1,out,cal}}} P_{tot}^{cal}. && (182) \end{aligned}$$

3.2.2 Measuring the concentration of an analyte reacting with a photoswitchable probe

The expressions of $\mathfrak{S}^{\mathfrak{o}}$ and $\mathfrak{S}^{\mathfrak{1,out}}$ again identify to the ones of $\mathfrak{O}^{\mathfrak{o}}$ and $\mathfrak{O}^{\mathfrak{n,out}}$ or to $\mathfrak{I}_{\mathfrak{F}}^{\mathfrak{o}}$ and $\mathfrak{I}_{\mathfrak{F}}^{\mathfrak{n,out}}$ (when one observes convolution of the concentrations with light intensity like for fluorescence emission).

In the absence of light modulation or in a regime of sinusoidal light modulation of small amplitude, the expression of $\mathfrak{S}^{\mathfrak{o}}$ is again given in Eq.(176) but with

$$\begin{aligned} Q_1 &= \frac{Q_{1F} + Q_{1B} K_1^{\Delta} A_{tot}}{1 + K_1^{\Delta} A_{tot}} && (183) \\ Q_2 &= \frac{Q_{2F} + Q_{2B} K_2^{\Delta} A_{tot}}{1 + K_2^{\Delta} A_{tot}} && (184) \\ K_{12}^{0} &= \frac{1 + K_2^{\Delta} A_{tot}}{1 + K_1^{\Delta} A_{tot}} \frac{\sigma_{12,F} I^0 + \sigma_{12,B} I^0 \; K_1^{\Delta} A_{tot}}{\left(\sigma_{21,F} I^0 + k_{21,F}^{\Delta}\right) + \left(\sigma_{21,B} I^0 + k_{21,B}^{\Delta}\right) \; K_2^{\Delta} A_{tot}}, && (185) \end{aligned}$$

which originate from Eqs.(34,35,40,41,49,50,52,55,84).

In the presence of light modulation, we again adopted the expression (178) obtained in the case of a sinusoidal light modulation of small amplitude. The dependence on A_{tot} is now explicited in Eqs.(183–190)

$$\begin{aligned} p_{21}^{\Delta} &= \frac{k_{21}^{\Delta}}{\frac{\sigma_{21,F} + \sigma_{21,B} \; K_2^{\Delta} A_{tot}}{1 + K_2^{\Delta} A_{tot}} I^0 + k_{21}^{\Delta}} && (186) \\ \sigma_{12} &= \frac{\sigma_{12,F} + \sigma_{12,B} \; K_1^{\Delta} A_{tot}}{1 + K_1^{\Delta} A_{tot}} && (187) \\ \sigma_{21} &= \frac{\left(\sigma_{21,F} I^0 + k_{21,F}^{\Delta}\right) + \left(\sigma_{21,B} I^0 + k_{21,B}^{\Delta}\right) \; K_2^{\Delta} A_{tot}}{1 + K_2^{\Delta} A_{tot}} && (188) \\ k_{21}^{\Delta} &= \frac{k_{21,F}^{\Delta} + k_{21,B}^{\Delta} \; K_2^{\Delta} A_{tot}}{1 + K_2^{\Delta} A_{tot}} && (189) \\ \tau_{12}^{0} &= \frac{1}{\frac{\sigma_{12,F} I^0 + \sigma_{12,B} I^0 \; K_1^{\Delta} A_{tot}}{1 + K_1^{\Delta} A_{tot}} + \frac{\left(\sigma_{21,F} I^0 + k_{21,F}^{\Delta}\right) + \left(\sigma_{21,B} I^0 + k_{21,B}^{\Delta}\right) \; K_2^{\Delta} A_{tot}}{1 + K_2^{\Delta} A_{tot}}} && (190) \end{aligned}$$

obtained from Eqs.(36–38,51,67).

Eqs.(187–189) first show that the values of I^0 and ω at resonance depend on A_{tot}. As classically practiced in any titration protocol, one should preliminarily have a guess of the concentration A_{tot}. Using this guess would permit to fix an initial set of resonance conditions (I^0,ω) and proceed as indicated below to extract a first evaluation of A_{tot}. This estimate would be subsequently used to fix a refined resonant (I^0,ω) set and extract a second evaluation of A_{tot}. This iteration should be performed until reaching convergence.

As shown in Eqs.(183–190), direct extraction of the concentration A_{tot} sought for requires a considerable amount of information about the dynamic system (**1F**,**1B**,**2F**,**2B**). In contrast, one can proceed by calibration as proposed above. The information to be extracted from $\mathfrak{S}^{0}$ or $\mathfrak{S}^{1,\mathrm{out}}$ is now contained in the amplitude of the **P** response to the light modulation, normalized by its concentration. Hence to retrieve the **A** concentration from a calibrating experiment requires to normalize $\mathfrak{S}^{0}$ or $\mathfrak{S}^{1,\mathrm{out}}$ by the total concentration of **P**. Then the most classical protocol is to proceed by a ratiometric analysis, where one collects the signal $S(t)$ upon adopting a same illumination but under two conditions of observation (for instance by recording the fluorescence emission at two different wavelengths), yielding to two sets of brightness, $\{Q_{1,1}, Q_{2,1}\}$ and $\{Q_{1,2}, Q_{2,2}\}$. The analyzed observables are now

$$\rho^{0} = \frac{\frac{Q_{1F,1}+Q_{1B,1}K_1^{\Delta}A_{tot}}{1+K_1^{\Delta}A_{tot}} + \frac{Q_{2F,1}+Q_{2B,1}K_2^{\Delta}A_{tot}}{1+K_2^{\Delta}A_{tot}}K_{12}^{0}}{\frac{Q_{1F,2}+Q_{1B,2}K_1^{\Delta}A_{tot}}{1+K_1^{\Delta}A_{tot}} + \frac{Q_{2F,2}+Q_{2B,2}K_2^{\Delta}A_{tot}}{1+K_2^{\Delta}A_{tot}}K_{12}^{0}} \tag{191}$$

$$\rho^{1,out} = \frac{\frac{Q_{1F,1}+Q_{1B,1}K_1^{\Delta}A_{tot}}{1+K_1^{\Delta}A_{tot}} - \frac{Q_{2F,1}+Q_{2B,1}K_2^{\Delta}A_{tot}}{1+K_2^{\Delta}A_{tot}}}{\frac{Q_{1F,2}+Q_{1B,2}K_1^{\Delta}A_{tot}}{1+K_1^{\Delta}A_{tot}} - \frac{Q_{2F,2}+Q_{2B,2}K_2^{\Delta}A_{tot}}{1+K_2^{\Delta}A_{tot}}} \tag{192}$$

Calibration requires to preliminarily investigate the dependence of ρ^{0} and $\rho^{1,out}$ on A_{tot}. Then quantification can be simply achieved by recording the observable from a calibrating solution where the photoswitchable probe is used to sense a known concentration A_{tot}^{cal}. The concentrations of the analyte, which are retrieved at zeroth- and first-order, are respectively

$$A_{tot}^{0} = \frac{\rho^{0}}{\rho^{0,cal}}A_{tot}^{cal} \tag{193}$$

$$A_{tot}^{1,out} = \frac{\rho^{1,out}}{\rho^{1,out,cal}}A_{tot}^{cal}. \tag{194}$$

4 Improvement of the spatial resolution

The light intensity-dependence of the first-order response of the concentration in photoswitchable fluorophore to the illumination modulation allows us for improving the spatial resolution of the out-of-phase fluorescence imaging protocol with respect to usual fluorescence imaging at zeroth-order. To evaluate the corresponding improvement, we computed the spatial profile of the fluorescence emission resulting from focusing a sinusoidally modulated light beam of wavelength λ (regime of small amplitude modulation) in a solution of photoswitchable fluorophore upon using both types of imaging protocols.

We assumed the light beam to be Gaussian and correspondingly adopted

$$I^0\left(r,z\right) = I^{0,R}\left(0,0\right)\left[\frac{w\left(0\right)}{w\left(z\right)}\right]^2 \exp\left[\frac{-2r^2}{w^2\left(z\right)}\right] \tag{195}$$

with

$$w\left(z\right) = w\left(0\right)\sqrt{1+\left(\frac{z}{z_R}\right)^2} \tag{196}$$

for the spatial dependence of light intensity. In Eq.(195), r and z respectively correspond to the radial distance from the center axis of the beam and the axial distance from the beam's narrowest point (the "waist"), $w(z)$ is the radius at which light intensity drop to $1/e^2$ of its axial value, and $I^{0,R}\left(0,0\right)$ is the intensity at the center of the beam at its waist, which is supposed to satisfy the resonance condition (14). In Eq.(196), $z_R = \frac{\pi w^2(0)}{\lambda}$ designates the Rayleigh range.

4.1 Fluorescence imaging at zeroth order

The fluorescence emission at zeroth order of the light modulation, I_F^0, is given in Eq.(84), where 1^0, 2^0, and I^0 depend on the coordinates (r,z). Using Eqs.(49,50,52) and introducing the average light intensity at resonance, $I^{0,R} = \frac{k_{21}^{\Delta}}{(\sigma_{12}+\sigma_{21})}$, one obtains

$$I_F^0 = Q_1\left[1+\left(\frac{Q_2}{Q_1}-1\right)\frac{\sigma_{12}}{(\sigma_{12}+\sigma_{21})}\frac{\frac{I^0}{I^{0,R}}}{\frac{I^0}{I^{0,R}}+1}\right]I^0P_{tot}. \tag{197}$$

Upon introducing the fluorescence emission at zeroth order of the light modulation at resonance, $I_F^{0,R}$, one eventually derives

$$\frac{I_F^0}{I_F^{0,R}} = \frac{1+\left(\frac{Q_2}{Q_1}-1\right)\frac{\sigma_{12}}{(\sigma_{12}+\sigma_{21})}\frac{\frac{I^0}{I^{0,R}}}{\frac{I^0}{I^{0,R}}+1}}{1+\frac{1}{2}\left(\frac{Q_2}{Q_1}-1\right)\frac{\sigma_{12}}{(\sigma_{12}+\sigma_{21})}}\frac{I^0}{I^{0,R}}. \tag{198}$$

In a homogeneous solution, one has thus

$$\frac{I_F^0(r,z)}{I_F^{0,R}(0,0)} = \frac{1+\left(\frac{Q_2}{Q_1}-1\right)\frac{\sigma_{12}}{(\sigma_{12}+\sigma_{21})}\frac{\frac{I^0(r,z)}{I^{0,R}(0,0)}}{\frac{I^0(r,z)}{I^{0,R}(0,0)}+1}}{1+\frac{1}{2}\left(\frac{Q_2}{Q_1}-1\right)\frac{\sigma_{12}}{(\sigma_{12}+\sigma_{21})}}\frac{I^0(r,z)}{I^{0,R}(0,0)}. \tag{199}$$

4.2 Out-of-Phase Fluorescence imaging at first order

The out-of-phase fluorescence emission at first order of the light modulation, $I_F^{1,out}$, is given in Eq.(86), where $2^{1,out}$, and I^0 depend on the coordinates (r, z). Assuming light modulation to occur at resonance ($\omega^R = 2k_{21}^{\Delta}$), we use Eqs.(51,52,67,75) to extract

$$I_F^{1,out} \quad = \quad -\varepsilon Q_1 \left(\frac{Q_2}{Q_1} - 1\right) \frac{2\sigma_{12}\frac{I^0}{I^{0,R}}}{(\sigma_{12} + \sigma_{21})\left(1 + \frac{I^0}{I^{0,R}}\right)\left[\left(1 + \frac{I^0}{I^{0,R}}\right)^2 + 4\right]} I^0 P_{tot}. \tag{200}$$

Upon introducing the out-of-phase fluorescence emission at first order of the light modulation at resonance, $I_F^{1,out,R}$, one eventually derives

$$\frac{I_F^{1,out}}{I_F^{1,out,R}} \quad = \quad \frac{16\frac{I^0}{I^{0,R}}}{\left(1 + \frac{I^0}{I^{0,R}}\right)\left[\left(1 + \frac{I^0}{I^{0,R}}\right)^2 + 4\right]} \frac{I^0}{I^{0,R}}. \tag{201}$$

In a homogeneous solution, one has thus

$$\frac{I_F^{1,out}(r, z)}{I_F^{1,out,R}(0, 0)} \quad = \quad \frac{16\frac{I^0(r,z)}{I^{0,R}(0,0)}}{\left(1 + \frac{I^0(r,z)}{I^{0,R}(0,0)}\right)\left[\left(1 + \frac{I^0(r,z)}{I^{0,R}(0,0)}\right)^2 + 4\right]} \frac{I^0(r, z)}{I^{0,R}(0, 0)}. \tag{202}$$

4.3 Comparison of the spatial resolutions from the fluorescence imaging protocols at zeroth- and first-order

Figure S13 displays the results from Eqs.(199,202). One can notice that the width of the fluorescence profile is larger with the zeroth-order protocol than with the out-of-phase first-order one. More specifically, the gain in spatial resolution is more pronounced along the optical axis (Figure S13a) than in the focal plane (Figure S13b).

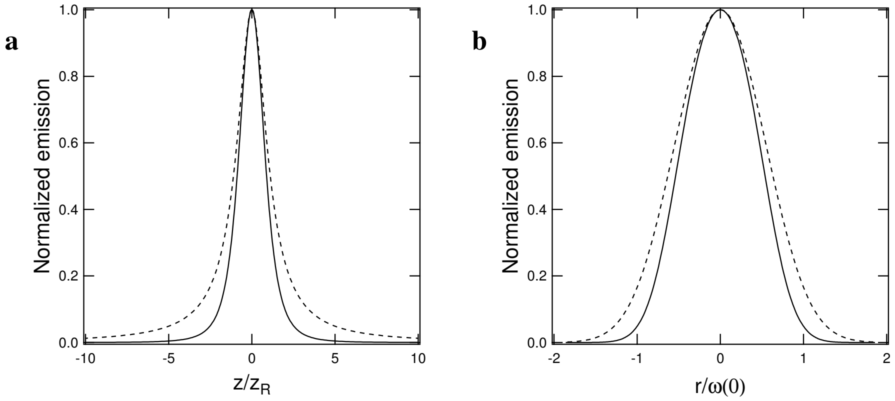

Figure S13: Normalized fluorescence intensity profiles resulting from applying a sinusoidally modulated Gaussian light beam (regime of small amplitude modulation) in a solution of photoswitchable fluorophore **1** $\rightleftharpoons$ **2**. The longitudinal (along the optical axis: $r = 0$; **a**) and lateral (in the focal plane: $z = 0$; **b**) profiles have been calculated with Eqs.(199) and (202) using adimensional units involving the Rayleigh range z_R and the beam waist at $z = 0$, $w(0)$. Dashed line: zeroth-order fluorescence imaging; Solid line: out-of-phase first-order fluorescence imaging. The numerical computation has been performed with σ_{12} = 73 m^2.mol^{-1}, σ_{21} = 84 m^2.mol^{-1}, $Q_2/Q_1 = 0$.

References

[1] B. Valeur, *Molecular Fluorescence: Principles and Applications*, Wiley-VCH, Weinheim, **2002**.

[2] M. Emond, T. Le Saux, S. Maurin, J.-B. Baudin, R. Plasson, L. Jullien, *Chem. Eur. J.*, **2010**, *16*, 8822–8831.

[3] M. Eigen, *Angew. Chem. Int. Ed.*, **1964**, *3*, 1–19.

Chapter 4

Out-of-phase imaging after optical modulation (OPIOM)

4.1 Introduction

4.1.1 Context

We showed in the chapter 3 that the first order out-of-phase response of a photoswitchable probe submitted to a monochromatic light modulation can be maximized simply by fixing the average light intensity I^0 and the radial frequency ω of the light excitation to the resonance conditions 4.1 and 4.2 of the targeted probe :

$$I^0 = \frac{k_{21}^{\Delta}}{\sigma_{12}+\sigma_{21}} \tag{4.1}$$

$$\omega = 2k_{21}^{\Delta} \tag{4.2}$$

Due to its photochromic behavior evidenced in chapter 2, Spinach first seemed us to be a good candidate to experimentally validate the OPTIMAL approach. Indeed, this probe fulfills the requirements developed in the General Introduction (photochromic, fluorescent and genetically encoded) and was thoroughly characterized (see chapter 2).

The first step was to calculate the values of the resonant intensity $I^{0,R}$ and the radial frequency ω^R. We showed in chapter 2 that a dynamic model consisting in a four-state mechanism accounts for the photochromic behavior of the Spinach-DFHBI system. For simplicity, this subsection uses the symbols **1F**, **2F**, **1B**, and **2B** to represent *cis*-DFHBI, *trans*-DFHBI, Spinach-*cis*-DFHBI, and Spinach-*trans*-DFHBI respectively. The associated rate constants are presented in Figure 4.1, where the superscripts hν and Δ respectively denote photochemical and thermal contributions.

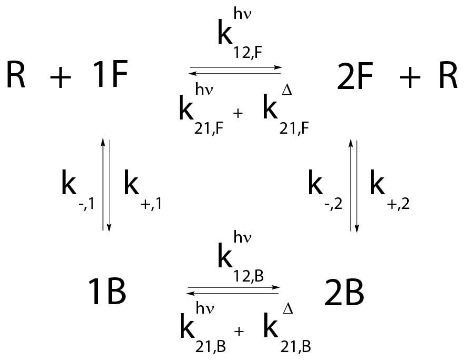

Figure 4.1: Four-state mechanism accounting for the photochemical and complexation behavior of the photochromic fluorogen DFHBI in the presence of the RNA aptamer Spinach

The concentration profiles within the four state model are governed by the equations:

$$\begin{aligned}
\frac{d1B}{dt} &= -\left(k_{\mathbf{1B\to1F}} + k_{\mathbf{1B\to2B}}\right)\,1B + k_{\mathbf{2B\to1B}}\,2B + k_{\mathbf{1F\to1B}}\,R\,1F && (4.3)\\
\frac{d2B}{dt} &= k_{\mathbf{1B\to2B}}\,1B - \left(k_{\mathbf{2B\to2F}} + k_{\mathbf{2B\to1B}}\right)\,2B + k_{\mathbf{2F\to2B}}\,R\,2F && (4.4)\\
\frac{d1F}{dt} &= k_{\mathbf{1B\to1F}}1B - \left(k_{\mathbf{1F\to1B}}\,R + k_{\mathbf{1F\to2F}}\right)\,1F + k_{\mathbf{2F\to1F}}\,2F && (4.5)\\
\frac{d2F}{dt} &= k_{\mathbf{2B\to2F}}2B + k_{\mathbf{1F\to2F}}\,1F - \left(k_{\mathbf{2F\to2B}}\,R + k_{\mathbf{2F\to1F}}\right)\,2F && (4.6)
\end{aligned}$$

Even if the temporal dependence of concentrations cannot be obtained in the most general case, it can be analyzed in asymptotic situations where either photochemical or complexation reactions are the rate-limiting steps. The relevant case for applying OPTIMAL corresponds to the regime where photoisomerization is rate-limiting.

In the corresponding regime, complexation reactions are considered to be at chemical equilibrium and we can introduce the average species $\overline{\mathbf{1}}$ and $\overline{\mathbf{2}}$ (concentrations $\overline{1} = 1F + 1B$ and $\overline{2} = 2F + 2B$). The "instantaneous" concentrations in **1F**, **1B**, **2F** and **2B** then follow,

$$\begin{aligned}
1F &= \frac{1}{1 + K_1^{\Delta} R}\overline{1} && (4.7)\\
1B &= \frac{K_1^{\Delta} R}{1 + K_1^{\Delta} R}\overline{1} && (4.8)\\
2F &= \frac{1}{1 + K_2^{\Delta} R}\overline{2} && (4.9)\\
2B &= \frac{K_2^{\Delta} R}{1 + K_2^{\Delta} R}\overline{2} && (4.10)
\end{aligned}$$

where

$$K_1^{\Delta} = \frac{k_{+,1}^{\Delta}}{k_{-,1}^{\Delta}} \quad (4.11)$$

$$K_2^{\Delta} = \frac{k_{+,2}^{\Delta}}{k_{-,2}^{\Delta}}. \quad (4.12)$$

Thus Eqs.(6.4–6.7) transform into Eq.(6.14):

$$\frac{d\overline{1}}{dt} = -\frac{d\overline{2}}{dt} = -k_{12}\,\overline{1} + k_{21}\,\overline{2} \quad (4.13)$$

with

$$k_{12} = \frac{k_{12,F}^{h\nu} + k_{12,B}^{h\nu}\,K_1^{\Delta}R}{1 + K_1^{\Delta}R} \quad (4.14)$$

$$k_{21} = \frac{\left(k_{21,F}^{h\nu} + k_{21,F}^{\Delta}\right) + \left(k_{21,B}^{h\nu} + k_{21,B}^{\Delta}\right)\,K_2^{\Delta}R}{1 + K_2^{\Delta}R}. \quad (4.15)$$

Thus, the four-state model shown in Figure 4.1 can be reduced to a two-state light-driven exchange in the regime where photoisomerization is rate-limiting :

$$\mathbf{1} \quad \underset{k_{21}}{\overset{k_{12}}{\rightleftharpoons}} \quad \mathbf{2} \quad (4.16)$$

Using Eq. 4.14 and 4.15, the molecular action cross-sections σ_{12} and σ_{21} and the thermal relaxation rate constant k_{21}^{Δ} can be written :

$$\sigma_{12} = \frac{\sigma_{12,F} + \sigma_{12,B}K_1^{\Delta}R}{1 + K_1^{\Delta}R} \quad (4.17)$$

$$\sigma_{21} = \frac{\sigma_{21,F} + \sigma_{21,B}K_2^{\Delta}R}{1 + K_2^{\Delta}R} \quad (4.18)$$

$$k_{21}^{\Delta} = \frac{k_{21,F}^{\Delta} + k_{21,B}^{\Delta}K_2^{\Delta}R}{1 + K_2^{\Delta}R} \quad (4.19)$$

We performed an *in vitro* validation upon choosing relevant experimental conditions that could mimic an *in vivo* sample : an excess of the fluorogen dye compared to the RNA aptamer. We chose a total DFHBI concentration F_{tot} of 2.5 and 5 μM and a total RNA aptamer concentration R_{tot} between 250 and 500 nM. Calculating the terms $K_i^{\Delta}R$ with the values of the two dissociation constants[120] $K_{d,1}(= 1/K_1^{\Delta}) = 1.3\ \mu M$ and $K_{d,2}(= 1/K_2^{\Delta}) = 4\ \mu M$ showed that they could be neglected compared to 1. In addition, since $\sigma_{12,F} \gg \sigma_{12,B}K_1^{\Delta}R$, $\sigma_{21,F} \gg \sigma_{21,B}K_2^{\Delta}R$ and $k_{21,F}^{\Delta} \gg k_{21,B}^{\Delta}K_2^{\Delta}R$ in this concentration regime, the photochemical parameters of the Spinach-DFHBI system could actually be approximated to those of the free

DFHBI. Thus, we obtained the following resonant light intensity $I^{0,R}$ and radial frequency ω^R :

$$I^{0,R} = 8.9 \times 10^{-5} \text{ ein} \cdot \text{ m}^{-2} \cdot \text{ s}^{-1} \quad (4.20)$$

$$\omega^R = 6.4 \times 10^{-3} \text{ rad} \cdot \text{ s}^{-1} \quad (4.21)$$

To experimentally evaluate the 'light modulation and quadrature detection' approach for detection in a mixture, we chose to selectively titrate the fluorescent Spinach complex in the presence of an interfering fluorophore emitting in a similar wavelength range. As a putative interfering species, we adopted Fluorescein. The samples to be analyzed were injected in the parallel channels (50 μm wide and 200 μm high) of a microfluidic device. Channels 1 and 2 contained increasing concentrations of the target (250 and 500 nM in Spinach RNA in the presence of 2.5 and 5 μM DFHBI respectively) in the presence of various concentrations of Fluorescein (75 and 50 nM in the channels 1 and 2 respectively). In channel 3, we introduced the Spinach system (500 nM in Spinach RNA and 5 μM in DFHBI) only, to subsequently be used as a calibration standard allowing us to convert into concentrations of the channels 1-2 responses. Yet we filled channel 4 with 100 nM Fluorescein, in order to control the selectivity of our protocol as well as to report on light excitation.

Using a LED illuminated home-built optical setup, we could selectively image green fluorescent species upon simultaneously monitoring light excitation using Fluorescein emission as a reporter. Indeed this non-reactive fluorophore responds instantaneously to any of the light variation applied in the present work. The titration experiment was performed at $I^0 = 2.4 \times 10^{-4}$ Ein$\cdot$ m$^{-2}\cdot$ s^{-1} with 10% light intensity modulation at 31.4 mrad$\cdot$s^{-1} angular frequency. We recorded the fluorescence intensity variations during 8 oscillations (200 s). Complete time-averaging of the resulting movie yielded the image displayed in Figure 4.2a. It corresponds to the result that would be obtained without any light modulation at constant intensity I^0. As shown in Figure 4.2a, we appropriately tuned the amounts of probes in solution to get nearly similar emissions from the four channels. Using the channel 3 for calibration and assuming F_{tot} to be known (equal to 2.5 and 5 μM in channels 1 and 2 respectively), we extracted $R^0_{tot,titration}$ from the fluorescence level I^0_F. We found 0.54±0.05 and 0.72±0.06 μM in channels 1 and 2 whereas 0.25±0.03 and 0.5±0.05 μM had been introduced in solution. Thus the extracted concentrations in the targeted probe that would be extracted upon neglecting the presence of the interfering Fluorescein would be clearly larger in the channels 1 and 2 than the various target concentrations. Taking advantage of the knowledge of the oscillating light phase measured and relying on a phase-sensitive detection scheme, we subsequently extracted for each pixel the amplitude of the fluorescence oscillations in quadrature with the light excitation. As shown in Figure 4.2b, the out-of-phase responses arising from the four channels were now different. In particular, the signal from sample 4, which did not include the photoactive probe, was completely extinguished. This observation agreed with the responses from channels 1 and 2: the signal increased from samples 1 to 2, in line with increasing F_{tot} and R_{tot}, independently on the concentration of the interfering compounds. Again using the channel 3 as a standard and assuming F_{tot} to be respectively equal to 2.5 and 5 μM in channels 1 and 2, we now extracted $R^{\text{out}}_{tot,titration}$ from $I^{\text{out}}_F(x,y)$ and found it equal to 0.31±0.04 and 0.58±0.05 μM, in line with the expected values. Thus, this protocol completely eliminated the contribution of the non-photoactive species, which validated the relevance of the present protocol for quantitative analysis and imaging without any preliminary separation. This *in vitro* validation enabled us to patent our 'light modulation and quadrature detection' approach.[121]

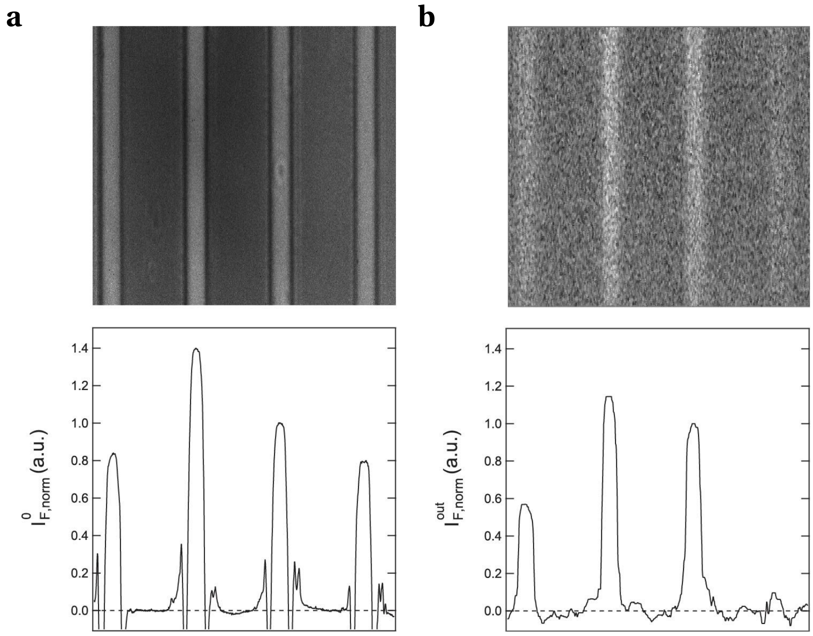

Figure 4.2: Selective imaging of the fluorescent Spinach target in a mixture containing Fluorescein as a model interfering fluorophore. **a**: Fluorescence emission map $I^0_{F,norm}(x,y)$ at constant illumination $I^0 = 2.4 \times 10^{-4}$ Ein· m^{-2}· s^{-1} and corresponding $I^0_{F,norm}(x)$ trace; **b**: Map of the amplitude of the out-of-phase response upon harmonic forcing around I^0, $I^{\text{out}}_{F,norm}(x,y)$, and corresponding $I^{\text{out}}_{F,norm}(x)$ trace. The amplitude of the light oscillations at $\omega = 31.4$ mrad·s^{-1} angular frequency was 10%. Traces were computed by signal averaging along the image vertical axis. Samples were prepared in 40 mM Hepes buffer, 125 mM KCl and 5 mM $MgCl_2$, pH 7.4 at T = 293 K. From left to the right, channel 1 to 4.

Despite the preceding experimental validation, Spinach suffers from several constraints. First, as mentioned before (see chapter 2), this fluorescent probe is not so bright.[114] Second, the resonant light intensity (P = 2.3 mW.cm^{-2} at 470 nm) is easily attainable with our light excitation set-up but is small compared to the typical values used in fluorescence microscopy (P ~ 1-100 W.cm^{-2} for an epifluorescence setup[106] , P ~ 10^5 W.cm^{-2} for a confocal microscope[122]) resulting in a poor signal-to-noise ratio. Third, applying the OPTIMAL protocol requires to record a time lapse or a movie of several periods of the light excitation. In the case of Spinach, the period at resonance is 980 s. Thus, it takes at least ~17 minutes to obtain the OPTIMAL image which is a very long acquisition time for microscopy devoted to biological applications. Finally, Spinach only enables to tag RNA. As a consequence, we looked in the literature for another good candidate with a wider scope of applications.

Photochromism and fluorescence are rarely encountered in small molecules since these two phenomena are competitive de-excitation pathways.[5,123] Nevertheless, 'Nature' has been able to evolve proteins combining these two properties called photochromic fluorescent proteins. These ones take part in photoactivatable proteins which can be divided in three classes[75–77] :

1. irreversible photoactivatable fluorescent proteins (irreversible PA-FPs), whose fluorescence can be switched on by illumination at a specific wavelength;
2. photoshiftable fluorescent proteins (PS-FPs), whose fluorescence excitation and emission spectra are shifted after illumination;
3. reversibly photoswitchable fluorescent proteins (RSFPs) or photochromic fluorescent proteins, whose fluorescence is reversibly switched on and off with light of appropriate wavelengths.

In the following, we focus on reversibly photoswitchable fluorescent proteins whose behavior upon illumination can be modeled by a two-state exchange at large enough time scale. In particular, we highlight the case of the Dronpa family, one of the most employed RSFP to date for imaging purpose. The other kinds of RSFPs and their applications in particular in the context of super-resolution imaging will also be evoked. The article that presents the experimental validation of OPTIMAL in fluorescence imaging will be subsequently introduced.

4.1.2 Presentation of Reversibly Photoswitchable Fluorescent Proteins

Photochromism in FPs has initially been reported for the YFPs (yellow-emitting) variants of GFP at the single molecular level.[124] Nevertheless, when measured in bulk, they did not exhibit any significant photochromism. As a consequence, many photochromic proteins have been engineered over the last decade to activate or inactivate at will their fluorescence emission.

4.1.2.1 Dronpa and its variants

The most famous reversibly photoswitchable fluorescent protein is probably Dronpa, which was cloned from *Pectiniidae*, a species of coral that fluoresces faintly upon illumination with ultraviolet light.[125] Dronpa is homologous to GFP and consequently exhibits a similar fold. This GFP-like protein is constituted of an 11-stranded β-barrel enclosing the p-hydroxybenzylidene imidazolinone chromophore (see Figure 4.4), which is covalently attached to the protein.[126–128] At neutral pH, the chromophore exists in its anionic form (pK_a = 5.0, see Figure 4.3a).[125] Dronpa strongly fluoresces in the green (λ_{Em} = 518 nm) with an absorption band at 503 nm (see Figure 4.3b).[125,127,128] The fluorescence quantum yield (Φ_{FL}) of the ON state is 0.85.[125] When illuminated with blue light, Dronpa is photoconverted to its OFF state (see Figure 4.3c) with the appearance of a major absorption band at 390 nm.[125] The ON state recovers spontaneously in the dark with a half-life ($t_{1/2}^{\mathrm{relax}}$) of 14 h at room temperature.[125] The recovering rate can be accelerated upon irradiation with ~390 nm light (see Figure 4.3c). Ando *et al* investigated the kinetics of the photochromic behavior of Dronpa. The quantum yields of photoconversion at 490 nm $\Phi_{\mathrm{ON}\rightarrow\mathrm{OFF}}$ and at 400 nm $\Phi_{\mathrm{OFF}\rightarrow\mathrm{ON}}$ were respectively found 3.2×10^{-4} and 3.7×10^{-1}.[125] Dronpa can be switched on and off for many cycles with no significant loss of fluorescence.[125]

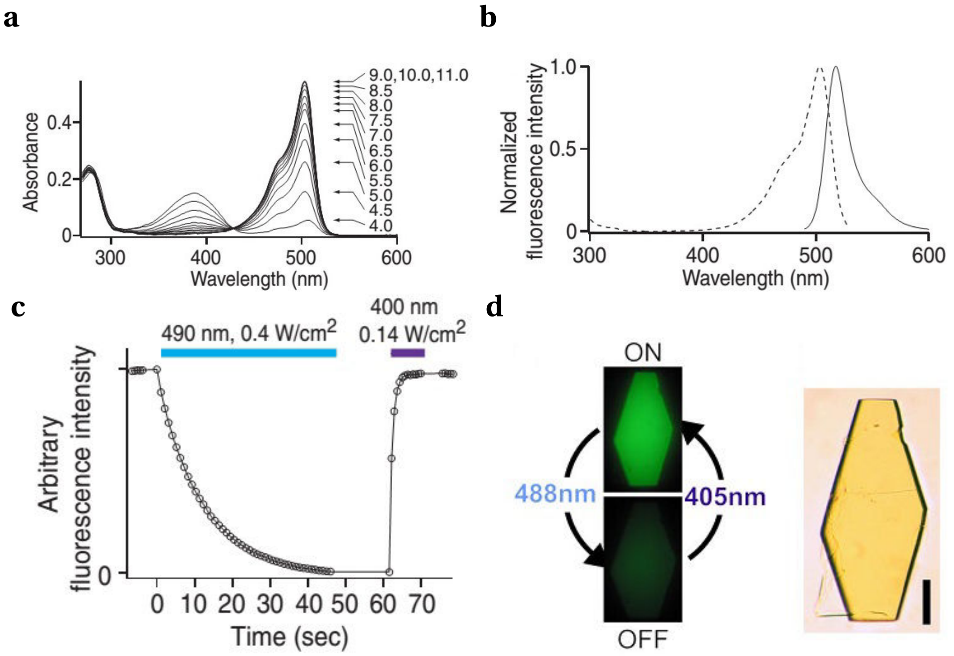

Figure 4.3: The photochromic properties of Dronpa. (**a**) The pH-dependence of Dronpa absorbance. (**b**) Normalized excitation (dotted line) and emission (solid line) spectra of Dronpa. (**c**) Time course of the green fluorescence emission of Dronpa in a fixed Hela cell upon illumination with blue or violet light. (**d**) Fluorescence images of a Dronpa crystal in the fluorescent (ON) and non-fluorescent(OFF) state and bright-field image of the same crystal. Adapted from Ando *et al* and Andresen *et al.*[125,126]

Several mutants of Dronpa were developed to improve the photoswitching kinetics. The first Dronpa variant carried only one mutation (M159T) and was named Dronpa-2.[129] A second mutant of the protein was generated using site-directed random mutagenesis. Exhibiting two mutations (V157I and M159A), it was named Dronpa-3.[129] Upon illumination with

490 nm light, they both exhibit faster photoinduced drops of fluorescence than Dronpa as shown by the $\Phi_{ON \rightarrow OFF}$ values : 4.7×10^{-2} for Dronpa-2 and 5.3×10^{-3} for Dronpa-3 respectively.[129] Like Dronpa, these two variants return to their ON state spontaneously in the dark but much more quickly[128,129] ($t_{1/2}^{relax}$ = 0.5 min for Dronpa-2).[128] Their photoactivation with violet light is as effective as the one of Dronpa.[129] Dronpa-2 and Dronpa-3 in their ON state exhibit lower fluorescence quantum yields (Φ_{FL}) than Dronpa : 0.23-0.33 and 0.28 respectively.[128,129] Independently, another group generated similar Dronpa variants with accelerated photoswitching. They identified Dronpa-2 and a second mutant bearing a single mutation (V157G) called rsFastLime.[128] The photoconversion with blue light of rsFastLime is ~50 times faster than the one of Dronpa. Whereas rsFastLime exhibits a slower switching kinetics than Dronpa-2 (~ 20 times), it is brighter with Φ_{FL} = 0.77.[128] Another variant (called bsDronpa) with a broader and blue-shifted absorption spectrum was also identified.[130]

Dronpa is a 'negative' photoswitcher that is to say that upon irradiation with blue light (that induces fluorescence), the fluorescent state of Dronpa is photoconverted to a non-fluorescent state, resulting in a fluorescence decay. Andresen *et al* reported a new variant of Dronpa exhibiting positive photoswitching characteristics : blue light illumination (λ_{Max} = 503 nm)[130] induces green fluorescence (λ_{Em} = 522 nm, Φ_{FL} = 0,64)[130] and photoconversion from the OFF to the ON state whereas ultraviolet light switched off fluorescence. Named Padron (reminding the reverse switching behavior compared to Dronpa), this variant carried eight mutations close to the chromophore.[130] Like Dronpa, its recovery in the dark is slow at room temperature ($t_{1/2}^{relax}$ = 150 min).[130]

	λ_{Max} (nm)	λ_{Em} (nm)	ε ($M^{-1} \cdot cm^{-1}$)	Φ_{FL}	$t_{1/2}^{relax}$ (min)	References
Dronpa	503	518	95000	0.85	840	[125]
Dronpa-2	489	515	61732	0.23-0.33	0.5	[128,129]
Dronpa-3	487	514	58000	0.28	ND	[129]
rsFastLime	496	518	39094	0.77	8	[128]
bsDronpa	460	504	45000	0.50	54	[130]
Padron	503	522	43000	0.64	150	[130]

Table 4.1: Absorption (λ_{Max}) and emission (λ_{Em}) maxima, molar absorption coefficient (ε) at λ_{Max}, fluorescence quantum yield (Φ_{FL}) and relaxation half-time ($t_{1/2}^{relax}$) at room temperature of Dronpa, Dronpa-2, Dronpa-3, rsFastLime, bsDronpa and Padron.

4.1.2.2 Mechanism of photoswitching in the Dronpa family

Many mechanistic investigations have been carried out to account for the photoswitching behavior of Dronpa and its variants. These studies are particularly interesting to give insights for designing novel photochromic fluorescent proteins.[131]

Mechanism for Dronpa X-ray cristallography enabled to determine the three dimensionnal structure of the ON[127,128] and OFF[126] states of Dronpa. The chromophore in the ON state adopts a *cis* configuration[127,128] whereas in the OFF state, it exhibits a *trans* isomeric state.[126] The *cis*-*trans* isomerization results in an important movement of the hydroxyl group of the p-hydroxyphenyl moiety whereas the imidazolinone ring stays almost in place.[126] As a consequence, some amino acids in the vicinity of the chromophore undergo spatial rearrangements during the switching.[126] The *cis* chromophore (ON) is slightly non coplanar (~15°)[128] whereas in the *trans* chromophore, the imidazole and the hydroxyphenyl rings are not coplanar (~30°).[126] Comparing the environment of the two configurations of the chromophore suggest that the *trans* state is more flexible than the *cis* due to less interactions with the rest of the protein. In particular, the only hydrogen bond stabilizing the hydroxyl group in the *cis* chromophore is not present in the *trans* chromophore.[126] Taken together, these observations suggest that the non fluorescent character of the OFF state is due to (i) the lower planarity of the *trans* chromophore and (ii) a lower rigid attachment to the rest of the protein compared to the *cis* chromophore favoring the non-radiative decay of the excited *trans*-chromophore.[126] It has been reported that the ON state is deprotonated whereas the OFF state is protonated (see Figure 4.4).[125,126,132,133] To sum up, the reversible photoswitching of Dronpa consists in a *cis*-*trans* isomerization coupled with a proton exchange accompanied by a spatial rearrangement of the residues close to the chromophore.

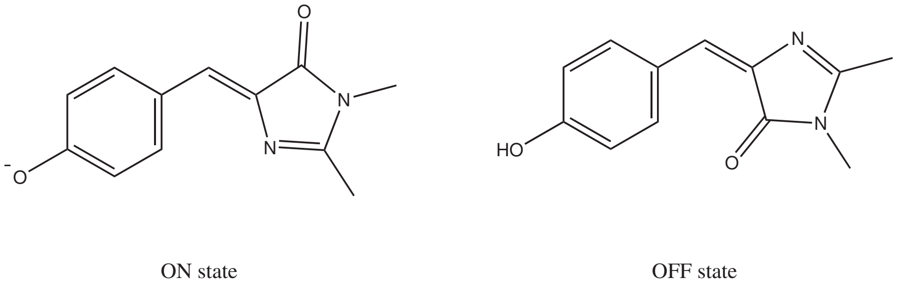

Figure 4.4: Structure of the chromophore of Dronpa in the ON (left) and OFF (right) states.

Cristallographic studies gives only a static view of the switching mechanism. Many investigations have been performed to understand the dynamics of switching. To date, the detailed mechanism involved in photoswitching and in particular in which order the two events : isomerization and proton transfer occur is the subject of much debates.

Some authors proposed the following mechanism : upon excitation of Dronpa with blue light, the excited state of the *cis*-deprotonated form (B) decays into its ground state by fluorescence and into the ground states of the photoswitched *trans*-protonated form (A_2) and an unknown metastable dark state D. A_2 is not interconvertible with A_1, the protonated form corresponding to B. Illumination with 405 nm light promotes A_1 and A_2 in their excited states. The switching of the excited state of A_2 to the ground state B is explained by ESPT (excited state proton transfer) from A_2 to a non-fluorescent intermediate I that converts into B in the ground state.[132–134] Recently, UV-visible transient absorption spectroscopy enabled to evidence that *trans*-to-*cis* isomerization of the chromophore precedes its deprotonation during the photoactivation of Dronpa and Dronpa-2.[135]

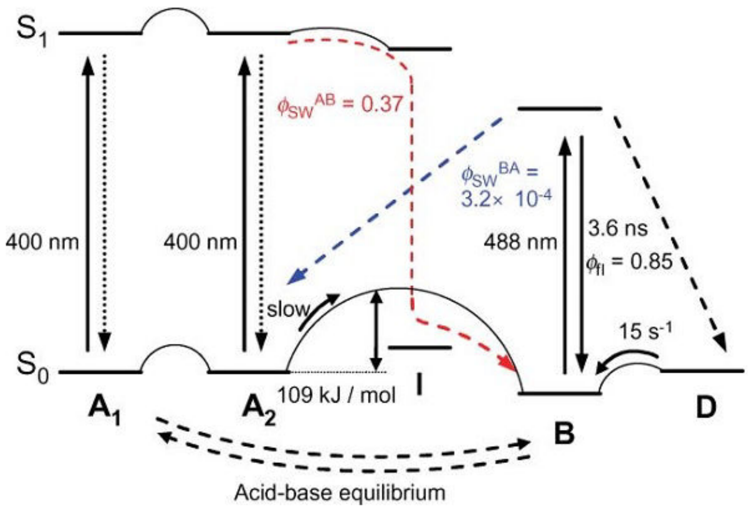

Figure 4.5: Proposed mechanism involved in the photoswitching of Dronpa. Adapted from Habuchi *et al.*[132]

Mechanism for Padron Similarly to Dronpa, the chromophore of the ON state of Padron adopts a *cis* configuration whereas the OFF state exhibits a *trans* configuration.[136,137] The chromophore in the ON and in the OFF states is mostly deprotonated (pK_a^{OFF} = ~ 4.5 and pK_a^{ON} = ~ 6.0).[137] The photoswitching involves a *trans*-to-*cis* isomerization coupled with a proton transfer.[131] However, unlike Dronpa, the spatial rearrangement of the amino acids in the chromophore environment is very weak.[136]

4.1.2.3 Other RSFPs

Several series of RSFPs exhibiting better brightnesses, improved photoswitching properties and resistance to photobleaching were generated after Dronpa. Some of them were designed to obtain a more red-shifted fluorescence emmission.

Procedure to generate new RSFPs A 'semirational' approach has been considered to design most of the new RSFPs (including Dronpa variants).[128] Starting from the X-ray structures of parent RSFPs or usual FPs such as EGFP[138] or mCherry[68] and based on the photoswitching mechanism, the residues that may facilitate the switching if they were replaced were identified.[128,139–141] Theoretical studies are also a useful tool for this purpose : theoretical calculations for instance confirmed the key role of the two residues Val157 and Met159 and pointed out a third residue Phe173 which may dramatically influence the photoswitching of Dronpa.[142] Several variants were generated by replacing the key amino acid(s) using saturated site-directed mutagenesis and then expressed in *Escherichia Coli* for instance. A screening of colonies expressing RSFPs was then performed and the clone exhibiting the best switching properties was identified and sequenced. The reversible photoswitching characteristics of the variant could be further optimized by performing a PCR-based multiple-site mutagenesis at amino-acid positions in the vicinity of the chromophore combined with an error-prone mutagenesis.

Cyan RSFPs To date, only one cyan RSFP has been reported.[143] When illuminated with 458 nm light, mTFP0.7 emits at 488 nm and undergoes simultaneously a switching to a OFF state. The back reaction in the dark requires few minutes at room temperature and can be accelerated with illumination at ultraviolet light.[143]

Other green RSFPs Two photoswitchable GFPs were identified by mutating GFP.[144] Grotjohann *et al* generated a variant of the EGFP that is reversibly photoswitchable and termed it rsEGFP for reversible switchable EGFP.[141] The ON state of rsEGFP exhibits an absorption band at 491nm and fluoresces in the green (Φ_{FL} = 0.36).[141] rsEGFP exhibits several advantages compared to Dronpa : the ON-to-OFF switching is more effective (~ 10 times faster) and rsEGFP is less sensitive to bleaching.[141] Another series of monomeric green RSFPs called mGeos has been developed with various properties such as pH-dependence, high photostability and a broad range of switching rate.[145]

Red RSFPs Isolated from the sea anemone *Anemonia sulcata*, the first family of red fluorescent RSFPs is asFP595 and its variants. This tetrameric protein was used for protein tracking in Hela cells[146,147] and for super-resolution microscopy[148] even though its quantum yield of fluorescence is relatively low.[146] The structure and the photoswitching mechanism of asFP595 was particularly investigated.[149–151] Two monomeric RSFPs emitting in the red were generated by transforming the nonswitchable fluorescent protein mCherry.[139] The ON state of rsCherry (reversibly switching Cherry) absorbs at 572 nm and fluoresces at 610 nm. This protein exhibits a positive switching behavior : yellow light (550 nm) switches on red fluorescence and photoconverts the OFF state of the protein to its ON state whereas blue light (450 nm) induces the ON-to-OFF photoconversion.[139] Another variant of mCherry consisting in a red fluorescent RSFP with a negative switching mode was designed. Absorbing at 572 nm, it emits red fluorescence (λ_{Em} = 608 nm). It was called rsCherryRev (for reverse switching properties) and was employed for time-lapse live-cell subdiffraction microscopy.[139] Another red RSFP was designed by transforming TagRFP, a recently reported monomeric red fluorescent protein.[140,152] Named rsTagRFP, it exhibits fluorescence at 585 nm and is ~ 20 times brighter than rsCherryRev.[140]

Particular RSFPs Among these photoactivatable fluorescent proteins, IrisFP, NijiFP and their derivatives both exhibit photoshifting and photoswitching properties. Illumination with 405 nm light enables photoconversion from the green to the red fluorescent form. Both forms can be reversibly switched between a fluorescent state and a non-fluorescent state with light of appropriate wavelengths.[131,153,154]

4.1.2.4 Using reversibly photoswitchable fluorescent proteins

RSFPs have been employed for protein tracking[75,125,146,147] thanks to repeated photoactivation, for detecting protein-protein interaction in live cells using pcFRET[140,144] (photochromic FRET) and for enhanced-contrast imaging using OLID.[86] The photochromic properties of Dronpa-3 were also used for mapping spatial distributions of the microviscosity in live cells.[155] rsEGFP was employed for re-writable data storage.[141]

RSFPs were in particular developed for super-resolution fluorescence imaging techniques[76,77,131] such as RESOLFT[148] (reversible saturable optically linear fluorescence transitions), PALM[156] (photoactivated localization microscopy), FPALM[157] (fluorescence photoactivation localization microscopy), PALMIRA[158] (photoactivated localization microscopy with independently running acquisition), STORM[159,160] (stochastic optical reconstruction microscopy) and pc-SOFI[161] (photochromic stochastic optical fluorescence imaging).

RESOLFT is based on a stimulated transition between two molecular states. This approach derived from STED[162] (Stimulated emission depletion). In this case, the sample is illuminated with two superimposed laser beams : a laser pulse promotes the fluorophores in their excited state and a red-shifted pulse called the STED beam transfers the excited fluorophores in their ground state thanks to stimulated emission. The STED beam exhibits actually a doughnut shape with a zero-intensity point at the center of the spot and high intensities at the periphery. Thus, only the fluorophores close to the center of the STED beam are able to fluoresce. The point spread function (PSF) is consequently narrowed and the spatial resolution is increased beyond the diffraction limit. The sub-diffraction image is obtained by scanning the sample with the two superimposed laser beams. STED requires very high light intensities. Instead of simple fluorophores (STED), RESOLFT employs RSFPs (asFP595,[148] Dronpa-2[163]) that reduces strongly the light power (six orders of magnitude) required to break the diffraction limit.[77,148,163] The RESOLFT approach was employed for optical nanoscopy of living cells[141] or living neurons[163] using respectively rsEGFP and Dronpa-2.

Unlike RESOLFT, the four super-resolution imaging techniques PALM, FPALM, PALMIRA and STORM are single-molecule-based. The individual fluorescent molecules are localized at a nanoscale level by sequentially switching them on and off using light of different wavelengths. During each cycle, only a few molecules are switched on, imaged and localized whereas most of them remains dark. A super-resolution image is then reconstructed by repeating this process for many cycles.[77]

SOFI (superresolution optical fluorescence imaging) is another kind of super-resolution technique. Its principle is based on the statistical analysis of temporal fluorescence fluctuations, using fluorophores that can be switched between a fluorescent and a non-fluorescent state (blinker).[164,165] Initially demonstrated with quantum dots[164] and organic fluorophores,[166] it has been recently implemented with Dronpa (pcSOFI).[161]

4.1.3 Investigated systems for experimental validation

The OPTIMAL approach has been experimentally validated stepwise with various systems. We performed first an *in vitro* validation with a microfluidic device which requires low amounts of proteins. We employed a PDMS stamp composed of four chambers 400 μm × 400 μm × 20 μm separated by walls of 200 μm. This allowed us to image simultaneously different mixtures under the same illumination conditions and to detect the targeted probe in four mixtures for instance.

We then evaluated the compatibility of the OPTIMAL protocol with biological samples. A series of experiments has been first performed with HEK cells transfected with the targeted photoswitchable protein and an interfering fluorescent protein.

Finally, we wanted to check the ability of the OPTIMAL protocol to eliminate the autofluorescence widely encountered in biological samples especially in multicellular organisms. We chose zebrafish (*Danio rerio*) embryos since it is a model system for the study of human diseases,[167,168] drug screening and discovery[169,170] whose yolk exhibits high levels of autofluorescence.

4.1.4 Presentation of the article

My third article is about the experimental validation of the OPTIMAL approach described in the previous chapter. Applied in fluorescence microscopy, this protocol was dubbed OPIOM for Out-of-Phase Imaging after Optical Modulation.

The first step of this work was to identify relevant reversibly photoswitchable fluorescent proteins. We chose to investigate the well-known Dronpa family for several reasons. First, these GFP-like proteins can be excited and monitored easily with standard GFP filter cubes that is interesting for an implementation with commercially available microscopes. Second, a library of several variants exhibiting promising photoswitching properties in particular for multiplexed experiments had been already developed. Third, Dronpa and its variants are monomeric. This is a great advantage compared to polymeric (or tetrameric) proteins which can be used to target only whole cells or organelles but may disrupt the localization, movement and function of their fusion partner.

Due to its very long spontaneous recovery in the dark ($t_{1/2}^{\mathrm{relax}} \sim 14$ h hence $k_{21}^{\Delta} = 1.4 \times 10^{-5} s^{-1}$),[125] the wild-type protein is not relevant for OPIOM (see resonance condition 4.2). Thus, we investigated the photoswitching kinetics of faster Dronpa variants : Dronpa-2 and Dronpa-3. Since some photochemical parameters were lacking in the literature or were determined without mentionning temperature or the buffer, we had to perform further characterizations before implementing OPIOM.

After producing and purifying these proteins, we performed simple light-jump experiments with blue light to investigate their photoswitching behavior. We checked that a two-state model enables to account for the fluorescence decay upon illumination and the fluorescence recovery in the dark (monoexponential curve with one relaxation time). By repeating these experiments with various light intensities, we determined the sum of the molecular action cross sections $\sigma_{12} + \sigma_{21}$ and the thermal rate constant k_{21}^{Δ} by plotting the reciprocal of the relaxation time as a function of the intensity of light. At the very end, we performed OPIOM with the two mutants Dronpa-2 and Dronpa-3 since they exhibit sufficiently different resonance conditions.

After calculating the resonance conditions for selective detection of either Dronpa-2 or Dronpa-3 with OPIOM, we first performed several *in vitro* validations using a microfluidic device. We demonstrated as expected that the amplitude of the out-of-phase fluorescence emission is proportional to the probe concentration. Even mixed with non photo-active fluorescent interfering compounds, we were able to accurately estimate the probe concentration using the OPIOM signal, which was not possible with the fluorescence emission upon constant illumination. Finally, we tested the ability of OPIOM to distinguish two photoswitchable fluorophores exhibiting two different resonance conditions. We selectively imaged either Dronpa-2 in the presence of Dronpa-3 or Dronpa-3 in the presence of Dronpa-2 by tuning illumination conditions to the resonance of Dronpa-2 or Dronpa-3. We also tested OPIOM for selective imaging in mammalian cells co-expressing nuclear Dronpa-3 and membrane-localized EGFP. OPIOM enabled to reveal the nucleus hidden by the interfering EGFP signal. Multicellular organisms exhibit often high levels of autofluorescence.

We used OPIOM to selectively image Lifeact-Dronpa-3 against autofluorescence in zebrafish embryos. Finally, we showed that OPIOM, combined with light sheet fluorescence microscopy, would enable selective three-dimensional-resolved fluorescence imaging.

4.2 Article 3 : Photoswitching kinetics and phase sensitive detection add discriminative dimensions for selective fluorescence imaging

Angewandte Chemie

Analytical Methods

DOI: 10.1002/ange.201408985

Photoswitching Kinetics and Phase-Sensitive Detection Add Discriminative Dimensions for Selective Fluorescence Imaging**

Jérôme Querard, Tal-Zvi Markus, Marie-Aude Plamont, Carole Gauron, Pengcheng Wang, Agathe Espagne, Michel Volovitch, Sophie Vriz, Vincent Croquette, Arnaud Gautier, Thomas Le Saux,* and Ludovic Jullien**

Abstract: *Non-invasive separation-free protocols are attractive for analyzing complex mixtures. To increase selectivity, an analysis under kinetic control, through exploitation of the photochemical reactivity of labeling contrast agents, is described. The simple protocol is applied in optical fluorescence microscopy, where autofluorescence, light scattering, as well as spectral crowding presents limitations. Introduced herein is OPIOM (out-of-phase imaging after optical modulation), which exploits the rich kinetic signature of a photoswitching fluorescent probe to increase selectively and quantitatively its contrast. Filtering the specific contribution of the probe only requires phase-sensitive detection upon matching the photoswitching dynamics of the probe and the intensity and frequency of a modulated monochromatic light excitation. After in vitro validation, we applied OPIOM for selective imaging in mammalian cells and zebrafish, thus opening attractive perspectives for multiplexed observations in biological samples.*

Measuring the concentration of a specific analyte in systems as complex as biological or medical samples remains a great challenge, in particular if the sample has to remain in its native state (e.g. living cells). In this context, non-invasive methods such as fluorescence microscopy have to be adopted. When one images fluorescent probes in cells,[1] contrast mainly results from the high brightness of the probe, which enables one to obtain a high signal to background ratio as long as the probe concentration is large enough and as long as the autofluorescence and light scattering of the medium is not too high. Other photophysical properties enable one to further distinguish fluorescent species. The one traditionally used for multiplexing is the emission wavelength. However only three or four probes can be distinguished using appropriate band pass filters since emission bands are rather broad and tend to overlap (spectral crowding).

Detecting individual emitters with similar emission properties thus requires efficient discrimination strategies. Time-gated detection is relevant if the fluorescence lifetimes of the emitters are sufficiently different,[2] but this is often challenging to achieve with the fluorescent proteins/probes commonly used in biology as they mostly display lifetimes within the same short nanosecond range. Hence imaging techniques exploiting the photochemical reactivity of photoswitchable fluorescent probes have been proposed to enhance contrast among fluorescence emitters. Optical lock-in detection[3,4] (OLID) images the correlation coefficient between the total fluorescence emission and an external reference signal from the photoswitchable fluorescent target over several cycles of dual-wavelength-driven optical switching. Synchronously amplified fluorescence image recovery[5–12] (SAFIRe) images the amplitude of the fluorescence modulation resulting from modulating a secondary light source, which depopulates long-lived dark states of the fluorescent probe.

---

[*] J. Querard, M.-A. Plamont, P. Wang, Dr. A. Espagne, Dr. A. Gautier, Dr. T. Le Saux, Prof. Dr. L. Jullien
École Normale Supérieure—PSL Research University
Department of Chemistry, 24 rue Lhomond, 75005 Paris (France)
E-mail: Arnaud.Gautier@ens.fr
Thomas.Lesaux@ens.fr
Ludovic.Jullien@ens.fr

J. Querard, M.-A. Plamont, P. Wang, Dr. A. Espagne, Dr. A. Gautier, Dr. T. Le Saux, Prof. Dr. L. Jullien
Sorbonne Universités, UPMC Univ Paris 06, PASTEUR
75005 Paris (France)

J. Querard, M.-A. Plamont, P. Wang, Dr. A. Espagne, Dr. A. Gautier, Dr. T. Le Saux, Prof. Dr. L. Jullien
CNRS, UMR 8640 PASTEUR, 75005 Paris (France)

Dr. T.-Z. Markus, Dr. V. Croquette
École Normale Supérieure, Département de Physique and Département de Biologie, Laboratoire de Physique Statistique UMR CNRS-ENS 8550, 75005 Paris (France)

C. Gauron, Prof. Dr. M. Volovitch, Prof. Dr. S. Vriz
Centre for Interdisciplinary Research in Biology (CIRB) CNRS UMR 7241/INSERM U1050/Labex MemoLife
PSL Research University/Collège de France, Paris (France)

C. Gauron, Prof. Dr. S. Vriz
Université Paris Diderot Sorbonne Paris Cité, Paris (France)

P. Wang
Institut Curie, Centre de Recherche, UMR 176 CNRS-Institut Curie
26 rue d'Ulm, 75248 Paris (France)

Prof. Dr. M. Volovitch
École Normale Supérieure, Institute of Biology at the Ecole Normale Supérieure (IBENS), CNRS UMR 8197, INSERM U1024, PSL Research University, 75005 Paris (France)

[**] We thank A. Miyawaki and S. Jakobs for providing the genes of Dronpa-3 and Dronpa-2, respectively, and E. Ipendey for her excellent technical assistance. D. Bensimon, M. Dahan, and Z. Gueroui are acknowledged for fruitful discussions. This work was supported by the ANR (France BioImaging, Morphoscope2), CNano Ile de France (Fluoroswitch), and PSL Research University (IMRE-SOLV).

Supporting information for this article is available on the WWW under http://dx.doi.org/10.1002/anie.201408985.

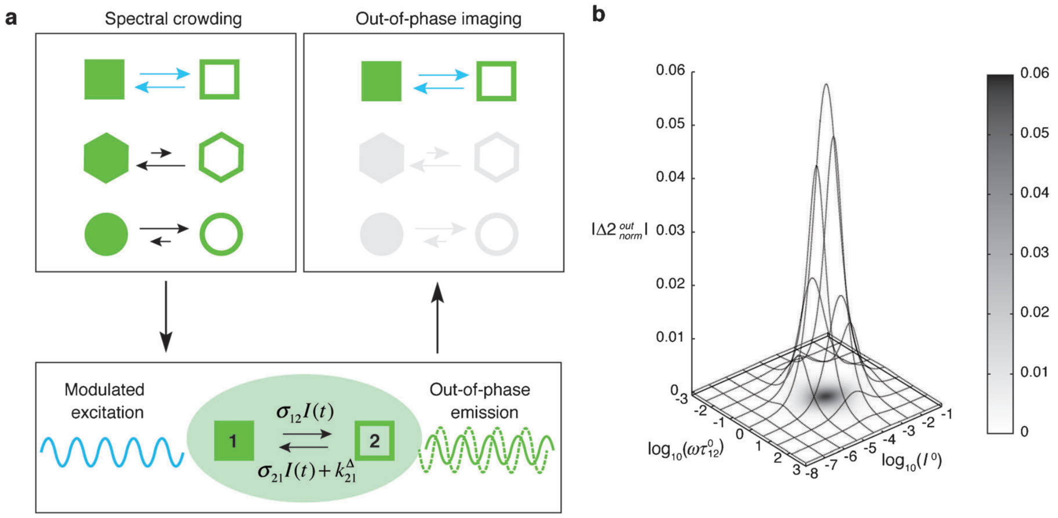

Figure 1. a) Out-of-phase imaging after optical modulation (OPIOM). A periodically modulated light generates modulation of the signal from photoswitchable fluorescent probes exchanging between two states (**1** and **2**), each having a different brightness. The image of a targeted probe is selectively and quantitatively retrieved from the amplitude of the out-of-phase component of the fluorescence emission at angular frequency (ω) upon matching I^0 and ω to its dynamic parameters (σ_{12}, σ_{21}, k_{21}^{Δ}). b) Theoretical response of a photoswitchable fluorophore, **1**$\rightleftharpoons$**2**, submitted to light harmonic forcing of small amplitude. The absolute value of the normalized amplitude of the out-of-phase oscillations in concentration of **2**, $|\Delta 2_{\mathrm{norm}}^{\mathrm{out}}|$, is plotted versus the light flux I^0 (in $\mathrm{ein\,s^{-1}\,m^{-2}}$) and the adimensional relaxation time $\omega\tau^0_{12}$. See Equation (18) and supplementary text 1 in the Supporting Information. $\sigma_{12}=73\ \mathrm{m^2\,mol^{-1}}$, $\sigma_{21}=84\ \mathrm{m^2\,mol^{-1}}$, $k_{21}^{\Delta}=1.5\times10^{-2}\ \mathrm{s^{-1}}$.

Herein, we exploit the unique discriminative kinetic parameters[13,14] of photoswitchable fluorescent probes to explore an alternative approach for selective and quantitative imaging. Our strategy relies on a periodically modulated monochromatic illumination with average light intensity and modulation frequency tuned so that the amplitude of the out-of-phase fluorescence response extracted from phase-sensitive detection results only from a fluorescent probe of interest, thus enabling extraction of its signal from a complicated fluorescence signal composed of several emitters. Our strategy notably differs from OLID and SAFIRe by its use of a single modulated light source whose average intensity and frequency depend on easily predictable resonant conditions, and by the exploitation of the phase lag between the modulated excitation and the fluorescence response. Our experimental set-up is correspondingly low cost and the acquisition protocol is simple and robust.

We first discuss the principle of our strategy and the analysis which enables selective detection (see supplementary text 1 in the Supporting Information). We consider a photoswitchable fluorophore **P** which exhibits two states of different brightnesses: state **1**, which is thermodynamically stable and state **2**, which is generated upon illumination (Figure 1 a). Note that this model applies for any photoactive system in which the kinetic behavior is dynamically reduced to light-driven exchanges between two states (see supplementary text 2).[2,15,16] Discrimination relies on the triplet of dynamic parameters (σ_{12}, σ_{21}, k_{21}^{Δ}) which characterize **P**, where σ_{12} and σ_{21} are the molecular action cross-sections of the forward and backward photochemical processes, and k_{21}^{Δ} is the rate constant of the thermal resetting. This discrimination is accomplished by using a periodically modulated monochromatic light excitation (average intensity I^0, fundamental angular frequency ω, modulation amplitude α), which forces the concentrations of the states **1** and **2** to oscillate with orthogonal in- and out-of-phase components exhibiting (σ_{12}, σ_{21}, k_{21}^{Δ})-dependent amplitudes. We apply phase-sensitive detection and focus on the amplitude of the out-of-phase first-order term $\Delta 1^{\mathrm{out}}=-\Delta 2^{\mathrm{out}}$ which reports on concentration oscillations at the angular frequency ω (see Figure S1). One can analytically show that this out-of-phase term in the concentration profile (proportional to the total concentration of **P** and easily retrieved from the fluorescence intensity) can be univocally maximized when the control parameters of illumination (I^0, ω) match the following simple resonance conditions in the space of the dynamic parameters [Equation (1); see also Figure 1 b].

$$I^0=\frac{k_{21}^{\Delta}}{\sigma_{12}+\sigma_{21}};\quad \omega=2k_{21}^{\Delta} \tag{1}$$

Conversely, the out-of-phase amplitude rapidly vanishes when (I^0, ω) diverge from these values (Figure 1 b). These resonance conditions are not significantly affected by photobleaching (see supplementary text 3). Importantly, the above resonance conditions maximize the out-of-phase response of **P**, but not that of another photoswitchable fluorophore, **X**, characterized by a different triplet of parameters ($\sigma_{12,\mathrm{X}}$, $\sigma_{21,\mathrm{X}}$, $k_{21,\mathrm{X}}^{\Delta}$).

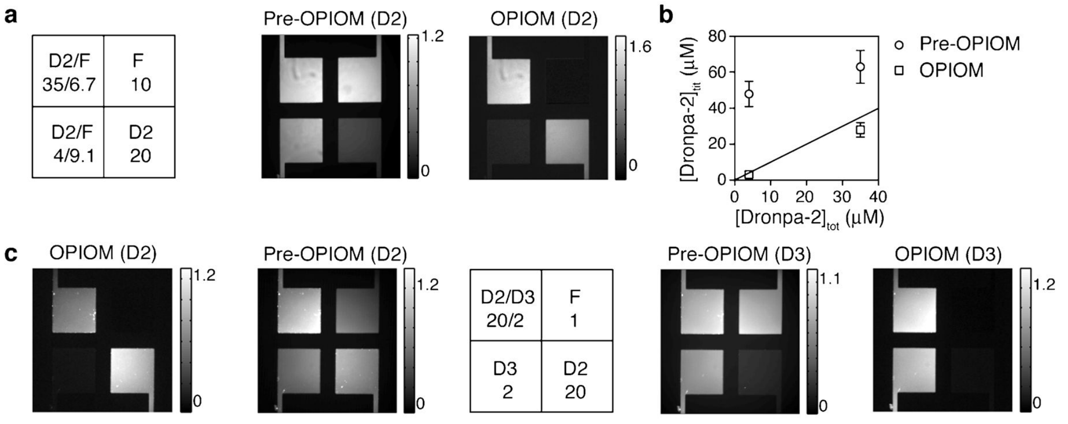

Figure 2. OPIOM validation in a microfluidic device composed of four chambers as described in the scheme (the numbers indicate the concentrations in μM). a) Selective imaging of Dronpa-2 (D2) against fluorescein (F). b) Titration of Dronpa-2 ([Dronpa-2]$_{\text{tit}}$) calculated from the pre-OPIOM (circle) and OPIOM (square) images in (a). The line shows the expected Dronpa-2 concentrations ([Dronpa-2]$_{\text{tot}}$). c) Selective imaging of Dronpa-2 and Dronpa-3 (D3). The microfluidic device was imaged using a sinusoidal light modulation of small amplitude tuned either to the resonance of Dronpa-2 (a,c) or Dronpa-3 (c). Images labeled Pre-OPIOM and OPIOM correspond to respectively the unfiltered and OPIOM-filtered images. $T = 37$ °C; pH 6.8 MES buffer. See the Supporting Information for details.

These theoretical predictions suggest that out-of-phase imaging after optical modulation (OPIOM;[*] see Figure 1 a) can enable highly selective imaging of a photoswitchable fluorescent target **P** in a mixture of spectrally interfering fluorophores, photoswitchable or not (see Figure S2). First the out-of-phase amplitude of the fluorescence signal does not contain any contribution from non-photoactive fluorescent interfering species, which respond as constant and in-phase terms with the light modulation. In contrast to spectral discrimination, phase discrimination here provides absolute orthogonality. Moreover, among photoswitchable interfering fluorophores, only **P** will display a significant out-of-phase amplitude.

To validate OPIOM experimentally, we used Dronpa-2 (or M159T)[17] and Dronpa-3 (or V157I/M159A).[18] These two variants of the reversibly photoswitchable green fluorescent protein Dronpa,[19] whose chromophore undergoes *cis*-to-*trans* and *trans*-to-*cis* photoisomerization, have been reported to display faster thermal resetting while exhibiting good quantum yields of fluorescence (0.23–0.33 for Dronpa-2[17,18] and 0.28[18] for Dronpa-3; 0.85 for Dronpa[19]). Note that a fast thermal resetting (large k_{21}^{Δ}) improves both the signal to noise ratio (by increasing I^0) and the temporal resolution (by increasing ω) of the imaging protocol (see the resonance conditions above), while a large quantum yield of fluorescence increases the OPIOM signal. In addition, the photochemical properties of these Dronpa mutants are poorly sensitive to environmental changes:[20] at most fourfold changes are expected for both the resonant ω and I^0 upon increasing viscosity, which remains lower than the bandwidth of the resonance (typically one order of magnitude; see Figure 1 b). This insensitivity enables one to benefit from widely applicable resonance conditions for OPIOM-selective detection of Dronpa-2 and Dronpa-3 in various environments.

The resonance conditions are calculated from the sum $\sigma_{12}+\sigma_{21}$ for the cis-to-trans and trans-to-cis photoisomerization action cross-sections and the thermal resetting rate constant k_{21}^{Δ}. Hence, we first submitted Dronpa-2 and Dronpa-3 to a straightforward series of light jump experiments (see supplementary text 4 and Table S1). Photoconversion of Dronpa-2 and Dronpa-3 revealed monoexponential relaxation of the fluorescence signal (see Figure S6), meaning that they both follow the two-state dynamic model underlying the OPIOM theory within the range of light intensity investigated. The $\sigma_{12}+\sigma_{21}$ value was extracted from the light intensity dependence of the relaxation time associated with the photoconversion of **P** upon irradiation (Figure S6): at 37 °C, we found (157 ± 5) and (21 ± 3) m^2 mol^{-1} for Dronpa-2 and Dronpa-3, respectively. k_{21}^{Δ} was directly obtained by monitoring the fluorescence recovery rate in the dark (see Figure S7), thus yielding $(1.50 \pm 0.05) \times 10^{-2}$ s^{-1} and (0.17 ± 0.01) s^{-1} for Dronpa-2 and Dronpa-3, respectively, at 37 °C. The measured kinetic parameters were in good agreement with literature results,[17,18] and were further confirmed by a series of light-modulation experiments (see supplementary text 5 and Figure S8).

To demonstrate OPIOM experimentally, we used a microfluidic device composed of four chambers containing solutions of Dronpa-2 at three different concentrations. The fourth chamber was filled with fluorescein, which is a non-photoactive fluorophore that emits in the Dronpa-2 wavelength range (see Figure S9) but characteristically responds

---

[*] OPIOM acts much like opium according to Thomas De Quincey in *Confessions of an English Opium-Eater* help long-buried memories resurface “veiled or unveiled, the inscription remains forever, just as the stars seem to withdraw before the common light of day, whereas in fact we all know that it is the light which is drawn over them as a veil, and that they are waiting to be revealed when the obscuring daylight shall have withdrawn”.

in-phase to the light modulation. The device was imaged using a classical epifluorescence microscope equipped with a light-emitting diode (LED; see Figure S10), whose intensity, radial frequency, and phase are easily controlled by driving electrical current. The illumination conditions were tuned to the Dronpa-2 resonance conditions. Two separate sets of images were collected: one corresponding to the average fluorescence intensity (hereafter called pre-OPIOM image) and a second corresponding to the processed OPIOM image (see supplementary text 6 and Figure S11a). Dronpa-2 fluorescence emission could be detected in both pre-OPIOM and OPIOM images. In contrast, as expected from the absence of an out-of-phase contribution in its fluorescence emission, fluorescein only gave a signal on the pre-OPIOM image, thus demonstrating the expected selective OPIOM imaging. More precisely, for fluorescein and Dronpa-2 at concentrations of 1 and 20 μM, respectively, the corresponding pre-OPIOM and OPIOM images with 1:1 and 1:200 intensity ratios were obtained. With a precision on phase retrieval of 3×10^{-3} rad, OPIOM imaging could typically enhance contrast of Dronpa-2 contribution against fluorescein by a factor $\chi_{D2/F}=10^2$–10^3 [see Eq. (78) in the Supporting Information] with respect to the pre-OPIOM image. Furthermore the three chambers with Dronpa-2 showed relative intensities directly reflecting their concentration (see Figure S11 b,c), which confirms the theoretical prediction that OPIOM signal is proportional to the probe concentration.

To further confirm this feature, we mixed Dronpa-2 and fluorescein in various ratios so that the resulting mixtures gave similar fluorescence intensities on the pre-OPIOM image (Figure 2 a). The excess fluorescein prevented estimation of the Dronpa-2 concentrations from the pre-OPIOM image, but the associated OPIOM image suppressed the contributions from fluorescein (Figure 2 a) and enabled us to accurately quantify the concentrations of Dronpa-2 in the fluorescein/Dronpa-2 mixtures by using the well containing only Dronpa-2 for concentration calibration [Figure 2 b and Eq. (38) in the Supporting Information]. This result demonstrates the capacity of OPIOM to image Dronpa-2 quantitatively within a mixture containing non-photoactive interfering fluorophores.

We next showed that one could distinguish two photoswitchable fluorophores exhibiting similar fluorescence emission (see Figure S9) as long as their dynamic parameters, $\sigma_{12}+\sigma_{21}$ and k_{21}^{Δ}, were different enough to give two different resonance conditions. Tuning the illumination to the resonance conditions of either Dronpa-2 or Dronpa-3 led to the contrast enhancements $\chi_{D2/D3}=20$ and $\chi_{D3/D2}=10$, respectively, thus enabling selective imaging of Dronpa-2 in presence of Dronpa-3 and vice versa (Figure 2 c and Figure S12). Therefore, OPIOM can selectively detect a photoswitchable target in a mixture of interfering photoswitchable fluorophores as long as they display different resonance conditions.

To test OPIOM for selective imaging in mammalian cells, we imaged fixed HEK293 cells co-expressing nuclear Dronpa-3 and membrane-localized EGFP using modulated excitation tuned to Dronpa-3 resonance. OPIOM enabled removal the interfering EGFP signal and revealed only a Dronpa-3 signal (Figure 3 a and Figure S13). Note that the acquisition time for each frame can be reduced to one period of light modulation (ca. 20 s for Dronpa-3) without any change in the contrast enhancement (see Figure S14). This feature enables imaging of live cells at a time resolution relevant for the study of biological processes and without any significant photobleaching or detrimental cell alteration (Figure 3 b and Figure S14).

Finally, we validated OPIOM for selective imaging in multicellular organisms, where the autofluorescence of tissues and compartments can strongly interfere. As such a model, we chose the zebrafish embryo, in which the yolk strongly fluoresces in the green, thus rendering it difficult to observe

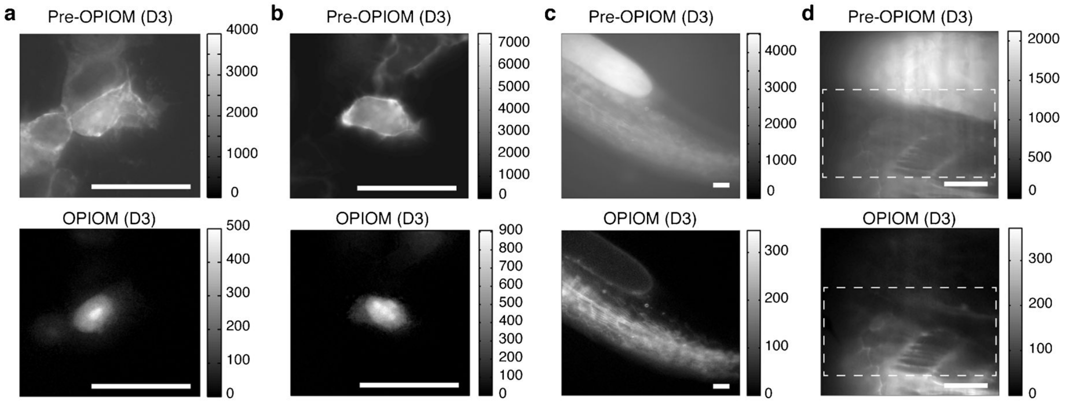

Figure 3. OPIOM application in mammalian HEK293 cells and in 24 hpf zebrafish embryos. a,b) Selective imaging of nuclear Dronpa-3 against membrane-localized EGFP. c,d) Selective imaging of Lifeact-Dronpa-3 against autofluorescence. Fixed (a) or live (b) cells, and zebrafish embryo (c,d) were imaged by epifluorescence (a–c) or single plane illumination microscope (SPIM; d; the dashed rectangles indicate the zone illuminated by the thinnest part of the light sheet) upon illuminating with sinusoidal (a–c) or square wave (d) light modulation of large amplitude tuned on the resonance of Dronpa-3. Images labeled Pre-OPIOM and OPIOM correspond to the unfiltered and OPIOM-filtered, respectively, images. Scale bars represent 50 μm. Experiments were performed either at 37 °C (a–c) or 20 °C (d). See the Supporting Information for details.

the popular green fluorescent probes such as GFP. We injected zebrafish embryos with Lifeact-Dronpa-3 mRNAs for actin targeting and imaged them 24 hours post-fertilization. OPIOM filtered out the yolk autofluorescence and selectively visualized Lifeact-Dronpa-3 in the embryo's tail (Figure 3c).

OPIOM is compatible with light sheet fluorescence microscopy (see Figure S15), which gives access to selective three-dimensional-resolved fluorescence imaging. Thus we selectively imaged Lifeact-Dronpa-3 against a background of autofluorescence (Figure 3d) or GFP-NLS (see Figure S16) in zebrafish embryos.

In conclusion, OPIOM is relevant for selective and quantitative imaging of photoswitchable fluorescent probes. Notably, OPIOM temporal resolution and multiplexing opportunities should benefit from developing bright photoswitchable fluorescent proteins with thermal resetting on the time scale of seconds. This would make OPIOM compatible with a 1 Hz image acquisition rate, which is relevant for most dynamic studies in biology. Finally, since a difference in either $\sigma_{12}+\sigma_{21}$ or k_{21}^{Δ} of only tenfold is sufficient to achieve efficient discrimination (Figure 1b and Figure S12), it should permit multiplex observation of up to ten different fluorophores in a single emission channel.[21,22]

Received: September 11, 2014
Revised: November 5, 2014

Keywords: analytical methods · fluorescence · fluorescent probes · imaging agents · photochemistry

---

[1] B. Giepmans, S. Adams, M. Ellisman, R. Tsien, *Science* **2006**, *312*, 217–224.
[2] G. Marriott, R. M. Clegg, D. J. Arndt-Jovin, T. M. Jovin, *Biophys. J.* **1991**, *60*, 1374–1387.
[3] G. Marriott, S. Mao, T. Sakata, J. Ran, D. K. Jackson, C. Petchprayoon, T. J. Gomez, E. Warp, O. Tulyathan, H. L. Aaron, et al., *Proc. Natl. Acad. Sci. USA* **2008**, *105*, 17789–17794.
[4] Y. Yan, M. E. Marriott, C. Petchprayoon, G. Marriott, *Biochem. J.* **2011**, *433*, 411–422.
[5] C. I. Richards, J.-C. Hsiang, D. Senapati, S. Patel, J. Yu, T. Vosch, R. M. Dickson, *J. Am. Chem. Soc.* **2009**, *131*, 4619–4621.
[6] C. I. Richards, J.-C. Hsiang, R. M. Dickson, *J. Phys. Chem. B* **2010**, *114*, 660–665.
[7] C. I. Richards, J.-C. Hsiang, A. M. Khalil, N. P. Hull, R. M. Dickson, *J. Am. Chem. Soc.* **2010**, *132*, 6318–6323.
[8] C. Fan, J.-C. Hsiang, A. E. Jablonski, R. M. Dickson, *Chem. Sci.* **2011**, *2*, 1080.
[9] C. Fan, J.-C. Hsiang, R. M. Dickson, *ChemPhysChem* **2012**, *13*, 1023–1029.
[10] A. E. Jablonski, J.-C. Hsiang, P. Bagchi, N. Hull, C. I. Richards, C. J. Fahrni, R. M. Dickson, *J. Phys. Chem. Lett.* **2012**, *3*, 3585–3591.
[11] S. Sarkar, C. Fan, J.-C. Hsiang, R. M. Dickson, *J. Phys. Chem. A* **2013**, *117*, 9501–9509.
[12] J.-C. Hsiang, A. E. Jablonski, R. M. Dickson, *Acc. Chem. Res.* **2014**, *47*, 1545–1554.
[13] D. Alcor, V. Croquette, L. Jullien, A. Lemarchand, *Proc. Natl. Acad. Sci. USA* **2004**, *101*, 8276–8280.
[14] K. Zrelli, T. Barilero, E. Cavatore, H. Berthoumieux, T. Le Saux, V. Croquette, A. Lemarchand, C. Gosse, L. Jullien, *Anal. Chem.* **2011**, *83*, 2476–2484.
[15] T. Sandén, G. Persson, P. Thyberg, H. Blom, J. Widengren, *Anal. Chem.* **2007**, *79*, 3330–3341.
[16] J. Vogelsang, C. Steinhauer, C. Forthmann, I. H. Stein, B. Person-Skegro, T. Cordes, P. Tinnefeld, *ChemPhysChem* **2010**, *11*, 2475–2490.
[17] A. C. Stiel, S. Trowitzsch, G. Weber, M. Andresen, C. Eggeling, S. W. Hell, S. Jakobs, M. C. Wahl, *Biochem. J.* **2007**, *402*, 35.
[18] R. Ando, C. Flors, H. Mizuno, J. Hofkens, A. Miyawaki, *Biophys. J.* **2007**, *92*, L97–L99.
[19] R. Ando, H. Mizuno, A. Miyawaki, *Science* **2004**, *306*, 1370–1373.
[20] Y.-T. Kao, X. Zhu, W. Min, *Proc. Natl. Acad. Sci. USA* **2012**, *109*, 3220–3225.
[21] D. Bourgeois, V. Adam, *IUBMB Life* **2012**, *64*, 482–491.
[22] X. X. Zhou, M. Z. Lin, *Curr. Opin. Chem. Biol.* **2013**, *17*, 682–690.

4.3 Supporting Information

The Supporting Information reports on:

Legends of Figures 2 and 3

Material and Methods

Supplementary texts 1-6

Table S1

Figures S1-S16

Legends of Figures 2 and 3

Fig. 2. Validation of out-of-phase imaging after optical modulation (OPIOM). **a**, **b**: Selective and quantitative imaging of Dronpa-2. **a**: A microfluidic device composed of four chambers (400 × 400 × 20 μm^3) was filled with solutions of Dronpa-2 (D2) and Fluorescein (F) as described in the scheme (the numbers indicate the concentrations in μM). The two images correspond respectively to the pre-OPIOM and OPIOM images taken at 525 nm after illuminating the microfluidic device under conditions tuned to the resonance of Dronpa-2 (λ_{exc}; I^0; ω; α) = (480 nm; 1 × 10^{-4} Ein.m^{-2}.s^{-1}; 31.4 mrad.s^{-1}; 10%). **b**: Titration of Dronpa-2 ([Dronpa-2]$_{tit}$) in Dronpa-2/Fluorescein mixtures calculated from the pre-OPIOM (circle) and OPIOM (square) image. The line shows the expected Dronpa-2 concentrations ([Dronpa-2]$_{tot}$). **c**: Selective imaging of Dronpa-2 and Dronpa-3 in a mixture containing the two photoswitchable fluorescent proteins. A microfluidic device with four square chambers (400 × 400 × 20 μm^3) was filled with mixtures of Dronpa-2 (D2) and Dronpa-3 (D3), or Fluorescein (F) as described in the scheme (the numbers indicate the concentrations in μM). The figures correspond to the pre-OPIOM and OPIOM images taken after illuminating the microfluidic device at 525 nm with sinusoidal light modulation of small amplitude tuned either to the resonance of Dronpa-2 (D2) (λ_{exc}; I^0; ω; α) = (480 nm; 1 × 10^{-4} Ein.m^{-2}.s^{-1}; 31.4 mrad.s^{-1}; 10%) or to the resonance of Dronpa-3 (D3) (λ_{exc}; I^0; ω; α) = (480 nm; 8.1 × 10^{-3} Ein.m^{-2}.s^{-1}; 314 mrad.s^{-1}; 10%). **a-c** Experiments were performed at 37℃ in pH 6.8 MES buffer.

Fig. 3. Application of out-of-phase imaging after optical modulation (OPIOM). **a**, **b**: Selective imaging of Dronpa-3 in mammalian cells. The figures correspond to the pre-OPIOM and OPIOM images of HEK293 cells co-expressing nuclear Dronpa-3 and membrane-localized EGFP. Fixed (**a**) and live cells with application of one period (**b**) of light modulation. Imaging was performed in epifluorescence with a 63× objective. Light modulation: sinusoidal modulation of large amplitude tuned on the resonance of Dronpa-3 (D3) at 37 °C (λ_{exc}; I^0; ω; α) = (480 nm; 8.1 × 10^{-3} Ein.m^{-2}.s^{-1}; 314 mrad.s^{-1}; 90%). Note that

the nuclear localization of Dronpa-3 on the OPIOM images is not perfect because of some leakage of the nuclear localization signal used. See Fig. S13 in Supporting Information for localization controls. Scale bars represent 50 μm. **c**, **d**: Selective imaging of Dronpa-3 in zebrafish embryos. The figures correspond to the pre-OPIOM and OPIOM images of the tail of a 24 hpf zebrafish embryo expressing Lifeact-Dronpa-3. Microscope specifications: (**c**) epifluorescence, 20× objective, (**d**) single plane illumination microscope (SPIM), 40× objective (the dashed rectangles indicate the zone illuminated by the thinnest part of the light sheet). Light modulation: (**c**) sinusoidal modulation of large amplitude tuned on the resonance of Dronpa-3 (D3) at 37 °C (λ_{exc}; I^0; ω; α) = (480 nm; 8.1×10^{-3} Ein.m^{-2}.s^{-1}; 314 mrad.s^{-1}; 90%), (**d**) square wave modulation of large amplitude tuned on the resonance of Dronpa-3 (D3) at 20 °C (λ_{exc}; I^0; ω; α) = (480 nm; 3.1×10^{-3} Ein.m^{-2}.s^{-1}; 44.9 mrad.s^{-1}; 96%). Imaging was performed at 525 nm. Scale bars represent 50 μm. Experiments were performed either at 37 °C (**a-c**) or 20 °C (**d**).

Materials and methods

Cloning. Dronpa-2 [1] and Dronpa-3 [2] are two variants of Dronpa with the mutation M159T and the mutations V157I / M159A respectively. The gene encoding Dronpa-3 was kindly provided by Atsushi Miyawaki. The gene encoding Dronpa-2 was kindly provided by Stefan Jakobs. The plasmids for bacterial expression of Dronpa-2/3 carrying an N-terminal hexahistidine tag were obtained by cloning their genes in the pProEX vector: the sequence coding for Dronpa-3 was inserted between *BamH* I and *EcoR* I restriction sites, while the sequence coding for Dronpa-2 was inserted between *Ehe* I and *Hind* III. The plasmids for mammalian expression of Lyn11-EGFP (with a N-terminal MGCIKSKGKDSAGGGS sequence for membrane targeting) and Dronpa-2/3-NLS (with a C-terminal GAGAPKKKRKVPKKKRKV as nuclear localisation signal) were obtained by inserting the genes encoding for Lyn11-EGFP and Dronpa-2/3-NLS in the pIRES vector (Invitrogen) using *Bgl* II and *Not* I restriction sites. For the zebrafish experiments, pCSGFPnls (eGFPnls coding sequence in pCS2) was derived from pCSGFPnERT [3] by substituting a stop codon for ER^{T2} coding sequence via synthetic oligonucleotides. pT2iU6LifactDronpa3, where Lifeact [4] and Dronpa-3 [2] coding sequences are driven by the SP6 promoter, was obtained by inserting synthetic molecules (obtained from Eurofins-MWG/Operon, Ebersberg, Germany) into a modified version of pCS2.

Protein production and purification. Dronpa-2/3 carrying an N-terminal hexahistidine tag were expressed in *E. coli* DH10B strain. Cells were grown in 1 L of Terrific Broth (TB) medium containing ampicillin (100 µg/mL) at 37°C, 140 rpm. Protein expression was induced at OD 0.6 by adding isopropyl β-D-1-thiogalactopyranoside (IPTG) to a final concentration of 1 mM. After an overnight induction at 30°C, 140 rpm, cells were harvested by centrifugation (25 min, 4200 rpm, 4°C). Cell pellet was resuspended in 20 mL of Lysis buffer (50 mM TRIS/HCl pH 7.5, 30/40 mM imidazole, 400 µM 4-(2-Aminoethyl) benzenesulfonyl fluoride hydrochloride, 0.125 mg/mL Lysozyme, and 1 mM dithiothreitol), and sonicated at 4°C. The extract was clarified by centrifugation (30 min, 15000 rpm, 4°C). The supernatant was then incubated with 0.5 mL Ni-NTA beads (Qiagen) under agitation for 2 hours at 4°C. Beads were collected by centrifugation (2 min, 2000 rpm), washed twice with 15 mL of N1 buffer (0.7 M NaCl, 30 mM imidazole, 30 mM sodium phosphate, pH 7.4) and twice with 15 mL of N2 buffer (0.1 M NaCl, 10 mM imidazole, 30 mM sodium phosphate, pH 7.4). Protein was eluted with N3 buffer (0.1 M NaCl, 300 mM imidazole, 30 mM sodium phosphate, pH 7.4), and then dialysed against TRIS/H_2SO_4 buffer (pH 8.0, 50 mM TRIS). All experiments with purified proteins aiming at characterizing their photochemical properties were performed in TRIS/H_2SO_4 buffer (pH 8.0, 50 mM TRIS). The solutions used for the titration experiments were prepared in MES buffer (pH 6.8, 50 mM MES, 100 µM BSA).

Mammalian cell culture and transfection. Human embryonic kidney 293 cells were grown at 37°C in 5% CO_2 atmosphere in DMEM with GlutaMAX-1 complemented with 10% fetal bovine serum (FBS) and 1 % penicillin / streptomycin. Cells were transiently transfected with Genejuice (Merck) according to the manufacturer's protocol. Cells were washed with Dulbecco's phosphate buffered saline (DPBS) and fixed with 2% paraformaldehyde (PFA) solution.

Zebrafish experiments. *Lifeact-Dronpa3* or *GFPnls* mRNA synthesis was performed using the mMESSAGE mMACHINE high yield capped RNA Transcription Kit from Ambion Inc. 130 ng/µL *Lifeact-Dronpa3* mRNA and/or 40 ng/µL *GFPnls* mRNA were injected into one-cell stage embryos (AB strain) and embryos maintained at 28°C in water until fixation. Embryos were fixed into PFA 4% at 4°C and then transferred into PBS (pH 7.4). The zebrafish embryos were imaged either in PBS or immobilized in 1% low melting agarose gel (Sigma-Aldrich) and mounted onto a home built sample holder under Millipore water.

Spectroscopic instruments. UV/Vis absorption spectra were recorded on a UV/Vis spectrophotometer (Cary 300 UV-Vis, Agilent Technologies, Santa Clara, CA) at 25 °C equipped with a Peltier 1 × 1 thermostated cell holder (Agilent Technologies). Samples (20 µL) were placed in 0.15 cm × 0.15 cm (light path) quartz cuvettes (Hellma Optics, Jena, Germany). Fluorescence measurements used for kinetic analysis were acquired on a LPS 220 spectrofluorometer (PTI, Monmouth Junction, NJ), equipped with a TLC50 cuvette holder (Quantum Northwest, Liberty Lake, WA) thermoregulated at 37°C. Light intensity was controlled by varying the current on a LED light source (LXML-PB01 from Philips Lumileds, San Jose, CA) filtered at 480 ± 20 nm (HQ 480-40 from Chroma Technology Corp, Rockingham, VT). The LED was supplied by a power supply (HM7042-5 from Hameg Instruments GmbH, Mainhausen, Germany). Excitation intensity was monitored over time with a photodiode (S1336-44BQ from Hamamatsu Photonics, Hamamatsu City, Japan) operating in the reversed polarization mode (+5V), while fluorescence emission was acquired simultaneously at 515 nm. Photon fluxes (excitation intensity I^0) were measured with a Nova II powermeter (Laser Measurement Instruments). During light modulation experiments, a waveform generator (33220A-20 MHz from Agilent Technologies) was added to the circuit to induce a small (10%) modulation of LED current. Excitation and emission measurements were acquired for ten periods (with 64 points per period) at each angular frequency ω.

Microfluidic device. The microdevice was composed of a circular glass coverslip (0.17 mm thick, 40 mm diameter; Menzel-Gläser, Braunschweig, Germany) and a PDMS stamp (RTV615; General Electrics, Fairfield, CT) including four 400 μm × 400 μm × 20 μm square chambers separated by 150 μm × 20 μm walls. Each chamber was connected to a sample reservoir punched in the PDMS stamp through a 40 μm × 20 μm channel. Before assembly, the coverslip and the PDMS stamp were rinced with ethanol and dried under a nitrogen flow. The bottom glass surface of the microdevice was placed on a 0.4 mm thick copper disk in which a 8 mm hole had been opened for further observation with the objective (see Microscopy section). To fill the micro-chambers with appropriate solutions, the air dissolved in the PDMS was pumped for 3 min at 50 mbar at room temperature and sample solutions were added to each reservoir, which resulted in the autonomous and controlled loading of the device.[5]

Microscopy epifluorescence setup. We used a home-built epifluorescence microscopy set-up (see Fig. S10). The samples (microfluidic device, cells and zebrafish embryos) were illuminated using a LED (LXML-PB01) as light source filtered at 480 ± 20 nm (F480-40; Semrock, Rodchester, NY) supplied by a LED driver (LEDD1B, Thorlabs Inc, Newton, NJ) and modulated by a waveform generator (33220A, Agilent Technologies). A first lens (FCN10804-LR1-RS; f = 3 mm, Ledil, Salo, Finland) was placed just after the LED and a second one (AC254-050-A; f = 50 mm, Thorlabs Inc, Newton, NJ) was used to focus the light in the back focal plane of the objective after going through the dichroic filter. Fluorescence images at 525 ± 15 nm (F525-30; Semrock) were acquired with a 10× fluar (NA 0.5, Carl Zeiss AG, Feldbach, Switzerland; for the microdevice and zebrafish experiments), a 20× Plan Apo (NA 0.75, Nikon Instruments, Amsterdam, Netherlands; for zebrafish experiments) or a 63× PL fluotar L (NA 0.7, Leica Microsystems, Germany; for cell experiments) objective mounted on a home-built microscope equipped with a Luca-R CCD camera (Andor Technology, Belfast, UK). The bottom glass surface of the imaged sample was placed on a 0.4 mm thick copper disk in which a hole of 8 mm in diameter had been opened for observation with the objective. This metal holder was itself mounted on an aluminum block thermostated at 37 ± 0.2 °C with two thermoelectric Peltier devices (CP 1.0-63-05 L-RTV; Melcor, Trenton, NJ). The stage temperature was monitored with a TCS610 thermistor (Wavelength Electronics, Bozeman, MT) and the feedback loop was driven by a MPT10000 temperature controller (Wavelength Electronics). The average excitation intensity was measured using the Nova II powermeter described previously. Under illumination conditions matching the resonance conditions of Dronpa-2 (resp. Dronpa-3), 512 images were recorded at 0.32 Hz (resp. 3.2 Hz) with 3 s exposure time (resp. 0.3116 s) corresponding to 8 periods of 200 s (resp. 20 s) (64 images per period in both cases). For imaging cells and zebrafish embryos, triggering of the camera acquisition was synchronized with the onset of the periodic excitation light (using the option "External start" in the Solis software, Andor Technology). A fixed phase delay ϕ_{acq} between the dates of camera recording and light excitation was observed (due to the exposure time and the triggering of the camera). This phase delay was calibrated using the microfluidic device described previously filled with Fluorescein: the temporal evolution of fluorescence emission of Fluorescein was fitted with $A[1 + \alpha \sin(\omega t + \phi_{\mathrm{acq}})]$ to extract the value of ϕ_{acq}. This value was then used for further image analysis of cells and zebrafish embryos.

Single plane illumination microscopy (SPIM) setup. An upright Olympus microscope (BX51WI) was converted to enable SPIM experiments (Fig. S15). The light sheet was created by a cylindrical lens (LJ1558RM-A, f = 300 mm, Thorlabs) shaping the illumination laser beam from a PhoxX 488-100 laser diode (Omicron-Laserage Laserprodukte, Rodgau-Dudenhofen, Germany) into a rectangle. This rectangle was then passed through a 20× objective (Olympus LMPLANFL, NA 0.40) which focuses it only in one plane generating a thin light sheet in the focal plane of the detection objective. The geometry of the illuminating beam can be approximated by Gaussian beam optics, with a central thickness of 3.4 μm (full width at half maximum). Average excitation intensity of the incident laser beam was calibrated by recording the photoswitching relaxation rate constant of Dronpa-3 in *Lifeact-Dronpa3* mRNA injected embryos after light jump experiments (at 20°C). To match the resonant conditions for Dronpa-3, the laser power was eventually varied between 0.1 mW to 5 mW using analog modulation input of the laserhead and a square waveform generator (33220A; Agilent Technologies) and the laser beam was further attenuated by a NE10A neutral density filter (Thorlabs) to deliver a light sheet intensity of 1.5 μW and 80 μW respectively. Fluorescence light was collected with a 40× water dipping objective (Olympus LUMPLFLN, NA 0.80), and filtered with a beam-splitter (Di01-R405/488/532/635 BrightLine quad-edge laser-flat dichroic beamsplitter, Semrock) and an emission filter (BA510-550, Olympus). Under illumination conditions matching the resonance conditions of Dronpa-3 at 20°C, 512 images were recorded at 0.46 Hz with 2.187 s exposure time corresponding to 8 periods of 140 s. In this series of experiments, triggering of the camera acquisition was synchronized with the onset of the square wave excitation light (using the option “External start”' in the Solis software, Andor Technology).

Softwares. Data treatment, image analysis and theoretical computations were performed using Igor Pro (WaveMetrics), MATLAB (The MathWorks) and Gnuplot softwares.

Protocols for Image analysis are described in Supplementary text 6.

Supplementary text 1: Photoswitchable fluorophore responses to light modulations

The model

The dynamic behavior of a photoswitchable probe **P** illuminated with a light of intensity $I(t)$ can be described by the two-state exchange (1)

$$\mathbf{1} \quad \underset{k_{21}(t)}{\overset{k_{12}(t)}{\rightleftharpoons}} \quad \mathbf{2} \tag{1}$$

where the thermodynamically most stable state **1** is photochemically converted to the thermodynamically less stable state **2** at rate constant $k_{12}(t) = \sigma_{12}I(t)$ from which it can relax back to the initial state **1** either by a photochemically- or a thermally-driven process at rate constant $k_{21}(t) = \sigma_{21}I(t) + k_{21}^{\Delta}$ where $\sigma_{21}I(t)$ and k_{21}^{Δ} are respectively the photochemical and the thermal contributions of the rate constant. In that case, the molecular action cross-sections for photoisomerization σ_{12} and σ_{21} and the thermal rate constant k_{21}^{Δ} fully define the behavior of the photoswitchable probe.

We assume that the system is either homogeneously illuminated or that it can be considered homogeneous at any time of its evolution. Then we rely on the two-state exchange (1) to write Eqs.(2–3) describing the concentration evolutions:

$$\frac{d1}{dt} = -k_{12}(t)\,1 + k_{21}(t)\,2 \tag{2}$$

$$\frac{d2}{dt} = k_{12}(t)\,1 - k_{21}(t)\,2. \tag{3}$$

Response to light jumps

When the system is submitted to a constant illumination defined by the intensity $I(t) = I^0$, the forward and backward rate constants become

$$k_{12}(t) = k_{12}^0 = \sigma_{12}I^0 \tag{4}$$

$$k_{21}(t) = k_{21}^0 = \sigma_{21}I^0 + k_{21}^{\Delta}. \tag{5}$$

The temporal evolution of the concentrations in **1** and **2** evolves as

$$2 - 2^0 = 1^0 - 1 = -2^0 \exp\left(-\frac{t}{\tau_{12}^0}\right) \tag{6}$$

where $\tau_{12}^0 = 1/(k_{12}^0 + k_{21}^0)$ designates the relaxation time of the photoswitchable fluorophore and 1^0 and 2^0 the concentrations of **1** and **2** at the photostationnary state reached after τ_{12}^0

$$1^0 = P_{tot} - 2^0 = \frac{1}{1 + K_{12}^0}P_{tot} \tag{7}$$

where $K_{12}^0 = k_{12}^0/k_{21}^0$ and the total concentration in photoswitchable probe **P**, $P_{tot} = 1 + 2$.

The fluorescence emission $I_F(t)$ results then from the individual contributions of the species **1** and **2**, and can be written

$$I_F(t) \quad = \quad (Q_1 1 + Q_2 2)\, I(t) \tag{8}$$

where Q_1 and Q_2 are the molecular brightnesses of **1** and **2**. From Eq.(6), one subsequently derives

$$\frac{I_F(t)}{Q_1 P_{tot} I^0} \quad = \quad 1 + \left(\frac{Q_2}{Q_1} - 1\right) \frac{\sigma_{12} I^0}{(\sigma_{12} + \sigma_{21}) I^0 + k_{21}^{\Delta}} \left\{1 - \exp\left\{-\left[(\sigma_{12} + \sigma_{21}) I^0 + k_{21}^{\Delta}\right] t\right\}\right\}. \tag{9}$$

At infinite times, fluorescence emission asymptotically tends toward $I_F^0 = \left(Q_1 1^0 + Q_2 2^0\right) I^0$.

Upon switching off illumination, the fluorescence emission relaxes to its initial value $Q_1 P_{tot} I^0$ according to

$$\frac{I_F(t)}{Q_1 P_{tot} I^0} \quad = \quad 1 + \left(\frac{Q_2}{Q_1} - 1\right) \frac{\sigma_{12} I^0}{(\sigma_{12} + \sigma_{21}) I^0 + k_{21}^{\Delta}} \exp\left(-k_{21}^{\Delta} t\right). \tag{10}$$

Response to sinusoidal light modulation of small amplitude

To illustrate the behavior of the system upon illumination with a periodically modulated light, we first consider a sinusoidally modulated illumination oscillating around the averaged value I^0 at angular frequency ω and with a small amplitude εI^0 ($\varepsilon \ll 1$) (see Figure S1a[1]) such that

$$I(t) = I^0 \left[1 + \varepsilon \sin(\omega t)\right]. \tag{11}$$

After introducing

$$k_{12}(t) \quad = \quad \sigma_{12} I^0 \left[1 + \varepsilon \sin(\omega t)\right] \tag{12}$$

$$k_{21}(t) \quad = \quad \sigma_{21} I^0 \left[1 + \varepsilon \sin(\omega t)\right] + k_{21}^{\Delta}, \tag{13}$$

the system of differential equations governing the temporal evolution of the concentrations in **1** and **2** is solved at the first-order expansion in the light perturbation. Beyond the relaxation time τ_{12}^0, one enters into the forced and permanent regime where the concentration

$$i = i^0 + \varepsilon i^1 \sin(\omega t - \phi_{12}) \tag{14}$$

in each species **i** (**i** = **1** or **2**) oscillates around a mean value i^0 (corresponding to the concentration of **i** at steady-state associated to the photon flux I^0; see Eq.(7)) at the angular frequency ω but with a phase delay of $\phi_{12} = \arctan\left(\omega \tau_{12}^0\right)$ (see Figure S1b[2]). The amplitudes of the concentration modulation are given in Eq.(15)

$$2^1 \quad = \quad -1^1 = \frac{\rho_{12}^0 \tau_{12}^0 p_{21}^{\Delta}}{\sqrt{1 + \left(\omega \tau_{12}^0\right)^2}} \tag{15}$$

---

[1] To facilitate notations in Figure S1a, we have adopted $\overrightarrow{I}(t) = \overrightarrow{I^0} + \overrightarrow{\Delta I}(t)$ where the projection of $\overrightarrow{\Delta I}$ along the y-axis $\Delta I_y = \varepsilon I^0 \sin(\omega t)$ contains the temporal dependence of light intensity.

[2] To facilitate notations in Figure S1b, we have adopted $\overrightarrow{1}(t) = \overrightarrow{1^0} - \overrightarrow{\Delta 2}(t)$ and $\overrightarrow{2}(t) = \overrightarrow{2^0} + \overrightarrow{\Delta 2}(t)$ where the projection of $\overrightarrow{\Delta 2}$ along the y-axis $\Delta 2_y = \varepsilon 2^1 \sin(\omega t - \phi_{12})$ contains the temporal dependence of the concentrations in **1** and **2**.

where $\rho_{12}^0 = k_{12}^0 1^0 = k_{21}^0 2^0$ and $p_{21}^\Delta = k_{21}^\Delta/(\sigma_{21}I^0 + k_{21}^\Delta)$ respectively designate the steady-state rate of reaction (1) and the relative thermal contribution to **2** relaxation upon illuminating at I^0.

The phase-delayed oscillating concentrations i can also be written

$$i(t) = i^0 + \varepsilon\left[i^{1,in}\sin(\omega t) + i^{1,out}\cos(\omega t)\right] \tag{16}$$

where $\varepsilon i^{1,in}\sin(\omega t)$ and $\varepsilon i^{1,out}\cos(\omega t)$ are in-phase and out-of-phase (or quadrature-delayed) oscillating terms at angular frequency ω. The amplitudes $i^{1,in}$ and $i^{1,out}$ of the in-phase and out-of-phase oscillating terms are (see Figure S1c[3])

$$2^{1,in} = -1^{1,in} = \rho_{12}^0\tau_{12}^0 p_{21}^\Delta \frac{1}{1+\left(\omega\tau_{12}^0\right)^2} = p_{21}^\Delta \frac{K_{12}^0}{\left(1+K_{12}^0\right)^2}\frac{1}{1+\left(\omega\tau_{12}^0\right)^2}P_{tot} \tag{17}$$

$$2^{1,out} = -1^{1,out} = -\rho_{12}^0\tau_{12}^0 p_{21}^\Delta \frac{\omega\tau_{12}^0}{1+\left(\omega\tau_{12}^0\right)^2} = -p_{21}^\Delta \frac{K_{12}^0}{\left(1+K_{12}^0\right)^2}\frac{\omega\tau_{12}^0}{1+\left(\omega\tau_{12}^0\right)^2}P_{tot} \tag{18}$$

where we used that $\rho_{12}^0\tau_{12}^0 = P_{tot}\left[K_{12}^0/\left(1+K_{12}^0\right)^2\right]$.

Since the fluorescence emission results from the contributions of the species **1** and **2**, the phase delay within the oscillating concentrations leads to a phase delay of the oscillating fluorescence emission. The phase-delayed oscillating fluorescence emission is therefore

$$I_F(t) = I_F^0 + I_F^{1,\mathrm{in}}\sin(\omega t) + I_F^{1,\mathrm{out}}\cos(\omega t) \tag{19}$$

where the amplitude $I_F^{1,\mathrm{in}}$ and $I_F^{1,\mathrm{out}}$ of the in-phase and out-of-phase terms are

$$I_F^{1,\mathrm{in}} = \varepsilon\left[\left(Q_1 1^0 + Q_2 2^0\right) + \left(Q_1 - Q_2\right)1^{1,in}\right]I^0 \tag{20}$$

$$I_F^{1,\mathrm{out}} = \varepsilon\left(Q_1 - Q_2\right)1^{1,out}I^0. \tag{21}$$

Optimal out-of-phase response

Figure 1b displays the dependence of the normalized out-of-phase $|\Delta 1_{norm}^{out}| = |1^{1,out}/\varepsilon P_{tot}|$ amplitude on the control parameters I^0 and ω for a given photoswitchable probe **P** characterized by the triplet of parameters $\left(\sigma_{12}, \sigma_{21}, k_{21}^\Delta\right)$. We typically adopted reasonable estimates for Dronpa-2 (*vide infra*). $|\Delta 1_{norm}^{out}|$ exhibits a single optimum when the control parameters (I^0,ω) verify

$$I^0 = \frac{k_{21}^\Delta}{\sigma_{12}+\sigma_{21}} \tag{22}$$

$$\omega = 2k_{21}^\Delta. \tag{23}$$

The optimization of $1^{1,out}$ results from the independent optimisation of the terms $p_{21}^\Delta K_{12}^0 P_{tot}/\left(1+K_{12}^0\right)^2$ and $\omega\tau_{12}^0/[1+\left(\omega\tau_{12}^0\right)^2]$ in Eq.(18) (see Figure S1c). $\varepsilon p_{21}^\Delta K_{12}^0 P_{tot}/\left(1+K_{12}^0\right)^2$ measures the composition shift $\Delta 2^0$ from the steady-state 2^0 after a light intensity jump of amplitude $\Delta I^0 = \varepsilon I^0$.[4] It depends on I^0

---

[3] To facilitate notations in Figure S1c, we have adopted $\overrightarrow{\Delta 2}(t) = \overrightarrow{\Delta 2^{in}}(t) + \overrightarrow{\Delta 2^{out}}(t)$ with $\varepsilon 2^{1,in}$ and $\varepsilon 2^{1,out}$ respective amplitudes for the in- and out-components.

[4] From the expression (7), one can show that $\frac{d2^0}{dLnI^0} = \frac{\Delta 2^0}{\varepsilon} = p_{21}^\Delta K_{12}^0 P_{tot}/\left(1+K_{12}^0\right)^2$ using $K_{12}^0 = k_{12}^0/k_{21}^0$ with the expressions of k_{12}^0 and k_{21}^0 given in Eqs.(4,5).

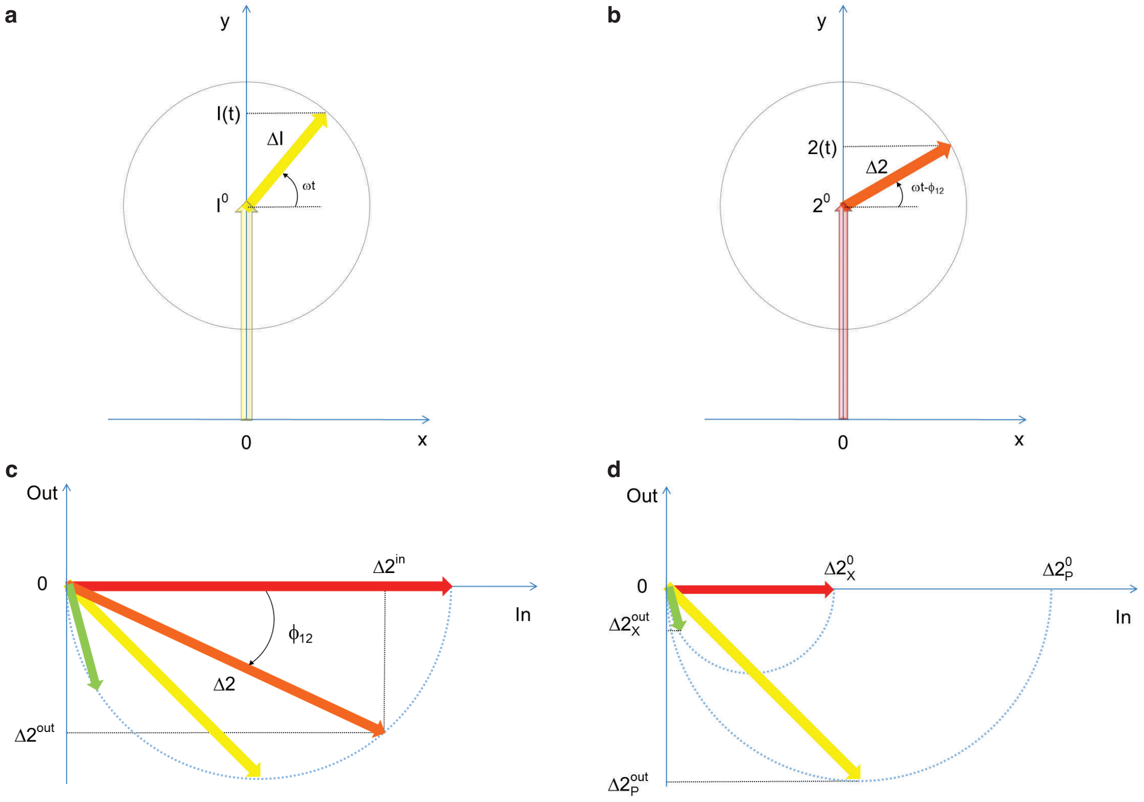

Figure S1: Vectorial representation of the dynamic behavior of a photoswitchable fluorophore submitted to a sinusoidal light modulation. **a**: Light intensity is the projection along the y axis of the sum of two vectors: the first (length I^0) is constant whereas the second (length ΔI; equal to εI^0 for a light modulation of small amplitude) rotates at ω radial frequency in the (x,y) plane; **b**: The concentration of the state **2**, $2(t)$, is similarly the projection along the y axis of the sum of two vectors: $\vec{2^0}$, which is fixed (length 2^0) and $\vec{\Delta 2}$ (length $\Delta 2$) (respectively identified to $\varepsilon \vec{2^1}$ and $\varepsilon 2^1$ for a light modulation of small amplitude), which rotates at ω radial frequency but with a phase delay of ϕ_{12}; **c**: In the rotating frame associated to light excitation, $\vec{\Delta 2}$ is fixed with $\Delta 2^{in}$ and $\Delta 2^{out}$ coordinates along the in- and out-of-phase axes. For a given photoswitchable fluorophore, increasing ω increases ϕ_{12} and decreases $\Delta 2$, as illustrated by the shift from the red to the green arrow. More precisely, denoting $\Delta 2^0$ the shift from the 2^0 steady-state **2** concentration upon increasing light intensity by ΔI^0, the extremity of the vector $\vec{\Delta 2}$ describes the circle of center coordinates ($\Delta 2^0/2$,0) and radius $\Delta 2^0/2$ when ω varies from zero to the infinite. $\Delta 2^{in}$ is maximized and equal to $\Delta 2^0$ when $\omega = 0$; it vanishes when ω becomes infinite. In contrast, $\Delta 2^{out}$ is vanishing for both zero and infinite ω values, but is maximized for $\phi_{12} = \pi/4$ (yellow arrow); **d**: In a mixture of photoswitchable fluorophores, the out-of-phase first-order concentration response can discriminate a given target **P** (yellow arrow) among interfering species **X** (red and green arrows) when I^0 and ω are tuned so as to maximize $\Delta 2^0_P$ and setting $\phi_{12,P} = \pi/4$. Most non-resonant interfering species are then characterized by $\Delta 2^0_X$ smaller than $\Delta 2^0_P$ and $\phi_{12,X} \neq \pi/4$ so as to yield vanishing $\Delta 2^{out}$ contributions.

and is maximized in a regime of intermediate illumination, in which thermally- and photochemically-driven reactions occur at the same rate such that $k_{21}^{\Delta} = (\sigma_{12} + \sigma_{21})I^0$ (see Eq. (22)). When the light intensity is too low, the thermal relaxation dominates the photoisomerization and the light intensity jump $\Delta I^0 = \varepsilon I^0$ cannot significantly shifts the photoswitchable probe from the state **1**. Conversely, when the light intensity is too large, the thermal relaxation does not contribute anymore to the dynamics of the exchange (1): the relative proportions in states **1** and **2** become independent of the light intensity, so there is no composition shift induced by the light jump. The second optimised term, $\omega\tau_{12}^0/[1+\left(\omega\tau_{12}^0\right)^2]$, is maximized upon matching the radial frequency of the light modulation ω with the exchange relaxation time τ_{12}^0 so that $\omega\tau_{12}^0 = 1$ (see Eqs. (22,23)). When $\omega \gg 1/\tau_{12}^0$, the exchange is slow compared to the light variations and the couple $\{\mathbf{1},\mathbf{2}\}$ has not enough time to respond: both $i^{1,in}$ and $i^{1,out}$ vanish. Conversely, when $\omega \ll 1/\tau_{12}^0$, $i^{1,out}$ cancels, so the concentrations of **1** and **2** oscillate in phase with the light modulation.

Response to periodic light modulation of large amplitude

The use of a sinusoidal modulation of small amplitude is favorable to derive simple analytical expressions. However, it generates only weak variations of the probe signal because of the small modulation, which is a drawback to reliably extract the out-of-phase amplitude of the first order response. To circumvent this drawback, we also analyzed the response of a photoswitchable probe to two different periodic modulations of large amplitude α:

- As a natural extension of the previous case, we first considered a sinusoidal modulation of large amplitude and correspondingly adopted

$$I(t) \quad = \quad I^0\left[1+\alpha\sin\left(\omega t\right)\right]; \tag{24}$$

- We then considered a square wave modulation because its experimental implementation (on-off illumination switching) is simple. Its Fourier series expansion obeys

$$I(t) \quad = \quad I^0\left\{1+\frac{4\alpha}{\pi}\sum_{p=0}^{\infty}\frac{1}{2p+1}\sin\left[\left(2p+1\right)\omega t\right]\right\} \tag{25}$$

  by choosing the starting time ($t = 0$) in this expansion halfway through the first pulse.

The theoretical developments are reported in another paper.[7] In this section, we only introduce the expressions, which are relevant to analyze the data reported in the Main Text.

At steady-state, a large periodic modulation of illumination causes modulation of the concentrations in **1** and **2** not only at one but at an infinite number of radial frequencies. The concentration of **i** now contains the amplitudes $\mathrm{i}^{\mathrm{n,in}}$ and $\mathrm{i}^{\mathrm{n,out}}$ of the in-phase and out-of phase terms oscillating at the radial frequency $n\omega$

$$i \quad = \quad \mathrm{i}^{\mathrm{o}}+\alpha\sum_{n=1}^{+\infty}\left[\mathrm{i}^{\mathrm{n,in}}\sin\left(n\omega t\right)+\mathrm{i}^{\mathrm{n,out}}\cos\left(n\omega t\right)\right]. \tag{26}$$

Interestingly, i^{o}, $\mathrm{i}^{\mathrm{n,in}}$ and $\mathrm{i}^{\mathrm{n,out}}$ are proportional to P_{tot}. Moreover we showed that $\mathrm{i}^{1,\mathrm{out}}$ exhibits an optimum in the space (I^0,ω), which coordinates and amplitude are very close to those observed with a sinusoidal modulation of small amplitude (upon taking into account a $\frac{4}{\pi}$ amplitude correction in the specific case of the square-wave light modulation, which originates from the Fourier series expression given in Eq.(25)).[5]

---

[5] In fact the error done when taking the analytical expression of the resonance conditions, valid only for a modulation of small amplitude, is always less than 20 %, no matter which amplitude α is used. Such an error would be of the order of magnitude of the experimental errors done when fixing the average light intensity and radial frequency to their values at resonance, $I^{0,R}$ and ω^R.

Considering that both concentrations of the states **1** and **2**, and light intensity are modulated, the fluorescence emission $I_F(t)$ can be written

$$I_F(t) \quad = \quad \left[Q_1 1(t) + Q_2 2(t)\right] I(t) = \mathfrak{I}_{\mathfrak{F}}^{\mathrm{0}} + \sum_{n=1}^{\infty}\left[\mathfrak{I}_{\mathfrak{F}}^{\mathrm{n,in}} \sin\left(n\omega t\right) + \mathfrak{I}_{\mathfrak{F}}^{\mathrm{n,out}} \cos\left(n\omega t\right)\right] \tag{27}$$

where

$$\mathfrak{I}_{\mathfrak{F}}^{\mathrm{1,out}} \quad = \quad \alpha\left(Q_2 - Q_1\right) I^0 \left[2^{\mathrm{1,out}} + g\left(2^{\mathrm{n,in}}, 2^{\mathrm{n,out}}\right)\right] \tag{28}$$

with $n \geq 1$. Whereas $g\left(2^{\mathrm{n,in}}, 2^{\mathrm{n,out}}\right) = 0$ for a sinusoidal modulation of small amplitude, $g\left(2^{\mathrm{n,in}}, 2^{\mathrm{n,out}}\right)$ is non-vanishing in the case of a periodic modulation of large amplitude.

In a regime of sinusoidal modulation of small amplitude, the out-of-phase amplitude of the fluorescence emission, $\mathfrak{I}_{\mathfrak{F}}^{\mathrm{1,out}}$, is proportional to $2^{1,out}$ and exhibits a resonant behavior. In contrast, such a conclusion cannot be directly drawn in the case of periodic modulation of large amplitude since analytical expressions are cumbersome. We therefore evaluated its relevance by means of numerical calculations using typical values found for photoswitchable fluorescent proteins. We showed that $\mathfrak{I}_{\mathfrak{F}}^{\mathrm{1,out}}$is proportional to $2^{\mathrm{1,out}}$ and exhibits an optimum in the space (I^0,ω), which coordinates and amplitude are very close to those observed with a sinusoidal modulation of small amplitude (with the $\frac{4}{\pi}$ amplitude correction in the case of the square-wave light modulation). Hence, the analysis of the out-of-phase first-order fluorescence emission $\mathfrak{I}_{\mathfrak{F}}^{\mathrm{1,out}}$ enables the selective and quantitative detection of a photoswitchable fluorophore.

Retrieval of concentrations from the fluorescence intensity

Extraction of $\mathfrak{I}_{\mathfrak{F}}^{\mathrm{0}}$, $\mathfrak{I}_{\mathfrak{F}}^{\mathrm{1,in}}$, and $\mathfrak{I}_{\mathfrak{F}}^{\mathrm{1,out}}$ from the overall signal $I_F(t)$

Upon modulating light, the fluorescence intensity associated to the photoswitchable probe adopts the general expression (27). $\mathfrak{I}_{\mathfrak{F}}^{\mathrm{0}}$, $\mathfrak{I}_{\mathfrak{F}}^{\mathrm{1,in}}$, and $\mathfrak{I}_{\mathfrak{F}}^{\mathrm{1,out}}$ can be easily retrieved from the experimental trace of the observed signal $I_F(t)$ (either global or from each analyzed pixel).

As shown in Eq.(27), $\mathfrak{I}_{\mathfrak{F}}^{\mathrm{0}}$ can be obtained upon averaging $I_F(t)$ over an integer number m of periods of the modulated illumination

$$Int^0 \quad = \quad \frac{1}{mT}\int_0^{mT} I_F(t)dt = \mathfrak{I}_{\mathfrak{F}}^{\mathrm{0}}. \tag{29}$$

In particular, upon observing fluorescence emission in a regime of sinusoidal light modulation of small amplitude, one has $Int^0 = I_F^0$.

The first-order amplitudes $\mathfrak{I}_{\mathfrak{F}}^{\mathrm{1,in}}$ and $\mathfrak{I}_{\mathfrak{F}}^{\mathrm{1,out}}$ can be extracted from the fluorescence signal upon computing the integrals $Int^{1,in}$ and $Int^{1,out}$

$$Int^{1,in} \quad = \quad \frac{2}{mT}\int_0^{mT} I_F(t)\sin\left(\omega t\right)dt = \mathfrak{I}_{\mathfrak{F}}^{\mathrm{1,in}} \tag{30}$$

$$Int^{1,out} \quad = \quad \frac{2}{mT}\int_0^{mT} I_F(t)\cos\left(\omega t\right)dt = \mathfrak{I}_{\mathfrak{F}}^{\mathrm{1,out}}. \tag{31}$$

Upon observing fluorescence emission in a regime of sinusoidal light modulation of small amplitude, one has $Int^{1,in} = I_F^{1,in}$ and $Int^{1,out} = I_F^{1,out}$, and $Int^{n,in} = I_F^{n,in} = 0$ and $Int^{n,out} = I_F^{n,out} = 0$.

Eqs.(30,31) illustrate orthogonality between the various components of the fluorescence intensity in Eq. (27). In particular, the computed integral $Int^{1,out}$ used to extract the OPIOM image does not contain any contribution from the constant amplitude $\mathfrak{I}_{\mathfrak{F}}^{0}$ as well as from the in-phase amplitude $\mathfrak{I}_{\mathfrak{F}}^{1,\mathfrak{in}}$. This mathematical property is crucial to eliminate the contributions of non-photoactive fluorescent interfering species, which fluorescence response contains constant and in-phase terms only.

Quantifying a targeted photoswitchable probe

In the absence of light modulation or in a regime of sinusoidal light modulation of small amplitude, the expression of $\mathfrak{I}_{\mathfrak{F}}^{0}$ is

$$\frac{\mathfrak{I}_{\mathfrak{F}}^{0}}{I^0} = Q_1 \frac{1}{1+K_{12}^0} P_{tot} + Q_2 \frac{K_{12}^0}{1+K_{12}^0} P_{tot} \tag{32}$$

where

$$K_{12}^0 = \frac{\sigma_{12} I^0}{\sigma_{21} I^0 + k_{21}^{\Delta}}. \tag{33}$$

In the presence of light modulation, $\mathfrak{I}_{\mathfrak{F}}^{1,\mathfrak{out}}$ can be reliably evaluated from its expression in the case of a sinusoidal light modulation of small amplitude

$$\frac{\mathfrak{I}_{\mathfrak{F}}^{1,\mathfrak{out}}}{I^0} = \varepsilon \left(Q_1 - Q_2\right) p_{21}^{\Delta} \frac{K_{12}^0}{\left(1+K_{12}^0\right)^2} \frac{\omega \tau_{12}^0}{1+\left(\omega \tau_{12}^0\right)^2} P_{tot} \tag{34}$$

where K_{12}^0 is given in Eq.(33) and where

$$p_{21}^{\Delta} = \frac{k_{21}^{\Delta}}{\sigma_{21} I^0 + k_{21}^{\Delta}} \tag{35}$$

$$\tau_{12}^0 = \frac{1}{\left(\sigma_{12}+\sigma_{21}\right) I^0 + k_{21}^{\Delta}}. \tag{36}$$

The theoretical expressions (32,34) make possible to directly retrieve the concentrations of the photoswitchable probe from the fluorescence intensity. However this approach requires the effort to acquire the values of all parameters involved in these expressions. Alternatively, quantification can proceed by calibration with the pure photoswitchable probe at a reference concentration. Eqs.(32,34) show that $\mathfrak{I}_{\mathfrak{F}}^{0}$ and $\mathfrak{I}_{\mathfrak{F}}^{1,\mathfrak{out}}$ are proportional to the overall concentration in photoswitchable probe. Thus quantification can be simply achieved by recording the fluorescence intensity from a calibrating solution of the photoswitchable probe at a known concentration P_{tot}^{cal}. The concentrations of the photoswitchable probe, which are retrieved at zeroth- and first-order, are respectively

$$P_{tot}^0 = \frac{\mathfrak{I}_{\mathfrak{F}}^{0}}{\mathfrak{I}_{\mathfrak{F}}^{0,\mathfrak{cal}}} P_{tot}^{cal} \tag{37}$$

$$P_{tot}^{1,out} = \frac{\mathfrak{I}_{\mathfrak{F}}^{1,\mathfrak{out}}}{\mathfrak{I}_{\mathfrak{F}}^{1,\mathfrak{out},\mathfrak{cal}}} P_{tot}^{cal}. \tag{38}$$

Selective and quantitative detection

Optimizing the out-of-phase first-order response by choosing a couple (I^0,ω) that verifies the resonance conditions (22) and (23) opens an interesting way to selectively image and quantify a photoswitchable fluorophore **P** in the presence of interfering compounds **X** (of total concentrations X_{tot}), each defined by a different set of parameters $\left(\sigma_{12,X}, \sigma_{21,X}, k_{21,X}^{\Delta}\right)$. Note that **X** can be non-photoswitchable: in that case $\sigma_{12,X}$ = $\sigma_{21,X}$ = 0 and $k_{21,X}^{\Delta}$ = 0. To illustrate this, let us take a simplified case of a mixture containing photoswitchable fluorophores, whose only the state **1** yields an observable fluorescence emission, and possessing all the same brightness Q_1. In that case, a protocol relying on illumination at constant light intensity I^0 leads to a signal I_F^0 which is proportional to the sum of the contributions of the different fluorophores such that:

$$I_F^0 \quad \propto \quad 1_P^0 + \sum_X 1_X^0 = (1_P^0/P_{tot})P_{titration}^0 \tag{39}$$

where

$$P_{titration}^0 \quad = \quad P_{tot} + \sum_X \frac{(1_X^0/X_{tot})}{(1_P^0/P_{tot})} X_{tot} > P_{tot} \tag{40}$$

When the signal I_F^0 is used to titrate the concentration of **P**, the titration result $P_{titration}^0$ always overestimates the total concentration P_{tot} because of the contributions of the interfering compounds (see Figure S2b).

In contrast, the corresponding out-of-phase first-order response to light modulation $\mathfrak{I}_{\mathfrak{F}}^{1,\mathfrak{out}}$

$$\mathfrak{I}_{\mathfrak{F}}^{1,\mathfrak{out}} \quad \propto \quad 1_P^{1,out} + \sum_X 1_X^{1,out} = (1_P^{1,out}/P_{tot})P_{titration}^{1,out} \tag{41}$$

where

$$P_{titration}^{1,out} = P_{tot} + \sum_X \frac{(1_X^{1,out}/X_{tot})}{(1_P^{1,out}/P_{tot})} X_{tot} \tag{42}$$

enables to determine P_{tot} when the light parameters (I^0,ω) are tuned to the resonance conditions of **P**. Indeed, the term $1_P^{1,out}$ is then maximal while the terms $1_X^{1,out}$ are negligible. Thus, the signal from **P** now dominates those of the other probes, and the titration result $P_{titration}^{1,out}$ is approximatively equal to P_{tot} (see Figure S2b). Figure S2a illustrates for various mixtures the superiority of this second strategy over measurements performed at constant light intensity: whereas all the $P_{titration}^0$ are several times larger than the actual P_{tot} concentration, the discrepancy between $P_{titration}^{1,out}$ and P_{tot} becomes negligible as soon as $\left(\sigma_{12}, \sigma_{21}, k_{21}^{\Delta}\right)$ deviates from $\left(\sigma_{12,X}, \sigma_{21,X}, k_{21,X}^{\Delta}\right)$.

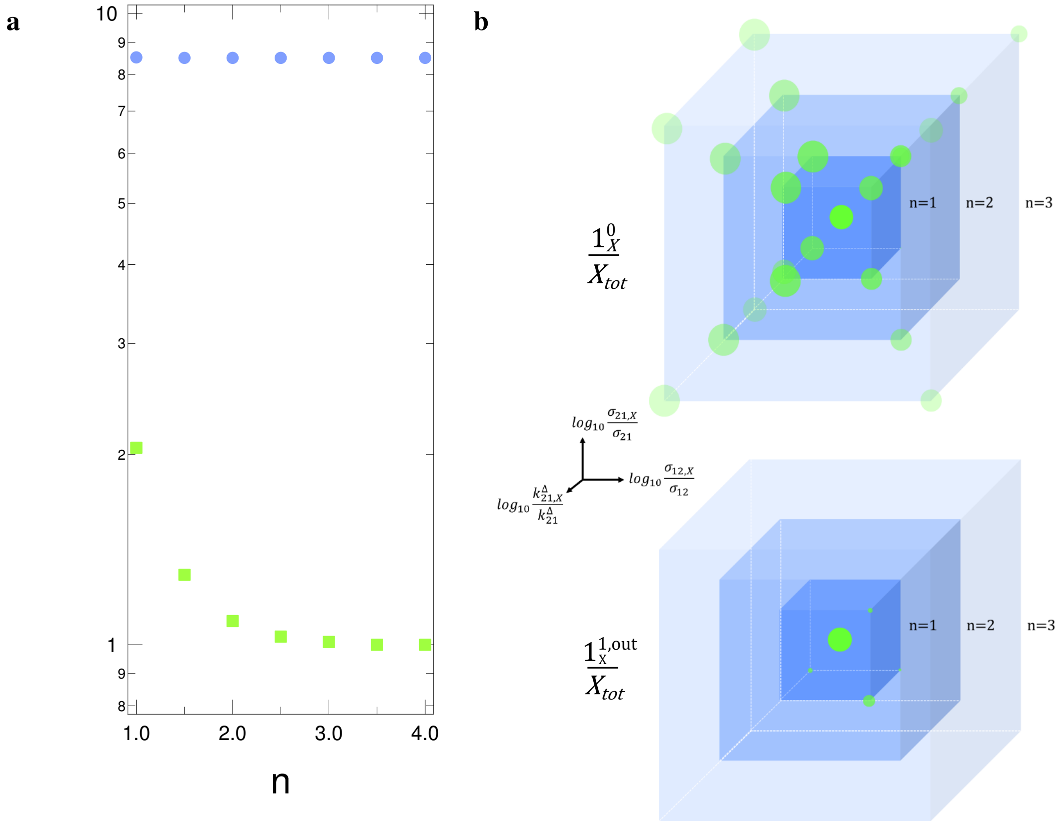

Figure S2: Theoretical computation of the ratio between the titration outcome $P_{titration}$ (which assumes that only the reactant of interest is present) and the effective target concentration P_{tot} (**a**). Results for both the constant light intensity (pre-OPIOM; disks) and the OPIOM (squares) methods are compared for seven different equimolar mixtures which include the targeted triplet $(\sigma_{12}, \sigma_{21}, k_{21}^{\Delta})$ plus eight other interfering ones. In each sample labelled n, the latter species correspond to the eight $(\sigma_{12,X}, \sigma_{21,X}, k_{21,X}^{\Delta})$ sets placed on the nodes of a cube centered on $(\sigma_{12}, \sigma_{21}, k_{21}^{\Delta})$ and which mesh size is n in decimal logarithmic units (**b**). In **b**, the individual responses $(1_X^0/X_{tot})$ and $(1_X^{1,out}/X_{tot})$ have been used to define the sphere radius associated to each $(\sigma_{12,X}, \sigma_{21,X}, k_{21,X}^{\Delta})$ set in $(1^0/P_{tot})$ and $(1^{1,out}/P_{tot})$ units. σ_{12} = 73 m^2.mol^{-1}, σ_{21} = 84 m^2.mol^{-1}, $k_{21}^{\Delta} = 1.5 \times 10^{-2}$ s^{-1}; $I^0 = k_{21}^{\Delta}/(\sigma_{12} + \sigma_{21}) = 9.6 \times 10^{-5}$ Ein.s^{-1}.m^{-2}, $\omega = 2k_{21}^{\Delta} = 3 \times 10^{-2}$ rad·s^{-1}.

Supplementary Text 2: Reduction of photo(physical)chemical mechanisms to a two-state exchange

In the following subsections, we show that various mechanisms involving light absorption can be reduced to the two-state model (1) at an appropriate time scale.

A photoswitchable probe

In a first step, we examine the behaviour of a photoswitchable probe. Light absorption is supposed to drive the exchange between two ground singlet states of a probe denoted **S**$_{0,i}$ (i=1 or 2). In the considered scheme, the state **S**$_{0,1}$ is supposed to be thermodynamically more stable than the state **S**$_{0,2}$. Mechanistically, this exchange involves light absorption leading each ground state **S**$_{0,i}$ to its corresponding first singlet excited state **S**$_{1,i}$. The latter is then assumed to relax either by leading back to the **S**$_{0,i}$ state (for instance by emission of a photon when the probe is a photoswitchable fluorophore) or by photoisomerization (yielding the other ground state). The ground state **S**$_{0,2}$ can also notably relax thermally toward the more stable **S**$_{0,1}$ state. The overall scheme is displayed in Figure S3.

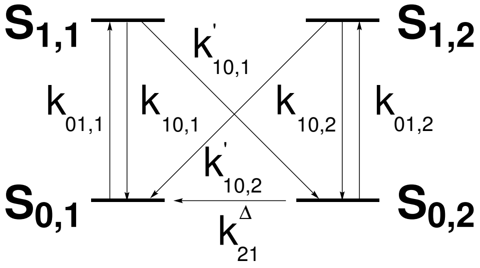

Figure S3: Mechanism accounting for the behaviour of a photoswitchable probe upon illuminating. The arrows and the associated rate constants refer to the exchange processes. See Text.

Relying on the mechanism displayed in Figure S3, we first write Eqs.(43–46) to describe the concentration evolutions:

$$\frac{dS_{0,1}}{dt} = -k_{01,1}S_{0,1} + k_{10,1}S_{1,1} + k_{21}^{\Delta}S_{0,2} + k_{10,2}^{'}S_{1,2} \tag{43}$$

$$\frac{dS_{0,2}}{dt} = k_{10,1}^{'}S_{1,1} - \left(k_{01,2} + k_{21}^{\Delta}\right)S_{0,2} + k_{10,2}S_{1,2} \tag{44}$$

$$\frac{dS_{1,1}}{dt} = k_{01,1}S_{0,1} - \left(k_{10,1} + k_{10,1}^{'}\right)S_{1,1} \tag{45}$$

$$\frac{dS_{1,2}}{dt} = k_{01,2}S_{0,2} - \left(k_{10,2} + k_{10,2}^{'}\right)S_{1,2}. \tag{46}$$

In Figure S3, the rate constants $k_{10,i}$ and $k_{10,i}^{'}$ are notably much larger than the rate constants $k_{01,i}$ and k_{21}^{Δ}. $k_{10,i}$ and $k_{10,i}^{'}$ are typically larger than $10^9\mathrm{s}^{-1}$.[6] In contrast, $k_{01,i}$ is in the 10 s^{-1} range under typical illumination conditions.[6] Moreover k_{21}^{Δ} is at most in the 10^6 s^{-1} range. Thus it is possible to apply the steady-

---

[6] Using $k_{01,i} = \sigma_{01,i}I^0$ by considering that the typical photon flux at the sample of an illumination setup is $I^0 = 10^{21}$ photons/m^{2}s and that the molecular cross section for light absorption $\sigma_{01,i} = 2.3\frac{\epsilon_i}{N_A}$ (N_A is the Avogadro number) is in the 10^{-20} m^2/molecule range for the considered probes.

state approximation to $\mathbf{S}_{1,1}$ and $\mathbf{S}_{1,2}$ beyond the nanosecond time scale. Under such conditions it is meaningful to consider that the states $\mathbf{S}_{0,i}$ and $\mathbf{S}_{1,i}$ are in a fast exchange so as to introduce an average species **i** for which $\mathbf{S}_{0,i}$ and $\mathbf{S}_{1,i}$ contribute in $p_{\mathbf{S}_{0,i}}$ and $p_{\mathbf{S}_{1,i}}$ respective proportions where

$$p_{\mathbf{S}_{0,i}} = \frac{1}{1+K_{01,i}} \tag{47}$$

$$p_{\mathbf{S}_{1,i}} = \frac{K_{01,i}}{1+K_{01,i}} \tag{48}$$

with

$$K_{01,i} = \frac{k_{01,i}}{k_{10,i}+k'_{10,i}}. \tag{49}$$

Under the experimental conditions used in this study, the relative proportions in the excited and ground states are typically $p_{\mathbf{S}_{1,i}} \sim 10^{-8}$ and $p_{\mathbf{S}_{0,i}} \sim 1$.

Considering that the concentration in **i**, i, is equal to $S_{0,i} + S_{1,i}$, Eqs.(43–46) reduce to Eq.(50) beyond the time scale at which the steady-state approximation is valid.

$$\frac{d2}{dt} = -\frac{d1}{dt} = \left(\frac{K_{01,1}}{1+K_{01,1}}k'_{10,1}\right)1 - \left(\frac{K_{01,2}}{1+K_{01,2}}k'_{10,2} + \frac{1}{1+K_{01,2}}k^{\Delta}_{21}\right)2. \tag{50}$$

Considering that, far from saturation, $K_{01,i}$ is proportional to the photon flux $I(t)$ and much lower than 1, one can write:

$$\frac{K_{01,1}}{1+K_{01,1}}k'_{10,1} \simeq K_{01,1}k'_{10,1} = \frac{k'_{10,1}}{k_{10,1}+k'_{10,1}}\sigma_{01,1}I(t) = \sigma_{12}I(t) \tag{51}$$

$$\frac{K_{01,2}}{1+K_{01,2}}k'_{10,2} \simeq K_{01,2}k'_{10,2} = \frac{k'_{10,2}}{k_{10,2}+k'_{10,2}}\sigma_{01,2}I(t) = \sigma_{21}I(t) \tag{52}$$

$$\frac{1}{1+K_{01,2}}k^{\Delta}_{21} \simeq k^{\Delta}_{21}. \tag{53}$$

Hence Eq.(50) can be alternatively written

$$\frac{d2}{dt} = -\frac{d1}{dt} = \sigma_{12}I(t)1 - \left(\sigma_{21}I(t) + k^{\Delta}_{21}\right)2. \tag{54}$$

Eq.(54) is dynamically identical to Eqs.(2–3).

A three-state electronic model

As a second relevant situation, we analyze the behavior of a chromophore, which light excitation yields its first excited singlet state $\mathbf{S}_1$ from its ground singlet state $\mathbf{S}_0$. $\mathbf{S}_1$ can subsequently relax to the ground state $\mathbf{S}_0$ (for instance by fluorescence emission) or be converted to its first triplet state $\mathbf{T}_1$. $\mathbf{T}_1$ then deexcites to give back the ground state $\mathbf{S}_0$. The overall scheme is displayed in Figure S4.

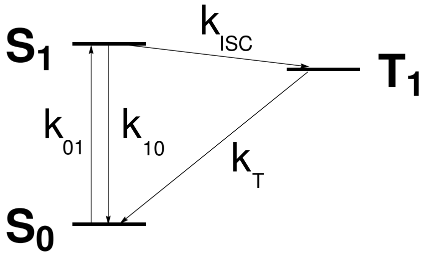

Figure S4: Mechanism accounting for the behaviour of a chromophore yielding its first singlet and triplet excited states upon illuminating. The arrows and the associated rate constants refer to the exchange processes. See Text.

Relying on the mechanism displayed in Figure S4, we write Eqs.(55–57) to describe the concentration evolutions:

$$\frac{dS_0}{dt} = -k_{01}S_0 + k_{10}S_1 + k_T T_1 \tag{55}$$

$$\frac{dS_1}{dt} = k_{01}S_0 - \left(k_{10} + k_{ISC}\right) S_1 \tag{56}$$

$$\frac{dT_1}{dt} = k_{ISC}S_1 - k_T T_1. \tag{57}$$

In Figure S4, the rate constant k_{10} (typically larger than $10^9\mathrm{s}^{-1}$;[6]) is notably much larger than the other rate constants. Again $k_{01,i}$ would be in the 10 s^{-1} under typical illumination conditions. In addition k_{ISC} and k_T are usually in the 10^6 and 10^3–10^6 s^{-1} range.[6] Thus we can apply the steady-state approximation to $\mathbf{S}_1$ beyond the nanosecond time scale. Under such conditions it is meaningful to consider that the states $\mathbf{S}_0$ and $\mathbf{S}_1$ are in a fast exchange so as to introduce an average species **1** for which $\mathbf{S}_0$ and $\mathbf{S}_1$ contribute in $p_{\mathbf{S}_0}$ and $p_{\mathbf{S}_1}$ respective proportions where

$$p_{\mathbf{S}_0} = \frac{1}{1 + K_{01}} \tag{58}$$

$$p_{\mathbf{S}_1} = \frac{K_{01}}{1 + K_{01}} \tag{59}$$

with

$$K_{01} = \frac{k_{01}}{k_{10}}. \tag{60}$$

Under typical experimental conditions, the relative proportions in the excited and ground states are typically $p_{\mathbf{S}_1} \sim 10^{-8}$ and $p_{\mathbf{S}_0} \sim 1$.

Considering that the concentration in **1**, 1, is equal to $S_0 + S_1$ and denoting $\mathbf{T}_1$ by **2** in the following, Eqs.(55–57) reduce to Eq.(61) beyond the time scale at which the steady-state approximation is valid.

$$\frac{d2}{dt} = -\frac{d1}{dt} = \left(\frac{K_{01}}{1 + K_{01}} k_{ISC}\right) 1 - k_T 2. \tag{61}$$

Considering that, far from saturation, K_{01} is proportional to the photon flux $I(t)$ and much lower than 1, one can write:

$$\begin{aligned}\frac{K_{01}}{1+K_{01}}k_{ISC} &\simeq K_{01}k_{ISC} = \frac{1}{k_{10}}\sigma_{01}I(t)k_{ISC} = \sigma_{12}I(t) &(62)\\ k_T &= k_{21}^{\Delta}. &(63)\end{aligned}$$

Hence Eq.(61) can be alternatively written

$$\frac{d2}{dt} = -\frac{d1}{dt} = \sigma_{12}I(t)1 - k_{21}^{\Delta}2. \qquad (64)$$

Eq.(64) is dynamically identical to Eqs.(2–3) upon noting that $\sigma_{21} = 0$.

Supplementary text 3: Significance of irreversible bleaching for OPIOM application

Any photoswitchable fluorescent probe experiences fatigue such that it irreversibly bleaches after some number of switching cycles. Bleaching is not included in the previously addressed two state model. In this section, we theoretically analyze how bleaching affects OPIOM application.

To account for the bleaching process, we start from the two-state exchange (1) and add an irreversible bleaching reaction converting the state **1** into a state **3**. The overall scheme is displayed in Figure S5.

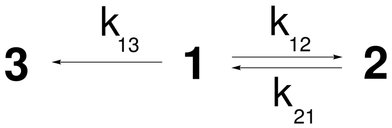

Figure S5: Model mechanism accounting for the behaviour of a photoswitchable fluorescent probe irreversibly yielding a bleached state upon illuminating. The arrows and the associated rate constants refer to the exchange processes. See Text.

Relying on the mechanism displayed in Figure S5, we write Eqs.(65–67) to describe the concentration evolutions:

$$\frac{d1}{dt} = -\left(k_{12}+k_{13}\right)1+k_{21}2 \tag{65}$$

$$\frac{d2}{dt} = k_{12}1-k_{21}2 \tag{66}$$

$$\frac{d3}{dt} = k_{13}1. \tag{67}$$

Eqs.(65–67) differ from Eqs.(2–3). Thus bleaching is expected to affect the expressions (17,18) as well as the resonance conditions (22,23) obtained with the two state model. More precisely, bleaching will affect the overall concentration in states **1** and **2**, previously denoted P_{tot}. From Eqs.(65–67), one can derive

$$\frac{d3}{dt} = -\frac{dP_{tot}}{dt}=k_{13}1. \tag{68}$$

Now specifically addressing the case of light modulation of weak amplitude, Eq.(68) is solved at first order of the perturbation.

To evaluate the corresponding perturbation, we assume the rate constant k_{13} to be notably much smaller than the other rate constants.[7] Then the relaxation time $\tau_{12}=1/\left(k_{12}+k_{21}\right)$ associated to light-driven exchange between the states **1** and **2** is much smaller than the relaxation time $\tau_{13}=1/k_{13}$ associated to bleaching. We eventually solve Eqs.(65–67) in the regime of intermediate times given by $\tau_{12}\ll t\ll\tau_{13}$. We adopt a sinusoidal light modulation of weak amplitude (Eq.(11)). The resonance conditions are expected to be only weakly affected by the contribution of bleaching in the considered kinetic regime (*vide infra*). As a consequence, one expects $\omega\sim 2/\tau_{12}^0$.

---

[7] In fact, any other situation would suggest that the photoswitchable fluorescent probe cannot sustain more than one photoswitching cycle, which would make the choice of the corresponding probe irrelevant in the present context.

The rate constant associated to photobleaching can be written

$$k_{13}(t) \quad = \quad k_{13}^{0}\left[1+\varepsilon\sin\left(\omega t\right)\right] \tag{69}$$

Moreover, since P_{tot} varies only slowly at the time scale of the light modulation, we adopt the expressions (16,7,17,18) to control the instantaneous concentration of **1**.

From Eq.(68), one can extract

$$\frac{P_{tot}(t)}{P_{tot}(0)}=1-\frac{1}{1+K_{12}^{0}}\left[k_{13}^{0}t-\frac{k_{13}^{0}}{\omega}\left(1-\frac{p_{21}^{\Delta}K_{12}^{0}}{1+K_{12}^{0}}\frac{1}{1+\left(\omega\tau_{12}^{0}\right)^{2}}\right)\varepsilon\cos\left(\omega t\right)+\frac{p_{21}^{\Delta}K_{12}^{0}}{1+K_{12}^{0}}\frac{\tau_{12}^{0}}{1+\left(\omega\tau_{12}^{0}\right)^{2}}\varepsilon\sin\left(\omega t\right)\right] \tag{70}$$

where we linearized the exponential temporal dependence of P_{tot}.

The resulting expression of $P_{tot}(t)$ was subsequently used to calculate at first order the iterated amplitude of the out-of-phase term of the concentration in **1** using Eqs.(16,7,17,18). Considering that k_{13}^{0}/ω is a vanishing term, we extracted

$$1^{1,out}=-2^{1,out}=p_{21}^{\Delta}\frac{K_{12}^{0}}{\left(1+K_{12}^{0}\right)^{2}}\frac{\omega\tau_{12}^{0}}{1+\left(\omega\tau_{12}^{0}\right)^{2}}P_{tot}(0)\left[1-\frac{k_{13}^{0}}{1+K_{12}^{0}}t\right]. \tag{71}$$

Thus the existence of bleaching is not expected to significantly complicate nor the acquisition nor the analysis of experimental data to extract OPIOM images. Eq.(71) first demonstrates that the resonance conditions given in Eqs.(22,23) are still relevant at first order of the perturbation. Eq.(71) also shows that, before analyzing the temporal evolution of the fluorescence signal to extract the OPIOM image with the two-state model, one has just to correct from the linear bleaching contribution, which can be easily evaluated from computing the drop of the fluorescence signal averaged over successive periods of light modulation (*vide infra*).

Supplementary text 4: Determination of the kinetic parameters through light jump experiments

Dronpa-2/3 solutions (1 μM) were illuminated at 480 nm at various light intensities I^0, while fluorescence emission was recorded at 515 nm. The photoswitching relaxation rate constant $(\sigma_{12} + \sigma_{21})I^0 + k_{21}^{\Delta}$ was obtained by fitting the temporal evolution of the normalised fluorescence emission intensity with the equation (9) (see Figure S6a,c). By repeating this experiments at various light intensities, we could determine the sum $(\sigma_{12} + \sigma_{21})$ by plotting $(\sigma_{12} + \sigma_{21})I^0 + k_{21}^{\Delta}$ in function of I^0 (see Figure S6b,d).

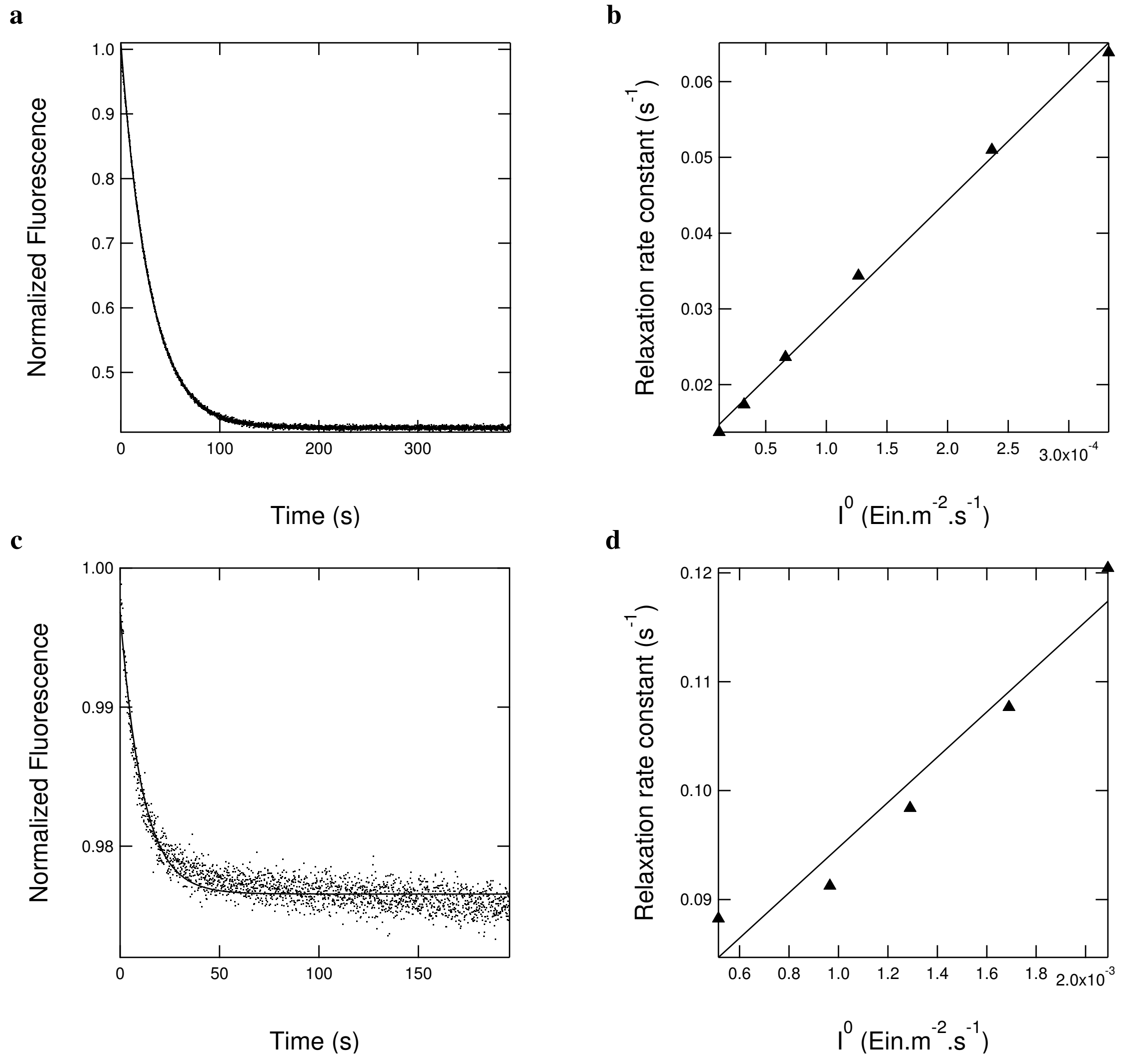

Figure S6: Photoisomerization kinetics of Dronpa-2 (**a**,**b**) and Dronpa-3 (**c**,**d**). (**a**,**c**) Temporal evolution of the normalized fluorescence emission at 515 nm of Dronpa-2/3 solutions (1 μM) upon illumination at 480 nm (light intensity 1.3×10^{-4} ein.s^{-1}.m^{-2}). Exponential fit with Eq.(9) gave the relaxation rate constant $(\sigma_{12}+\sigma_{21})I^0 + k_{21}^{\Delta}$; (**b**,**d**) Dependence of the relaxation rate constant $(\sigma_{12} + \sigma_{21})I^0 + k_{21}^{\Delta}$ associated to the fluorescence decay in function of the light intensity I^0 . Linear fit enabled to extract $\sigma_{12} + \sigma_{21}$ from the slope. Experiments were performed at 37 $^\circ$ C in pH 8.0 Tris buffer.

For determining the thermal resetting rate constant k_{21}^{Δ}, solutions of Dronpa-2/3 (1 μM) were first illuminated at 480 nm in order to reach the photostationary state, then the light was switched off and the solutions were left in the dark for various times. To extract a point associated with a given time in Figure S7, we recorded the whole temporal evolution of the fluorescence signal at 515 nm at high frequency (10 Hz) and extrapolated its value at initial time. The value of the extrapolated fluorescence emission intensity at 515 nm was recorded at various times. k_{21}^{Δ} was obtained by fitting the temporal evolution of the fluorescence recovery with the equation (10) (Figure S7a,b). The results are given in Table S1.

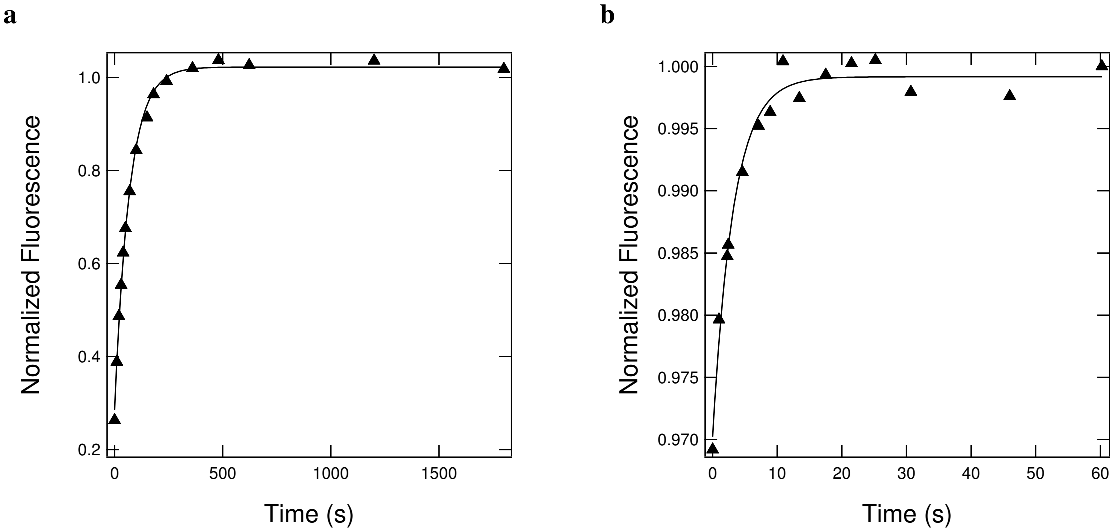

Figure S7: Thermal resetting of photoisomerized Dronpa-2 (**a**) and Dronpa-3 (**b**). Dronpa-2/3 solutions (1 μM) were first illuminated at 480 nm to reach the photostationary state and then left in the dark for various times. The graphs show the normalized fluorescence emission at 515 nm upon illumination at 480 nm after various times of recovery under dark conditions. Exponential fit with Eq.(10) gave the thermal resetting rate constant k_{21}^{Δ}. Experiments were performed at 37 ° C in pH 8.0 Tris buffer.

Table S1: Kinetic parameters of Dronpa-2 and Dronpa-3 at 37 ° C and Dronpa-3 at 20 ° C in pH 8.0 Tris buffer and resonance conditions for optimal out-of-phase response.

		Kinetic parameters		Resonance conditions	
	° C	$\sigma_{12} + \sigma_{21}$ (m^2.mol^{-1})	k_{21}^{Δ} (s^{-1})	I^0 (Ein· m^{-2}· s^{-1})	ω (rad.s^{-1})
Dronpa-2	37	157±5	$(1.50 \pm 0.05) \times 10^{-2}$	9.6×10^{-5}	2.9×10^{-2}
Dronpa-3	37	21±3	0.17 ± 0.01	8.1×10^{-3}	0.34
Dronpa-3	20	21±1	$(2.32 \pm 0.03) \times 10^{-2}$	1.1×10^{-3}	4.5×10^{-2}

Our results are in line with estimates from the literature. From the data reported in Ando et al 2007,[2] we extracted 280 and 29 m^{2}mol^{-1} for the values of $\sigma_{12} + \sigma_{21}$ ($\lambda_{exc} = 484$ nm, pH 7.4) for Dronpa-2 and Dronpa-3 respectively. From the data reported in Stiel et al 2007,[1] we extracted 360 m^{2}mol^{-1} and 0.03 s^{-1} for the values of $\sigma_{12} + \sigma_{21}$ ($\lambda_{exc} = 488$ nm) and k_{21}^{Δ} for Dronpa-2.

Supplementary text 5: Determination of the kinetic parameters through light modulation experiments

Since OPIOM relies on matching light modulation with the rate constants of the targeted photoswitchable fluorophore, we additionally performed a series of relaxation experiments using light modulation to extract the kinetic parameters of Dronpa-2 and check their consistency with the data obtained with the light jump protocol. Hence we submitted a solution of Dronpa-2 (1 μM) to a sinusoidally periodic 480 nm light modulation of weak amplitude (approximately 10$\%$) around the average light intensity $I^0 = 1 \ \times 10^{-4}$ ein$\cdot$ m$^{-2}\cdot$ s^{-1} at 310 K. Upon monitoring excitation intensity, we simultaneously acquired fluorescence emission at 515 nm (see Figure S8a,b). The excitation data were analyzed by a sinusoidal fit to acquire reference values for the amplitude and the phase of light oscillation. Fluorescence emission $I_F(t)$ was subsequently analyzed by means of Eqs.(29–31) to extract $\alpha^{1,\mathrm{in}} = \frac{Int^{1,in}/\varepsilon - Int^0}{Int^0}$ and $\alpha^{1,\mathrm{out}} = \frac{Int^{1,out}/\varepsilon}{Int^0}$. The same experiment and data analyses were reproduced at various angular frequencies ω (see Figure S8c,d). The relaxation time associated with Dronpa-2 photoisomerization, τ_{12}^0, was then extracted from analyzing the frequency dependence of $\alpha^{1,\mathrm{in}}$ and $\alpha^{1,\mathrm{out}}$ with the theoretical expressions $\alpha^{1,\mathrm{in}} = (Q_1 - Q_2)\, 1^{1,in}/\left(Q_1 1^0 + Q_2 2^0\right)$ and $\alpha^{1,\mathrm{out}} = (Q_1 - Q_2)\, 1^{1,out}/\left(Q_1 1^0 + Q_2 2^0\right)$, which frequency dependence could be derived from Eqs.(17, 18). The analysis gave respectively $\tau_{12}^0 = 26$ s and $\tau_{12}^0 = 31$ s, which was in good agreement with the value $\tau_{12}^0 = 33$ s obtained from the kinetic parameters of Table S1.

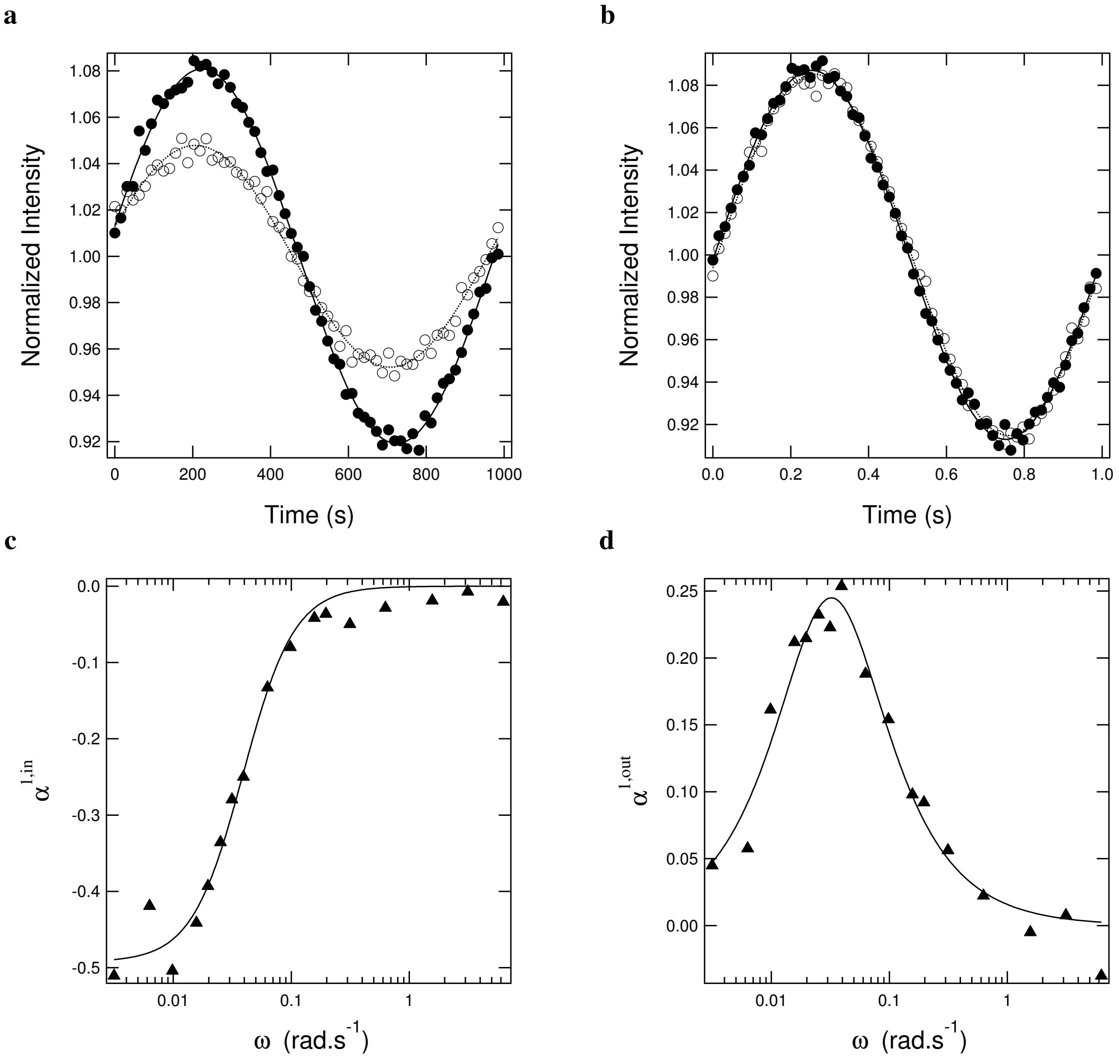

Figure S8: Extraction of the photoisomerization relaxation time of Dronpa-2 from analyzing the fluorescence response at 515 nm of a solution of Dronpa-2 (1 μM) to a sinusoidally periodic 480 nm light modulation of weak amplitude (approximately 10%) around the average light intensity $I^0 = 1 \times 10^{-4}$ Ein$\cdot$ m$^{-2}\cdot$ s^{-1}. **a–b**: Normalized intensity of light excitation (disks and solid line) and fluorescence emission (circles and dotted line) at two angular frequencies ω = 6.28 mrad.s^{-1} (**a**) and 6.28 rad.s^{-1} (**b**). Markers : experimental points; lines : sinusoidal fits; **c–d**: The graphs show the dependence of the amplitudes of the normalized in- and out-of-phase modulation terms of the fluorescence emission, (**a**) $\alpha^{1,\mathrm{in}}$ and (**b**) $\alpha^{1,\mathrm{out}}$, on the angular frequency ω. Markers : experimental points; lines : fits yielding $\tau_{12}^0 = 26$ s and 31 s respectively. Solvent: pH 8.0 Tris buffer; T = 37 $^\circ$C.

Supplementary text 6: Imaging protocols

Video acquisition In the subsequent imaging experiments, we recorded movies over an integer number of periods of light modulation (in general $4m$ periods, where m is an integer). The acquisition frequency of the camera was set in order to transfer $2n$ (n is an integer) frames per period of light excitation, which triggered CCD acquisition start. Thus, using Eq. 19, the fluorescence emission at pixel (x,y) of the k^{th} frame is equal to

$$I_F(x,y,k) = I_F^0(x,y) + I_F^{1,in}(x,y)\ \sin\left(\frac{k\pi}{n} + \phi_{acq}\right) + I_F^{1,out}\ \cos\left(\frac{k\pi}{n} + \phi_{acq}\right) \tag{72}$$

In Eq.(72), the phase lag ϕ_{acq} reflects the fact that the present setup does not allow us to precisely phase CCD recording and light modulation. However ϕ_{acq} can be easily calibrated by using the fluorescence emission from an instantaneously responding fluorophore (e.g. Fluorescein). Acquisition in quadrature was subsequently achieved through phase sensitive detection.[8]–[12] The pre-OPIOM image corresponding to the average signal over the whole movie, equal to $I_F^0(x,y)$, was first computed using Eq.(73)

$$\langle I_F(x,y,k)\rangle_{k=0}^{8nm-1} = \frac{1}{8nm}\sum_{k=0}^{8nm-1} I_F(x,y,k). \tag{73}$$

Using Eq.(31), the k^{th} frames $I_F(x,y,k)$ were next multiplied by $\cos\left(\frac{k\pi}{n} + \phi_{acq}\right)$ and averaged over the whole duration of the movie to give rise to the OPIOM image :

$$I_F^{1,out}(x,y) = \frac{1}{4nm}\sum_{k=0}^{8nm-1}\left[(I_F(x,y,k)) \times \cos\left(\frac{k\pi}{n} + \phi_{acq}\right)\right] \tag{74}$$

In the presence of photobleaching of the probe, image analysis has to be modified to correct from bleaching (see supplementary text 3). Assuming a linear decay of the fluorescence signal due to photobleaching, the recorded emission signal at pixel (x,y) of the k^{th} frame $I_F^{raw}(x,y,k)$ was written using Eq.(72)

$$I_F^{raw}(x,y,k) = I_F(x,y,k) + B(x,y) \times k. \tag{75}$$

$B(x,y)$ was calculated from the average signals $\langle I_F^{raw}(x,y,k)\rangle_{k=0}^{4nm-1}$ and $\langle I_F^{raw}(x,y,k)\rangle_{k=4nm}^{8nm-1}$ computed over the first and last $2m$ periods

$$B(x,y) = \frac{\langle I_F^{raw}(x,y,k)\rangle_{k=4nm}^{8nm-1} - \langle I_F^{raw}(x,y,k)\rangle_{k=0}^{4nm-1}}{4nm} \tag{76}$$

Then, all frames were corrected for photobleaching using :

$$I_F^{corr}(x,y,k) = I_F^{raw}(x,y,k) - B(x,y) \times k. \tag{77}$$

$I_F^{corr}(x,y,k)$ was subsequently processed as $I_F(x,y,k)$ above to extract the OPIOM image.

In Appendix A at the end of the Supporting Information, we provide the Matlab code, which we used to compute $I_F^{1,out}(x,y)$ (OPIOM image) for our imaging experiments.

Microdevice imaging This series of experiments has been performed upon applying a sinusoidal light modulation of small amplitude.

To correct from inhomogeneities in the spatially dependent photon collection yield as well as to access quantitative information, the images $I_F(x,y,t)$ acquired during this series of experiments were first corrected from the background and then divided by a reference image $I^0_{F,ref}(x,y)$ recorded with a solution of a fluorescent non photochromic compound (Fluorescein) under the same but constant illumination to yield a movie $I_{F,cor}(x,y,t)$. Then we relied on Eqs.(73–77) to extract the images sought for.

Upon averaging $I_{F,cor}(x,y,t)$ over the 512 recorded images, we thus derived from Int^0_{cor} the corrected value of the average fluorescence intensity $I^0_{F,cor}$. The whole image $I^0_{F,cor}(x,y)$ was eventually normalized by its largest value to obtain the corrected normalized fluorescence emission $I^0_{F,norm}(x,y)$ corresponding to the pre-OPIOM image.

Adopting a reference pixel in the chamber containing only Fluorescein to extract both the amplitude ε and the phase ϕ (which was arbitrarily fixed to zero) of the light modulation, we computed $Int^{1,out}_{cor}$ calculated from $I_{F,cor}(x,y,t)$ over 8 periods to yield $I^{1,out}_{F,cor}(x,y)$. The whole image $I^{1,out}_{F,cor}(x,y)$ was finally normalized by its largest value to obtain the normalized out-of-phase fluorescence emission $I^{1,out}_{F,norm}(x,y)$ corresponding to the OPIOM image.

Quantitative analysis of the information contained in the $I^0_{F,norm}(x,y)$ and the $I^{1,out}_{F,norm}(x,y)$ maps to extract the concentrations $P^0_{titration}$ and $P^{\mathrm{1,out}}_{titration}$ was eventually performed as follows. The signal arising from the calibration chamber (containing a known concentration of species to be titrated) was first averaged over a square of 60 pixel × 60 pixel (corresponding to the size of the chamber) to extract $\langle I^0_{F,norm}(x,y)\rangle$ and $\langle I^{1,out}_{F,norm}(x,y)\rangle$. Using these two values, we then determined the proportionality factor A^0_{ref} (resp. $A^{\mathrm{1,out}}_{ref}$) linking the observed signal in any chamber i, $I^0_{F,norm}(i)$ (resp. $I^{1,out}_{F,norm}(i)$), to the corresponding $P^0_{titration}(i)$ (resp. $P^{\mathrm{1,out}}_{titration}(i)$). Eventually, by dividing the observed signal in each chamber i $I^0_{F,norm}(i)$ (resp. $I^{1,out}_{F,norm}(i)$) by the proportionality factor A^0_{ref} (resp. $A^{\mathrm{1,out}}_{ref}$), we retrieved $P^0_{titration}$ (resp. $P^{\mathrm{1,out}}_{titration}$).

Cell imaging and zebrafish embryo imaging with epifluorescence microscopy This series of experiments has been performed upon applying a sinusoidal light modulation of large amplitude (90%). Since we did not attempt to be quantitative for analysis, a simpler imaging protocol was adopted than with the microdevice. Triggering of the camera acquisition was synchronized with the onset of the periodic excitation light (using the option "External start" in the Solis software, Andor Technology). 512 frames (8 periods of 20 s) were recorded using a Luca-R CCD camera (Andor Technology) at 3.2 Hz (0.3125 s for image cycle time) with 0.3116 s exposure time. A fixed phase delay ϕ_{acq} between the dates of camera recording and light excitation was observed (due to the exposure time and the triggering of the camera). This phase delay was calibrated using the microfluidic device described previously filled with Fluorescein: the temporal evolution of fluorescence emission of Fluorescein was fitted with $A[1+\alpha\sin(\omega t+\phi_{acq})]$ to extract the value of ϕ_{acq}. Otherwise indicated, the temporal dependence of the fluorescence intensity $I_F(x,y,t)$ of each image pixel was analyzed over 8 periods with Eqs.(73–77) to provide the $\mathfrak{I}^{0}_{\mathfrak{F}}(x, y)$ (pre-OPIOM) and the $\mathfrak{I}^{1,\mathrm{out}}_{\mathfrak{F}}(x, y)$ (OPIOM) images.

Embryo imaging with Single Plane Illumination Microscopy (SPIM) In this series of experiments, triggering of the camera acquisition was again synchronized with the onset of the square wave excitation light (using the option “External start” in the Solis software, Andor Technology) and 512 images corresponding to 8 periods of 140 s were recorded using an iXonEM+ 897 EMCCD camera (Andor Technology) operated at 0.46 Hz (2.1875 s for image cycle time) with 2.187 s exposure time. The temporal dependence of the fluorescence intensity $I_F(x, y, t)$ of each image pixel was subsequently analyzed with Eqs.(73–77) to provide the $\mathfrak{I}^{0}_{\mathfrak{F}}(x, y)$ (pre-OPIOM) and the $\mathfrak{I}^{1,\mathrm{out}}_{\mathfrak{F}}(x, y)$ (OPIOM) images.

Image filtering To reduce noise, the processed images have been subsequently filtered upon applying a 3 pixels × 3 pixels median filter.

Evaluation of contrast enhancement associated to OPIOM image processing The contrast enhancement $\chi_{target/interf}$ associated to OPIOM image processing was calculated from the signals $I^{0}_{F,target}$, $I^{1,out}_{F,target}$, $I^{0}_{F,interf}$, $I^{1,out}_{F,interf}$ originating from areas containing the targeted photoswitchable fluorophore (Dronpa-2 or Dronpa-3) and the interfering fluorophore (Fluorescein, Dronpa-2, or Dronpa-3 depending on the experiments in the microfluidic device)

$$\chi_{target/interf} = \frac{\frac{I^{1,out}_{F,target}}{I^{1,out}_{F,interf}}}{\frac{I^{0}_{F,target}}{I^{0}_{F,interf}}}. \tag{78}$$

In the case of microdevice imaging, $I^{0}_{F,target}$, $I^{1,out}_{F,target}$, $I^{0}_{F,interf}$ and $I^{1,out}_{F,interf}$ were extracted from signal integration over the chambers containing the targeted or the interfering species.

Supplementary Figures

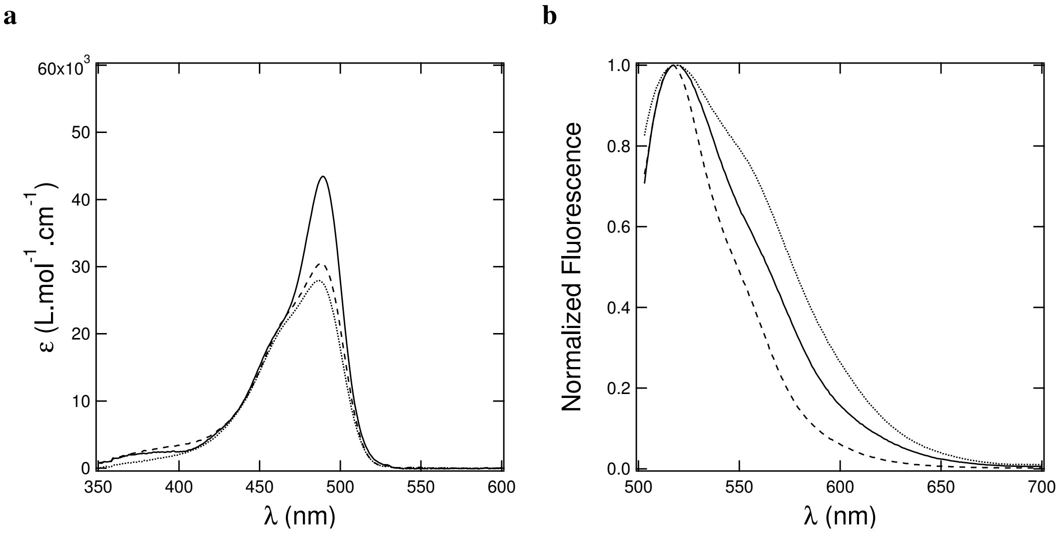

Figure S9: Absorption (**a**) and normalized emission (**b**; $\lambda_{exc} = 480$ nm) spectra of Fluorescein (2.5 μM, solid line), Dronpa 2 (2.5 μM, dashed line), and Dronpa 3 (3.8 μM, dotted line). Solvent: pH 6.8 MES buffer; T = 25 $^\circ$ C.

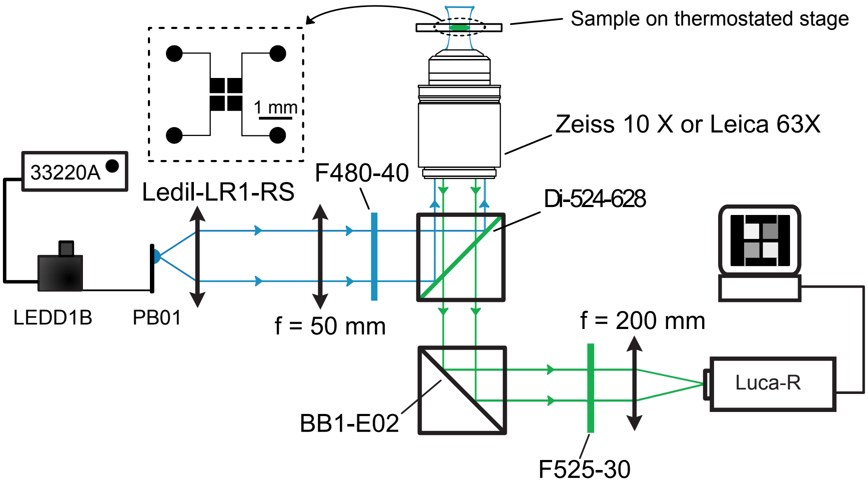

Figure S10: Epifluorescence setup and PDMS Imaging device.

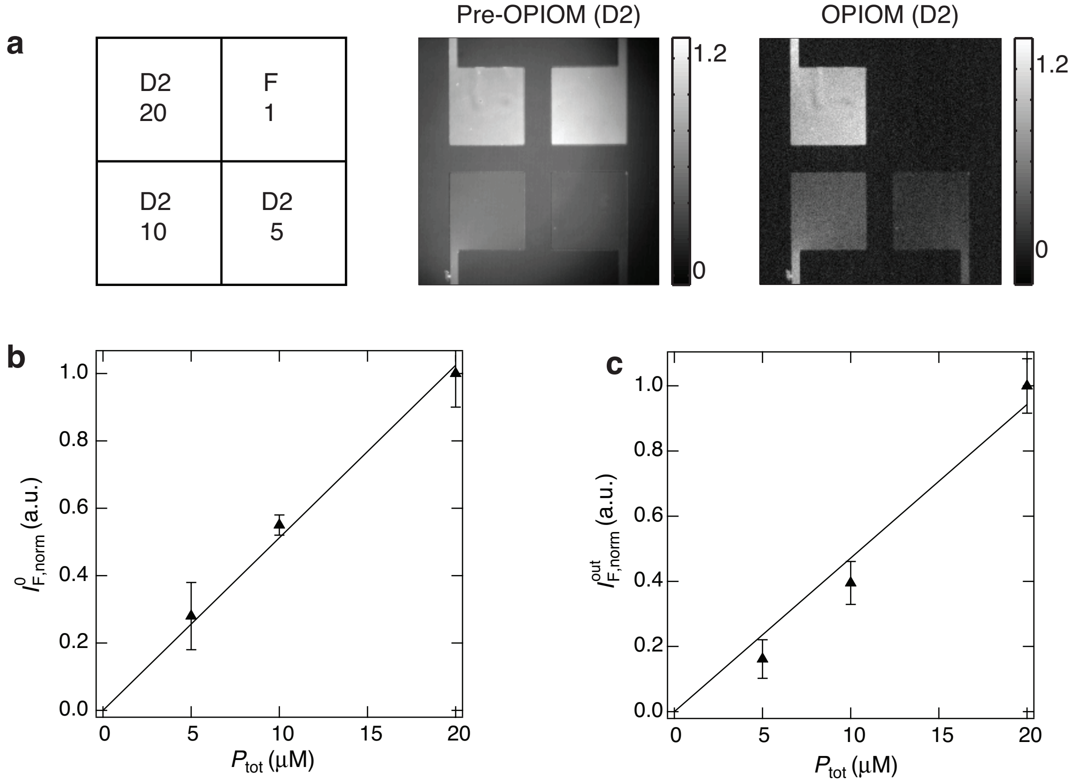

Figure S11: Quantitative imaging of Dronpa-2. (**a**) A microfluidic device with four square chambers (400×400×20 μm^3) was filled with solutions of Dronpa-2 or fluorescein as described on the scheme (the numbers indicate the concentrations in μM). The images correspond to the pre-OPIOM and OPIOM images resulting from imaging the microfluidic device at 525 nm under sinusoidal light modulation of small amplitude tuned to the resonance of Dronpa-2 (λ_{exc}; I^0; ω; α) = (480 nm; 1×10^{-4} Ein· m^{-2}· s^{-1}; 31.4 mrad.s^{-1}; 10%). (**b,c**) Normalized average value, $\langle I^0_{F,norm} \rangle$, and normalized amplitude of the out-of-phase response, $\langle I^{1,\text{out}}_{F,norm} \rangle$, in function of the total concentration P_{tot} = [Dronpa-2]$_{tot}$ of Dronpa-2. Experiments were performed at 37 °C in pH 6.8 MES buffer.

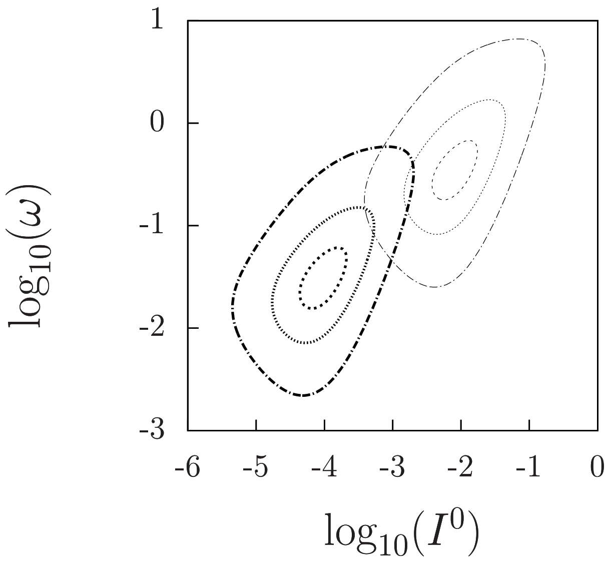

Figure S12: Theoretical computation of the out-of-phase first order response of Dronpa-2 (bold) and Dronpa-3 (unbolded) submitted to light harmonic forcing of small amplitude. The normalized amplitude of the out-of-phase oscillations in **1** concentration, $|\Delta 1^{out}_{norm}|$, is plotted versus the light flux I^0 (in ein·s^{-1}·m^{-2}) and the radial frequency ω (in rad.s^{-1}). See Eqs.(17,18). We used Dronpa-2: σ_{12} = 73 m^2.mol^{-1}, σ_{21} = 84 m^2.mol^{-1}, $k_{21}^{\Delta} = 1.5 \times 10^{-2}$ s^{-1}; Dronpa-3: σ_{12} = 9.7 m^2.mol^{-1}, σ_{21} = 11.3 m^2.mol^{-1}, $k_{21}^{\Delta} = 1.7 \times 10^{-1}$ s^{-1}. The markers correspond to isodensity curves : 0.01 (dot dashed), 0.03 (dot) and 0.05 (dashed).

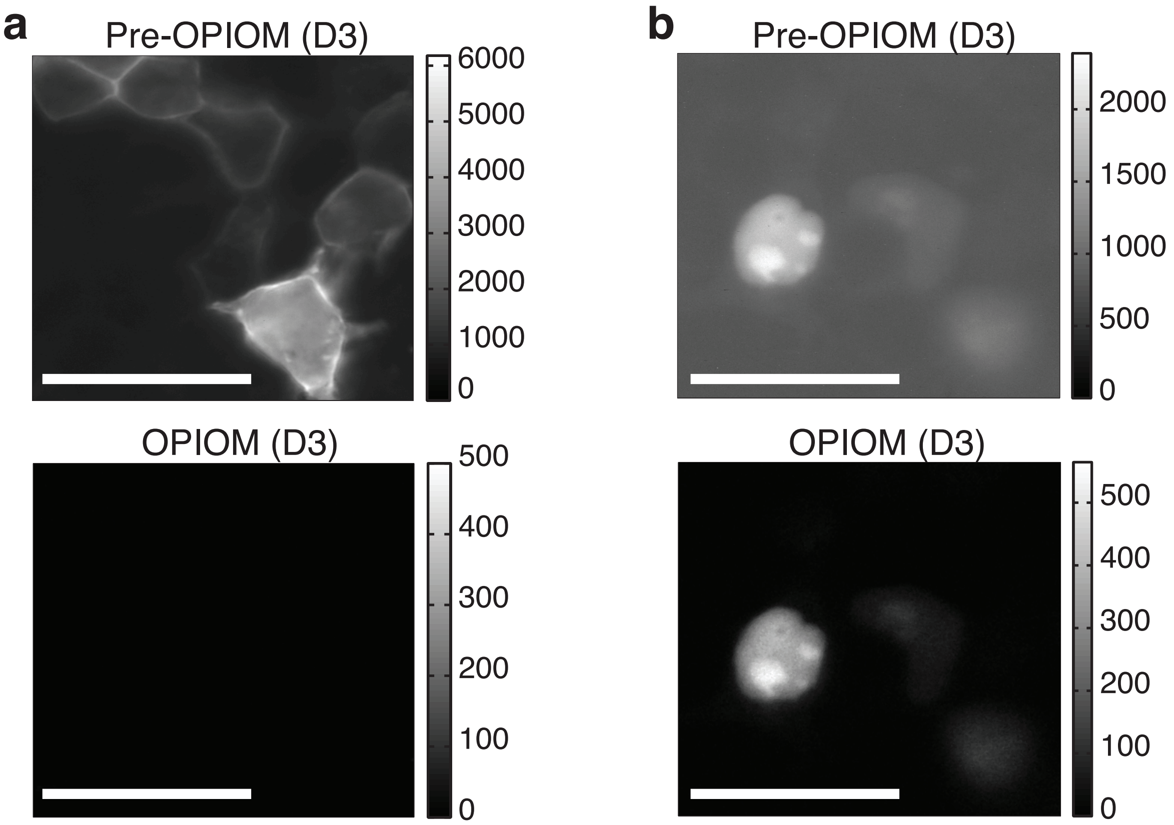

Figure S13: Imaging of fixed HEK293 cells expressing either (**a**) membrane-localised EGFP or (**b**) nuclear Dronpa-3. Pre-OPIOM and OPIOM images result from analyzing a movie recorded at 525 nm under sinusoidal light modulation of large amplitude tuned on the resonance of Dronpa-3 (D3) (λ_{exc}; I^0; ω; α) = (480 nm; 8.1×10^{-3} Ein$\cdot$ m$^{-2}\cdot$ s^{-1}; 314 mrad.s^{-1}; 90%). Experiments were performed at 37 $^\circ$ C. Scale bars represent 50 μm.

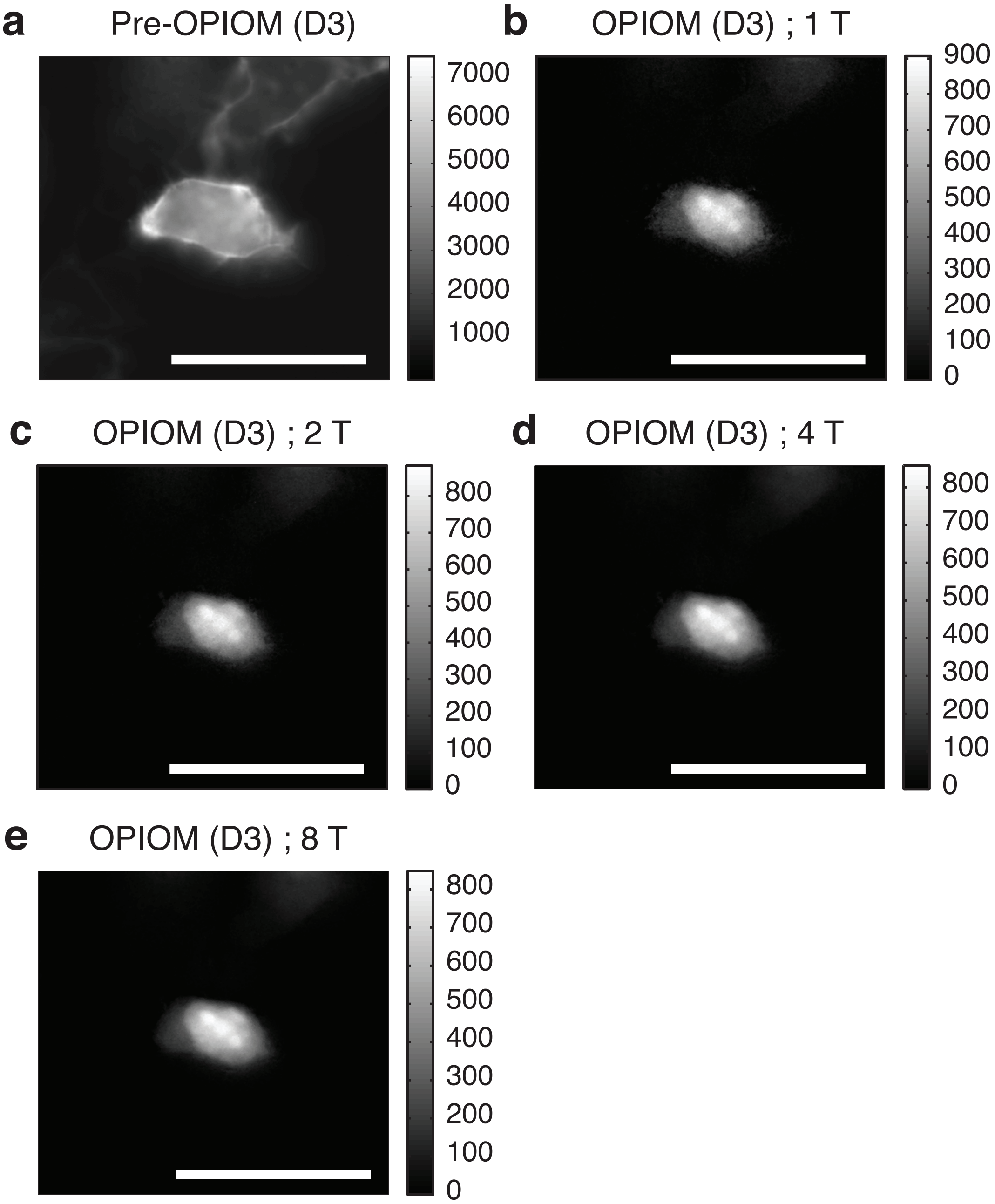

Figure S14: Selective imaging of Dronpa-3 in live HEK293 cells co-expressing nuclear Dronpa-3 and membrane-localized EGFP. Pre-OPIOM (**a**) and OPIOM (**b-e**) images result from analyzing a movie recorded at 525 nm over 1 (**b**), 2 (**c**), 4 (**d**), or 8 (**e**) periods $T = 2\pi/\omega$ under sinusoidal light modulation of large amplitude tuned on the resonance of Dronpa-3 (D3) (λ_{exc}; I^0; ω; α) = (480 nm; 8.1×10^{-3} Ein$\cdot$ m$^{-2}\cdot$ s^{-1}; 314 mrad.s^{-1}; 90%). Experiments were performed at 37 $^\circ$ C. Scale bars represent 50 μm.

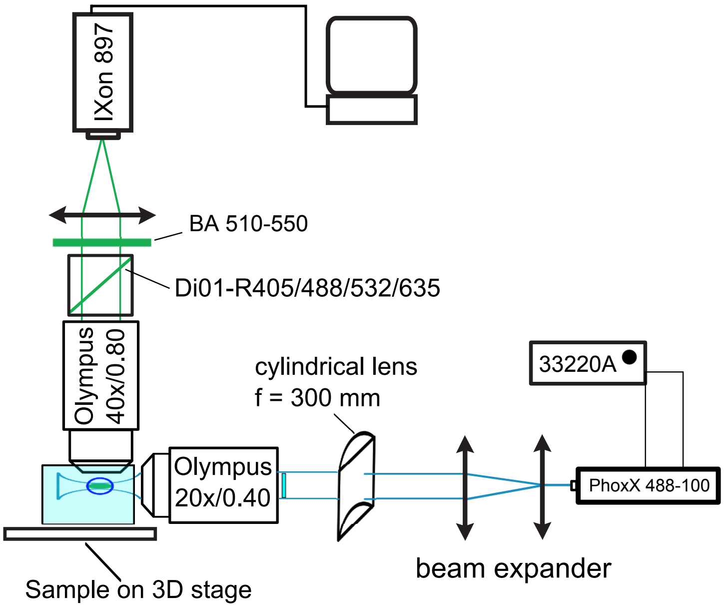

Figure S15: Light sheet setup .

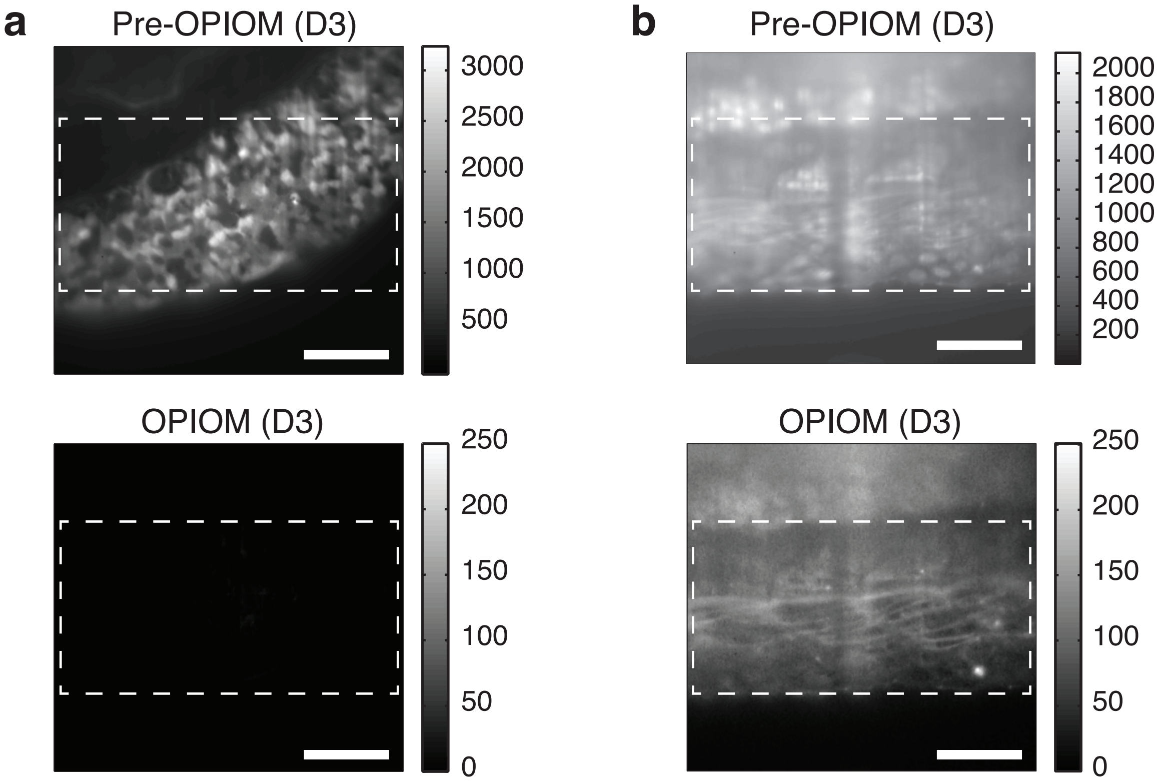

Figure S16: Selective single plane illumination microscope (SPIM) imaging of Dronpa-3 in zebrafish embryo co-expressing Lifeact-Dronpa-3 and GFP-NLS. The figures **b** correspond to the pre-OPIOM and OPIOM images of the tail of a 24 hpf zebrafish embryo under square wave modulation of large amplitude tuned on the resonance of Dronpa-3 (D3) at 20 ° C (λ_{exc}; I^0; ω; α) = (480 nm; 3.1 × 10^{-3}Ein· m^{-2}· s^{-1}; 44.9 mrad.s^{-1}; 96%). As a control experiment, the figures **a** recorded under the same conditions correspond to the pre-OPIOM and OPIOM images of a zebrafish embryo expressing GFP-NLS only. The dashed rectangles indicates the zone illuminated by the thinnest part of the light sheet. Experiments were performed at 20 ° C. Scale bars represent 50 μm.

A Matlab code for OPIOM imaging

```
function [IF0,IF1out,IF1outmed]=opiom(filename,period,phi_acq,timePoints,
nframesperperiod)
% Computes pre-OPIOM (IF0), OPIOM (IF1out) and OPIOM
% median-filtered (IF1outmed) images from ascii-formated file
% Eight periods are acquired with 64 frames per period (512 frames)
% 'period' is the period of the light excitation
% 'phi_acq' is the phase delay between the dates of camera recording
% and light excitation previously calibrated with fluorescein
% 'timePoints' is the total number of frames
% Calculate the angular frequency w
w=2*pi/period;
% Produces temporal base over 8 periods
time=zeros(timePoints,1);
for i=1:timePoints
    time(i)=(i-1)*period/nframesperperiod;
end

%%%%%% Produces a 3D-array containing the whole movie%%%%%%
for i=1:timePoints
      M=dlmread([filename sprintf('%04d.asc',i)]);
    % Obtain image dimensions that will be used for the rest of the program
    % from the first image
    if i==1
        [rows,columns]=size(M);
        Holder=zeros(rows,columns,timePoints);
    end
    Holder(:,:,i)=M(1:rows,1:columns);
    clearvars M;
end

%%%%%% Photobleaching correction assuming a linear decay%%%%%%
% Calculate the average signal over the first four periods
linePoint1=mean(Holder(:,:,1:((timePoints)/2)),3);
%Calculate the average signal over the last four periods
```

```
linePoint2=mean(Holder(:,:,((timePoints)/2+1):end),3);
% Calculate the slope B(x,y) (See Eq. 75)
slope=(linePoint2-linePoint1)/(time(timePoints/2));
%Correction for photobleaching
for i=1:timePoints
    Holder(:,:,i)=(Holder(:,:,i)-slope.*time(i));
end

%%%%%% Data processing %%%%%%
% Compute pre-OPIOM image
meanMatrix=mean(Holder,3);
IF0=meanMatrix; % pre-OPIOM image
% Compute OPIOM image
for i=1:timePoints
Holder(:,:,i)=(Holder(:,:,i)).*cos(w*time(i)+phi_acq);
end
IF1out=2*mean(Holder,3); % OPIOM image
% Compute the OPIOM median-filtered image
IF1outmed=medfilt2(IF1out,[3,3]);
% Plot images
figure;imagesc(IF0);colormap('gray');colorbar;
figure;imagesc(IF1out);colormap('gray');colorbar;
figure;imagesc(IF1outmed);colormap('gray');colorbar;
```

References

[1] A. C. Stiel, S. Trowitzsch, G. Weber, M. Andresen, C. Eggeling, S. W. Hell, S. Jakobs, M. C. Wahl, Biochem. J., 2007, 402, 35–42.

[2] R. Ando, C. Flors, H. Mizuno, J. Hofkens, A. Miyawaki, Biophys. J. Biophys. Lett., 2007, L97–L99.

[3] D. K. Sinha, P. Neveu, N. Gagey, I. Aujard, C. Benbrahim-Bouzidi, T. Le Saux, C. Rampon, C. Gauron, B. Goetz, S. Dubruille, M. Baaden, M. Volovitch, D. Bensimon, S. Vriz, L. Jullien, *Chem. Bio. Chem.*, **2010**, *11*, 653–663.

[4] J. Riedl, A. H. Crevenna, K. Kessenbrock, J. H. Yu, D. Neukirchen, M. Bista, F. Bradke, D. Jenne, T. A. Holak, Z. Werb, M. Sixt, R. Wedlich-Soldner, *Nat. Methods*, **2008**, *5*, 605–607.

[5] T. Ito, A. Inoue, K. Sato, K. Hosokawa, M. Maeda, *Anal Chem.*, **2005**, *77*, 4759–4764.

[6] B. Valeur, *Molecular Fluorescence: Principles and Applications*, Wiley-VCH, Weinheim, **2002**.

[7] J. Querard, A. Gautier, T. Le Saux, L. Jullien, *unpublished*.

[8] U. P. Fringeli, D. Baurecht, H. H. Günthard in *Infrared and Raman Spectroscopy of Biological Materials* (Eds.: H.-U. Gremlich, B. Yan), Marcel Dekker, New-York, **2000**, pp. 143–191.

[9] D. Baurecht, U. P. Fringeli, *Rev. Sci. Inst.* **2001**, *72*, 3782–3792.

[10] A. Urakawa, T. Bürgi, A. Baiker, *Chem. Eng. Sci.* **2008**, *63*, 4902–4909.

[11] L. McGown, F. Bright, *Anal. Chem* **1984**, *56*, 1400A–1417A.

[12] J. H. Scofield, *Am. J. Phys.* **1994**, *62*, 129–133.

Chapter 5

Out-of-phase imaging after optical modulation with two colors

5.1 Introduction

The OPIOM protocol enables to detect selectively and quantitatively a targeted photoswitchable probe in a complex mixture containing other interfering compounds, photoswitchable or not. In addition, it is straightforward to implement and compatible with many microscope facilities. In spite of all these advantages, the temporal resolution of OPIOM is limited by the thermal return rate constant of the employed RSFP (see the resonance condition 4.2). Currently, we need at least ~20 s to record an OPIOM image with the fastest variant of Dronpa (largest k_{21}^{Δ}). Such a temporal resolution is not sufficient to analyse dynamic biological phenomena[171] such as phosphorylation (second timescale), tracking of biomolecules (subsecond-second timescale) and translocation (a few minutes). To reduce the acquisition time of OPIOM, two strategies can be considered.

First, we could follow the same approach used to generate the variants of Dronpa. By mutating the Dronpa sequence, we could hope to select new variants exhibiting a larger thermal ressetting rate constant (~1 s^{-1} or more). Furthermore, increasing k_{21}^{Δ} would enable not only to reduce the acquisition time but also to improve the signal-to-noise ratio since the resonant light intensity is proportional to the thermal rate constant (see the resonance condition 4.1). However, this approach remains time-consuming and uncertain : in addition to a large k_{21}^{Δ}, the mutants need to be bright enough and to have an effective photoswitching. Furthermore, the OPIOM theory relies on photoswitchable probes whose behavior upon illumination can be described accurately with a two-state dynamic model. Thus, among all the selected mutants, only the ones that satisfy this last criterion could be used.

As already mentioned, the photoactivation of the OFF state of Dronpa-2 and Dronpa-3 (see chapter 4) with violet light accelerates the back reaction from the OFF to the ON state.

Combining these two colors can strongly reduce the relaxation time associated to the photoswitching and conversely increase the resonant radial frequency of light modulation. Relying on the same principle developed for OPIOM, we implemented a selective fluorescence imaging protocol using two light sources. This approach was dubbed Two-color OPIOM and is described below.

5.2 Two-color OPIOM

5.2.1 Principle

The principle of our strategy and the analysis that enables selective detection is the same as the one discussed in the chapter 4 (see subsection 5.3.1). We consider a photoswitchable fluorophore **P** illuminated with two light sources at wavelength λ_1 and λ_2 which exhibits two states of different brightnesses : state **1**, which is thermodynamically stable and state **2**, which is generated upon illumination.

$$\mathbf{1} \quad \underset{k_{21}(t)}{\overset{k_{12}(t)}{\rightleftharpoons}} \quad \mathbf{2} \tag{5.1}$$

P is characterized by the quintuplet of parameters ($\sigma_{12,1}$, $\sigma_{21,1}$, $\sigma_{12,2}$, $\sigma_{21,2}$, k_{21}^{Δ}) where $\sigma_{12,i}$ and $\sigma_{21,i}$ are the molecular action cross-sections of the forward and backward photochemical processes at λ_i, and k_{21}^{Δ} is the rate constant of the thermal resetting. The discrimination results from employing a modulated light excitation at the wavelength λ_1 (average intensity : I_1^0, angular frequency ω, modulation amplitude α) and a constant light intensity I_2^0 at the wavelength λ_2. Since we want to reach the largest angular frequency at resonance, we focus on a regime of intensities (I_1^0, I_2^0) where we can neglect the thermal return rate constant compared to the ones of the backward photochemical reaction. Like in one-color OPIOM, the modulated light source forces the concentrations of the states **1** and **2** to oscillate at the angular frequency ω with an in- and an out-of-phase contributions whereas the constant light source accelerates the backward photoswitching kinetics. The amplitudes of the two oscillating terms depend on the four parameters $\sigma_{12,1}$, $\sigma_{21,1}$, $\sigma_{12,2}$ and $\sigma_{21,2}$. As demonstrated in the subsection 5.3.1, the out-of-phase first order term of the concentration response can be maximized when the illumination conditions (I_1^0, I_2^0, ω) match the following simple resonance conditions (see Figure 5.8) :

$$\frac{I_1^0}{I_2^0} = \frac{\sigma_{12,2}+\sigma_{21,2}}{\sigma_{12,1}+\sigma_{21,1}} \tag{5.2}$$

$$\omega = 2\left(\sigma_{12,1}+\sigma_{21,1}\right) I_1^0 \tag{5.3}$$

5.2.2 Determination of the photochemical parameters

To validate two-color OPIOM experimentally, we used again Dronpa-2 and Dronpa-3[a]. The resonance conditions are calculated from the sum $\sigma_{12,1}+\sigma_{21,1}$ and $\sigma_{12,2}+\sigma_{21,2}$ for the cis-to-trans and trans-to-cis photoisomerization action cross-sections. The $\sigma_{12,480}+\sigma_{21,480}$ values at 37°C had been already measured (see chapter 4). We found (157 ± 5) and (21 ± 3) $\mathrm{m}^2\cdot\mathrm{mol}^{-1}$ for Dronpa-2 and Dronpa-3, respectively.[172] To determine the $\sigma_{12,405}+\sigma_{21,405}$ values at 37°C, Dronpa-2 and Dronpa-3 were submitted to a series of light jump experiments combining two light sources. Dronpa-2/3 solutions (1 μM) were first illuminated at 480 nm (constant light intensity). Once the photosteady state was reached, the 405 nm light source was additionally switched on, while recording fluorescence emission at 515 nm. Back photoconversion of Dronpa-2 and Dronpa-3 revealed mono-exponential relaxation of the fluorescence signal (see Figure 5.1**a**,**c**), meaning that they both satisfied the two-state dynamic model upon double illumination. By repeating this experiment at various light intensities I_2^0 (but constant I_1^0), the $\sigma_{12,405}+\sigma_{21,405}$ value was extracted from the dependence of the relaxation time associated with the photoconversion of **P** upon irradiation on light intensity I_2^0 (see Figure 5.1**b**,**d**): at 37°C, we found (1139 ± 31) and (509 ± 44) $\mathrm{m}^2\cdot\mathrm{mol}^{-1}$ for Dronpa-2 and Dronpa-3, respectively. The results are summarized in Table 5.1.

	$\sigma_{12,480}+\sigma_{21,480}$ ($\mathrm{m}^2\cdot\mathrm{mol}^{-1}$)	$\sigma_{12,405}+\sigma_{21,405}$ ($\mathrm{m}^2\cdot\mathrm{mol}^{-1}$)	k_{21}^{Δ} (s^{-1})
Dronpa-2	157 ± 5	1139 ± 31	$(1.50 \pm 0.05)\times 10^{-2}$
Dronpa-3	21 ± 3	509 ± 44	0.17 ± 0.01

Table 5.1: Kinetic parameters of Dronpa-2 and Dronpa-3 at 37 °C. pH 6.8 MES buffer.

---

[a] Other characterizations are currently performed with the two RSFPs Padron[130] and rsFastLime.[128] They will be soon employed for applications in imaging of the two-color OPIOM approach.

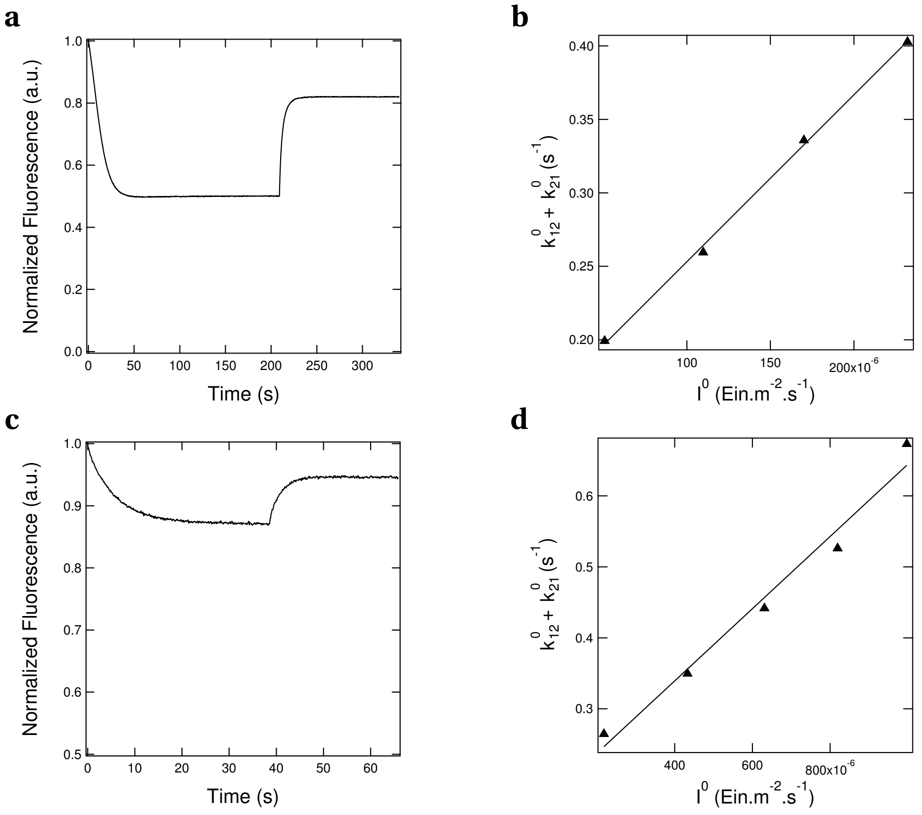

Figure 5.1: Photoisomerization kinetics of Dronpa-2 (**a**,**b**) and Dronpa-3 (**c**,**d**). (**a**,**c**) Temporal evolution of the normalized fluorescence emission at 515 nm of Dronpa-2/3 solutions (1 μM) upon illumination at 480 nm (I_1^0 = 4.7×10^{-4} ein.s^{-1}.m^{-2} (**a**) or 6.1×10^{-5} ein.s^{-1}.m^{-2} (**c**)) and 405 nm (I_2^0 = 1.1×10^{-4} ein.s^{-1}.m^{-2} (**a**) or 6.3×10^{-4} ein.s^{-1}.m^{-2}(**c**)). The 405 nm light is turned on at the onset of the rise of the fluorescence emission. Exponential fit of the corresponding rise yields the relaxation rate constant $(\sigma_{12,480} + \sigma_{21,480})I_1^0 + (\sigma_{12,405} + \sigma_{21,405})I_2^0 + k_{21}^{\Delta}$; (**b**,**d**) Dependence of the relaxation rate constant $(\sigma_{12,480}+\sigma_{21,480})I_1^0+(\sigma_{12,405}+\sigma_{21,405})I_2^0+k_{21}^{\Delta}$ associated to the fluorescence recovery in function of the light intensity I_2^0 . Linear fit enables to extract $\sigma_{12,405} + \sigma_{21,405}$ from the slope. $T = 37°C$ in pH 6.8 Mes buffer.

5.2.3 Application in imaging

To validate the two-color OPIOM approach, we performed similar experiments as the ones introduced in the chapter 4. The results are presented in the following subsections.

5.2.3.1 Selective and quantitative imaging

To demonstrate two-color OPIOM experimentally, we used a microfluidic device composed of four chambers containing solutions of Dronpa-2 at three different concentrations. The fourth chamber was filled with fluorescein, which is a non-photoactive fluorophore that emits in the Dronpa-2 wavelength range but characteristically responds in-phase to the light modulation. The device was imaged using a home-built epifluorescence microscope equipped with two light emitting diodes (LEDs; see Figure 5.10), whose intensities, radial frequency, and phase are easily controlled by driving electrical current. The illumination conditions were tuned to the Dronpa-2 resonance conditions. For this purpose, we chose to modulate the 480 nm LED and keep constant the 405 nm LED. Two separate sets of images were collected : one corresponding to the average fluorescence intensity (hereafter called pre-OPIOM image) and a second corresponding to the processed two-color OPIOM image (see subsection 5.3.2 and Figure 5.2). Dronpa-2 fluorescence emission could be detected in both pre-OPIOM and two-color OPIOM images. In contrast, as expected from the absence of an out-of-phase contribution in its fluorescence emission, fluorescein only gave a signal on the pre-OPIOM image, thus demonstrating the expected selective two-color OPIOM imaging. Furthermore the three chambers with Dronpa-2 showed relative intensities directly reflecting their concentration (see Figure 5.2**d**,**e**), which confirms the theoretical prediction that two-color OPIOM signal is proportional to the probe concentration.

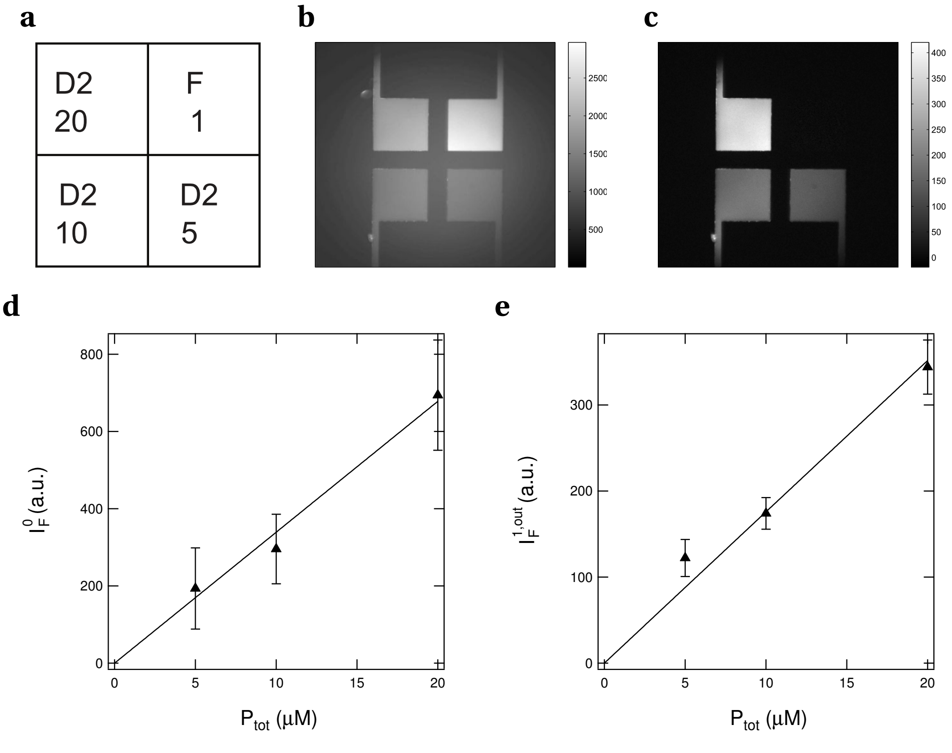

Figure 5.2: Quantitative imaging of Dronpa-2. (**a**–**c**) A microfluidic device with four square chambers ($400\times400\times20$ μm^3) was filled with solutions of Dronpa-2 or fluorescein as described on the scheme (the numbers indicate the concentrations in μM). Pre-OPIOM (**b**) and two-color OPIOM (**c**) images result from imaging the microfluidic device with a 10 × objective at 525 nm under sinusoidal light modulation tuned to the resonance of Dronpa-2 (λ_1; I_1^0; ω; α) = (480 nm; 9.3×10^{-4} Ein$\cdot$ m$^{-2}\cdot$ s^{-1}; 0.29 rad.s^{-1}; 90%), (λ_2; I_2^0) = (405 nm; 1.3×10^{-4} Ein$\cdot$ m$^{-2}\cdot$ s^{-1}); (**d**,**e**) Average value, $\langle I_F^0\rangle$, and average amplitude of the out-of-phase response, $\langle I_F^{1,\mathrm{out}}\rangle$, in function of the total concentration P_{tot} = [Dronpa-2]$_{tot}$ of Dronpa-2. T = 37°C; pH 6.8 MES buffer.

We confirmed this feature by mixing Dronpa-2 and fluorescein in various ratios so that the resulting mixtures gave similar fluorescence intensities on the pre-OPIOM image (Figure 5.3**b**). The excess fluorescein prevented estimation of the Dronpa-2 concentrations from the pre-OPIOM image, but the associated two-color OPIOM image suppressed the contributions from fluorescein (Figure 5.3**c**) and enabled us to accurately quantify the concentrations of Dronpa-2 in the fluorescein/Dronpa-2 mixtures by using the well containing only Dronpa-2 for concentration calibration (Figure 5.3**d**). This result demonstrates the capacity of two-color OPIOM to image Dronpa-2 quantitatively within a mixture containing non-photoactive interfering fluorophores.

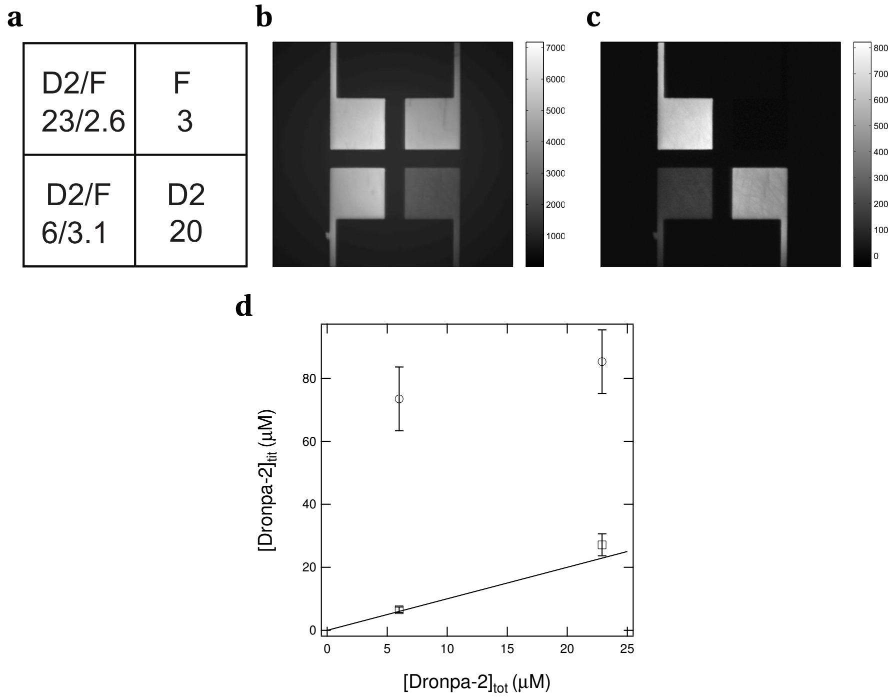

Figure 5.3: Selective and quantitative imaging of Dronpa-2. (**a–c**) A microfluidic device with four square chambers (400×400×20 μm^3) was filled with solutions of Dronpa-2 or fluorescein as described on the scheme (the numbers indicate the concentrations in μM). Pre-OPIOM (**b**) and two-color OPIOM (**c**) images result from imaging the microfluidic device with a 10 × objective at 525 nm under sinusoidal light modulation tuned to the resonance of Dronpa-2 (λ_1; I_1^0; ω; α) = (480 nm; 9.3×10^{-4} Ein$\cdot$ m$^{-2}\cdot$ s^{-1}; 0.29 rad.s^{-1}; 90%), (λ_2; I_2^0) = (405 nm; 1.3×10^{-4} Ein$\cdot$ m$^{-2}\cdot$ s^{-1}); (**d**) Titration of Dronpa-2 ([Dronpa-2]$_{tit}$) in Dronpa-2/Fluorescein mixtures calculated from the pre-OPIOM (circle) and OPIOM (square) image. The line shows the expected Dronpa-2 concentrations ([Dronpa-2]$_{tot}$). T = 37°C; pH 6.8 MES buffer.

We next tried to distinguish two photoswitchable fluorophores exhibiting similar fluorescence emission but different dynamic parameters, $\sigma_{12,480} + \sigma_{21,480}$ and $\sigma_{12,405} + \sigma_{21,405}$. The illumination was tuned to the resonance conditions of either Dronpa-2 or Dronpa-3 to selectively image Dronpa-2 in presence of Dronpa-3 and vice versa (Figure 5.4). Applying two-color OPIOM enabled us to observe the predominant response of the targeted probe even though the contribution of the non-resonant species is not completely extinguished as expected from the rather small difference between the photochemical parameters of Dronpa-2 and Dronpa-3 (see Table 5.1).

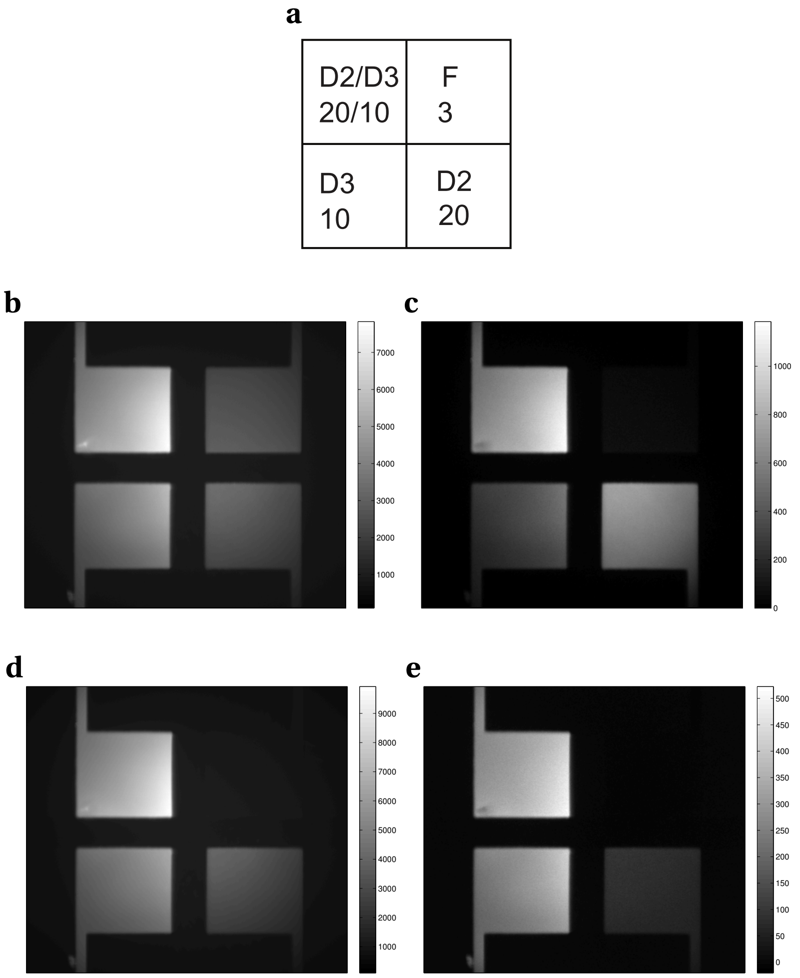

Figure 5.4: Selective and quantitative imaging of Dronpa-2 or Dronpa-3. A microfluidic device with four square chambers (400×400×20 μm^3) was filled with solutions of Dronpa-2, Dronpa-3 or fluorescein as described on the scheme (**a**; the numbers indicate the concentrations in μM). The pre-OPIOM (**b**,**d**) and two-color OPIOM (**c**,**e**) images result from imaging the microfluidic device with a 10 × objective at 525 nm under sinusoidal light modulation tuned to the resonance of either (**b**, **c**) Dronpa-2 (λ_1; I_1^0; ω; α) = (480 nm; 9.3 × 10^{-4} Ein· m^{-2}· s^{-1}; 0.29 rad.s^{-1}; 90%), (λ_2; I_2^0) = (405 nm; 1.3 × 10^{-4} Ein· m^{-2}· s^{-1}) or (**d**, **e**) Dronpa-3 (λ_1; I_1^0; ω; α) = (480 nm; 8.1 × 10^{-2} Ein· m^{-2}· s^{-1}; 3.4 rad.s^{-1}; 90%), (λ_2; I_2^0) = (405 nm; 3.3 × 10^{-3} Ein· m^{-2}· s^{-1}). T = 37°C. pH 6.8 MES buffer.

5.2.3.2 Selective imaging in cells

To test two-color OPIOM for selective imaging in mammalian cells, we imaged fixed HEK293 cells co-expressing nuclear Dronpa-3 and membrane-localized EGFP using modulated excitation tuned to Dronpa-3 resonance. Two-color OPIOM enabled removal of the interfering EGFP signal and revealed only a Dronpa-3 signal (see Figure 5.5 and Figure 5.11 for control experiment).

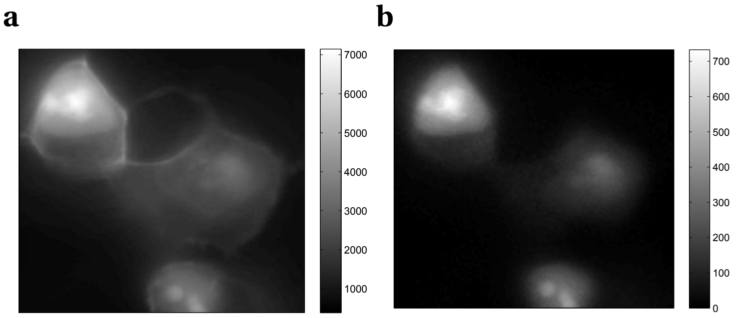

Figure 5.5: Selective imaging of Dronpa-3 in live HEK293 cells co-expressing nuclear Dronpa-3 and membrane-localized EGFP. Pre-OPIOM (**a**) and two-color OPIOM (**b**) images result from analyzing a movie recorded with a 63 × objective at 525 nm under sinusoidal light modulation tuned to the resonance of Dronpa-3 (λ_1; I_1^0; ω; α) = (480 nm; 8.1×10^{-2} Ein· m^{-2}· s^{-1}; 3.41 rad.s^{-1}; 90%), (λ_2; I_2^0) = (405 nm; 3.3×10^{-3} Ein· m^{-2}· s^{-1}). T = 37°C.

In the previous experiment, the period at resonance was fixed to 1.84 s. We then tried to reach an even better temporal resolution. The frequency at resonance is proportional to the sum $\sigma_{12,1} + \sigma_{21,1}$ or $\sigma_{12,2} + \sigma_{21,2}$ for the cis-to-trans and trans-to-cis photoisomerization action cross-sections respectively at λ_1 or λ_2 (see Eq. 5.3). As a consequence, for the same light intensity, the more effective the photoswitching, the larger the frequency at resonance. Thus we chose to employ Dronpa-2 which exhibits larger values of action cross-sections than Dronpa-3. We imaged fixed HEK293 cells co-expressing nuclear Dronpa-2 and membrane-localized EGFP using modulated excitation tuned to Dronpa-2 resonance. Two-color OPIOM efficiently eliminated the EGFP interfering signal and revealed only the signal of Dronpa-2 (see Figure 5.6 and Figure 5.12 for control experiment). With the employed illumination conditions, we were able to reach a period at resonance of 200 ms. This temporal resolution is adapted for dynamic studies of biological processes.

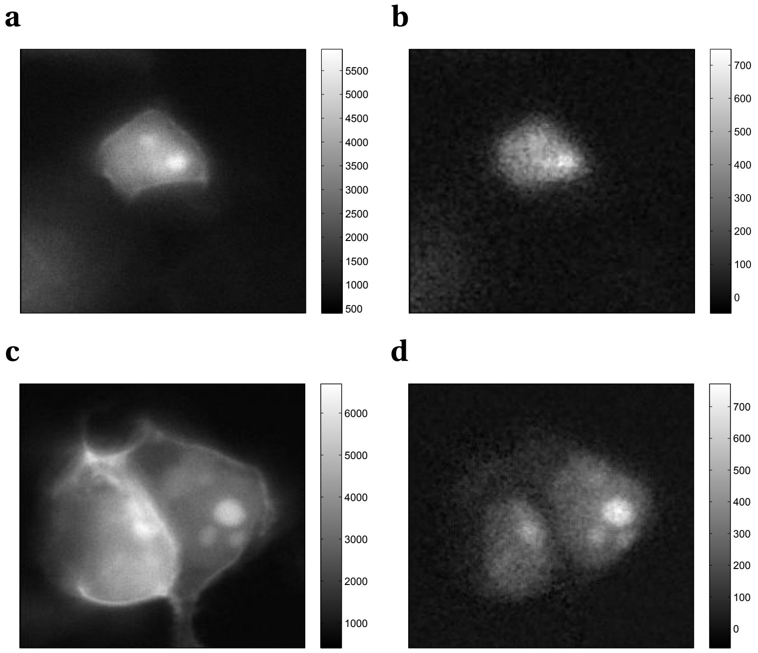

Figure 5.6: Selective imaging of Dronpa-2 in live HEK293 cells co-expressing nuclear Dronpa-2 and membrane-localized EGFP. Pre-OPIOM (**a**,**c**) and two-color OPIOM (**b**,**d**) images result from analyzing a movie recorded with a 63 × objective at 525 nm under sinusoidal light modulation tuned to the resonance of Dronpa-2 (λ_1; I_1^0; ω; α) = (480 nm; 1×10^{-1} Ein$\cdot$ m$^{-2}\cdot$ s^{-1}; 31.4 rad.s^{-1}; 90%), (λ_2; I_2^0) = (405 nm; 1.4×10^{-2} Ein$\cdot$ m$^{-2}\cdot$ s^{-1}). T = 37°C.

5.2.3.3 Selective imaging in multicellular organisms

Finally, two-color OPIOM was tested for selective imaging in multicellular organisms. We used again zebrafish embryo as a model organism. We injected zebrafish with Lifeact-Dronpa-3 mRNAs for actin targeting and imaged them 24 hours post-fertilization. Two-color OPIOM canceled out the yolk autofluorescence and selectively visualized Lifeact-Dronpa-3 in the embryo's head (Figure 5.7).

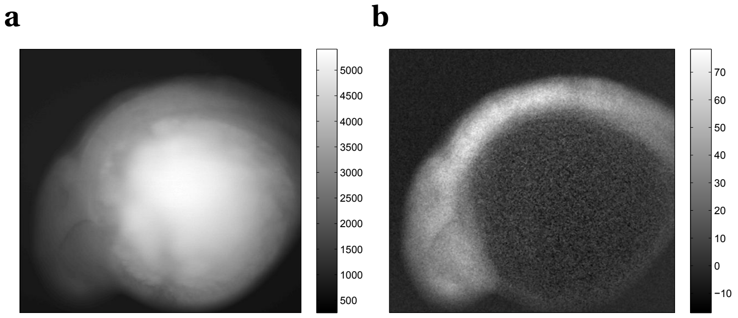

Figure 5.7: Selective imaging of Dronpa-3 in zebrafish embryos expressing Dronpa-3 Lifeact. Pre-OPIOM (**a**) and two-color OPIOM (**b**) images result from analyzing a movie recorded with a 10 × objective at 525 nm under sinusoidal light modulation tuned to the resonance of Dronpa-3 (λ_1; I_1^0; ω; α) = (480 nm; 8.1×10^{-2} Ein· m^{-2}· s^{-1}; 3.41 rad.s^{-1}; 90%), (λ_2; I_2^0) = (405 nm; 3.3×10^{-3} Ein· m^{-2}· s^{-1}). T = 37°C.

5.2.4 Conclusion

Like one-color OPIOM, two-color OPIOM allows us for selective and quantitative imaging of photoswitchable fluorescent probes. In particular, we strongly improved the temporal resolution of the OPIOM protocol by employing two light sources to drive the photoswitching. We reached a frequency at resonance of 5 Hz which is relevant for studying in real-time most of dynamic biological processes.

5.3 Supporting information

5.3.1 Supplementary text 1: Photoswitchable fluorophore responses to illuminations

5.3.1.1 The model

The dynamic behavior of a photoswitchable probe **P** illuminated with a light of intensity $I(t)$ involving two components $I_1(t)$ and $I_2(t)$ at wavelengths λ_1 and λ_2 can be described by the two-state exchange (5.4)

$$\mathbf{1} \quad \underset{k_{21}(t)}{\overset{k_{12}(t)}{\rightleftharpoons}} \quad \mathbf{2} \tag{5.4}$$

where the thermodynamically most stable state **1** is photochemically converted to the thermodynamically less stable state **2** at rate constant $k_{12}(t) = \sigma_{12,1}I_1(t) + \sigma_{12,2}I_2(t)$ from which it can relax back to the initial state **1** either by a photochemically- or a thermally-driven process at rate constant $k_{21}(t) = \sigma_{21,1}I_1(t) + \sigma_{21,2}I_2(t) + k_{21}^{\Delta}$ where $\sigma_{12,1}I_1(t)$, $\sigma_{12,2}I_2(t)$, $\sigma_{21,1}I_1(t)$, $\sigma_{21,2}I_2(t)$, and k_{21}^{Δ} are respectively the photochemical and the thermal contributions of the rate constant. In that case, the molecular action cross-sections for photoisomerization $\sigma_{12,1}$ and $\sigma_{21,1}$ (at λ_1), $\sigma_{12,2}$ and $\sigma_{21,2}$ (at λ_2), and the thermal rate constant k_{21}^{Δ} fully define the behavior of the photoswitchable probe.

We assume that the system is either uniformly illuminated or that it can be considered homogeneous at any time of its evolution. Then we rely on the two-state exchange (5.4) to write Eqs.(5.5–5.6) describing the concentration evolutions:

$$\frac{d1}{dt} = -k_{12}(t)\,1 + k_{21}(t)\,2 \tag{5.5}$$

$$\frac{d2}{dt} = k_{12}(t)\,1 - k_{21}(t)\,2. \tag{5.6}$$

5.3.1.2 Response to light jumps

When the system is submitted to a constant illumination defined by the intensity $I(t) = I_1^0 + I_2^0 = I^0$, the forward and backward rate constants become

$$k_{12}(t) = k_{12}^0 = \sigma_{12,1}I_1^0 + \sigma_{12,2}I_2^0 \tag{5.7}$$

$$k_{21}(t) = k_{21}^0 = \sigma_{21,1}I_1^0 + \sigma_{21,2}I_2^0 + k_{21}^{\Delta}. \tag{5.8}$$

The temporal evolution of the concentrations in **1** and **2** evolves as

$$2 - 2^0 = 1^0 - 1 = -2^0 \exp\left(-\frac{t}{\tau_{12}^0}\right) \tag{5.9}$$

where

$$\tau_{12}^0 = \frac{1}{k_{12}^0 + k_{21}^0} \tag{5.10}$$

designates the relaxation time of the photoswitchable fluorophore and 1^0 and 2^0 the concentrations of **1** and **2** at the photostationnary state reached after τ_{12}^0

$$1^0 = P_{tot} - 2^0 = \frac{1}{1 + K_{12}^0} P_{tot} \tag{5.11}$$

where

$$K_{12}^0 = \frac{k_{12}^0}{k_{21}^0} \tag{5.12}$$

and the total concentration in photoswitchable probe **P**, $P_{tot} = 1 + 2$.

The fluorescence emission $I_F(t)$ results then from the individual contributions of the species **1** and **2**, and can be written

$$I_F(t) = (Q_1 1 + Q_2 2)\, I(t) \tag{5.13}$$

where Q_1 and Q_2 are the molecular brightnesses of **1** and **2**. From Eq.(5.9), one subsequently derives

$$\frac{I_F(t)}{Q_1 P_{tot} I^0} = 1 + \left(\frac{Q_2}{Q_1} - 1\right) \frac{K_{12}^0}{1 + K_{12}^0} \left[1 - \exp\left(-\frac{t}{\tau_{12}^0}\right)\right]. \tag{5.14}$$

At infinite times, fluorescence emission asymptotically tends toward $I_F^0 = \left(Q_1 1^0 + Q_2 2^0\right) I^0$.

5.3.1.3 Response to sinusoidal light modulation of small amplitude

To illustrate the behavior of the system upon illumination with a periodically modulated light, we consider a sinusoidally modulated illumination oscillating around the averaged value I_1^0 at angular frequency ω_1 and with a small amplitude εI_1^0 ($\varepsilon \ll 1$) on which we superpose a constant illumination I_2^0. Hence

$$I(t) = I_1^0 \left[1 + \varepsilon \sin(\omega t)\right] + I_2^0. \tag{5.15}$$

After introducing

$$k_{12,1}^0 = \sigma_{12,1} I_1^0 \tag{5.16}$$

$$k_{21,1}^0 = \sigma_{21,1} I_1^0 \tag{5.17}$$

$$k_{12,2}^0 = \sigma_{12,2} I_2^0 \tag{5.18}$$

$$k_{21,2}^0 = \sigma_{21,2} I_2^0 \tag{5.19}$$

we write

$$\begin{aligned} k_{12}(t) &= k^0_{12,1}\left[1+\varepsilon\sin(\omega t)\right]+k^0_{12,2} && (5.20)\\ k_{21}(t) &= k^0_{21,1}\left[1+\varepsilon\sin(\omega t)\right]+k^0_{21,2}+k^{\Delta}_{21}, && (5.21)\end{aligned}$$

and the system of differential equations governing the temporal evolution of the concentrations in **1** and **2** is solved at the first-order expansion in the light perturbation. Beyond the relaxation time τ^0_{12}, one enters into the forced and permanent regime where the concentration

$$i = i^0 + \varepsilon i^1 \sin\left(\omega t - \phi_{12}\right) \tag{5.22}$$

in each species **i** (**i** = **1** or **2**) oscillates around a mean value i^0 (corresponding to the concentration of **i** at steady-state associated to the photon flux I^0; see Eq.(5.11)) at the angular frequency ω but with a phase delay of $\phi_{12} = \arctan\left(\omega\tau^0_{12}\right)$. The amplitudes of the concentration modulation are given in Eq.(5.23)

$$2^1 = -1^1 = \frac{\rho^0_{12}\tau^0_{12}\Delta^0_{12}}{\sqrt{1+\left(\omega\tau^0_{12}\right)^2}} \tag{5.23}$$

where

$$\rho^0_{12} = k^0_{12}1^0 = k^0_{21}2^0 \tag{5.24}$$

and

$$\Delta^0_{12} = \frac{k^0_{12,1}}{k^0_{12,1}+k^0_{12,2}} - \frac{k^0_{21,1}}{k^0_{21,1}+k^0_{21,2}+k^{\Delta}_{21}} \tag{5.25}$$

designate the steady-state rate of reaction (5.4) and the contributions of the photochemical process by the modulated light to the transition from **1** to **2** or from **2** to **1** respectively upon illuminating at I^0.

The phase-delayed oscillating concentrations i can also be written

$$i(t) = i^0 + \varepsilon\left[i^{1,in}\sin(\omega t) + i^{1,out}\cos(\omega t)\right] \tag{5.26}$$

where $\varepsilon i^{1,in}\sin(\omega t)$ and $\varepsilon i^{1,out}\cos(\omega t)$ are in-phase and out-of-phase (or quadrature-delayed) oscillating terms at angular frequency ω. The amplitudes $i^{1,in}$ and $i^{1,out}$ of the in-phase and out-of-phase oscillating terms are

$$\begin{aligned} 2^{1,in} &= -1^{1,in} = \rho^0_{12}\tau^0_{12}\Delta^0_{12}\frac{1}{1+\left(\omega\tau^0_{12}\right)^2} = \Delta^0_{12}\frac{K^0_{12}}{\left(1+K^0_{12}\right)^2}\frac{1}{1+\left(\omega\tau^0_{12}\right)^2}P_{tot} && (5.27)\\ 2^{1,out} &= -1^{1,out} = -\rho^0_{12}\tau^0_{12}\Delta^0_{12}\frac{\omega\tau^0_{12}}{1+\left(\omega\tau^0_{12}\right)^2} = -\Delta^0_{12}\frac{K^0_{12}}{\left(1+K^0_{12}\right)^2}\frac{\omega\tau^0_{12}}{1+\left(\omega\tau^0_{12}\right)^2}P_{tot} && (5.28)\end{aligned}$$

where we used that $\rho_{12}^0\tau_{12}^0 = P_{tot}\left[K_{12}^0/\left(1+K_{12}^0\right)^2\right]$.

Since the fluorescence emission results from the contributions of the species **1** and **2**, the phase delay within the oscillating concentrations leads to a phase delay of the oscillating fluorescence emission. The phase-delayed oscillating fluorescence emission is therefore

$$I_F(t) \quad = \quad I_F^0 + I_F^{1,in}\sin(\omega t) + I_F^{1,out}\cos(\omega t) \tag{5.29}$$

where the amplitude $I_F^{1,in}$ and $I_F^{1,out}$ of the in-phase and out-of-phase terms are

$$I_F^{1,in} \quad = \quad \varepsilon\left[\left(Q_1 1^0 + Q_2 2^0\right) I_1^0 + \left(Q_1 - Q_2\right) 1^{1,in} I^0\right] \tag{5.30}$$

$$I_F^{1,out} \quad = \quad \varepsilon\left(Q_1 - Q_2\right) 1^{1,out} I^0. \tag{5.31}$$

5.3.1.4 Optimal out-of-phase response

Two-color OPIOM differs from One-color OPIOM in the limit where the exchange between the states **1** and **2** is essentially driven by the photochemical contributions. We correspondingly chose to focus the subsequent analysis in a range of light intensities (I_1^0,I_2^0) such that $\sigma_{21,1}I_1^0 + \sigma_{21,2}I_2^0 \gg k_{21}^{\Delta}$. Moreover, we adopted Dronpa-2 for illustration (*vide infra*). It is characterized by a quintuplet of parameters $\left(\sigma_{12,1}, \sigma_{21,1}, \sigma_{12,2}, \sigma_{21,2}, k_{21}^{\Delta}\right)$ such that $\sigma_{12,1} \gg \sigma_{12,2}$ and $\sigma_{21,2} \gg \sigma_{21,1}$. Its normalized out-of-phase $|\Delta 1_{norm}^{out}| = |1^{1,out}/\varepsilon P_{tot}|$ amplitude as a function of the control parameters I_2^0/I_1^0 and ω/I_1^0 is plotted in Figure 5.8.

$|\Delta 1_{norm}^{out}|$ exhibits a single optimum when the two resonance conditions (5.32,5.33) are fulfilled

$$\left(\sigma_{12,1} + \sigma_{21,1}\right) I_1^0 = \left(\sigma_{12,2} + \sigma_{21,2}\right) I_2^0 \tag{5.32}$$

$$\omega = 2\left(\sigma_{12,1} + \sigma_{21,1}\right) I_1^0. \tag{5.33}$$

The optimization of $1^{1,out}$ results from the independent optimisation of the terms $\rho_{12}^0\tau_{12}^0\Delta_{12}^0$ and $\omega\tau_{12}^0/[1+\left(\omega\tau_{12}^0\right)^2]$ in Eq.(5.28). $\rho_{12}^0\tau_{12}^0\Delta_{12}^0$ measures the composition shift $\Delta 2^0$ from the steady-state 2^0 after a light intensity jump of amplitude $\Delta I_1^0 = \varepsilon I_1^0$.[b] It is maximized when the photochemical reactions driven by the two light sources occur at the same rate. The second optimised term, $\omega\tau_{12}^0/[1+\left(\omega\tau_{12}^0\right)^2]$, is maximized upon matching the radial frequency of the light modulation ω with the exchange relaxation time τ_{12}^0 so that $\omega\tau_{12}^0 = 1$ (see Eqs. (5.32,5.33)). When $\omega \gg 1/\tau_{12}^0$, the exchange is slow compared to the light variations and the couple $\{\mathbf{1},\mathbf{2}\}$ has not enough time to respond: both $i^{1,in}$ and $i^{1,out}$ vanish. Conversely, when $\omega \ll 1/\tau_{12}^0$, $i^{1,out}$ cancels, so the concentrations of **1** and **2** oscillate in phase with the light modulation.

---

[b] From the expression (5.11), one can show that $\frac{d2^0}{dLnI_1^0} = \frac{\Delta 2^0}{\varepsilon} = \Delta_{12}^0 K_{12}^0 P_{tot}/\left(1+K_{12}^0\right)^2$ using $K_{12}^0 = k_{12}^0/k_{21}^0$ with the expressions of k_{12}^0 and k_{21}^0 given in Eqs.(5.7,5.8).

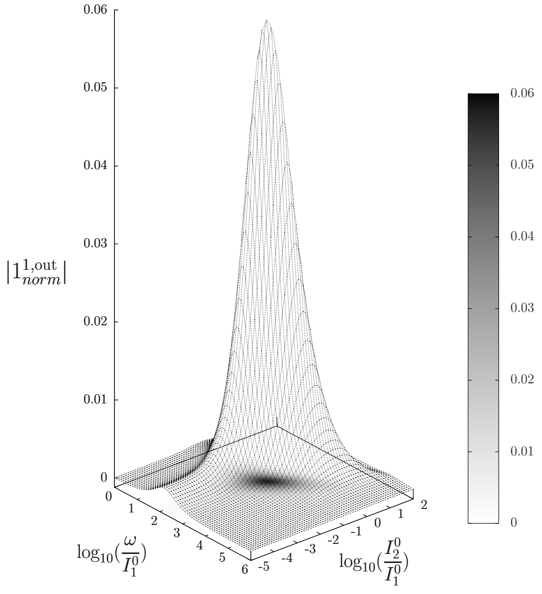

Figure 5.8: Theoretical computation of the response of a photoswitchable fluorophore **1** $\rightleftharpoons$ **2** submitted to light harmonic forcing of small amplitude. The normalized amplitude of the out-of-phase oscillations in **1** concentration, $|1^{1,out}_{norm}|$, is plotted versus the ratios I_2^0/I_1^0 and ω/I_1^0 when $I_1^0 = 100\frac{k_{21}^{\Delta}}{\sigma_{12,1}+\sigma_{21,1}}$. $\sigma_{12,1}$ = 73 m^2.mol^{-1}, $\sigma_{21,1}$ = 84 m^2.mol^{-1}, $\sigma_{12,2}$ = 0 m^2.mol^{-1}, $\sigma_{21,2}$ = 1149 m^2.mol^{-1}, $k_{21}^{\Delta} = 1.5 \times 10^{-2}$ s^{-1}.

5.3.1.5 Response to periodic light modulation of large amplitude

The use of a sinusoidal modulation of small amplitude for $I_1(t)$ is favorable to derive simple analytical expressions. However, it generates only weak variations of the probe signal because of the small modulation, which is a drawback to reliably extract the out-of-phase amplitude of the first order response. To circumvent this drawback, we also analyzed the response of a photoswitchable probe to two different periodic modulations of large amplitude α:

- As a natural extension of the previous case, we first considered a sinusoidal modulation of large amplitude for $I_1(t)$ and correspondingly adopted

$$I(t) \quad = \quad I_1^0\left[1+\alpha\sin(\omega t)\right]+I_2^0; \tag{5.34}$$

- We then considered a square wave modulation for $I_1(t)$ because its experimental implementation (on-off illumination switching) is simple. We retained its Fourier series expansionby choosing the starting time ($t = 0$) in this expansion halfway through the first pulse. We correspondingly used

$$I(t) \quad = \quad I_1^0\left\{1+\frac{4\alpha}{\pi}\sum_{p=0}^{\infty}\frac{1}{2p+1}\sin\left[\left(2p+1\right)\omega t\right]\right\}+I_2^0. \tag{5.35}$$

To cover both types of modulation of large amplitude, we wrote the following expression for the light intensity

$$I(t) = I_1^0\left[1+\alpha h(\omega t)\right]+I_2^0 \tag{5.36}$$

where $h(\omega t)$ designate a periodic function with fundamental radial frequency ω. Eq.(5.36) was used to express the rate constants with Eqs.(5.5,5.6). Then, upon expanding the concentration expressions as

$$2 = 2^0+\alpha f(\omega t) \tag{5.37}$$

$$1 = 1^0-\alpha f(\omega t), \tag{5.38}$$

the system of differential equations governing the temporal evolution of the concentrations in **1** and **2** becomes

$$\frac{df(\theta x)}{dx} = -f(\theta x)+\left[a-bf(\theta x)\right]h(\theta x) \tag{5.39}$$

where

$$x = \frac{t}{\tau_{12}^0} \tag{5.40}$$

$$a = \rho_{12}^0\Delta_{12}^0\tau_{12}^0 \tag{5.41}$$

$$b = \alpha\left(\sigma_{12,1}+\sigma_{21,1}\right)I_1^0\tau_{12}^0 \tag{5.42}$$

$$\theta = \omega\tau_{12}^0. \tag{5.43}$$

The equation (5.39) is exactly the same as the one, which was derived to address the response to periodic light modulation of large amplitude in the absence of secondary light source to accelerate the back conversion of **2** into **1** (One color-OPIOM; see Eq.19).[172] In fact, only the interpretation of the a and b parameters differs between both OPIOM modalities. In particular, all the results derived with one-color OPIOM in the case of light modulation of large amplitude are here relevant after taking into account the new interpretation of a and b. In the following, we just summarize the main results; the reader should refer to the theoretical account[172] for more details.

Beyond the relaxation time τ_{12}^0, one enters into a permanent regime in which $f(\theta x)$ is a continuous periodic function. In contrast to the preceding situation (sinusoidal modulation of small amplitude), one cannot anymore restrict the $f(\theta x)$ analysis to the first-order. The $f(\theta x)$ function has to be expressed as a Fourier series

$$f(\theta x) = a_0+\sum_{n=1}^{+\infty}\left[a_n\cos(n\theta x)+b_n\sin(n\theta x)\right] \tag{5.44}$$

where a_n and b_n designate the amplitudes of the n-th components of the Fourier series. The a_n and b_n terms can be extracted from Eq.(5.39) upon identifying the amplitudes of the components of same order. Then one can obtain the expressions of the concentrations in **1** and **2**:

$$2 = 2^0 + \alpha \left\{ a_0 + \sum_{n=1}^{+\infty} \left[a_n \cos(n\theta x) + b_n \sin(n\theta x) \right] \right\} \tag{5.45}$$

$$1 = 1^0 - \alpha \left\{ a_0 + \sum_{n=1}^{+\infty} \left[a_n \cos(n\theta x) + b_n \sin(n\theta x) \right] \right\}. \tag{5.46}$$

Consequently, at steady-state, a large periodic modulation of illumination now causes modulation of the concentrations in **1** and **2** at an infinite number of radial frequencies. Eqs.(5.45,5.46) can be transformed to explicit the amplitudes $\mathrm{i}^{\mathrm{n,in}}$ and $\mathrm{i}^{\mathrm{n,out}}$ of the in-phase and out-of phase terms oscillating at the radial frequency $n\omega$. The concentration of **i** can be now written

$$i = \mathrm{i}^{\mathrm{o}} + \alpha \sum_{n=1}^{+\infty} \left[\mathrm{i}^{\mathrm{n,in}} \sin(n\omega t) + \mathrm{i}^{\mathrm{n,out}} \cos(n\omega t) \right]. \tag{5.47}$$

Interestingly, i^{o}, $\mathrm{i}^{\mathrm{n,in}}$ and $\mathrm{i}^{\mathrm{n,out}}$ are proportional to P_{tot}. Moreover we showed that $\mathrm{i}^{1,\mathrm{out}}$ exhibits an optimum in the space (I^0,ω), which coordinates and amplitude are very close to those observed with a sinusoidal modulation of small amplitude (upon taking into account a $\frac{4}{\pi}$ amplitude correction in the specific case of the square-wave light modulation, which originates from the Fourier series expression given in Eq.(5.35)).[c]

Considering that both concentrations of the states **1** and **2**, and light intensity are modulated, the fluorescence emission $I_F(t)$ can be written

$$I_F(t) = \left[Q_1 1(t) + Q_2 2(t) \right] I(t) = \mathfrak{I}_{\mathfrak{F}}^{\mathrm{o}} + \sum_{n=1}^{\infty} \left[\mathfrak{I}_{\mathfrak{F}}^{\mathrm{n,in}} \sin(n\omega t) + \mathfrak{I}_{\mathfrak{F}}^{\mathrm{n,out}} \cos(n\omega t) \right] \tag{5.48}$$

where

$$\mathfrak{I}_{\mathfrak{F}}^{1,\mathrm{out}} = \alpha (Q_2 - Q_1) I^0 \left[2^{1,\mathrm{out}} + g\left(2^{\mathrm{n,in}}, 2^{\mathrm{n,out}} \right) \right] \tag{5.49}$$

with $n \geq 1$. Whereas $g\left(2^{\mathrm{n,in}}, 2^{\mathrm{n,out}}\right) = 0$ for a sinusoidal modulation of small amplitude, $g\left(2^{\mathrm{n,in}}, 2^{\mathrm{n,out}}\right)$ is non-vanishing in the case of a periodic modulation of large amplitude.

In a regime of sinusoidal modulation of small amplitude, the out-of-phase amplitude of the fluorescence emission, $\mathfrak{I}_{\mathfrak{F}}^{1,\mathrm{out}}$, is proportional to $2^{1,out}$ and exhibits a resonant behavior. In contrast, such a conclusion cannot be directly drawn in the case of periodic modulation of large amplitude since analytical expressions are cumbersome. We therefore evaluated its relevance by means of numerical calculations using typical values found for photoswitchable fluorescent proteins.[172] We showed that $\mathfrak{I}_{\mathfrak{F}}^{1,\mathrm{out}}$is proportional to $2^{1,\mathrm{out}}$ and exhibits an optimum in the space (I_1^0,I_2^0,ω), which coordinates and amplitude are very close to those

---

[c] In fact the error done when taking the analytical expression of the resonance conditions, valid only for a modulation of small amplitude, is always less than 20 %, no matter which amplitude α is used. Such an error would be of the order of magnitude of the experimental errors done when fixing the average light intensity and radial frequency to their values at resonance, $I^{0,R}$ and ω^R.

observed with a sinusoidal modulation of small amplitude (with the $\frac{4}{\pi}$ amplitude correction in the case of the square-wave light modulation). Hence, the analysis of the out-of-phase first-order fluorescence emission $\mathfrak{I}_{\mathfrak{F}}^{\mathfrak{1,out}}$ enables the selective and quantitative detection of a photoswitchable fluorophore.

5.3.1.6 Retrieval of concentrations from the fluorescence intensity

Extraction of $\mathfrak{I}_{\mathfrak{F}}^{\mathfrak{0}}$, $\mathfrak{I}_{\mathfrak{F}}^{\mathfrak{1,in}}$, and $\mathfrak{I}_{\mathfrak{F}}^{\mathfrak{1,out}}$ from the overall signal $I_F(t)$ Upon modulating light, the fluorescence intensity associated to the photoswitchable probe adopts the general expression (5.48). $\mathfrak{I}_{\mathfrak{F}}^{\mathfrak{0}}$, $\mathfrak{I}_{\mathfrak{F}}^{\mathfrak{1,in}}$, and $\mathfrak{I}_{\mathfrak{F}}^{\mathfrak{1,out}}$ can be easily retrieved from the experimental trace of the observed signal $I_F(t)$ (either global or from each analyzed pixel).

As shown in Eq.(5.48), $\mathfrak{I}_{\mathfrak{F}}^{\mathfrak{0}}$ can be obtained upon averaging $I_F(t)$ over an integer number m of periods of the modulated illumination

$$Int^0 = \frac{1}{mT}\int_0^{mT} I_F(t)dt = \mathfrak{I}_{\mathfrak{F}}^{\mathfrak{0}}. \tag{5.50}$$

In particular, upon observing fluorescence emission in a regime of sinusoidal light modulation of small amplitude, one has $Int^0 = I_F^0$.

The first-order amplitudes $\mathfrak{I}_{\mathfrak{F}}^{\mathfrak{1,in}}$ and $\mathfrak{I}_{\mathfrak{F}}^{\mathfrak{1,out}}$ can be extracted from the fluorescence signal upon computing the integrals $Int^{1,in}$ and $Int^{1,out}$

$$Int^{1,in} = \frac{2}{mT}\int_0^{mT} I_F(t)\sin(\omega t)\,dt = \mathfrak{I}_{\mathfrak{F}}^{\mathfrak{1,in}} \tag{5.51}$$

$$Int^{1,out} = \frac{2}{mT}\int_0^{mT} I_F(t)\cos(\omega t)\,dt = \mathfrak{I}_{\mathfrak{F}}^{\mathfrak{1,out}}. \tag{5.52}$$

Upon observing fluorescence emission in a regime of sinusoidal light modulation of small amplitude, one has $Int^{1,in} = I_F^{1,in}$ and $Int^{1,out} = I_F^{1,out}$, and $Int^{n,in} = I_F^{n,in} = 0$ and $Int^{n,out} = I_F^{n,out} = 0$.

Eqs.(5.51,5.52) illustrate orthogonality between the various components of the fluorescence intensity in Eq. (5.48). In particular, the computed integral $Int^{1,out}$ used to extract the OPIOM image does not contain any contribution from the constant amplitude $\mathfrak{I}_{\mathfrak{F}}^{\mathfrak{0}}$ as well as from the in-phase amplitude $\mathfrak{I}_{\mathfrak{F}}^{\mathfrak{1,in}}$. This mathematical property is crucial to eliminate the contributions of non-photoactive fluorescent interfering species, which fluorescence response contains constant and in-phase terms only.

Quantifying a targeted photoswitchable probe In the absence of light modulation or in a regime of sinusoidal light modulation of small amplitude, the expression of $\mathfrak{I}_{\mathfrak{F}}^{\mathfrak{0}}$ is

$$\frac{\mathfrak{I}_{\mathfrak{F}}^{\mathfrak{0}}}{I^0} = Q_1\frac{1}{1+K_{12}^0}P_{tot} + Q_2\frac{K_{12}^0}{1+K_{12}^0}P_{tot}. \tag{5.53}$$

In the presence of light modulation, $\mathfrak{I}_{\mathfrak{F}}^{1,\mathfrak{out}}$ can be reliably evaluated from its expression in the case of a sinusoidal light modulation of small amplitude

$$\frac{\mathfrak{I}_{\mathfrak{F}}^{1,\mathfrak{out}}}{I^0} = \varepsilon\left(Q_1 - Q_2\right)\Delta_{12}^0 \frac{K_{12}^0}{\left(1+K_{12}^0\right)^2}\frac{\omega\tau_{12}^0}{1+\left(\omega\tau_{12}^0\right)^2}P_{tot}. \tag{5.54}$$

The theoretical expressions (5.53,5.54) make possible to directly retrieve the concentrations of the photoswitchable probe from the fluorescence intensity. However this approach requires the effort to acquire the values of all parameters involved in these expressions. Alternatively, quantification can proceed by calibration with the pure photoswitchable probe at a reference concentration. Eqs.(5.53,5.54) show that $\mathfrak{I}_{\mathfrak{F}}^{0}$ and $\mathfrak{I}_{\mathfrak{F}}^{1,\mathfrak{out}}$ are proportional to the overall concentration in photoswitchable probe. Thus quantification can be simply achieved by recording the fluorescence intensity from a calibrating solution of the photoswitchable probe at a known concentration P_{tot}^{cal}. The concentrations of the photoswitchable probe, which are retrieved at zeroth- and first-order, are respectively

$$P_{tot}^{0} = \frac{\mathfrak{I}_{\mathfrak{F}}^{0}}{\mathfrak{I}_{\mathfrak{F}}^{0,\mathfrak{cal}}}P_{tot}^{cal} \tag{5.55}$$

$$P_{tot}^{1,out} = \frac{\mathfrak{I}_{\mathfrak{F}}^{1,\mathfrak{out}}}{\mathfrak{I}_{\mathfrak{F}}^{1,\mathfrak{out},\mathfrak{cal}}}P_{tot}^{cal}. \tag{5.56}$$

5.3.1.7 Selective and quantitative detection

Optimizing the out-of-phase first-order response by choosing a triplet (I_1^0,I_2^0,ω) that verifies the resonance conditions (5.32) and (5.33) opens an interesting way to selectively image and quantify a photoswitchable fluorophore **P** in the presence of interfering compounds **X** (of total concentrations X_{tot}), each defined by a different set of parameters ($\sigma_{12,1,X}$, $\sigma_{21,1,X}$, $\sigma_{12,2,X}$, $\sigma_{21,2,X}$, $k_{21,X}^{\Delta}$). Note that **X** can be non-photoswitchable: in that case $\sigma_{12,i,X} = \sigma_{21,i,X} = 0$ (i=1 or 2) and $k_{21,X}^{\Delta} = 0$. To illustrate this, let us take a simplified case of a mixture containing photoswitchable fluorophores, whose only the state **1** yields an observable fluorescence emission, and possessing all the same brightness Q_1. In that case, a protocol relying on illumination at constant light intensities I_i^0 leads to a signal I_F^0 which is proportional to the sum of the contributions of the different fluorophores such that:

$$I_F^0 \propto \mathbf{1}_P^0 + \sum_X \mathbf{1}_X^0 = (\mathbf{1}_P^0/P_{tot})P_{titration}^0 \tag{5.57}$$

where

$$P_{titration}^0 = P_{tot} + \sum_X \frac{(\mathbf{1}_X^0/X_{tot})}{(\mathbf{1}_P^0/P_{tot})}X_{tot} > P_{tot} \tag{5.58}$$

When the signal I_F^0 is used to titrate the concentration of **P**, the titration result $P_{titration}^0$ always overestimates the total concentration P_{tot} because of the contributions of the interfering compounds (see Figure 5.9a).

In contrast, the corresponding out-of-phase first-order response to light modulation $\mathfrak{I}_{\mathfrak{F}}^{1,\mathfrak{out}}$

$$\mathfrak{I}_{\mathfrak{F}}^{1,\mathfrak{out}} \quad \propto \quad 1_P^{1,out} + \sum_X 1_X^{1,out} = (1_P^{1,out}/P_{tot})P_{titration}^{1,out} \tag{5.59}$$

where

$$P_{titration}^{1,out} = P_{tot} + \sum_X \frac{(1_X^{1,out}/X_{tot})}{(1_P^{1,out}/P_{tot})} X_{tot} \tag{5.60}$$

enables to determine P_{tot} when the light parameters (I_1^0, I_2^0, ω) are tuned to the resonance conditions of **P**. Indeed, the term $1_P^{1,out}$ is then maximal while the terms $1_X^{1,out}$ are negligible. Thus, the signal from **P** now dominates those of the other probes, and the titration result $P_{titration}^{1,out}$ is approximatively equal to P_{tot} (see Figure 5.9a). Figure 5.9b illustrates for various mixtures the superiority of this second strategy over measurements performed at constant light intensity: whereas all the $P_{titration}^0$ are several times larger than the actual P_{tot} concentration, the discrepancy between $P_{titration}^{1,out}$ and P_{tot} becomes negligible as soon as $\left(\sigma_{12,1}, \sigma_{21,1}, \sigma_{12,2}, \sigma_{21,2}\right)$ deviates from $\left(\sigma_{12,1,X}, \sigma_{21,1,X}, \sigma_{12,2,X}, \sigma_{21,2,X}\right)$.

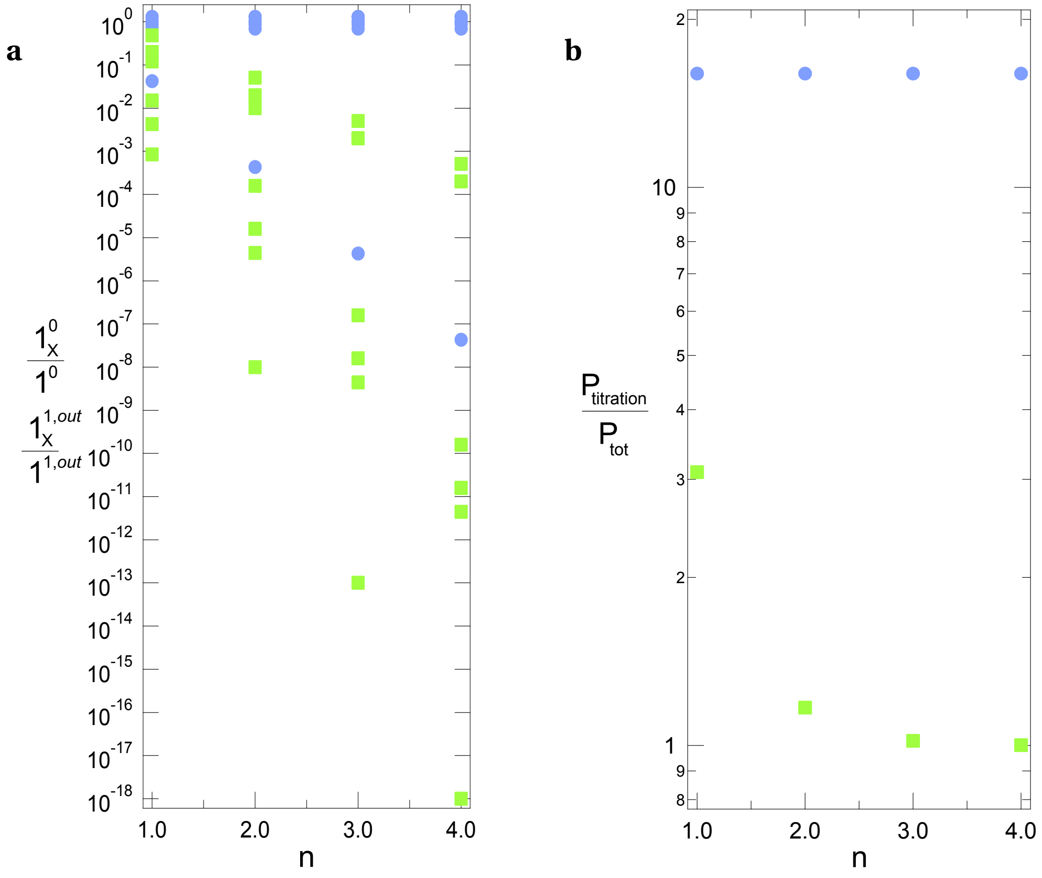

Figure 5.9: Theoretical computation of $P_{titration}$ in four different equimolar mixtures, which include the targeted quintuplet $\left(\sigma_{12,1},\sigma_{21,1},\sigma_{12,2},\sigma_{21,2},k_{21}^{\Delta}\right)$ plus sixteen other interfering ones. In each sample labelled n, the latter species correspond to the sixteen $\left(\sigma_{12,1,X},\sigma_{21,1,X},\sigma_{12,2,X},\sigma_{21,2,X},k_{21}^{\Delta}\right)$ sets, which four photochemical parameters differ by n order of magnitude from $\left(\sigma_{12,1},\sigma_{21,1},\sigma_{12,2},\sigma_{21,2}\right)$. **a**; individual normalized responses $1_X^0/1^0$ (disks) and $1_X^{1,out}/1^{1,out}$ (squares); **b**: n-dependence of the ratio of $P_{titration}$ to the effective target concentration P_{tot} for both the constant light intensity (disks) and the two-color OPIOM (squares) methods. $\sigma_{12,1} = 73$ m^2.mol^{-1}, $\sigma_{21,1} = 84$ m^2.mol^{-1}, $\sigma_{12,2} = 0$ m^2.mol^{-1}, $\sigma_{21,2} = 1149$ m^2.mol^{-1}, $k_{21}^{\Delta} = 1.5 \times 10^{-2}$ s^{-1}; $I_1^0 = 100\frac{k_{21}^{\Delta}}{\sigma_{12,1}+\sigma_{21,1}} = 9.6 \times 10^{-3}$ Ein.s^{-1}.m^{-2}, $I_2^0 = \frac{\sigma_{12,1}+\sigma_{21,1}}{\sigma_{12,2}+\sigma_{21,2}} I_1^0 = 1.3 \times 10^{-3}$ Ein.s^{-1}.m^{-2}, $\omega = 2\left(\sigma_{12,1}+\sigma_{21,1}\right) = 3$ rad·s^{-1}.

5.3.2 Supplementary text 2: Imaging protocols

Video acquisition We used the same protocol as the one described in the Supporting Information of chapter 4 page 174. We employed the Matlab code provided in Appendix A at the end of the Supporting Information of chapter 4 page 185 to compute $I_F^{1,out}(x,y)$ (OPIOM image) for our imaging experiments.

Microdevice imaging This series of experiments has been performed upon applying a sinusoidal light modulation at 480 nm and constant light intensity at 405 nm. During in vitro experiments, 512 images (corresponding to 8 periods of 22 s) were recorded using a Luca-R CCD camera operating at 2.9 Hz (34.375 ms image cycle time) with an exposure time of 34.285 ms. We used the same protocol as the one described in the Supporting Information of chapter 4 page 175 for data treatment.

Cell imaging and zebrafish embryo imaging with epifluorescence microscopy This series of experiments has been performed upon applying a sinusoidal light modulation of large amplitude (90%) at 480 nm and constant light intensity at 405 nm. The acquisition parameters used to image cells are provided in the table 5.2.

Target	Period (s)	Number of images	Image cycle time (ms)	Exposure time (ms)
Dronpa-2	0.2	80	20	19.1
Dronpa-3	1.84	512	28.75	27.85

Table 5.2: Acquisition parameters used to image Dronpa-2 or Dronpa-3 at 37 °C during cell experiments with a Luca-R CCD camera (Andor Technology).

To selectively image D3-Lifeact in zebrafish embryos, 256 images corresponding to 8 periods of 1.84 s were recorded using a Luca-R CCD camera (Andor Technology) operating at 17.4 Hz (57.5 ms image cycle time) with an exposure time equal to 56.6 ms.

Image filtering To reduce noise, the processed images have been subsequently filtered upon applying a 3 pixels × 3 pixels median filter.

Supplementary Figures

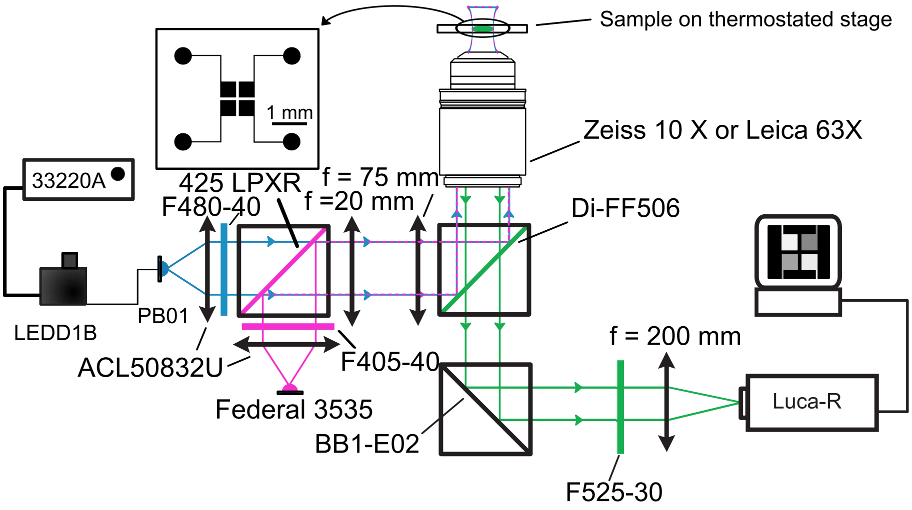

Figure 5.10: Epifluorescence setup for two-color OPIOM and PDMS Imaging device.

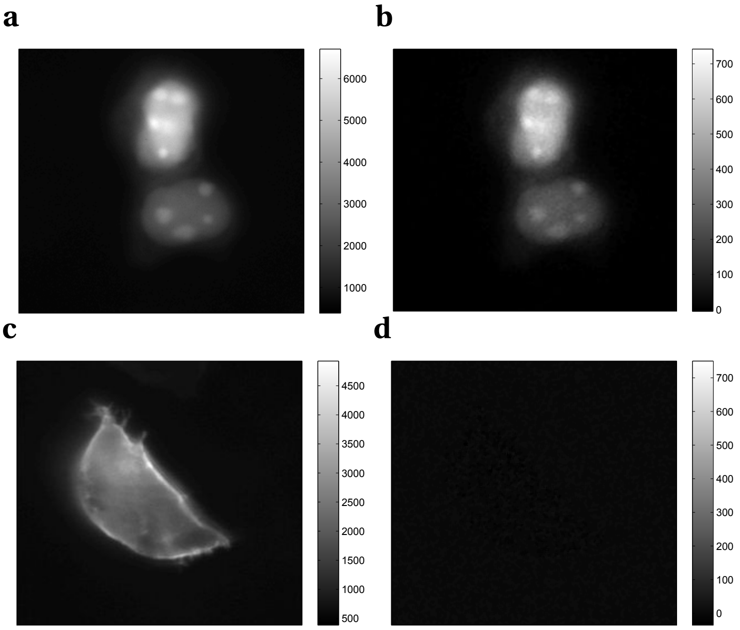

Figure 5.11: Imaging of fixed HEK293 cells expressing either (**a**,**b**) nuclear Dronpa-3 or (**c**,**d**) membrane-localised EGFP. Pre-OPIOM (**a**,**c**) and OPIOM (**b**,**d**) images result from analyzing a movie recorded with a 63 × objective at 525 nm under sinusoidal light modulation tuned to the resonance of Dronpa-3 (λ_1; I_1^0; ω; α) = (480 nm; 8.1×10^{-2} Ein· m^{-2}· s^{-1}; 3.41 rad.s^{-1}; 90%), (λ_2; I_2^0) = (405 nm; 3.3×10^{-3} Ein· m^{-2}· s^{-1}). T = 37°C.

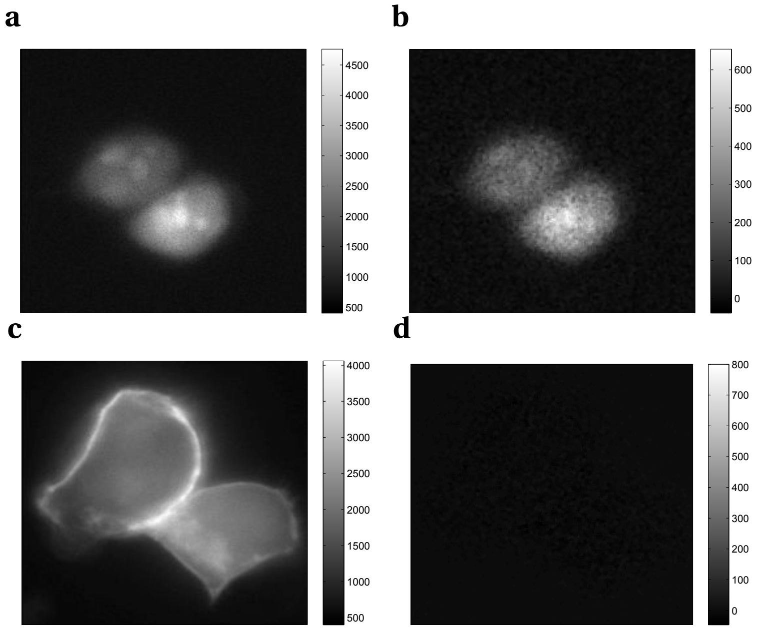

Figure 5.12: Imaging of fixed HEK293 cells expressing either (**a**,**b**) nuclear Dronpa-2 or (**c**,**d**) membrane-localised EGFP. Pre-OPIOM (**a**,**c**) and OPIOM (**b**,**d**) images result from analyzing a movie recorded with a 63 × objective at 525 nm under sinusoidal light modulation tuned to the resonance of Dronpa-2 (λ_1; I_1^0; ω; α) = (480 nm; 1×10^{-1} Ein· m^{-2}· s^{-1}; 31.4 rad.s^{-1}; 90%), (λ_2; I_2^0) = (405 nm; 1.4×10^{-2} Ein· m^{-2}· s^{-1}). T= 37°C.

5.3.3 Materials and methods

Cloning We used the same protocol as the one described in the Material and Methods of chapter 4 page 149.

Protein production and purification We used the same protocol as the one described in the Material and Methods of chapter 4 page 150.

Mammalian cell culture and transfection We used the same protocol as the one described in the Material and Methods of chapter 4 page 150.

Zebrafish experiments We used the same protocol as the one described in the Material and Methods of chapter 4 page 151.

Spectroscopic instruments Fluorescence measurements used for kinetic analysis were acquired on a LPS 220 spectrofluorometer (PTI, Monmouth Junction, NJ), equipped with a TLC50 cuvette holder (Quantum Northwest, Liberty Lake, WA) thermoregulated at 37°C. Samples (20 μL) were placed in 0.15 cm × 0.15 cm (light path) quartz cuvettes (Hellma Optics, Jena, Germany). Light intensities were controlled by varying the current on two LED light sources. The first one (LXML-PB01 from Philips Lumileds, San Jose, CA) was filtered at 480 ± 20 nm (HQ 480-40 from Chroma Technology Corp, Rockingham, VT) whereas the second one (Federal-3535 or Luxeon LHUV-0405 from Philips Lumileds) was filtered at 405 ± 20 nm (F405-40; Semrock, Rodchester, NY). The LEDs were supplied by a power supply (HM7042-5 from Hameg Instruments GmbH, Mainhausen, Germany). The two light beams were combined thanks to a dichroic filter (Di-FF506, Semrock, Rodchester, NY). Photon fluxes (excitation intensities I_1^0 and I_2^0) were measured with a Nova II powermeter (Laser Measurement Instruments).

Microfluidic device We followed the same protocol as the one described in the Material and Methods of chapter 4 page 152.

Microscopy epifluorescence setup The home-built epifluorescence microscopy set-up we used for OPIOM imaging was modified to allow illumination at 480 nm and 405 nm (see Figure 5.10). The samples (microfluidic device and cells) were illuminated using a first LED (LXML-PB01) as light source filtered at 480 ± 20 nm (F480-40; Semrock, Rodchester, NY) supplied by a LED driver (LEDD1B, Thorlabs Inc, Newton, NJ) and modulated by a waveform generator (33220A, Agilent Technologies) and a second LED (Federal-3535 or Luxeon LHUV-0405) filtered at 405 ± 20 nm (F405-40; Semrock, Rodchester, NY) supplied by a power supply (HM7042-5 from Hameg Instruments GmbH, Mainhausen, Germany). A lens (ACL50832U;

Thorlabs, f = 32 mm) was placed just after each LED. The two light beams were combined thanks to a dichroic mirror (LPXR 425, Chroma, Bellows Falls, VT) and a second lens was used to focus the light in the back focal plane of the objective after being reflected by the dichroic filter (Di-FF506, Semrock, Rodchester, NY). Fluorescence images at 525 ± 15 nm (F525-30; Semrock) were acquired with a 10× fluar (NA 0.5, Carl Zeiss AG, Feldbach, Switzerland; for the microdevice and zebrafish embryo experiments) or a 63× PL fluotar L (NA 0.7, Leica Microsystems, Germany; for cell experiments) objective mounted on a home-built microscope equipped with a Luca-R CCD camera (Andor Technology, Belfast, UK).

Softwares Data treatment, image analysis and theoretical computations were performed using Igor Pro (WaveMetrics), MATLAB (The MathWorks) and Gnuplot softwares.

Chapter 6

Discussion

In this chapter, we first discuss and compare our own approach and the optical imaging techniques relying on kinetics and using light as action parameter reported in the literature. The second section deals with the development of photoswitchable probes fully optimized for OPTIMAL or OPIOM.

6.1 Comparison of FLIM, OLID, SAFIRe and OPIOM

6.1.1 Contrast enhancement

OLID is efficient to discriminate the fluorescence signal emitted from a targeted species and the autofluorescent background or the signal of non-photoactive fluorophores emitting in the same wavelength range as the targeted photoswitchable fluorescent probe. Depending on the optical switch and the imaged sample, the contrast enhancement[a] χ^{OLID} reached with OLID varies between ~5- to ~20-fold.[86]

The autofluorescence and the signal of non-modulatable probes are eliminated by applying SAFIRe. Like OLID, a ~5- to ~20-fold[98,99,102] contrast enhancement can be achieved depending on the modulatable probe.

OPIOM permitted to eliminate the signal of non-photoactive fluorescent probes (such as

---

[a] The contrast enhancement χ^{Method} associated to a given method (OLID, SAFIRe or OPIOM) was calculated thanks to the values of the four signals $I^0_{F,target}$, $I^0_{F,interf}$, S_{target} and S_{interf} originating from ROIs containing the targeted probe and the interfering compound in the intensity ($I^0_{F,target}$ and $I^0_{F,interf}$) and the processed (S_{target} and S_{interf}) images.

$$\chi^{Method} = \frac{\dfrac{S_{target}}{S_{interf}}}{\dfrac{I^0_{F,target}}{I^0_{F,interf}}} \tag{6.1}$$

For OLID, the signal S is the cross-correlation coefficient ρ. For SAFIRe, the signal S is the modulation depth m. For OPIOM, the signal S is the out-of-phase first order fluorescence response $I_F^{1,out}$.

fluorescein and EGFP) and the autofluorescence. In the case of microfluidic device imaging, we showed that OPIOM could typically enhance contrast of Dronpa-2 against fluorescein by a factor $\chi^{OPIOM} = 10^2$-10^3 (see chapter 4) depending on the precision on the phase retrieval.

6.1.2 Choice of the illumination conditions

The choice of the experimental conditions (relative intensities of the two lasers and modulation frequency of secondary excitation) to obtain the optimal response using SAFIRe is not really discussed nor carefully explained by Dickson *et al.* In particular, there is no analytical expressions enabling to fix the optimal experimental conditions depending on the photophysical properties of the targeted modulatable fluorophore (dark-state lifetime, action cross sections for dark-state depopulation...). It seems that a trial-and-error process has been followed to determine these conditions by numerical simulations. This choice remains non rationalized and has to be investigated experimentally. In addition, the choice of the modulation frequency of the secondary excitation does not seem always consistent and the modulation strategy changes according to the systems. Hence, in the case of the modulatable AcGFP, modulation was performed at 300 Hz whereas the cutoff frequency is around 800 Hz and the plateau appears for a frequency lower than 80 Hz (see Figure 1.11).[98] On the contrary, a frequency of 2 Hz corresponding to the plateau of the frequency response was chosen to image modBFP-H148K.[99]

Similarly, in the case of OLID, no information is provided to choose the right illumination conditions to obtain the best contrast enhancement.

The extensive theoretical framework we developed (see chapter 3) enabled us to determine the optimal illumination conditions that maximize the out-of-phase response of a photoswitchable probe submitted to periodic light excitation. These robust resonance conditions only depend on the dynamic set of parameters of the targeted photoswitchable probe : k_{21}^{Δ} and $\sigma_{12}+\sigma_{21}$ for one-color OPIOM and $\sigma_{12,1}+\sigma_{21,1}$ and $\sigma_{12,2}+\sigma_{21,2}$ for two-color OPIOM. This set of parameters is easily accessible from a series of light jump experiments with a standard fluorometer apparatus. Thus, it is very simple to set the values of the average light intensity(ies) and the frequency of modulation to optimize the OPTIMAL or OPIOM response.

6.1.3 The retrieval of the kinetic information

Several strategies have been explored to retrieve the kinetic information of the targeted reactive exogenous probe. OLID relies on the correlation of the overall response of the imaged medium to light perturbation with the response of the pure optical switch to be imaged. Thus, a reference is required. In doing so, OLID is not an implementation of lock-in or phase-sensitive detection since the trajectory of the fluorescence signal (at the pixel level) is not projected over a specific frequency, as already pointed out by Braun *et al.*[22] Indeed, the noise reduction observed in the images is likely due to the inherent averaging process of the computation algorithm. In the case of OPIOM, quadrature detection by means of a lock-in approach enables to extract the out-of-phase response of the photoswitchable probe. It requires only a preliminary experiment to calibrate the phase lag between the dates of the onset of light excitation and the triggering of the camera. Extracting the modulation amplitude of the fluorescence signal by Fourier transform performed during SAFIRe is analogous to our strategy. It is even a little more simple than in our approach since only the amplitude term is evaluated and in that case one does not need to determine the phase lag between the fluorescence and excitation signals. In addition, the lock-in detection scheme allows a decrease of the noise since all the frequencies apart the targeted one are eliminated, resulting in an improved signal-to-noise ratio with these two last protocols.

6.1.4 Selectivity

FLIM discriminates two emitters only if their fluorescence lifetimes are sufficiently different,[83] but this is often challenging to achieve with the fluorescent probes commonly encountered in biology as they mostly display similar lifetimes (in the same nanosecond range).[5]

To evaluate the ability of the OLID protocol to distinguish two optical switches emitting in the same wavelength range but differing only by their relaxation times τ, we simulated the following experiment : a sample is prepared with beads coated with two equally bright optical switches differing only by their photoconversion times (τ_A and τ_B). The field of view contains the two kinds of beads and the OLID protocol is performed as described previously. We wondered whether we could image selectively the beads A (respectively B) using a bead A (respectively B) as reference waveform. For this purpose, we computed the cross-correlation coefficient between the fluorescence decay of a bead B using the one of a bead A as reference to estimate the correlation between the two kinetic signatures. Assuming that the photoswitching behavior of the optical switches upon illumination can be described by a two-state exchange (6.2) :

$$\mathbf{1} \quad \underset{k_{21}}{\overset{k_{12}}{\rightleftharpoons}} \quad \mathbf{2} \tag{6.2}$$

where k_{12} and k_{21} are respectively the forward and the backward rate constants, the temporal dependence of the fluorescence signals[b] can be written thanks to Eq. 6.3 :

$$I_F(t) = \left[Q_1 1^0 + Q_2 2^0 + (Q_1 - Q_2) 2^0 \exp\left(\frac{-t}{\tau}\right)\right] I^0 \tag{6.3}$$

where Q_1 and Q_2 are the molecular brightnesses of **1** and **2**, 1^0 and 2^0 are the concentrations of **1** and **2** at photo-steady-state, $\tau = \frac{1}{k_{12}+k_{21}}$ the relaxation time associated to the photoconversion and I^0 the light intensity. The values of the cross-correlation coefficient were calculated using Eqs. 1.6 and 6.3 and are displayed in Table 6.1. Even if the two relaxation times

---

[b] The detailed calculations leading this equation are provided in the Supporting Information of the chapter 3.

differ by two orders of magnitude, the cross-correlation coefficient is still around 0.21. Thus, it seems difficult to discriminate two optical switches based on their relaxation times using the OLID protocol. In addition, Marriott *et al* noticed that photobleaching may generate a correlation with the reference waveform.[91] Taking a characteristic time of 10000 s for a slow photobleaching, the cross-correlation coefficient is around 0.08 for a reference with a 1 s relaxation time.

τ_B (s) / τ_A (s)	1	10	100	10000
1	1	0.59	0.21	0.08
10		1	0.58	0.25
100			1	0.70

Table 6.1: Computed values of the cross-correlation coefficient between two optical switches exhibiting two different relaxation times τ_A and τ_B assuming an optical switching cycle of 1000 s. $Q_1^A = Q_1^B = 1$, $Q_2^A = Q_2^B = 0$, $1_A^0 = 2_A^0 = 1_B^0 = 2_B^0$ and $I^0 = 1$ a. u. See Eqs. 1.6 and 6.3.

Dickson *et al* assumed that SAFIRe could discriminate modulatable fluorophores sharing the same spectral properties based on the characteristic lifetimes of their dark-states.[102] However, this feature has not yet been evidenced. In addition, with the to-date SAFIRe approach, it will be limited and demanding to achieve. The selectivity of SAFIRe was evaluated by computing the frequency response of a mixture containing two modulatable fluorophores sharing the same brightnesses with different (by 1 or 2 order(s) of magnitude) relaxation times τ_{cA} and τ_{cB}. The global response was assumed to be the sum of the individual responses for an equimolar mixture. The results are displayed in Figure 6.1. A difference of one order of magnitude between τ_{cA} and τ_{cB} is not sufficient to observe a significant change in the frequency-dependence of the response of the mixture compared to the individual ones (see Figure 6.1**a**). If $\tau_{cB} = 100\tau_{cA}$, two regimes are observed (see Figure 6.1**b**). In particular, for a cutoff frequency (frequency for which the response decreases by 50% of its highest value) corresponding to the fastest fluorophore, the response of the slowest one is almost negligible at this large frequency (compared to $1/\tau_{cB}$). Imaging the slowest fluorophore requires to employ a lower frequency. Nevertheless, the response of the fastest fluorophore is not eliminated and is even larger than the response of slowest one (see Figure 6.1**b**). In conclusion, SAFIRe would only enable to visualize the fastest modulatable fluorophore alone in a mixture.

The out-of-phase response of a photoswitchable probe submitted to light modulation is a peaked function. The coordinates of this maximum only depend on the dynamic parameters of the considered photoswitchable probe. Thus, the main advantage of OPIOM compared to SAFIRe and OLID is its ability to easily discriminate two photoswitchable probes exhibiting

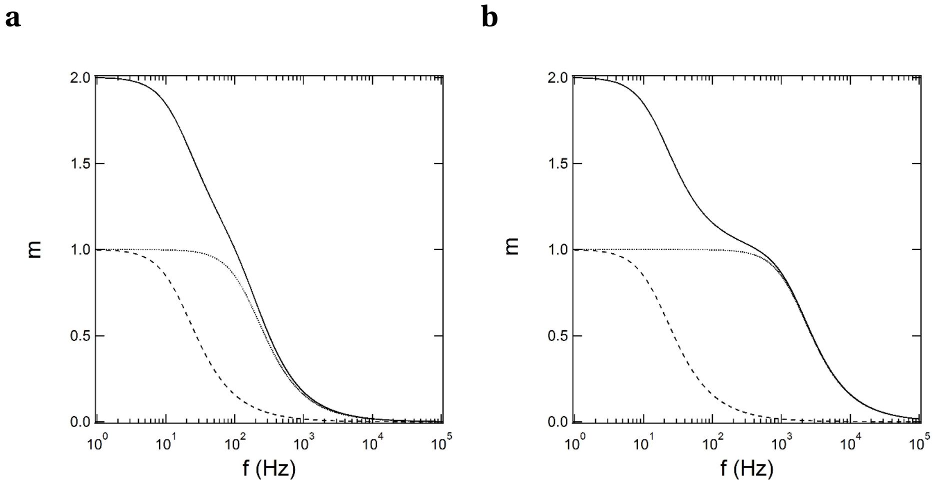

Figure 6.1: Computed frequency response of a mixture of two modulatable fluorophores at the same concentration with distinct charateristic times (τ_{cA} and τ_{cB}) using Eq. 1.11 and assuming that A (see Eq. 1.11) is equal to one in both cases. (**a**) τ_{cA} = 1 ms and τ_{cB} = 10 ms (**b**) τ_{cA} = 100 μs and τ_{cB} = 10 ms. The solid line represents the response of the mixture (same concentration of the two fluorophores) whereas the dotted and the dashed lines represent the individual responses.

sufficiently different resonance conditions thanks to the peaked response. This opens opportunities for multiplexed experiments with several photoswitchable probes.

6.1.5 Quantitative character

Although OLID enables to discriminate fluorescence signals of interest against background or interfering species, the resulting image will not reflect the local concentrations of the species. In fact, the computation of the correlation values will eventually redistribute the pixel values in the -1:1 range, whatever the values explored for fluorescence intensity (see Eqs. 1.6, 1.7 and 1.8). In this case, any information related to the initial concentration of the targeted species is lost and the protocol is not quantitative.

One experiment demonstrated the ability of SAFIRe to accurately estimate the concentration of a modulatable probe in the presence of a high autofluorescent background.[102] However, no calculation or theoretical development supported this observation. In addition, several signal processing have been proposed by Dickson *et al* to obtain the final SAFIRe signal. In particular, the demodulated signal (respectively image) is sometimes divided by the average signal (respectively raw fluorescence image) that renders in this case SAFIRe not quantitative.[98]

The quantitative character of the OPTIMAL/OPIOM approaches has been demonstrated theoretically (see chapter 3) and evidenced experimentally (see chapters 4 and 5). In particular, it allows to accurately determine the concentration of a targeted photoswitchable probe in a mixture even in the presence of interfering compounds, photoswitchable or not.

6.1.6 Acquisition time and temporal resolution

The time needed to acquire FLIM data depends on several parameters such as the number of pixels of the image, the photon count rate, the expected accuracy on the fluorescence lifetime and the kind of FLIM implementation. For instance, the acquisition time of an image of 256 × 256 pixels with a count rate of 10^6 photons per second and an accuracy of 10% on the fluorescence lifetime is typically 6 s. Nevertheless, the accuracy on the measurement of the fluorescence lifetime needs to be very good to enable to discriminate two fluorophores even if their lifetimes are very close. Thus, for an image of 512 × 512 pixels and an accuracy of 1%, it would take around one hour to obtain the FLIM image.[85]

The OLID protocol requires to record typically ~5 switching cycles leading to an acquisition time of a few minutes with the reported systems.[86] Several probes have been developed especially in the context of the OLID-FRET approach. Nevertheless, the temporal resolution has not been dramatically improved with a decrease of the acquisition time to a few tens of seconds.[89,90]

Due to the very high light intensities required, SAFIRe was mostly implemented in bioimaging in a confocal arrangement[98] A scanning of the whole sample is required leading to a poor temporal resolution. For instance, selective imaging of AcGFP against EGFP (see Figure 1.9 in the General introduction) was performed with the following experimental conditions : a dwell time per pixel and a step-size equal to 50 ms and 300 nm respectively. Assuming a field of view of 60 μm by 60 μm (see Figure 1.9), the acquisition time is around 2000 s, that is very long for bioimaging purpose.

To perform the OPIOM analysis, it is necessary to record several periods of light modulation. With the Dronpa-3[129] mutant which exhibits the fastest thermal return, the period at resonance is 20 s requiring around two minutes to obtain the processed image (see chapter 4). Even though the OPIOM processing can be reduced to one period of light modulation without significant decrease of the contrast enhancement (see chapter 4), we tried to further improve the temporal resolution of this protocol. This was achieved by employing two light sources to accelerate the photoswitching dynamics (see chapter 5). With Dronpa-2[129] (exhibiting more effective photoswitching properties than Dronpa-3), we reached 200 ms for the period[c] of light modulation. The resulting temporal resolution (improved by a one hundred factor) is more adapted to the investigation of dynamic biological processes.

---

[c] Up to now, we only reached a frequency of modulation of 5 Hz because we are limited by the acquisition frequency of our camera, but larger frequencies could be reached close to video-rate by increasing the light excitation intensities and implementing real-time demodulation.

6.1.7 Experimental setup, wide-field imaging and 3D-resolved imaging

Even though the instrumentation of FLIM becomes simpler and less expensive, performing this kind of experiment requires dedicated setups due to the required temporal resolution.[5,84,85]

As far as OLID is concerned, it seems compatible with commercial microscopes without any modification. OLID can be employed either with a confocal microscope[86] or with a wide-field epifluorescence microscope (see chapter 2). Obviously, this protocol is compatible with 3D-resolved fluorescence imaging.

SAFIRe has been implemented in bioimaging with home-built setups mostly in a confocal arrangement[98] and so is compatible with 3D imaging. Epifluorescence imaging was performed with SAFIRe but only with a reduced field of view of around 10 μm in diameter.[99] The compatibility of SAFIRe with wide-field imaging has not really been evidenced and seems hardly achievable with respect to the up-to-now employed light intensities. Its implementation in labs not specialized in optics or microscopy seems difficult.

The complete optical setup we used to modulate light is composed of LEDs, a waveform generator and a modulatable current supply. This setup is cheap, simple and easy to implement. In addition, the light intensities usually employed in epifluorescence microscopy can easily be reached with this setup. For light sheet experiments, we employed laser diodes as light sources. The modulation of their intensities was performed simply by using the analog modulation input and a waveform generator. Two home-built microscopy setups (epifluorescence and light sheet) were used to collect the fluorescence. In particular, the SPIM experiments have been performed with a commercial Olympus microscope modified in house to enable light sheet illumination. Apart from the triggering of the camera to the excitation waveform, the compatibility of OPIOM with commercially available microscopes does not seem to present any specific difficulties. The OPIOM protocol has been validated with an epifluorescence microscope and thus enables wide-field imaging (this explains in part the good temporal resolution we can reach since no scanning of the sample is necessary). In addition, selective 3D-resolved fluorescence imaging is possible since OPIOM is compatible with light sheet microscopy (see chapter 4).

6.2 Development of photoswitchable probes for OPTIMAL and OPIOM

The OPTIMAL/OPIOM protocols rely on using a photoswitchable probe. The availability of appropriate photoswitchable probes is necessary to allow a wide scope of applications of these protocols. The development of OPTIMAL labels with different kinds of observables seems conceivable since many organic[173] as well as inorganic[174] photoswitchable probes have been already designed. In addition, molecular switches as photocontrollable receptors[175] could be employed as OPTIMAL sensors.

In the specific context of OPIOM, only very few RSFPs can currently be employed with a reasonable acquisition time. There is a strong interest to engineer new RSFPs fully optimized for OPIOM. The required properties of these RSFPs depend on the considered implementation of the OPIOM protocol : one color or two colors.

6.2.1 RSFPs for one-color OPIOM

A RSFP suitable for one-color OPIOM must exhibit a large thermal rate constant to reach both good temporal resolution and good signal-to-noise ratio. In addition, an intermediate value of the sum of the action cross section of photoconversion is preferable. Indeed, if $\sigma_{12}+\sigma_{21}$ is too large, it would result in a low excitation intensity at resonance and so a lowered signal-to-noise ratio. On the contrary, a too ineffective photoswitching (low $\sigma_{12}+\sigma_{21}$) would require a large excitation intensity which could be not necessarily easily attainable or provoke a photobleaching of the probe.

6.2.2 RSFPs for two-color OPIOM

As far as two-color OPIOM is concerned, the choice of the experimental values of the resonance conditions is much more free. They depend only on the sum of the action cross section of photoconversion at the two wavelengths of excitation ($\sigma_{12,i}+\sigma_{21,i}$; $i = 1$ or 2) in the range of light intensities where we can neglect the thermal return compared to the photochemical rate constants. The probes with large $\sigma_{12,i}+\sigma_{21,i}$ and with very slow thermal return rate constants (no restriction on the lower limit of the light intensities) are the most interesting candidates. Indeed, the more effective the photoswitching, the larger the frequency at resonance. In this case, relatively low light intensities could be used thus limiting the photobleaching without being detrimental for the temporal resolution. In addition, increasing the light intensities at resonance results in both a higher signal-to-noise ratio and a better temporal resolution. The only restriction on the upper limit of the light intensities comes from the limited acquisition frequency of the camera. Modulating the detection would allow to overcome this issue by using gated CCD cameras or applying strategies developed for FLIM.[5,84,85]

6.2.3 RSFPs for multiplexed observations

The development of probes optimized for OPIOM is also relevant in the context of multiplexed observations. It would be interesting to generate libraries of photoswitchable probes with values of their dynamic parameters (k_{21}^{Δ} and $\sigma_{12}+\sigma_{21}$ for one-color OPIOM and $\sigma_{12,1}+$

$\sigma_{21,1}$ and $\sigma_{12,2}+\sigma_{21,2}$ for two-color OPIOM) covering at least two orders of magnitude ranges. This should allow to observe up to ten fluorophores emitting in the same wavelength range. We evoked in the introduction of the chapter 4 that RSFPs of different colors have already been engineered.[139–141,143–145] Thus, the emission wavelength and the photoswitching dynamics of RSFPs of different colors could be combined ultimately for multiplexed experiments to simultaneously visualize up to twenty fluorophores.

6.2.4 Turn on fluorescent probes

The engineering of photoswitchable probes for applications with OPTIMAL or OPIOM is not limited to RSFPs. In fact, photochromic turn on fluorescent probes could also provide a palette of objects optimized for the OPIOM imaging protocol. We provide in the appendix 6.A of this chapter the calculations for an application of OPIOM relying on this kind of systems using the example of Spinach.

Appendix of chapter 6

6.A OPIOM and Spinach (Theoretical analyses)

6.A.1 The generic dynamic model

The generic dynamic model is a four-state mechanism consisting of two *cis*-DFHBI states (bound and unbound) and two *trans*-DFHBI states (bound and unbound). Both *cis*- and *trans*-DFHBI interact with Spinach RNA to yield the corresponding fluorescent bound states, Spinach-*cis*-DFHBI and Spinach-*trans*-DFHBI. The two isomers interconvert by photoisomerization in both the bound and unbound states. In contrast, since *cis*-DFHBI is thermodynamically much more stable than *trans*-DFHBI, we only retained *trans*-*cis* isomerization as a thermally-driven exchange in the dynamic scheme. For simplicity, this section uses the symbols **1F**, **2F**, **1B**, and **2B** to represent *cis*-DFHBI, *trans*-DFHBI, Spinach-*cis*-DFHBI, and Spinach-*trans*-DFHBI respectively. The associated rate constants are presented in Figure 6.2, where the superscripts $h\nu$ and Δ respectively denote photochemical and thermal contributions.

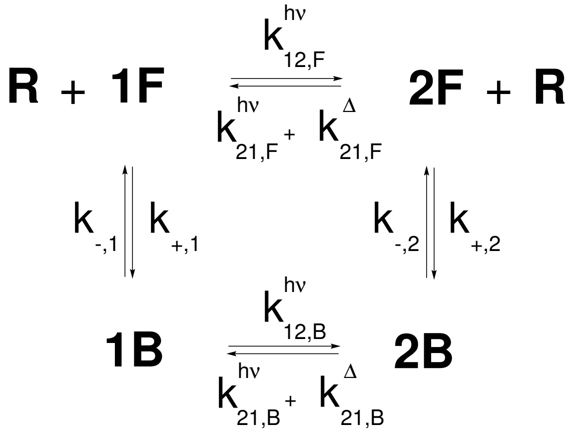

Figure 6.2: Four-state mechanism accounting for the photochemical and complexation behavior of a photochromic fluorogen in the presence of a receptor.

The theoretical framework closely mirrors that described in a previous work by Emond et al.[176] The concentration profiles within the four state model are governed by the equations:

$$\frac{d1B}{dt} = -\left(k_{\mathbf{1B\to 1F}} + k_{\mathbf{1B\to 2B}}\right) 1B + k_{\mathbf{2B\to 1B}}\, 2B + k_{\mathbf{1F\to 1B}}\, R\, 1F \tag{6.4}$$

$$\frac{d2B}{dt} = k_{\mathbf{1B\to 2B}}\, 1B - \left(k_{\mathbf{2B\to 2F}} + k_{\mathbf{2B\to 1B}}\right) 2B + k_{\mathbf{2F\to 2B}}\, R\, 2F \tag{6.5}$$

$$\frac{d1F}{dt} = k_{\mathbf{1B\to 1F}} 1B - \left(k_{\mathbf{1F\to 1B}}\, R + k_{\mathbf{1F\to 2F}}\right) 1F + k_{\mathbf{2F\to 1F}}\, 2F \tag{6.6}$$

$$\frac{d2F}{dt} = k_{\mathbf{2B\to 2F}} 2B + k_{\mathbf{1F\to 2F}}\, 1F - \left(k_{\mathbf{2F\to 2B}}\, R + k_{\mathbf{2F\to 1F}}\right) 2F \tag{6.7}$$

The temporal dependence of concentrations cannot be obtained in the most general case. However, it can be analyzed in asymptotic situations according to the nature of the rate-limiting steps, which are associated to either the photochemical reactions or the complexation reactions. Crossing between both kinetic regimes typically occurs when the relaxation times associated to the photoisomerization and the complexation reactions are equal. Relying on the values reported for the Spinach system[120] at micromolar concentrations used in the present study, we predicted that photoisomerization would remain rate-limiting up to $\sim 10^{-2}$ ein.s^{-1}.m^{-2}, a value lying much above our typical light flux. Thus we reduced further theoretical analysis in the kinetic regime where photoisomerization is rate-limiting.

6.A.2 The reduced dynamic model

Upon considering that photoisomerization is rate-limiting, the mechanism displayed in Figure 6.2 reduces to a two-state exchange between two virtual species $\overline{\mathbf{1}}$ and $\overline{\mathbf{2}}$ (concentrations $\overline{1} = 1F + 1B$ and $\overline{2} = 2F + 2B$) (Figure 6.3).

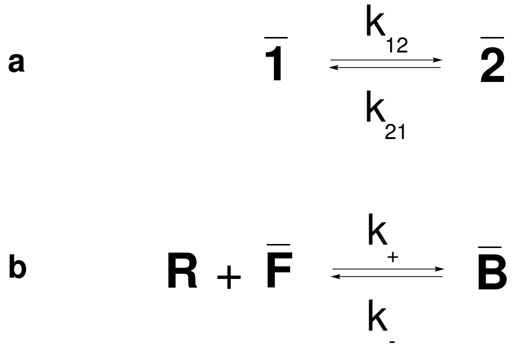

Figure 6.3: : Kinetic model resulting from reduction of the mechanism shown in Figure 6.2 upon considering that photoisomerization is rate-limiting.

The “instantaneous” concentrations in **1F**, **1B**, **2F** and **2B** then follow,[d]

$$1F = \frac{1}{1+K_1^{\Delta}R}\overline{1} \tag{6.8}$$

$$1B = \frac{K_1^{\Delta}R}{1+K_1^{\Delta}R}\overline{1} \tag{6.9}$$

$$2F = \frac{1}{1+K_2^{\Delta}R}\overline{2} \tag{6.10}$$

$$2B = \frac{K_2^{\Delta}R}{1+K_2^{\Delta}R}\overline{2} \tag{6.11}$$

where

$$K_1^{\Delta} = \frac{k_{+,1}^{\Delta}}{k_{-,1}^{\Delta}} \tag{6.12}$$

$$K_2^{\Delta} = \frac{k_{+,2}^{\Delta}}{k_{-,2}^{\Delta}}. \tag{6.13}$$

Thus Eqs.(6.4–6.7) transform into Eq.(6.14):

$$\frac{d\overline{1}}{dt} = -\frac{d\overline{2}}{dt} = -k_{12}\,\overline{1} + k_{21}\,\overline{2} \tag{6.14}$$

with

$$k_{12} = \frac{k_{12,F}^{h\nu} + k_{12,B}^{h\nu}\,K_1^{\Delta}R}{1+K_1^{\Delta}R} \tag{6.15}$$

$$k_{21} = \frac{\left(k_{21,F}^{h\nu} + k_{21,F}^{\Delta}\right) + \left(k_{21,B}^{h\nu} + k_{21,B}^{\Delta}\right)\,K_2^{\Delta}R}{1+K_2^{\Delta}R}. \tag{6.16}$$

6.A.3 Kinetic analysis

6.A.3.1 Assumptions

In the most general case, Eq.(6.14) has no analytical solution, because k_{12} and k_{21} are time-dependent as a result of the $R(t)$ term. In the following, we analyze the specific case, which would be relevant for most experimental conditions. We assumed that the total concentration of the fluorogen **F**, F_{tot}, is (i) larger than the concentration in receptor **R**, R_{tot}, and tuned so as to fulfil at any time of the temporal evolution (ii) $R \ll K_{d,1} \times Inf(1, k_{12,F}^{h\nu}/k_{12,B}^{h\nu})$ and $R \ll K_{d,2} \times Inf(1, (k_{21,F}^{h\nu}+k_{21,F}^{\Delta})/(k_{21,B}^{h\nu}+k_{21,B}^{\Delta}))$. In fact such conditions are not restrictive.

---

[d] The association constants, K_1^{Δ} and K_2^{Δ} are the inverse of the dissociation constants $K_{d,1}$ and $K_{d,2}$. Furthermore, $k_{+,1}$ and $k_{-,1}$ have been replaced with $k_{+,1}^{\Delta}$ and $k_{-,1}^{\Delta}$ to articulate that these rate constants are only affected by temperature rather than light.

Indeed $k_{12,F}^{h\nu}/k_{12,B}^{h\nu} \sim 0.67$ and $(k_{21,F}^{h\nu}+k_{21,F}^{\Delta})/(k_{21,B}^{h\nu}+k_{21,B}^{\Delta}) \sim 0.49$ under our illumination conditions. To perform this calculation, we first determined the light intensity corresponding to the optimal response of the free DFHBI under sinusoidal modulation[172] using the values reported for the Spinach system.[120] Then numerical simulations show that typical (F_{tot},R_{tot}) concentration sets allow us to fulfil the conditions (ii).

R_{tot} (μM)	R^0 (μM)	$K_1^{\Delta}R^0$	$K_2^{\Delta}R^0$
0.5	0.02	0.015	0.005
1	0.04	0.031	0.01
2	0.08	0.063	0.02
4	0.16	0.13	0.04

Table 6.2: For a mixture containing 40 μM of F_{tot} and various amounts of R_{tot}, we calculated the corresponding values of R^0, $K_1^{\Delta}R^0$ and $K_2^{\Delta}R^0$. The conditions (ii) are fulfilled up to 2 μM of R_{tot}.

Under the preceding conditions, Eqs.(6.15,6.16) yield at the zeroth order:

$$k_{12} = k_{12,F}^{h\nu} \tag{6.17}$$

$$k_{21} = k_{21,F}^{h\nu} + k_{21,F}^{\Delta}. \tag{6.18}$$

One has also

$$1F = \overline{1} \tag{6.19}$$

$$2F = \overline{2} \tag{6.20}$$

$$1F + 2F = F_{tot} \tag{6.21}$$

$$R + 1B + 2B = R_{tot} \tag{6.22}$$

$$1B = K_1^{\Delta} R 1F = \frac{K_1^{\Delta} 1F}{1 + K_1^{\Delta} 1F + K_2^{\Delta} 2F} R_{tot} \tag{6.23}$$

$$2B = K_2^{\Delta} R 2F = \frac{K_2^{\Delta} 2F}{1 + K_1^{\Delta} 1F + K_2^{\Delta} 2F} R_{tot} \tag{6.24}$$

$$R = \frac{1}{1 + K_1^{\Delta} 1F + K_2^{\Delta} 2F} R_{tot}. \tag{6.25}$$

The photochemical behavior is here mainly driven by the free states **1F** and **2F**. Light modulation is expected to modulate the concentration of **1F** and **2F**, which “instantaneously” fix the concentrations in **R**, **1B**, and **2B** by means of fast complexation.

6.A.3.2 Sinusoidal modulation of small amplitude

In the following subsection, we are interested to derive the theoretical expressions of (i) the concentrations in **1F**, **1B**, **2F**, and **2B**, and (ii) the overall fluorescence emission, upon applying a periodic modulation of the illumination. In relation with our preceding work, we have adopted a sinusoidal modulation of small amplitude, which provides results, which are as well relevant to analyze the outcome of the experiments performed upon applying a sinusoidal modulation of large amplitude.

Expression of the concentrations We consider that the system is submitted to a weak sinusoidal modulation of illumination around the averaged value I^0. We correspondingly adopt

$$I(t) = I^0\,[1+\varepsilon\sin(\omega t)] \tag{6.26}$$

with $\varepsilon \ll 1$. One has

$$k^{h\nu}_{12,F}(t) = k^{h\nu,0}_{12,F}\,[1+\varepsilon\sin(\omega t)] \tag{6.27}$$

$$k^{h\nu}_{21,F}(t) = k^{h\nu,0}_{21,F}\,[1+\varepsilon\sin(\omega t)]\,. \tag{6.28}$$

Eq.(6.14) is solved at first order of the light perturbation upon writing:

$$2F = 2F^0+\varepsilon 2F^1(t) = 2F^0-\varepsilon 1F^1(t) \tag{6.29}$$

$$1F = 1F^0-\varepsilon 2F^1(t) = 1F^0+\varepsilon 1F^1(t) \tag{6.30}$$

$$k_{12,F}(t) = k^{h\nu,0}_{12,F}\,[1+\varepsilon\sin(\omega t)] \tag{6.31}$$

$$k_{21,F}(t) = k^{h\nu,0}_{21,F}\,[1+\varepsilon\sin(\omega t)]+k^{\Delta}_{21} \tag{6.32}$$

to yield

$$\frac{d2F^1}{dt}+\frac{1}{\tau^0_{12,F}}2F^1 = \rho^0_{12,F}\,p^{\Delta}_{21,F}\sin(\omega t) \tag{6.33}$$

where

$$\begin{aligned} 2F^0 &= \frac{K^0_{12,F}}{1+K^0_{12,F}}F_{tot} && (6.34)\\ 1F^0 &= \frac{1}{1+K^0_{12,F}}F_{tot} && (6.35)\\ K^0_{12,F} &= \frac{k^0_{12,F}}{k^0_{21,F}} && (6.36)\\ k^0_{12,F} &= k^{h\nu,0}_{12,F} && (6.37)\\ k^0_{21,F} &= k^{h\nu,0}_{21,F}+k^{\Delta}_{21,F} && (6.38)\\ \tau^0_{12,F} &= \frac{1}{k^0_{12,F}+k^0_{21,F}} && (6.39)\\ \rho^0_{12,F} &= k^0_{12,F}1F^0 = k^0_{21,F}2F^0 && (6.40)\\ p^{\Delta}_{21,F} &= \frac{k^{\Delta}_{21,F}}{k^{h\nu,0}_{21,F}+k^{\Delta}_{21,F}}. && (6.41) \end{aligned}$$

In Eqs.(6.34–6.41), $2F^0$, $1F^0$, $K^0_{12,F}$, $k^0_{12,F}$, $k^0_{21,F}$, $\tau^0_{12,F}$,$\rho^0_{12,F}$, and $p^{\Delta}_{21,F}$ respectively designate the steady-state value of the concentrations in **2F** and **1F**, the apparent photoisomerization constant, the forward and backward rate constants, the relaxation time, and the steady-state rate associated to the **1F**-**2F** exchange, and the relative thermal contribution to **2F** relaxation upon illuminating at I^0. Noteworthily, at I^0, one has also

$$\begin{aligned} 1B^0 &= \frac{K^{\Delta}_1 1F^0}{1+K^{\Delta}_1 1F^0+K^{\Delta}_2 2F^0}R_{tot} && (6.42)\\ 2B^0 &= \frac{K^{\Delta}_2 2F^0}{1+K^{\Delta}_1 1F^0+K^{\Delta}_2 2F^0}R_{tot} && (6.43)\\ R^0 &= \frac{1}{1+K^{\Delta}_1 1F^0+K^{\Delta}_2 2F^0}R_{tot}. && (6.44) \end{aligned}$$

Beyond the relaxation time $\tau^0_{12,F}$, one enters into a permanent regime in which the respective contributions of the in- and out-phase terms $2F^{1,in}$ and $2F^{1,out}$ such that $2F^1(t) = 2F^{1,in}\sin(\omega t) + 2F^{1,out}\cos(\omega t)$ respectively obey[e]

$$\begin{aligned} 2F^{1,in} &= -1F^{1,in} = \rho^0_{12,F}\tau^0_{12,F}p^{\Delta}_{21}\frac{1}{1+\left(\omega\tau^0_{12,F}\right)^2} && (6.48)\\ 2F^{1,out} &= -1F^{1,out} = -\rho^0_{12,F}\tau^0_{12,F}p^{\Delta}_{21,F}\frac{\omega\tau^0_{12,F}}{1+\left(\omega\tau^0_{12,F}\right)^2}. && (6.49) \end{aligned}$$

---

[e] Alternatively, one has

$$2F^1(t) = -1F^1(t) = \frac{\rho^0_{12,F}\tau^0_{12,F}p^{\Delta}_{21,F}}{\sqrt{1+\left(\omega\tau^0_{12,F}\right)^2}}\sin\left(\omega t-\phi_{12,F}\right) \tag{6.45}$$

Upon noting that

$$\rho^0_{12,F}\tau^0_{12,F} = \frac{K^0_{12,F}}{\left(1+K^0_{12,F}\right)^2}F_{tot}, \tag{6.50}$$

Eqs.(6.48,6.49) become

$$\begin{aligned} 2F^{1,in} &= -1F^{1,in} = p^{\Delta}_{21,F}\frac{K^0_{12,F}}{\left(1+K^0_{12,F}\right)^2}\frac{1}{1+\left(\omega\tau^0_{12,F}\right)^2}F_{tot} && (6.51)\\ 2F^{1,out} &= -1F^{1,out} = -p^{\Delta}_{21,F}\frac{K^0_{12,F}}{\left(1+K^0_{12,F}\right)^2}\frac{\omega\tau^0_{12,F}}{1+\left(\omega\tau^0_{12,F}\right)^2}F_{tot} && (6.52)\end{aligned}$$

Expression of the fluorescence intensity Fluorescence intensity results from the individual contributions of the states **1F**, **1B**, **2F**, and **2B**. Denoting Q_i for the molecular brightness, we first introduce

$$O(t) = Q_{1F}1F(t) + Q_{1B}1B(t) + Q_{2F}2F(t) + Q_{2B}2B(t). \tag{6.53}$$

Then fluorescence intensity $I_F(t)$ can be written

$$I_F(t) = O(t)I(t) \tag{6.54}$$

In the case of a sinusoidal modulation of light intensity obeying Eq.(6.26), the temporal dependence of the overall observable $O(t)$ originates from the temporal dependence of $1^1(t)$ and $2^1(t)$. Whereas $1F(t)$ and $2F(t)$ adopt simple expressions extracted from Eqs.(6.29,6.30,6.51,6.52),

$$\begin{aligned} 1F &= 1F^0 + \varepsilon\left[1F^{1,in}\sin(\omega t) + 1F^{1,out}\cos(\omega t)\right] && (6.55)\\ 2F &= 2F^0 - \varepsilon\left[1F^{1,in}\sin(\omega t) + 1F^{1,out}\cos(\omega t)\right], && (6.56)\end{aligned}$$

the derivation of the expressions of $1B(t)$ and $2B(t)$ deserves more attention. $1B(t)$ and $2B(t)$ can be derived from Eqs.(6.23,6.24,6.55,6.56). To simplify the expressions, we subsequently made approximations.

---

with

$$\begin{aligned} \cos\phi_{12,F} &= \frac{1}{\sqrt{1+\left(\omega\tau^0_{12,F}\right)^2}} && (6.46)\\ \sin\phi_{12,F} &= \frac{\omega\tau^0_{12,F}}{\sqrt{1+\left(\omega\tau^0_{12,F}\right)^2}}. && (6.47)\end{aligned}$$

After numerical simulations using values observed for Spinach, we first noticed that

$$\varepsilon \frac{K_1^\Delta - K_2^\Delta}{1 + K_1^\Delta 1F^0 + K_2^\Delta 2F^0} \left[1F^{1,in} \sin(\omega t) + 1F^{1,out} \cos(\omega t) \right] \ll 1 \tag{6.57}$$

at any time of the temporal evolution.[f] Thus we were allowed us to write at first order

$$\frac{1}{1 + K_1^\Delta 1F + K_2^\Delta 2F} = \frac{1}{1 + K_1^\Delta 1F^0 + K_2^\Delta 2F^0} \left\{ 1 - \varepsilon\gamma \left[1F^{1,in} \sin(\omega t) + 1F^{1,out} \cos(\omega t) \right] \right\} \tag{6.58}$$

where we introduced

$$\gamma = \frac{K_1^\Delta - K_2^\Delta}{1 + K_1^\Delta 1F^0 + K_2^\Delta 2F^0}. \tag{6.59}$$

We could subsequently derive

$$\begin{aligned} \frac{1B}{1B^0} = & \left\{ 1 + \frac{\varepsilon}{1F^0} \left[1F^{1,in} \sin(\omega t) + 1F^{1,out} \cos(\omega t) \right] \right\} \times \\ & \left\{ 1 - \varepsilon\gamma \left[1F^{1,in} \sin(\omega t) + 1F^{1,out} \cos(\omega t) \right] \right\} \end{aligned} \tag{6.60}$$

$$\begin{aligned} \frac{2B}{2B^0} = & \left\{ 1 - \frac{\varepsilon}{2F^0} \left[1F^{1,in} \sin(\omega t) + 1F^{1,out} \cos(\omega t) \right] \right\} \times \\ & \left\{ 1 - \varepsilon\gamma \left[1F^{1,in} \sin(\omega t) + 1F^{1,out} \cos(\omega t) \right] \right\} \end{aligned} \tag{6.61}$$

Upon considering that the amplitudes of the oscillating terms, $\frac{1}{1F^0} \left[1F^{1,in} \sin(\omega t) + 1F^{1,out} \cos(\omega t) \right]$, $\frac{1}{2F^0} \left[1F^{1,in} \sin(\omega t) + 1F^{1,out} \cos(\omega t) \right]$ and $\gamma \left[1F^{1,in} \sin(\omega t) + 1F^{1,out} \cos(\omega t) \right]$ in the right terms of Eqs.(6.60,6.61) remain both much smaller than one,[g] we could simplify Eqs.(6.60,6.61) and write at first order

$$1B = 1B^0 + \varepsilon\eta_1 \left[1F^{1,in} \sin(\omega t) + 1F^{1,out} \cos(\omega t) \right] \tag{6.62}$$

$$2B = 2B^0 - \varepsilon\eta_2 \left[1F^{1,in} \sin(\omega t) + 1F^{1,out} \cos(\omega t) \right] \tag{6.63}$$

with

$$\eta_1 = K_1^\Delta R^0 \left(1 - \gamma 1F^0 \right) \tag{6.64}$$

$$\eta_2 = K_2^\Delta R^0 \left(1 + \gamma 2F^0 \right). \tag{6.65}$$

Then we could deduce

$$O(t) = O^0 + O^{1,in} \sin(\omega t) + O^{1,out} \cos(\omega t) \tag{6.66}$$

---

[f] For a mixture containing 40 μM of F$_{tot}$ and 2 μM of R$_{tot}$ under resonance conditions for the free DFHBI, we obtained for both terms 0.074.

[g] For a mixture containing 40 μM of F$_{tot}$ and 2 μM of R$_{tot}$ under resonance conditions for the free DFHBI, we obtained respectively 0.13, 0.25 and 0.074.

with

$$O^0 = Q_{1F}1F^0 + Q_{1B}1B^0 + Q_{2F}2F^0 + Q_{2B}2B^0 \tag{6.67}$$

$$\Delta Q = Q_{1F} - Q_{2F} + \eta_1 Q_{1B} - \eta_2 Q_{2B} \tag{6.68}$$

$$O^{1,in} = \varepsilon \Delta Q 1F^{1,in} \tag{6.69}$$

$$O^{1,out} = \varepsilon \Delta Q 1F^{1,out} \tag{6.70}$$

and[h]

$$I_F(t) = I_F^0 + I_F^{1,in} \sin(\omega t) + I_F^{1,out} \cos(\omega t) \tag{6.74}$$

with

$$I_F^0 = O^0 I^0 \tag{6.75}$$

$$I_F^{1,in} = \varepsilon \left(I_F^0 + \Delta Q 1F^{1,in} I^0 \right) \tag{6.76}$$

$$I_F^{1,out} = \varepsilon \Delta Q 1F^{1,out} I^0. \tag{6.77}$$

---

[h] Similarly, using Eq.(6.45), Eq.(6.66) can be rewritten to explicit the phase delay between the fluorescence emission and the exciting light :

$$O(t) = O^0 - \varepsilon \Delta Q \frac{\rho^0_{12,F} \tau^0_{12,F} p^{\Delta}_{21,F}}{\sqrt{1 + \left(\omega \tau^0_{12,F}\right)^2}} \sin\left(\omega t - \phi_{12,F}\right) \tag{6.71}$$

Therefore, the temporal dependence of the fluorescence emission given in Eq.(6.74) becomes :

$$I_F(t) = I_F^0 \left[1 + \varepsilon \sin(\omega t) - \varepsilon R^0_{12,F} \sin\left(\omega t - \phi_{12,F}\right) \right] \tag{6.72}$$

with

$$R^0_{12,F} = \frac{\Delta Q}{O^0} \frac{\rho^0_{12,F} \tau^0_{12,F} p^{\Delta}_{21,F}}{\sqrt{1 + \left(\omega \tau^0_{12,F}\right)^2}} \tag{6.73}$$

Chapter 7

General conclusion and perspectives

This PhD work has pointed out the interest of exploiting the kinetic signature of a given reactive probe to improve the selectivity of imaging methods upon relying on photochromism and fluorescence. In this final chapter, we first highlight the main results we obtained during this PhD. In a second section, we propose and discuss a few perspectives and potential applications of the OPTIMAL/OPIOM approaches.

7.1 Photochromism and light modulation

We first evidenced that the Spinach probe exhibits a previously unreported photochemical behavior. The Spinach system combines both fluorogenicity and photochromism, that makes it singular compared to the other usual fluorescence turn-on probes. These two properties permit to tune both the amplitude and the rate constant associated to the photoconversion. Based on the photochemical properties of Spinach, we implemented a selective fluorescence imaging method and showed that OLID could be performed with one color light excitation.

Second, we have designed the OPTIMAL strategy that discriminates a targeted photoswitchable probe in a mixture containing interfering compounds, photoswitchable or not, without any preliminary separation or washing step. This approach relies on the first order out-of-phase response of the targeted photoswitchable probe to periodic light modulation. This one can be maximized by appropriately tuning the two control parameters, the average light intensity and the radial frequency of the modulated light excitation so as to satisfy robust resonance conditions. This strategy opens opportunities for selective and quantitative analyses in complex mixtures such as the ones encountered in biology.

Third, we experimentally validated the OPTIMAL approach in the context of fluorescence imaging. OPIOM permitted selective and quantitative imaging of photoswitchable fluorescent probes among fluorescent interfering compounds, photoswitchable or not. Notably, we demonstrated the multiplexed observations opportunities provided by OPIOM using RSFPs exhibiting sufficiently different resonance conditions.

Eventually, we achieved to greatly improve the temporal resolution of the original OPIOM protocol by using a second constant light source that accelerates the photoswitching dynamics. Such an acquisition rate should permit most dynamic studies in biology.

7.2 Perspectives

7.2.1 FRET and OPIOM

Förster (or Fluorescence) resonance energy transfer (FRET) is a phenomenon that occurs between a fluorescent donor in its excited state and a fluorescent acceptor in its ground state.[84] A first condition for FRET to be observed is that the emission spectrum of the donor overlaps the absorption spectrum of the acceptor. Energy is transfered non-radiatively from the donor to the acceptor due to long-range dipole-dipole interactions. The efficiency of the energy transfer depends on several parameters such as : the extent of the spectral overlap of the emission spectrum of the donor and the absorption spectrum of the acceptor, the fluorescence quantum yield of the donor, the relative orientation of the donor and the acceptor and the distance between the donor and the acceptor molecules.[84] Exciting the donor of a FRET pair leads to a quenching of the donor fluorescence and an increased acceptor fluorescence emission if they are close enough from each other (less than ~10 nm).[177] FRET can be used to detect protein-protein interactions in a living cell in real time.[177–179] The two different proteins of interest are respectively labeled with the donor (often a CFP) and the acceptor (often a YFP) of a FRET pair. Upon interaction between the two partners, the fluorophores are close enough for FRET to occur (see Figure 7.1**a**). Several intramolecular FRET-based indicators have been designed to report on dynamic conformational changes by sandwiching the two interacting protein domains with the donor and the acceptor of the FRET pair.[177] Many sensors based on FRET transfer are employed to measure intracellular concentrations of ions, metabolites... to report for the activity of proteins...[177–179] The most famous FRET-sensor is probably cameleon to detect Ca^{2+}.[180] A conformational change of the sensor is induced by the recognition of the target resulting in an alteration of FRET efficiency (see Figure 7.1**b**).

The quantitative analysis of these FRET experiments consists in the ratiometric measurement of acceptor to donor fluorescence. Nevertheless, an accurate analysis can be rendered difficult by the small signal variation arising from FRET as well as by the autofluorescence of the background. Employing a photoswitchable donor submitted to light modulation could modulate not only the fluorescence signal of the donor but also the one of the acceptor. Thus, applying the OPIOM protocol would here enable to benefit from the lock-in detection scheme to improve the signal-to-noise ratio as well to cancel out the background contribu-

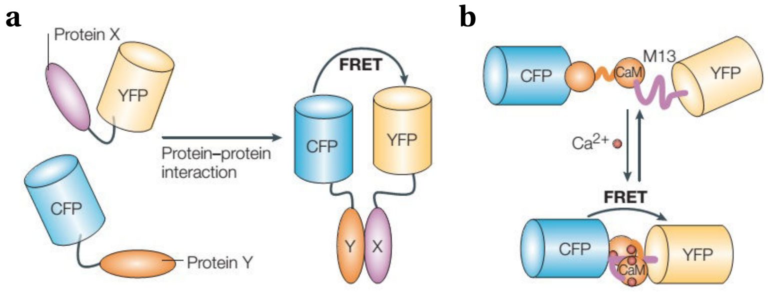

Figure 7.1: FRET-based methods. (**a**) Detection of protein-protein interaction with FRET. The interaction of two different proteins (X and Y) that are labeled with a CFP donor and a YFP acceptor respectively (**b**) FRET-sensor. Recognition of Ca^{2+} induces a conformational change of the Cameleon sensor and alters FRET efficiency. Adapted from Zhang *et al.*[177]

tion to accurately estimate the FRET efficiency. Recently, a combined OLID-FRET approach has been implemented to improve the sensitivity detection of FRET efficiency[88] and to improve contrast in immunofluorescence imaging.[89]

7.2.2 Brainbow and OPIOM

Neuroscience aims at understanding how neuronal circuits account for mental activities and behaviors and how alterations in them lead to neurological or psychiatric disorders.[181] For this purpose, it is necessary to visualize neuronal networks architecture. One of the key points is to be able to distinguish individual neurons from their neighbors and localize the different interconnections between them. In the past decade, a very promising strategy has been developed based on the following observation : the mixing of several colors with different intensities gives rise to a large number of hues. Called *Brainbow*, it relies on a stochastic expression of fluorescent proteins of different colors (XFPs). Individual neurons produce random mixtures of XFPs in various amounts resulting in many distinguishable hues enabling to discriminate them spectrally. With only three XFPs, around 100 colors are generated with the *Brainbow* approach allowing multicolour labeling of individual neurons according to hues. This strategy has already been used for multicolour labeling in mice,[182] zebrafish[183,184] and drosophila.[185]

Relying on the *Brainbow* approach, stochastic expression of several RSFPs emitting in the same wavelength range but differing by their dynamic parameters would produce random mixtures with various values of the first order out-of-phase fluorescence response ($\mathfrak{I}_{\mathfrak{F}}^{1,\mathrm{out}}$). By applying OPIOM, the autofluorescence currently observed when conditioning the brain to become transparent could be eliminated. In addition, relying on only one emission channel would avoid the chromatic aberration issues encountered nowadays with the *Brainbow* strategy.

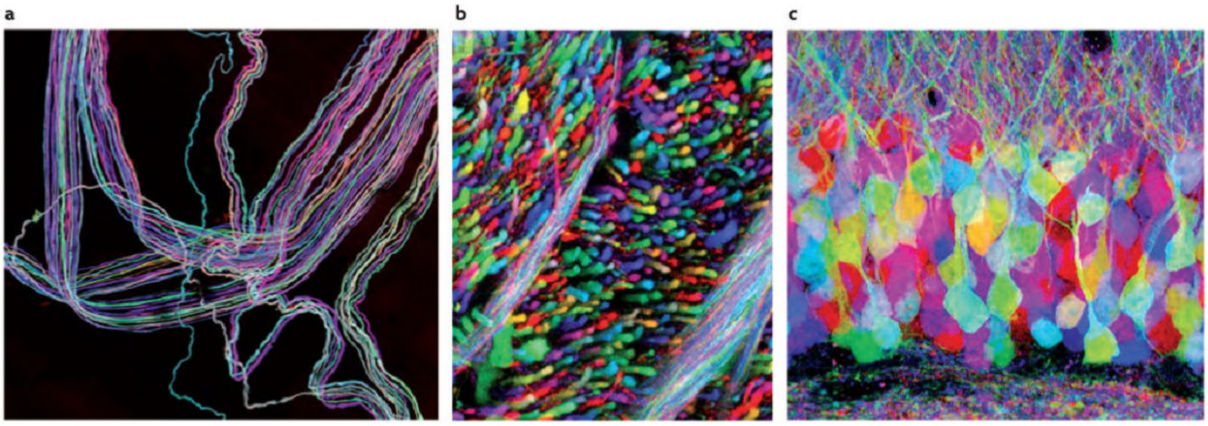

Figure 7.2: Multicolour labeling with the *Brainbow* strategy in transgenic mice. (**a**) A motor nerve innervating ear muscle. (**b**) An axon tract in the brainstem. (**c**) The hippocampal dentate gyrus. In the Brainbow mice from which these images were taken, up to ~ 160 colours were observed. The images were obtained by the superposition of separate red, green and blue channels. Adapted from Lichtman *et al.*[181]

7.2.3 Remote sensing in plants

Among biological samples, plants and micro-algae are organisms that are particularly difficult to image by relying on fluorescence. Indeed, in addition to pigments that absorb light, the presence of endogenous emitters (namely flavin and chlorophyll) in plants and light scattering contaminate the fluorescence signal. Since OPIOM precisely extinguishes the autofluorescence, we would like to evaluate its relevance for plant macro-imaging.

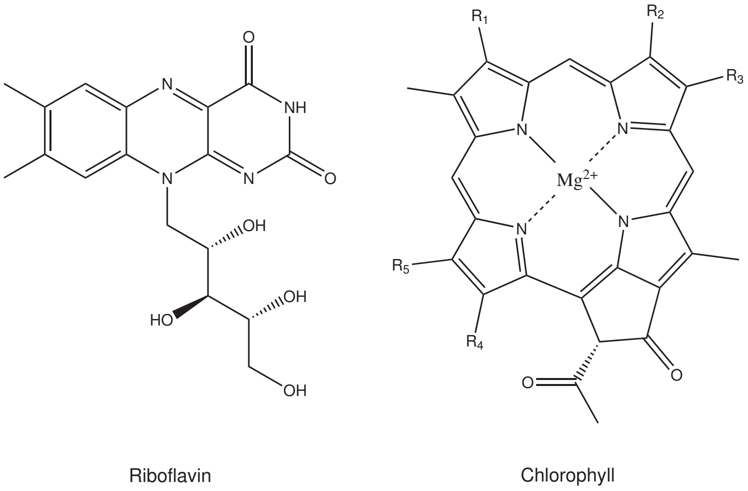

Figure 7.3: General structures of riboflavin and chlorophyll.

To evaluate the potential use of OPIOM for selective imaging in plants, we have relied on tobacco (*Nicotiana benthamiana*) as a model organism, which is widely used for its transformation abilities. Dronpa-3 was expressed in the nucleus and cytoplasm of tobacco cells transiently transfected by *Agrobacterium tumefaciens*. We applied the OPIOM protocol in epifluorescence microscopy with the same set-up we used to perform our preceding experiments (see chapter 4). We imaged Dronpa-3 in leaf epidermal cells (see Figure 7.4**a**) with excitation modulation tuned to Dronpa-3 resonance. OPIOM efficiently canceled out the intrinsic fluorescence of non-transfected cells and revealed selectively the Dronpa-3 signal of labeled cells. We then tested the ability of OPIOM for remote detection of fluorescence in living plants. For this purpose, we employed our usual light excitation setup consisting in a LED collimated by a condenser lens to illuminate 1 cm^2 of the leaf of a tobacco plant placed at around 25 cm of the light source (see Figure 7.4**b**). The fluorescence emission was detected at 525 ± 15 nm with a camera equipped with an objective for industrial vision also placed at 25 cm of the plant. Applying OPIOM enabled us to efficiently extinguish the autofluorescent background (visible on the non-transfected control plant) and reveal selectively the signal of Dronpa-3 of the transfected tobacco plant (see Figure 7.4**c**). These preliminary results suggest that OPIOM could be employed for remote sensing of a RSFP in a living plant.

Figure 7.4: OPIOM application in tobacco plants transfected by *Agrobacterium tumefaciens*. (**a**) Selective imaging of Dronpa-3 in leaf epidermal cells : the leaf of transfected plants shows fluorescent epidermal cells with typical morphology whereas background fluorescence from internal compartments is detected for the non-transfected plant; With OPIOM, background fluorescence is canceled out while Dronpa-3 tagged cells are easily recovered. Imaging was performed in epifluorescence with a 63x objective. Field of view is 100×100 μm. (**b**) View of the instrumental setup for remote detection of Dronpa-3; (**c**) Remote sensing of Dronpa-3 in tobacco leaf. Under constant illumination of the plants placed in the dark, the contrast between transfected and non-transfected tobacco is poor. With sinusoidal light modulation tuned to the resonance of Dronpa-3, the signal arising from Dronpa-3 is selectively revealed and autofluorescence of the leaf is efficiently suppressed. Field of view is 2×2 cm. Images labeled Pre-OPIOM and OPIOM correspond to the unfiltered and OPIOM-filtered, respectively, images.

In relation to these preliminary satisfactory results, we are presently considering to use OPIOM for reading-out the physiological state of ’sensor’ plants. Indeed, the expression of FPs in plants can be controlled by a wide range of promoters[186–188] inducible by stress (salinity, flooding, drought, temperature, wounding, pathogen or insect attack, heavy metals), nutrients (nitrate, phosphate and copper) and chemicals (pollutants, herbicides and insecticides).[189] In this context, the physiological information regarding the status of plants in relation to their environment could be read-out by employing ’sensor’ plants expressing RSFPs under promoter control combined with the OPIOM protocol. This would permit to reliably and early identify the source(s) of stress of the plants in their specific environmental conditions so as to optimize plant fitness.

Chapter 8

Experimental Part

The experimental protocols are thoroughly described in the Material and Methods or in the Supporting Information of the different articles. The page numbers regarding each procedure are indicated in the following.

8.1 Probes production

- DFHBI synthesis : see Material and Methods page 51.
- Spinach : see Material and Methods page 51.
- Protein
  - Cloning : see Material and Methods page 149.
  - Protein production and purification : see Material and Methods page 150.

8.2 Spectroscopic Instruments

- See Material and Methods page 51 for Spinach.
- See Material and Methods page 151 for one-color OPIOM.
- See Material and Methods page 213 for two-color OPIOM.

8.3 Determination of the kinetic parameters of the RSFPs

- Photoconversion experiment at 480 nm: see Material and Methods page 151 and Supplementary text page 170.

- Thermal return experiment : see Material and Methods page 151 and Supplementary text page 170.
- Light modulation experiment in cuvettes at 480 nm : see Material and Methods page 151 and Supplementary text page 172.
- Photoconversion experiment at 480 nm and 405 nm : see Material and Methods page 213 and subsection 5.2.2 page 191.

8.4 Systems

- Microfluidic device : see Material and Methods page 152.
- Mammalian cell culture and transfection : see Material and Methods page 150.
- Zebrafish : see Material and Methods page 151.

8.5 Microscopy setups

- Epifluorescence microscope setup for one-color OLID : see Material and Methods page 51.
- Epifluorescence microscope setup for one-color OPIOM : see Material and Methods page 152. A scheme is provided in the subsection Supplementary Figures page 177.
- Single-Plane Illumination Microscope (SPIM) setup : see Material and Methods page 153. A scheme is provided in the subsection Supplementary Figures page 177.
- Epifluorescence microscope setup for two-color OPIOM : see Material and Methods page 213. A scheme is provided in the subsection Supplementary Figures page 211.

8.6 Imaging protocols

- One-color OPIOM
  - Video acquisition : see Supplementary text page 174.
  - Microdevice imaging : see Supplementary text page 175.
  - Cell and zebrafish embryo imaging with epifluorescence microscopy : see Supplementary text page 175.
  - Embryo imaging with Single Plane Illumination Microscopy : see Supplementary text page 176.

  - Matlab code for OPIOM imaging : see Appendix A in the Supporting Information page 185.

- Two-color OPIOM
  - Video acquisition : see Supplementary text page 174.
  - Microdevice imaging : see Supplementary text page 175.
  - Cell and zebrafish embryo imaging with epifluorescence microscopy : see Supplementary text page 175.
  - Matlab code for OPIOM imaging : see Appendix A in the Supporting Information page 185.

Bibliography

[1] N. L. Anderson and N. G. Anderson, The Human Plasma Proteome, *Molecular and cellular proteomics*, 2002, **1.11**, 845–867.

[2] V. E. Velculescu, L. Zhang, W. Zhou, J. Vogelstein, M. A. Basrai, D. E. Basset, P. Hieter, B. Vogelstein and K. W. Kinzler, Characterization of the yeast transcriptome, *Cell*, 1997, **88**, 243–251.

[3] M. J. Holland, Transcript Abundance in Yeast Varies over Six Orders of Magnitude, *J. Biol. Chem.*, 2002, **277**, 14363–14366.

[4] D. A. Skoog, D. M. West and J. Holler, *Fundamentals of analytical chemistry*, De Boeck, 1997.

[5] B. Valeur, *Molecular fluorescence: principles and applications*, Wiley-VCH, 2001.

[6] P. Atkins and J. de Paula, *Physical chemistry seventh edition*, De Boeck, 2004.

[7] W. E. Huang, M. Li, R. M. Jarvis, R. Goodacre and S. A. Banwart, Shining light on the microbial world: The Application of Raman Microspectroscopy, *Adv. Appl. Microbiol.*, 2010, **70**, 153–186.

[8] J. X. Cheng and X. S. Xie, Coherent anti-Stokes Raman scattering microscopy: instrumentation, theory, and applications, *J. Phys. Chem. B*, 2004, **108**, 827–840.

[9] J. P. Pezacki, J. A. Blake, D. C. Danielson, D. C. Kennedy, R. K. Lyn and R. Singaravelu, Chemical contrast for imaging living systems: molecular vibrations drive CARS microscopy, *Nat. Chem. Biol.*, 2011, **7**, 137–145.

[10] C. W. Freudiger, W. Min, B. G. Saar, S. Lu, C. H. Gary R. Holtom and, J. C. Tsai, J. X. Kang and X. S. Xie, Label-Free Biomedical Imaging with High Sensitivity by Stimulated Raman Scattering Microscopy, *Science*, 2008, **322**, 1857–1861.

[11] C. W. Freudiger, W. Min, G. R. Holtom, B. Xu, M. Dantus and X. S. Xie, Highly specific label-free molecular imaging with spectrally tailored excitation stimulated Raman scattering (STE-SRS) microscopy, *Nat. Photonics*, 2011, **5**, 103–109.

[12] M. Eigen and L. de Mayer, *Relaxation Methods in Techniques of Organic Chemistry*, Interscience Publishers, John Wiley and Sons, New York, London, 2nd edn, 1963, vol. VIII, pp. 895–1054.

[13] R. Labruère, A. Alouane, T. Le Saux, I. Aujard, P. Pelupessy, A. Gautier, S. Dubruille, F. Schmidt and L. Jullien, Self-immolative spacer for uncaging with fluorescence reporting, *Angew. Chem. Int. Ed.*, 2012, **51**, 9344–9347.

[14] I. Aujard, C. Benbrahim, M. Gouget, O. Ruel, J. B. Baudin, P. Neveu and L. Jullien, o-Nitrobenzyl photolabile protecting groups with red-shifted absorption: Syntheses and uncaging cross-sections for one- and two-photon excitation, *Chem. Eur. J.*, 2006, **12**, 6865–6879.

[15] N. Gagey, P. Neveu and L. Jullien, Reporting Two-Photon Uncaging with the Efficient 3,5-dibromo-2,4-dihydroxycinnamic Caging Group, *Angew. Chem. Int. Ed.*, 2007, **46**, 2467–2469.

[16] N. Gagey, P. Neveu, C. Benbrahim, B. Goetz, I. Aujard, J. B. Baudin and L. Jullien, Two-photon uncaging with fluorescence reporting: Evaluation of the o-hydroxycinnamic platform, *J. Am. Chem. Soc.*, 2007, **129**, 9986–9998.

[17] N. Gagey, M. Emond, P. Neveu, C. Benbrahim, B. Goetz, I. Aujard, J.-B. Baudin and L. Jullien, Alcohol Uncaging with Fluorescence Reporting: Evaluation of ortho-Acetoxyphenyl Methyloxazolone Precursors, *Org. Lett.*, 2008, **10**, 2341–2344.

[18] T. Barilero, P.-O. Chapuis, D. Pujade, S. Guilet, V. Croquette, L. Jullien, S. Volz and C. Gosse, Thermal characterization of a microfluidic cell using the 3ω method, *Proceedings of the Transducers and Eurosensors XXI Conference*, 2007, U933–U934.

[19] T. Barilero, T. Le Saux, C. Gosse and L. Jullien, Fluorescent Thermometers for Dual-Emission-Wavelength Measurements: Molecular Engineering and Application to Thermal Imaging in a Microsystem, *Anal. Chem.*, 2009, **81**, 7988–8000.

[20] K. Zrelli, T. Barilero, E. Cavatore, H. Berthoumieux, T. Le Saux, V. Croquette, A. Lemarchand, C. Gosse and L. Jullien, Temperature Modulation and Quadrature Detection for Selective Titration of Two-State Exchanging Reactants, *Anal. Chem.*, 2011, **83**, 2476–2484.

[21] D. Braun and A. Libchaber, Lock-in by molecular multiplication, *Appl. Phys. Lett.*, 2003, **83**, 5554–5556.

[22] I. Schoen, H. Krammer and D. Braun, Hybridization kinetics is different inside cells, *Proc. Natl. Acad. Sci. U. S. A.*, 2009, **106**, 21649–21654.

[23] M. R. Reichl and D. Braun, Thermophoretic Manipulation of Molecules inside Living Cells, *J. Am. Chem. Soc*, 2014, **136**, 15955–15960.

[24] H. Kato, T. Nishizaka, T. Iga, K. Kinosita and S. Ishiwata, Imaging of thermal activation of actomyosin motors, *Proc. Nat. Acad. Sci. U. S. A.*, 1999, **96**, 9602–9606.

[25] K. Hamad-Schifferli, J. J. Schwartz, A. T. Santos, S. Zhang and J. M. Jacobson, Remote electronic control of DNA hybridization through inductive coupling to an attached metal nanocrystal antenna, *Nature*, 2002, **415**, 152–155.

[26] J. Stehr, C. Hrelescu, R. A. Sperling, G. Raschke, M. Wunderlich, A. Nichtl, D. Heindl, K. Kurzinger, W. J. Parak, T. A. Klar and J. Feldmann, Gold NanoStoves for Microsecond DNA Melting Analysis, *Nano Lett.*, 2008, **8**, 619–623.

[27] C. F. Bernasconi, *Relaxation kinetics*, Academic Press, Inc, 1976.

[28] *Chemical kinetics and mechanism*, Royal Society of Chemistry, 2002.

[29] G. Porter, Forty years of photochemistry, *J. Chem. Soc., Faraday Trans. 2*, 1986, **82**, 2445–2451.

[30] P. Neveu, I. Aujard, C. Benbrahim, T. Le Saux, J.-F. Allemand, S. Vriz, D. Bensimon and L. Jullien, A caged retinoic acid for use with one- and two-photon excitation in zebrafish embryos, *Angew. Chem. Int. Ed.*, 2008, **47**, 3744–3746.

[31] H. Berthoumieux, L. Jullien and A. Lemarchand, Response to a Temperature Modulation as a Signature of Chemical Mechanisms, *Phys. Rev. E*, 2007, **76**, 056112.

[32] D. Baurecht and U. P. Fringeli, Quantitative modulated excitation Fourier transform infra-red (ME-FTIR) spectroscopy, *Rev. Mod. Sci. Inst.*, 2001, **72**, 3782–3792.

[33] A. Urakawa, T. Burgi and A. Baiker, Sensitivity enhancement and dynamic behavior analysis by modulation excitation spectroscopy: Principle and application in heterogeneous catalysis, *Chem. Eng. Sci.*, 2008, **63**, 4902 – 4909.

[34] Q. Wei and A. Wei, Optical Imaging with Dynamic Contrast Agents, *Chem. Eur. J.*, 2011, **17**, 1080–1091.

[35] J. H. Scofield, Frequency-domain description of a lock-in amplifier, *Am. J. Phys.*, 1994, **62**, 129–133.

[36] B. N. G. Giepmans, S. R. Adams, M. H. Ellisman and R. Y. Tsien, The Fluorescent Toolbox for Assessing Protein Location and Function, *Science*, 2006, **312**, 217–224.

[37] T. Gronemeyer, G. Godin and K. Johnsson, Adding value to fusion proteins through covalent labelling, *Curr. Opin. Biotechnol.*, 2005, **16**, 453 – 458.

[38] I. Chen and A. Y. Ting, Site-specific labeling of proteins with small molecules in live cells, *Curr. Opin. Biotechnol.*, 2005, **16**, 35 – 40.

[39] L. W. Miller and V. W. Cornish, Selective chemical labeling of proteins in living cells, *Curr. Opin. Chem. Biol.*, 2005, **9**, 56 – 61.

[40] A. Keppler, H. Pick, C. Arrivoli, H. Vogel and K. Johnsson, Labeling of fusion proteins with synthetic fluorophores in live cells, *Proc. Natl. Acad. Sci. U. S. A.*, 2004, **101**, 9955–9959.

[41] A. L. Efros, Interband absorption of light in a semiconductor sphere, *Sov. Phys. Semicond.*, 1982, **16**, 772–775.

[42] A. L. Efros and M. Rosen, The electronic structure of semiconductor nanocrystals, *Annu. Rev. Mater. Sci.*, 2000, **30**, 475–521.

[43] L. Qu and X. Peng, Control of Photoluminescence Properties of CdSe Nanocrystals in Growth, *J. Am. Chem. Soc.*, 2002, **124**, 2049–2055.

[44] X. Michalet, F. Pinaud, T. D. Lacoste, M. Dahan, M. P. Bruchez, A. P. Alivisatos and S. Weiss, Properties of Fluorescent Semiconductor Nanocrystals and their Application to Biological Labeling, *Single Mol.*, 2001, **2**, 261–276.

[45] W. C. W. Chan, D. J. Maxwell, X. Gao, R. E. Bailey, M. Han and S. Nie, Luminescent quantum dots for multiplexed biological detection and imaging, *Curr. Opin. Biotechnol.*, 2002, **13**, 40 – 46.

[46] X. Gao, L. Yang, J. A. Petros, F. F. Marshall, J. W. Simons and S. Nie, In vivo molecular and cellular imaging with quantum dots, *Curr. Opin. Biotechnol.*, 2005, **16**, 63 – 72.

[47] X. Michalet, F. F. Pinaud, L. A. Bentolila, J. M. Tsay, S. Doose, J. J. Li, G. Sundaresan, A. M. Wu, S. S. Gambhir and S. Weiss, Quantum Dots for Live Cells, in Vivo Imaging, and Diagnostics, *Science*, 2005, **307**, 538–544.

[48] J. K. Jaiswal and S. M. Simon, Potentials and pitfalls of fluorescent quantum dots for biological imaging, *Trends Cell Biol.*, 2004, **14**, 497 – 504.

[49] A. P. Alivisatos, W. Gu and C. Larabell, Quantum dots as cellular probes, *Annu. Rev. Biomed. Eng.*, 2005, **7**, 55–76.

[50] F. Pinaud, D. King, H.-P. Moore and S. Weiss, Bioactivation and Cell Targeting of Semiconductor CdSe/ZnS Nanocrystals with Phytochelatin-Related Peptides, *J. Am. Chem. Soc.*, 2004, **126**, 6115–6123.

[51] F. Pinaud, X. Michalet, L. A. Bentolila, J. M. Tsay, S. Doose, J. J. Li, G. Iyer and S. Weiss, Advances in fluorescence imaging with quantum dot bio-probes, *Biomaterials*, 2006, **27**, 1679 – 1687.

[52] A. Agrawal, R. Deo, G. D. Wang, M. D. Wang and S. Nie, Nanometer-scale mapping and single-molecule detection with color-coded nanoparticle probes, *Proc. Natl. Acad. Sci. U. S. A.*, 2008, **105**, 3298–3303.

[53] M. Dahan, S. Levi, C. Luccardini, P. Rostaing, B. Riveau and A. Triller, Diffusion Dynamics of Glycine Receptors Revealed by Single-Quantum Dot Tracking, *Science*, 2003, **302**, 442–445.

[54] D. S. Lidke, P. Nagy, R. Heintzmann, D. J. Arndt-Jovin, J. N. Post, H. E. Grecco, E. A. Jares-Erijman and T. M. Jovin, Quantum dot ligands provide new insights into erbB/HER receptor-mediated signal transduction, *Nat. Biotech.*, 2004, **22**, 198–203.

[55] B. Dubertret, P. Skourides, D. J. Norris, V. Noireaux, A. H. Brivanlou and A. Libchaber, In vivo imaging of quantum dots encapsulated in phospholipid micelles, *Science*, 2002, **298**, 1759–1762.

[56] X. H. Gao, Y. Y. Cui, L. W. K. Levenson, R. M.and Chung and N. S. M., In vivo cancer targeting and imaging with semiconductor quantum dots, *Nat. Biotechnol.*, 2004, **22**, 969–976.

[57] A. M. Derfus, W. C. W. Chan and S. N. Bhatia, Probing the Cytotoxicity of Semiconductor Quantum Dots, *Nano Lett.*, 2004, **4**, 11–18.

[58] B. Ballou, B. C. Lagerholm, L. A. Ernst, M. P. Bruchez and A. S. Waggoner, Noninvasive Imaging of Quantum Dots in Mice, *Bioconj. Chem.*, 2004, **15**, 79–86.

[59] F. H. Johnson, O. Shimomura, Y. Saiga, L. C. Gershman, G. T. Reynolds and J. R. Waters, Quantum efficiency of Cypridina luminescence, with a note on that of Aequorea, *J. Cell. Comp. Physiol.*, 1962, **60**, 85–103.

[60] O. Shimomura, F. H. Johnson and Y. Saiga, Extraction, Purification and Properties of Aequorin, a Bioluminescent Protein from the Luminous Hydromedusan, Aequorea, *J. Cell. Comp. Physiol.*, 1962, **59**, 223–239.

[61] D. C. Prasher, V. K. Eckenrode, W. W. Ward, F. G. Prendergast and M. J. Cormier, Primary structure of the Aequorea victoria green-fluorescent protein, *Gene*, 1992, **111**, 229 – 233.

[62] M. Chalfie, Y. Tu, G. Euskirchen, W. W. Ward and D. C. Prasher, Green fluorescent protein as a marker for gene expression, *Science*, 1994, **263**, 802–805.

[63] R. Heim, D. C. Prasher and R. Y. Tsien, Wavelength mutations and posttranslational autoxidation of green fluorescent protein, *Proc. Natl. Acad. Sci. U. S. A.*, 1994, **91**, 12501–12504.

[64] M. Ormo, A. B. Cubitt, K. Kallio, L. A. Gross, R. Y. Tsien and S. J. Remington, Crystal Structure of the Aequorea victoria Green Fluorescent Protein, *Science*, 1996, **273**, 1392–1395.

[65] R. Y. Tsien, The green fluorescent protein, *Annu. Rev. Biochem.*, 1998, **67**, 509–544.

[66] D. M. Chudakov, S. Lukyanov and K. A. Lukyanov, Fluorescent proteins as a toolkit for in vivo imaging, *Trends Biotechnol.*, 2005, **23**, 605 – 613.

[67] N. C. Shaner, G. H. Patterson and M. W. Davidson, Advances in fluorescent protein technology, *J. Cell Sci.*, 2007, **120**, 4247–4260.

[68] N. C. Shaner, R. E. Campbell, P. A. Steinbach, B. N. G. Giepmans, A. E. Palmer and R. Y. Tsien, Improved monomeric red, orange and yellow fluorescent proteins derived from Discosoma sp. red fluorescent protein, *Nat. Biotech.*, 2004, **22**, 1567–1572.

[69] L. Wang, W. C. Jackson, P. A. Steinbach and R. Y. Tsien, Evolution of new nonantibody proteins via iterative somatic hypermutation, *Proc. Natl. Acad. Sci. U. S. A.*, 2004, **101**, 16745–16749.

[70] J.-D. Pedelacq, S. Cabantous, T. Tran, T. C. Terwilliger and G. S. Waldo, Engineering and characterization of a superfolder green fluorescent protein, *Nat. Biotech.*, 2006, **24**, 79–88.

[71] R. Heim, A. B. Cubitt and R. Y. Tsien, Improved green fluorescence, *Nature*, 1995, **373**, 663–664.

[72] B. P. Cormack, R. H. Valdivia and S. Falkow, FACS-optimized mutants of the green fluorescent protein (GFP), *Gene*, 1996, **173**, 33 – 38.

[73] N. C. Shaner, M. Z. Lin, M. R. McKeown, P. A. Steinbach, K. L. Hazelwood, M. W. Davidson and R. Y. Tsien, Improving the photostability of bright monomeric orange and red fluorescent proteins, *Nat. Methods*, 2008, **5**, 545–551.

[74] D. A. Zacharias, J. D. Violin, A. C. Newton and R. Y. Tsien, Partitioning of Lipid-Modified Monomeric GFPs into Membrane Microdomains of Live Cells, *Science*, 2002, **296**, 913–916.

[75] K. Lukyanov, D. M. Chudakov, S. Lukyanov and V. V. Verkhusha, Photoactivatable fluorescent proteins, *Nat. Rev. Mol. Cell. Biol.*, 2005, **6**, 885–890.

[76] J. Lippincott-Schwartz and G. H. Patterson, Photoactivatable fluorescent proteins for diffraction-limited and super-resolution imaging, *Trends in Cell Biology*, 2009, **19**, 555 – 565.

[77] M. Fernandez-Suarez and A. Y. Ting, Fluorescent probes for super-resolution imaging in living cells, *Nat. Rev. Mol. Cell. Biol.*, 2008, **9**, 929–943.

[78] R. D. Jenison, S. C. Gill, A. Pardi and B. Polisky, High-resolution molecular discrimination by RNA, *Science*, 1994, **263**, 1425–1429.

[79] J. R. Babendure, S. R. Adams and R. Y. Tsien, Aptamers Switch on Fluorescence of Triphenylmethane Dyes, *J. Am. Chem. Soc.*, 2003, **125**, 14716–14717.

[80] T. P. Constantin, G. L. Silva, K. L. Robertson, T. P. Hamilton, K. Fague, A. S. Waggoner and B. A. Armitage, Synthesis of New Fluorogenic Cyanine Dyes and Incorporation into RNA Fluoromodules, *Org. Lett.*, 2008, **10**, 1561–1564.

[81] J. Paige, K. Y. Wu and S. R. Jaffrey, RNA Mimics of Green Fluorescent Protein, *Science*, 2011, **333**, 642–646.

[82] J. Paige, T. Nguyen-Ducand, W. Song and S. R. Jaffrey, Fluorescence Imaging of Cellular Metabolites with RNA, *Science*, 2012, **335**, 1194.

[83] G. Marriott, R. M. Clegg, D. J. Arndt-Jovin and T. M. Jovin, Time resolved imaging microscopy. Phosphorescence and delayed fluorescence imaging, *Biophys. J.*, 1991, **60**, 1374 – 1387.

[84] J. R. Lakowicz, *Principles of Fluorescence Spectroscopy*, Springer, 2006.

[85] *Fluorescence lifetime spectroscopy and imaging*, ed. L. Marcu, P. M. W. French and D. S. Elson, CRC Press, 2014.

[86] G. Marriott, S. Mao, T. Sakata, J. Ran, D. K. Jackson, C. Petchprayoon, T. J. Gomez, E. Warp, O. Tulyathan, H. L. Aaron, E. Y. Isacoff and Y. Yan, Optical lock-in detection imaging microscopy for contrast-enhanced imaging in living cells, *Proc. Natl. Acad. Sci. U. S. A.*, 2008, **105**, 17789–17794.

[87] Y. Yan, M. E. Marriott, C. Petchprayoon and G. Marriott, Optical switch probes and optical lock-in detection (OLID) imaging microscopy: high-contrast fluorescence imaging within living systems, *Biochem. J.*, 2011, **433**, 411–422.

[88] S. Mao, R. K. Benninger, Y. Yan, C. Petchprayoon, D. Jackson, C. J. Easley, D. W. Piston and G. Marriott, Optical Lock-In Detection of FRET Using Synthetic and Genetically Encoded Optical Switches, *Biophys. J.*, 2008, **94**, 4515 – 4524.

[89] Y. Yan, C. Petchprayoon, S. Mao and G. Marriott, Reversible optical control of cyanine fluorescence in fixed and living cells: optical lock-in detection immunofluorescence imaging microscopy, *Philos. Trans. R. Soc. Lond. B. Biol. Sci.*, 2012, **368**, 1–9.

[90] C. Petchprayoon, Y. Yan, S. Mao and G. Marriott, Rational design, synthesis, and characterization of highly fluorescent optical switches for high-contrast optical lock-in detection (OLID) imaging microscopy in living cells, *Bioorg. Med. Chem.*, 2011, **19**, 1030 – 1040.

[91] G. Du, G. Marriott and Y. Yan, 4th International Conference on Bioinformatics and Biomedical Engineering (iCBBE), 2010, pp. 1–5.

[92] L. Wu, Y. Dai, X. Jiang, C. Petchprayoon, J. E. Lee, T. Jiang, Y. Yan and G. Marriott, High-Contrast Fluorescence Imaging in Fixed and Living Cells Using Optimized Optical Switches, *PLoS ONE*, 2013, **8**, e64738.

[93] C. I. Richards, J.-C. Hsiang and R. M. Dickson, Synchronously amplified fluorescence image recovery (SAFIRe), *J. Phys. Chem. B*, 2010, **114**, 660–665.

[94] C. I. Richards, J.-C. Hsiang, D. Senapati, S. Patel, J. Yu, T. Vosch and R. M. Dickson, Optically modulated fluorophores for selective fluorescence signal recovery, *J. Am. Chem. Soc.*, 2009, **131**, 4619–4621.

[95] C. Fan, J.-C. Hsiang and R. M. Dickson, Optical modulation and selective recovery of Cy5 fluorescence, *ChemPhysChem*, 2012, **13**, 1023–1029.

[96] C. I. Richards, J.-C. Hsiang, A. M. Khalil, N. P. Hull and R. M. Dickson, FRET-enabled optical modulation for high sensitivity fluorescence imaging, *J. Am. Chem. Soc.*, 2010, **132**, 6318–6323.

[97] C. Fan, J.-C. Hsiang, A. E. Jablonski and R. M. Dickson, All-optical fluorescence image recovery using modulated Stimulated Emission Depletion, *Chem. Sci.*, 2011, **2**, 1080–1085.

[98] A. E. Jablonski, J.-C. Hsiang, P. Bagchi, N. Hull, C. I. Richards, C. J. Fahrni and R. M. Dickson, Signal Discrimination Between Fluorescent Proteins in Live Cells by Long-Wavelength Optical Modulation, *J. Phys. Chem. Lett.*, 2012, **3**, 3585–3591.

[99] A. E. Jablonski, R. B. Vegh, J.-C. Hsiang, B. Bommarius, Y.-C. Chen, K. M. Solntsev, A. S. Bommarius, L. M. Tolbert and R. M. Dickson, Optically Modulatable Blue Fluorescent Proteins, *J. Am. Chem. Soc.*, 2013, **135**, 16410–16417.

[100] S. Sarkar, C. Fan, J.-C. Hsiang and R. M. Dickson, Modulated Fluorophore Signal Recovery Buried within Tissue Mimicking Phantoms, *J. Phys. Chem. A*, 2013, **117**, 9501–9509.

[101] D. P. Mahoney, E. A. Owens, C. Fan, J.-C. Hsiang, M. M. Henary and R. M. Dickson, Tailoring Cyanine Dark States for Improved Optically Modulated Fluorescence Recovery, *J. Phys. Chem. B*, 2015, **119**, 4637–4643.

[102] J.-C. Hsiang, A. E. Jablonski and R. M. Dickson, Optically modulated fluorescence bioimaging: visualizing obscured fluorophores in high background, *Acc. Chem. Res.*, 2014, **47**, 1545–1554.

[103] J. Dong, K. M. Solntsev, O. Poizat and L. M. Tolbert, The Meta-Green Fluorescent Protein Chromophore, *J. Am. Chem. Soc.*, 2007, **129**, 10084–10085.

[104] J. Dong, F. Abulwerdi, A. Baldridge, J. Kowalik, K. M. Solntsev and L. M. Tolbert, Isomerization in Fluorescent Protein Chromophores Involves Addition/Elimination, *J. Am. Chem. Soc.*, 2008, **130**, 14096–14098.

[105] B. Wu, K. D. Piatkevich, T. Lionnet, R. H. Singer and V. V. Verkhusha, Modern fluorescent proteins and imaging technologies to study gene expression, nuclear localization, and dynamics, *Curr. Opin. Cell. Biol.*, 2011, **23**, 310–317.

[106] N. C. Shaner, P. A. Steinbach and R. Y. Tsien, A guide to choosing fluorescent proteins, *Nat. Methods*, 2005, **2**, 905–909.

[107] A. D. Ellington and J. W. Szostak, In vitro selection of RNA molecules that bind specific ligands, *Nature*, 1990, **346**, 818–822.

[108] C. Tuerk and L. Goldberg, Systematic evolution of ligands by exponential enrichment: RNA ligands to bacteriophage T4 DNA, *Science*, 1990, **249**, 505.

[109] W. Song, R. L. Strack and S. R. Jaffrey, Imaging bacterial protein expression using genetically encoded RNA sensors, *Nat. Methods*, 2013, **10**, 873–875.

[110] C. A. Kellenberger, S. C. Wilson, J. Sales-Lee and M. C. Hammond, RNA-Based Fluorescent Biosensors for Live Cell Imaging of Second Messengers Cyclic di-GMP and Cyclic AMP-GMP, *J. Am. Chem. Soc.*, 2013, **135**, 4906–4909.

[111] R. L. Strack, W. Song and S. R. Jaffrey, Using Spinach-based sensors for fluorescence imaging of intracellular metabolites and proteins in living bacteria, *Nat. Protocols*, 2014, **9**, 146–155.

[112] K. Hofer, L. V. Langejurgen and A. Jaschke, Universal Aptamer-Based Real-Time Monitoring of Enzymatic RNA Synthesis, *J. Am. Chem. Soc.*, 2013, **135**, 13692–13694.

[113] G. Pothoulakis, F. Ceroni, B. Reeve and T. Ellis, The Spinach RNA Aptamer as a Characterization Tool for Synthetic Biology, *ACS Synth. Biol.*, 2014, **3**, 182–187.

[114] R. L. Strack, M. D. Disney and S. R. Jaffrey, A superfolding Spinach2 reveals the dynamic nature of trinucleotide repeat-containing RNA, *Nat. Methods*, 2013, **10**, 1219–1224.

[115] W. Song, R. L. Strack, N. Svensen and S. R. Jaffrey, Plug-and-Play Fluorophores Extend the Spectral Properties of Spinach, *J. Am. Chem. Soc.*, 2014, **136**, 1198–1201.

[116] G. S. Filonov, J. D. Moon, N. Svensen and S. R. Jaffrey, Broccoli: Rapid Selection of an RNA Mimic of Green Fluorescent Protein by Fluorescence-Based Selection and Directed Evolution, *J. Am. Chem. Soc.*, 2014, **136**, 16299–16308.

[117] H. Huang, N. B. Suslov, N.-S. Li, S. A. Shelke, M. E. Evans, Y. Koldobskaya, P. A. Rice and J. A. Piccirilli, A G-quadruplex-containing RNA activates fluorescence in a GFP-like fluorophore, *Nat. Chem. Biol.*, 2014, **10**, 686–691.

[118] K. D. Warner, M. C. Chen, W. Song, R. L. Strack, A. Thorn, S. R. Jaffrey and A. R. Ferré-D'Amaré, Structural basis for activity of highly efficient RNA mimics of green fluorescent protein, *Nat. Struct. Mol. Biol.*, 2014, **21**, 658–663.

[119] K. Zrelli, *PhD thesis*, 2011.

[120] P. Wang, J. Querard, S. Maurin, S. S. Nath, T. Le Saux, A. Gautier and L. Jullien, Photochemical properties of Spinach and its use in selective imaging, *Chem. Sci.*, 2013, **4**, 2865–2873.

[121] S. Albright, V. Croquette, A. Gautier, L. Jullien, T. Le Saux, S. S. Nath, J. Querard and P. Wang, *Method for the detection of reversibly photoswitchable fluorescent species*, Patent PCT/EP2014/075336, 2013.

[122] R. Y. Tsien, L. Ernst and A. Waggoner, *Handbook of Biological Confocal Microscopy*, Springer Science, 2006.

[123] T. Fukaminato, Single-molecule fluorescence photoswitching : Design and synthesis of photoswitchable fluorescent molecules, *J. Photochem. Photobiol. C : Photochem. Rev.*, 2011, **12**, 177–208.

[124] R. M. Dickson, R. Y. Tsien and W. E. Moerner, On/off blinking and switching behaviour of single molecules of green fluorescent protein, *Nature*, 1997, **388**, 355–358.

[125] R. Ando, H. Mizuno and A. Miyawaki, Regulated Fast Nucleocytoplasmic Shuttling Observed by Reversible Protein Highlighting, *Science*, 2004, **306**, 1370–1373.

[126] M. Andresen, A. C. Stiel, S. Trowitzsch, G. Weber, C. Eggeling, M. C. Wahl, S. W. Hell and S. Jakobs, Structural basis for reversible photoswitching in Dronpa, *Proc. Natl. Acad. Sci. U. S. A.*, 2007, **104**, 13005–13009.

[127] P. G. Wilmann, K. Turcic, J. M. Battad, M. C. Wilce, R. J. Devenish, M. Prescott and J. Rossjohn, The 1.7 Å Crystal Structure of Dronpa : A Photoswitchable Green Fluorescent Protein, *J. Mol. Biol.*, 2006, **364**, 213 – 224.

[128] A. C. Stiel, S. Trowitzsch, G. Weber, M. Andresen, C. Eggeling, S. W. Hell, S. Jakobs and M. C. Wahl, 1.8 Å bright-state structure of the reversibly switchable fluorescent protein Dronpa guides the generation of fast switching variants, *Biochem. J.*, 2007, **402**, 35–42.

[129] R. Ando, C. Flors, H. Mizuno, J. Hofkens and A. Miyawaki, Highlighted Generation of Fluorescence Signals Using Simultaneous Two-Color Irradiation on Dronpa Mutants, *Biophys. J.*, 2007, **92**, L97 – L99.

[130] M. Andresen, A. C. Stiel, J. Follig, D. Wenzel, A. Schoenle, A. Egner, C. Eggeling, S. W. Hell and S. Jakobs, Photoswitchable fluorescent proteins enable monochromatic multilabel imaging and dual color fluorescence nanoscopy, *Nat. Biotech.*, 2008, **26**, 1035–1040.

[131] D. Bourgeois and V. Adam, Reversible Photoswitching in Fluorescent Proteins : A Mechanistic View, *IUBMBLife*, 2012, **64**, 482–491.

[132] S. Habuchi, R. Ando, P. Dedecker, W. Verheijen, H. Mizuno, A. Miyawaki and J. Hofkens, Reversible single-molecule photoswitching in the GFP-like fluorescent protein Dronpa, *Proc. Natl. Acad. Sci. U. S. A.*, 2005, **102**, 9511–9516.

[133] S. Habuchi, P. Dedecker, J.-I. Hotta, C. Flors, R. Ando, H. Mizuno, A. Miyawaki and J. Hofkens, Photo-induced protonation/deprotonation in the GFP-like fluorescent protein Dronpa : mechanism responsible for the reversible photoswitching, *Photochem. Photobiol. Sci.*, 2006, **5**, 567–576.

[134] E. Fron, C. Flors, G. Schweitzer, S. Habuchi, H. Mizuno, R. Ando, F. C. De Schryver, A. Miyawaki and J. Hofkens, Ultrafast Excited-State Dynamics of the Photoswitchable Protein Dronpa, *J. Am. Chem. Soc.*, 2007, **129**, 4870–4871.

[135] D. Yadav, F. Lacombat, N. Dozova, F. Rappaport, P. Plaza and A. Espagne, Real-Time Monitoring of Chromophore Isomerization and Deprotonation during the Photoactivation of the Fluorescent Protein Dronpa, *J. Phys. Chem. B*, 2015, **119**, 2404–2414.

[136] A. Regis Faro, P. Carpentier, G. Jonasson, G. Pompidor, D. Arcizet, I. Demachy and D. Bourgeois, Low-Temperature Chromophore Isomerization Reveals the Photoswitching Mechanism of the Fluorescent Protein Padron, *J. Am. Chem. Soc.*, 2011, **133**, 16362–16365.

[137] T. Brakemann, G. Weber, M. Andresen, G. Groenhof, A. C. Stiel, S. Trowitzsch, C. Eggeling, H. Grubmuller, S. W. Hell, M. C. Wahl and S. Jakobs, Molecular basis of the light-driven switching of the photochromic fluorescent protein Padron, *J. Biol. Chem.*, 2010, **285**, 14603–14609.

[138] G. Patterson, S. Knobel, W. Sharif, S. Kain and D. Piston, Use of the green fluorescent protein and its mutants in quantitative fluorescence microscopy, *Biophys. J.*, 1997, **73**, 2782 – 2790.

[139] A. C. Stiel, M. Andresen, H. Bock, M. Hilbert, J. Schilde, A. Schoenle, C. Eggeling, A. Egner, S. W. Hell and S. Jakobs, Generation of Monomeric Reversibly Switchable Red Fluorescent Proteins for Far-Field Fluorescence Nanoscopy, *Biophys. J.*, 2008, **95**, 2989–2997.

[140] F. V. Subach, L. Zhang, T. W. J. Gadella, N. G. Gurskaya, K. A. Lukyanov and V. V. Verkhusha, Red Fluorescent Protein with Reversibly Photoswitchable Absorbance for Photochromic FRET, *Chem. Biol.*, 2010, **17**, 745–755.

[141] T. Grotjohann, I. Testa, M. Leutenegger, H. Bock, N. T. Urban, F. Lavoie-Cardinal, K. I. Willig, C. Eggeling, S. Jakobs and S. W. Hell, Diffraction-unlimited all-optical imaging and writing with a photochromic GFP, *Nature*, 2011, **478**, 204–208.

[142] S. L. C. Moors, S. Michielssens, C. Flors, P. Dedecker, J. Hofkens and A. Ceulemans, How Is cis-trans Isomerization Controlled in Dronpa Mutants ? A Replica Exchange Molecular Dynamics Study, *J. Chem. Theory Comput.*, 2008, **4**, 1012–1020.

[143] J. N. Henderson, H.-W. Ai, R. E. Campbell and S. J. Remington, Structural basis for reversible photobleaching of a green fluorescent protein homologue, *Proc. Natl. Acad. Sci. U. S. A.*, 2007, **104**, 6672–6677.

[144] R. Bizzarri, M. Serresi, F. Cardarelli, S. Abbruzzetti, B. Campanini, C. Viappiani and F. Beltram, Single Amino Acid Replacement Makes Aequorea victoria Fluorescent Proteins Reversibly Photoswitchable, *J. Am. Chem. Soc.*, 2010, **132**, 85–95.

[145] H. Chang, M. Zhang, W. Ji, J. Chen, Y. Zhang, B. Liu, J. Lu, J. Zhang, P. Xu and T. Xu, A unique series of reversibly switchable fluorescent proteins with beneficial properties for various applications, *Proc. Natl. Acad. Sci. U. S. A.*, **109**, 4455–4460.

[146] K. Lukyanov, A. F. Fradkov, N. G. Gurskaya, M. V. Matz, Y. A. Labas, A. P. Savitsky, M. L. Markelov, A. G. Zaraisky, X. Zhao, Y. Fang, W. Tan and S. A. Lukyanov, Natural animal coloration can be determined by a nonfluorescent green fluorescent protein homolog, *J. Biol. Chem.*, 2000, **275**, 25879–25882.

[147] D. M. Chudakov, T. V. Chepurnykh, V. V. Belousov, S. Lukyanov and K. A. Lukyanov, Fast and Precise Protein Tracking Using Repeated Reversible Photoactivation, *Traffic*, 2006, **7**, 1304–1310.

[148] M. Hofmann, C. Eggeling, S. Jakobs and S. W. Hell, Breaking the diffraction barrier in fluorescence microscopy at low light intensities by using reversibly photoswitchable proteins, *Proc. Natl. Acad. Sci. U. S. A.*, 2005, **102**, 17565–17569.

[149] M. Andresen, M. C. Wahl, A. C. Stiel, F. Graeter, L. V. Schaefer, S. Trowitzsch, G. Weber, C. Eggeling, H. Grubmueller, S. W. Hell and S. Jakobs, Structure and mechanism of the reversible photoswitch of a fluorescent protein, *Proc. Natl. Acad. Sci. U. S. A.*, 2005, **102**, 13070–13074.

[150] T. A. Schuttrigkeit, T. von Feilitzsch, C. K. Kompa, K. A. Lukyanov, A. P. Savitsky, A. A. Voityuk and M. E. Michel-Beyerle, Femtosecond study of light-induced fluorescence increase of the dark chromoprotein asFP595, *Chem. Phys.*, 2006, **323**, 149 – 160.

[151] L. Schafer, G. Groenhof, A. R. Klingen, G. M. Ullmann, M. Boggio-Pasqua, M. Robb and H. Grubmuller, Photoswitching of the Fluorescent Protein asFP595 : Mechanism, Proton Pathways, and Absorption Spectra, *Angew. Chem. Int. Ed.*, 2007, **119**, 536–542.

[152] J. Merzlyak, E. M.and Goedhart, D. Shcherbo, M. E. Bulina, A. S. Shcheglov, A. F. Fradkov, A. Gaintzeva, K. A. Lukyanov, S. Lukyanov, T. W. J. Gadella and D. M. Chudakov, Bright monomeric red fluorescent protein with an extended fluorescence lifetime, *Nat. Methods*, 2007, **4**, 555–557.

[153] V. Adam, M. Lelimousin, S. Boehme, G. Desfonds, K. Nienhaus, M. J. Field, J. Wiedenmann, S. McSweeney, G. U. Nienhaus and D. Bourgeois, Structural characterization of IrisFP, an optical highlighter undergoing multiple photo-induced transformations, *Proc. Natl. Acad. Sci. U. S. A.*, 2008, **105**, 18343–18348.

[154] V. Adam, B. Moeyaert, C. C. David, H. Mizuno, M. Lelimousin, P. Dedecker, R. Ando, A. Miyawaki, J. Michiels, Y. Engelborghs and J. Hofkens, Rational Design of Photoconvertible and Biphotochromic Fluorescent Proteins for Advanced Microscopy Applications, *Chem. Biol.*, 2011, **18**, 1241–1251.

[155] Y.-T. Kao, X. Zhu and W. Min, Protein-flexibility mediated coupling between photoswitching kinetics and surrounding viscosity of a photochromic fluorescent protein, *Proc. Natl. Acad. Sci. U. S. A.*, 2012, **109**, 3220–3225.

[156] E. Betzig, G. H. Patterson, R. Sougrat, O. W. Lindwasser, S. Olenych, J. S. Bonifacino, M. W. Davidson, J. Lippincott-Schwartz and H. F. Hess, Imaging Intracellular Fluorescent Proteins at Nanometer Resolution, *Science*, 2006, **313**, 1642–1645.

[157] S. T. Hess, T. J. Gould, M. V. Gudheti, S. A. Maas, K. D. Mills and J. Zimmerberg, Dynamic clustered distribution of hemagglutinin resolved at 40 nm in living cell membranes discriminates between raft theories, *Proc. Natl. Acad. Sci. U. S. A.*, 2007, **104**, 17370–17375.

[158] A. Egner, C. Geisler, C. von Middendorff, H. Bock, D. Wenzel, R. Medda, M. Andresen, A. C. Stiel, S. Jakobs, C. Eggeling, A. Schoenle and S. W. Hell, Fluorescence Nanoscopy in Whole Cells by Asynchronous Localization of Photoswitching Emitters, *Biophys. J.*, 2007, **93**, 3285 – 3290.

[159] M. J. Rust, M. Bates and X. Zhuang, Sub-diffraction-limit imaging by stochastic optical reconstruction microscopy (STORM), *Nat. Methods*, 2006, **3**, 793–796.

[160] M. Bates, B. Huang, G. T. Dempsey and X. Zhuang, Multicolor Super-Resolution Imaging with Photo-Switchable Fluorescent Probes, *Science*, 2007, **317**, 1749–1753.

[161] P. Dedecker, G. C. H. Mo, T. Dertinger and J. Zhang, Widely accessible method for superresolution fluorescence imaging of living systems, *Proc. Natl. Acad. Sci. U. S. A.*, 2012, **109**, 10909–10914.

[162] S. W. Hell and J. Wichmann, Breaking the diffraction resolution limit by stimulated emission : stimulated-emission-depletion fluorescence microscopy, *Opt. Lett.*, 1994, **19**, 780–782.

[163] I. Testa, N. T. Urban, S. Jakobs, C. Eggeling, K. I. Willig and S. W. Hell, Nanoscopy of Living Brain Slices with Low Light Levels, *Neuron*, 2012, **75**, 992 – 1000.

[164] T. Dertinger, R. Colyer, G. Iyer, S. Weiss and J. Enderlein, Fast, background-free, 3D super-resolution optical fluctuation imaging (SOFI), *Proc. Natl. Acad. Sci. U. S. A.*, 2009, **106**, 22287–22292.

[165] T. Dertinger, R. Colyer, R. Vogel, J. Enderlein and S. Weiss, Achieving increased resolution and more pixels with Superresolution Optical Fluctuation Imaging (SOFI), *Opt. Express*, 2010, **18**, 18875–18885.

[166] T. Dertinger, M. Heilemann, R. Vogel, M. Sauer and S. Weiss, Superresolution Optical Fluctuation Imaging with Organic Dyes, *Angew. Chem. Int. Ed.*, 2010, **122**, 9631–9633.

[167] K. Dooley and L. I. Zon, Zebrafish : a model system for the study of human disease, *Curr. Opin. Genet. Develop.*, 2000, **10**, 252–256.

[168] G. J. Lieschke and P. D. Currie, Animal models of human disease: zebrafish swim into view, *Nat. Rev. Genet.*, 2007, **8**, 353–367.

[169] A. L. Rubinstein, Zebrafish : From disease modeling to drug discovery, *Curr. Opin. Drug. Discov. Devel.*, 2003, **6**, 218–223.

[170] L. I. Zon and R. T. Peterson, In vivo drug discovery in the zebrafish, *Nat. Rev. Drug. Discov.*, 2005, **4**, 35–44.

[171] R. Milo, P. Jorgensen, U. Moran, G. Weber and G. M. Springer, BioNumbers–the database of key numbers in molecular and cell biology, *Nucleic Acids Res.*, 2010, **38**, D750–D753.

[172] J. Querard, T.-Z. Markus, M.-A. Plamont, C. Gauron, P. Wang, A. Espagne, M. Volovitch, S. Vriz, V. Croquette, A. Gautier, T. Le Saux and L. Jullien, Photoswitching Kinetics and Phase-Sensitive Detection Add Discriminative Dimensions for Selective Fluorescence Imaging, *Ang. Chem. Int. Ed.*, 2015, **127**, 2671–2675.

[173] H. Bouas-Laurent and H. Dürr, Organic Photochromism, *Pure Appl. Chem.*, 2001, **73**, 639–665.

[174] M.-S. Wang, G. Xu, Z.-J. Zhang and G.-C. Guo, Inorganic-organic hybrid photochromic materials, *Chem. Commun.*, 2010, **46**, 361–376.

[175] M. Natali and S. Giordani, Molecular switches as photocontrollable smart receptors, *Chem. Soc. Rev.*, 2012, **41**, 4010–4029.

[176] M. Emond, T. Le Saux, S. Maurin, J.-B. Baudin, R. Plasson and L. Jullien, 2-Hydroxyazobenzenes to Tailor pH Pulses and Oscillations with Light, *Chem. Eur. J.*, 2010, **16**, 8822–8831.

[177] J. Zhang, R. E. Campbell, A. Y. Ting and R. Y. Tsien, Creating new fluorescent probes for cell biology, *Nat. Rev. Mol. Cell. Biol.*, 2002, **3**, 906–918.

[178] E. A. Jares-Erijman and T. M. Jovin, FRET imaging, *Nat. Biotech.*, 2003, **21**, 1387–1395.

[179] H. Wallrabe and A. Periasamy, Imaging protein molecules using FRET and FLIM microscopy, *Curr. Opin. Biotechnol.*, 2005, **16**, 19 – 27.

[180] A. Miyawaki, O. Griesbeck, R. Heim and R. Y. Tsien, Dynamic and quantitative Ca^{2+} measurements using improved cameleons, *Proc. Natl. Acad. Sci. U. S. A.*, 1999, **96**, 2135–2140.

[181] J. W. Lichtman, J. Livet and J. R. Sanes, A technicolour approach to the connectome, *Nat. Rev. Neurosci.*, 2008, **9**, 417–422.

[182] J. Livet, T. A. Weissman, H. Kang, R. W. Draft, J. Lu, R. A. Bennis, J. R. Sanes and J. W. Lichtman, Transgenic strategies for combinatorial expression of fluorescent proteins in the nervous system, *Nature*, 2007, **450**, 56–62.

[183] Y. A. Pan, J. Livet, J. R. Sanes, J. W. Lichtman and A. F. Schier, Multicolor Brainbow imaging in zebrafish, *Cold. Spring. Harb. Protoc.*, 2011, **2011**, 1–8.

[184] Y. A. Pan, T. Freundlich, T. A. Weissman, D. Schoppik, X. C. Wang, S. Zimmerman, B. Ziruna, J. R. Sanes, J. W. Lichtman and A. F. Schier, Zebrabow: multispectral cell labeling for cell tracing and lineage analysis in zebrafish, *Development*, 2013, **140**, 2835–2846.

[185] S. Hampel, P. Chung, C. E. McKellar, D. Hall, L. L. Looger and J. H. Simpson, Drosophila Brainbow: a recombinase-based fluorescence labeling technique to subdivide neural expression patterns, *Nat. Methods*, 2011, **8**, 253–259.

[186] B. A. Krizek, V. Prost, R. M. Joshi, T. Stoming and T. C. Glenn, Developing transgenic arabidopsis plants to be metal-specific bioindicators, *Environ. Toxicol. Chem.*, 2003, **22**, 175–181.

[187] M. Kooshki, A. Mentewab and C. N. S. Jr., Pathogen inducible reporting in transgenic tobacco using a GFP construct, *Plant Sci.*, 2003, **165**, 213 – 219.

[188] M. H. Fethe, W. Liu, J. N. Burris, R. J. Millwood, M. Mazarei, M. R. Rudis, D. G. Yeaman, M. Dubosquielle and C. N. Stewart, The performance of pathogenic bacterial phytosensing transgenic tobacco in the field, *Plant Biotech. J.*, 2014, **12**, 755–764.

[189] M. Padidam, Chemically regulated gene expression in plants, *Curr. Opin. Plant Biol.*, 2003, **6**, 169 – 177.

Résumé

Les milieux biologiques sont des mélanges chimiques d'un intérêt exceptionnel. Leur étude nécessite la conception d'outils analytiques respectant les caractéristiques singulières et contraignantes de ces milieux. Nous avons développé un protocole d'imagerie non-invasif permettant de détecter sélectivement et de quantifier une espèce cible dans un mélange complexe telle qu'une cellule vivante. Notre approche exploite la réponse au premier ordre en quadrature de phase d'une sonde photochrome soumise à une modulation lumineuse périodique. Un cadre théorique complet nous a permis d'identifier les conditions d'illumination qui maximisent cette réponse en ajustant les deux paramètres de contrôle, l'intensité lumineuse moyenne et la fréquence angulaire de l'excitation lumineuse modulée, de sorte à satisfaire des conditions de résonance robustes. La contribution spécifique de la sonde photochrome ciblée au sein d'un mélange de composés interférents (photochromes ou non) est sélectivement extraite du signal global grâce à une détection en quadrature de phase. Après une validation *in vitro*, ce protocole a été appliqué en microscopie de fluorescence pour l'imagerie sélective dans des cellules de mammifères et des poissons zèbres. Cette approche ouvre des perspectives pour l'observation multiplexée dans des échantillons biologiques. Des améliorations ont été apportées au protocole original afin d'atteindre une résolution temporelle suffisante pour la plupart des études dynamiques en biologie.

Mots-clés : méthodes analytiques, dosage sous contrôle cinétique, sondes photochromes, modulation lumineuse, détection en quadrature de phase, imagerie sélective en fluorescence.

Abstract

Biological media are chemical mixtures of exceptional interest. Their investigation requires conceiving analytical tools fulfilling the singular and demanding features of these media. We have designed a non-invasive imaging protocol allowing to selectively detect and quantify a given target in a complex mixture such as a living cell. Our approach relies on the first order out-of-phase response of a targeted photoswitchable probe to periodic light modulation. An extensive theoretical framework enabled us to identify the illumination conditions that maximize this response by appropriately tuning the two control parameters, the average light intensity and the radial frequency of the modulated light excitation, so as to satisfy robust resonance conditions. The specific contribution of the targeted probe within a mixture of interfering species (photoswitchable or not) is selectively retrieved from the overall signal thanks to quadrature detection. After *in vitro* validation, this protocol was applied in optical fluorescence microscopy for selective imaging in mammalian cells and zebrafish. This approach opens attractive perspectives for multiplexed observations in biological samples. Further refinements allowed to reach a temporal resolution relevant for most dynamic studies in biology.

Keywords : analytical methods, titration under kinetic control, photoswitchable probes, light modulation, quadrature detection, selective fluorescence imaging.